Stress Corrosion Cracking of Low Pressure Steam Turbine Blade and Rotor Materials

By

Claire Louise Verona

Department of Materials

A doctoral thesis submitted in partial fulfilment of the requirements for the award of Doctor of Philosophy

September 2010

Abstract

Stress corrosion cracking of a 14 wt% Cr martensitic stainless steel, with commercial names PH-15Cr5Ni, FV520B or X4CrNiCuMo15-5, used for the manufacture of low pressure turbine blades, has been studied with the intention of gaining a better understanding of the processes involved, how they occur and why. Industrially this is very important as stress corrosion cracking is considered to be a delayed failure process, whereby microscopic cracks can potentially propagate through a metal undetected until catastrophic failure occurs. The aim of this work is to establish links between crack length and external factors, such as exposure time, in order to devise a method of dating stress corrosion cracks and therefore predicting their possible occurrence in-service.

Within the current literature there are three main theories used to describe the possible mechanisms of stress corrosion cracking, which are the mechanical-electrochemical theory, the electrochemical theory and the adsorption theory, although no definitive explanation has been determined.

To simulate the conditions experienced by low pressure turbine blades and rotors in steam power plant, Wedge Opening Loading (WOL) and Single Edge Notched Bend (SENB) test specimens have been stressed and exposed to condensing steam at 95°C for approximate times between 0.7 and 98.3 kh. A set of unstressed "Free Surface" specimens were also exposed to condensing steam at 95°C for comparison with the WOL and SENB specimens. The results of the examination of these specimens are presented and discussed in this thesis.

Evidence has been found linking crack length and oxide development to exposure time for the WOL specimens. Crack length is most likely related to exposure time but relative to the stress intensity at the crack tip, because higher initial stress intensity values may promote earlier crack initiation and hence longer crack growth.

Acknowledgements

Firstly, thanks must be given to Loughborough University's Department of Materials and the Loughborough Materials Characterisation Centre (LMCC) for the provision of the research facilities that have made this study possible.

I would like to express my gratitude to the EPSRC and Alstom Power Materials Research, Rugby, for their financial support and for supplying test specimens.

I sincerely appreciate the supervision, guidance and friendship of Dr Rebecca Higginson throughout this project.

I am very grateful to Dr Geoff West for sharing his electron microscopy expertise and for always having time to help me.

I would like to thank Dr Simon Hogg and Dr Caroline Kirk for their combined help with X-ray Diffraction analysis and without them I would not have been fortunate enough use the Diamond Light Source Synchrotron in Oxford. On that theme I would like to acknowledge Dr Paul Quinn for his expert knowledge of the I18 beam line, Enzo Liotti for helping me to collect and analyse the data and the Natural History Museum for the provision of reference samples.

I gratefully acknowledge the academic, technical and administrative staff for their help, with special thanks to Professor Rachel Thomson, Andy Woolley, Trevor Atkinson, Mac Callender and Pat Storer.

I would like to thank Mark Jepson, Nick Riddle and Dan Child for their friendship and willingness to help.

Finally I would like to thank Chris Keogh for his endless support, encouragement and patience.

Contents

1. Introduction

In 1831 Michael Faraday noticed that a small current was produced in a loop of wire when rotated between the poles of a stationary magnet. This proved to be the first recorded evidence of the discovery of modern electricity generation, as it demonstrated that electricity can be generated from moving machinery and does not rely on the use of chemical batteries (Foster and Parfitt, 1970). Nowadays the world is heavily dependent on the generation of electricity; the UK alone consumes approximately 300 billion kWh every year, a figure that is ever increasing.

Electricity can be produced from combustion of fossil fuels such as oil, coal and gas, by nuclear fission or by harnessing the energy of the earth in the form of wind, solar, hydro, tidal and geothermal (Breeze, 2005). The majority of the UK's electricity is produced by coal fired power stations with a smaller amount produced from gas fired power stations and wind turbines. Apart from finite fuel supply, the issue with fossil fuelled power generation is pollution from particulate, CO_2, SO_x and NO_x. This has lead to a drive towards electricity production from renewable sources, with limited success to date. So, for the foreseeable future the UK will be reliant on electricity generated by fossil fuelled power stations.

There are continuing efforts to reduce pollution from coal fired power stations. CO_2 has been reduced in some stations by a process called boiler overfire air (BOFA) in which extra air is injected near the top of the boiler to improve combustion. NO_x was found to be caused by high temperature flames so the burners have been detuned to reduce the temperature and hence the amount of NO_x. Some stations are going a stage further and retrofitting a selective catalytic reduction (SCR) system in which ammonia is injected into the flue gas, and with the help of a catalyst, a chemical reaction takes place which results in nitrogen and water being emitted from the stack instead of NO_x. Pollution from SO_x has been reduced by the addition of flue gas desulphurisation (FGD). The flue gas is mixed with limestone which results in the production of gypsum which is sold to the building trade to make products such as plasterboard. Electrostatic

precipitators filter out most of the particulate that would otherwise be emitted from the stack.

All of these additional systems require electricity, which is siphoned off the power station, reducing the efficiency and hence the output of electricity to the national grid. With the UK's energy demand ever increasing, it is necessary to increase the efficiency of existing power stations to the maximum achievable. This is generally done by aiming for higher steam temperatures and pressures whilst reducing the back pressure. Unfortunately harsher conditions push power plant materials to their limit, causing various phenomena which need investigating so that their future occurrence can either be prevented or predicted.

The aim of this investigation is to gain a better understanding of the phenomena known as stress corrosion cracking (SCC). This is a process which can occur in metals that are subject to stress whilst in a corrosive environment and can lead to catastrophic failure with very little external warning. The majority of the tubes, pipes, headers etc in coal fired power plant are fairly immune to SCC due to the high temperatures that produce very dry steam conditions. Furnace wall tubes suffer from fireside corrosion and sootblower erosion or steam side oxidation and erosion. Headers and pipes suffer from creep as they are subject to high steam temperature under loading for long periods of time.

SCC is a particular problem in low pressure steam turbine blades where the steam temperature and pressure falls below the saturation point and produces water droplets and wet steam. Water droplets cause erosion of the low pressure turbine blades; this can aid pit formation which is often a precursor for SCC initiation. Wet steam condenses onto the blades, creating the corrosive environment to add to the stresses induced by blade rotation, which is usually around 3000 rpm. Condensation of steam also leads to the deposition of corrosive species such as chlorides and sulphates which are carried over in the steam from around the power plant. This can be a particular problem when a generating unit is on a two-shifting operating regime. In this instance, corrosive species repeatedly dissolve into and precipitate out of solution, gradually becoming more aggressive as more species are carried over in the steam.

SCC of various materials in various environments has been studied for many years by numerous investigators. From this, a lot of insight into the phenomenon has been gained, but there is still much debate on most of the key issues. There are several

theories as to the mechanisms of SCC, but no definitive explanation. In many cases, authors have conducted seemingly identical experiments but achieve contradictory results. There is also a lot of work written about SCC experiments in concentrated corrosive solutions, but not so much relating to the steam conditions experienced by low pressure steam turbines.

At present, SCC initiation, propagation and final failure cannot be reliably predicted so components such as low pressure turbines have to be regularly shut down and inspected using non destructive techniques to either identify new cracks or monitor existing cracks. This is a very costly exercise, not just because non destructive testing techniques are time consuming, require specialist equipment and highly trained operatives to interpret the results, but also because every second a turbine is not running is a loss in electricity generation and loss of profit to electricity companies.

In recent years there have been some high profile low pressure turbine blade and rotor failures as a result of SCC, which were not only financially costly, but in some instances have resulted in the loss of human life. As such, electricity generating companies tend to err on the side of caution and schedule inspections more frequently.

The aim of this project is to gain a better understanding of SCC in low pressure steam turbine blade and rotor materials. This will be achieved by examining test specimens fabricated from the same material as that used to make low pressure steam turbine blades and rotors. The steam and stress conditions experienced by these components in-service have been recreated to the best standard that is reasonably practicable. Test specimens have been exposed to condensing steam at 95°C for various times under different loads. This project is dedicated to the examination of SCC test specimens with the aim to link together variables such as exposure time and crack length.

It is hoped that eventually, SCC could be more reliably predicted so that there could be more confidence that low pressure turbines are running safely and inspections intervals could be determined appropriately.

2. Literature Review

In this Chapter the literature related to the project is reviewed and discussed. Firstly the generation of power from renewable and non-renewable fuel sources is described with particular attention given to electricity generated from coal-fired steam power plant as this is the most common method used in the UK. Next steam turbines are discussed in detail including design, type and materials, which outlines the main area of interest of this project. Possible turbine failure types are described such as creep and fatigue in addition to the main types of corrosion, which is followed by information on the oxidation of iron and its alloys. Finally stress corrosion cracking is discussed with regards to its mechanisms and testing methods.

2.1. Power Generation

The modern world relies on the generation of electricity. Although the basic principle for electricity generation remains unchanged, there are many methods by which it can be achieved using both renewable and non-renewable sources. Table 2.1 shows data for the United Kingdom's power generation, consumption, importation and exportation between 1993 and 2003. Throughout the reported period net consumption progressively increased from 296.2 billion kWh to 346.1 billion kWh. Approximately two thirds of the UK's power was generated from conventional thermal methods, with coal as the preferred fuel. There were minor fluctuations in the quantity of power generated by hydroelectric and nuclear methods and there was a progressive increase in geothermal/solar/wind/biomass power from 1.5 to 7.1 billion kWh. This information highlights the need for increased power plant efficiency to accommodate the UK's future demands.

Table 2.1: Energy generation, consumption, importation and exportation data in billion kWh for the United Kingdom between 1993 and 2003 (reproduced from http://www.cslforum.org/uk.htm, date viewed 18/04/2007).

	Year										
	1993	1994	1995	1996	1997	1998	1999	2000	2001	2002	2003
Net Generation	300.5	302.8	308.2	329.2	327.4	340.8	344.6	353.2	361.4	360.1	369.9
Hydroelectric	4.2	5.0	4.8	3.4	4.1	5.1	5.3	5.0	4.0	4.7	4.5
Nuclear	84.9	83.9	84.5	89.9	93.2	94.5	90.4	80.8	85.4	83.6	84.5
Geo/solar/wind/biomass	1.5	2.1	2.3	2.6	3.1	3.9	4.6	5.0	5.7	6.3	7.1
Conventional thermal	209.8	211.8	216.6	233.3	226.9	237.4	244.3	262.4	266.3	265.5	273.7
Net Consumption	296.2	298.5	303.0	322.8	321.0	329.5	344.7	342.7	346.5	343.3	346.1
Imports	16.7	16.9	16.4	16.7	16.6	12.6	14.5	14.3	10.7	9.2	5.1
Exports	0.0	0.0	0.0	0.0	0.0	0.2	0.3	0.1	0.3	0.8	3.0

2.2. Steam Power Plant

The majority of the electricity in the UK and around the world is generated by steam power plant, whereby fossil fuel is combusted to heat water into superheated steam, which is used to transfer heat energy into rotational kinetic energy and then into electrical energy. The use of fossil fuels has a large environmental impact and there is considerable debate into the use of the renewable energy sources, however these technologies are not yet sufficiently advanced to meet the global energy demand.

2.2.1. Coal Combustion

Large worldwide coal reserves, in combination with vast experience and expertise associated with its successful use, have made coal one of the most viable solutions to the World's future energy demands (Viswanathan and Bakker, 2000). In the 2001 Survey of Energy Resources carried out by the World Energy Council it was reported that 38% of the World's electricity was produced from the combustion of coal (Breeze, 2005). Pulverised Coal Combustion (PCC) technology has been developed over several decades and is used to produce more than 90% of coal fired electricity within thousands of power plant around the world. PCC can be used with numerous coal grades, except those with high ash content (Viswanathan and Bakker, 2000). Figure 2.1 is a schematic of a coal fired power plant showing the successive stages of power generation. Coal is delivered to the rail unloading house (Figure 2.1 No. 1) where is it unloaded onto the coal conveyor, (Figure 2.1 No. 3) and transported to the boiler bunker, (Figure 2.1 No. 4). When the coal is required it is put through the coal feeder (Figure 2.1 No. 6) into the pulverising mill (Figure 2.1 No. 7) where it is ground into a fine powder. For a bitumous coal less than 2% of the particles can be larger than 300 μm with 70-75% of particles smaller than 75 μm (Viswanathan and Bakker, 2000). Pulverised coal is mixed with some combustion air (Figure 2.1 No. 8) and blown through the burners (Figure 2.1 No. 9) into the furnace where it is combusted within the temperature range 1300°C - 1700°C, depending on the coal grade, for 2-5 seconds in which time complete burnout must occur (Foster and Parfitt, 1970).

1. Rail Unloading House	2. Junction House	3. Coal Conveyor	4. Boiler Coal Bunker	5. Bucket Wheel Machine
6. Coal Feeder	7. Pulverising Mill	8. Primary Air Fan	9. Boiler Burners	10. Boiler
11. Forced Draught Fan	12. Air Heater	13. Electrostatic Precipitator	14. Induced Draught Fan	15. Main Chimney
16. Superheater	17. High Pressure Turbine	18. Boiler Reheater	19. Intermediate Pressure Turbine	20. Low Pressure Turbine
21. Rotor	22. Stator	23. Generator Transformer	24. Condenser	25. Condensate Extraction Pump
26. Low Pressure Feed Heaters	27. Deaerator	28. Boiler Feed Pump	29. High Pressure Feed Heaters	30. Economiser
31. Steam Drum	32. Cooling Tower	33. Circulating Water Pumps	34. Circulating Water Make-Up	35. FGD Absorber Tower
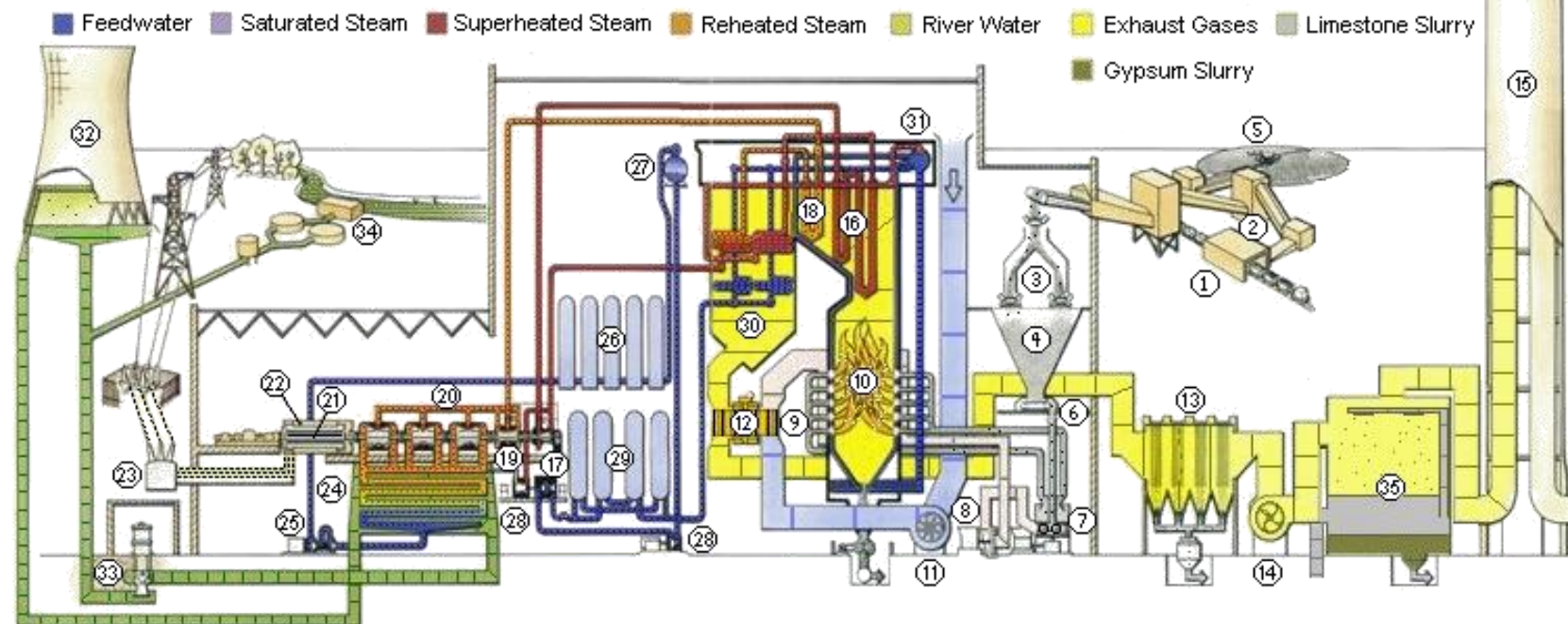
Figure 2.1: Schematic of Drax power station showing the successive stages of power generation (http://www.draxpower.com, viewed 20/04/2007).

2.2.2. Steam Path

The steam plant boiler consists of a large furnace connected to many metres of steel pipes and tubes. Warm water is fed through the boiler in tubes where the heat from the combustion of coal is used to transform the water into steam. The steam moves into the superheater (Figure 2.1 No. 16), which consists of multiple tubes that fit closely together in rows which make up the pendants. At Drax power station the steam exits the final superheater pendant at ~568°C/166 bar, but this figure is different for every power station. It is transferred to the high pressure (HP) turbine where it enters at 565°C/156 bar. The steam expands through the HP turbine giving exhaust conditions of 340°C/42 bar (http://www.draxpower.com, viewed 20/04/2007). The steam is collected and transferred to the boiler reheater (Figure 2.1 No. 18), where it reaches the same temperature as the superheater but not such high pressure. The reheated steam then leaves the boiler for the final time, entering the intermediate pressure (IP) turbine (Figure 2.1 No. 19) at 565°C/40.2 bar and then the low pressure (LP) turbines (Figure 2.1 No. 20) at 306°C/6.32 bar (http://www.draxpower.com, viewed 20/04/2007)

2.2.3. Electricity Generation

When steam is fed into a turbine it rotates blades that are attached to a central shaft, which is connected to the rotor (Figure 2.1 No.21). The rotor is a large electromagnet housed inside a cylinder of copper windings called the stator (Figure 2.1 No.22) and together these make up the generator. Rotation of the rotor within the stator generates an alternating electric current. The electricity then travels into the generator transformer (Figure 2.1 No.23) where it is converted from 22,000 V to 400,000 V and entered on to the national grid transmission system (http://www.draxpower.com, viewed 20/04/2007). Turbines are discussed in more detail in Section 2.3.

2.2.4. Water Recycling

No more useful energy can be efficiently extracted from the steam that leaves the LP turbines so it is recycled. The steam is passed to the condenser, (Figure 2.1 No. 24), which consists of many small tubes filled with cooling river water into which heat from the steam is transferred. The condensate is pumped (Figure 2.1 No. 25) though a series of LP feed heaters (Figure 2.1 No. 26) from which it exits at 160°C. This feed water is deaerated (Figure 2.1 No. 27) and pumped into the HP feed heaters where the temperature reaches 252°C (http://www.draxpower.com, viewed 20/04/2007). This

water passes through the economiser (Figure 2.1 No. 30) where the temperature is raised to 292°C using heat from the flue gases (http://www.draxpower.com, viewed 20/04/2007). The feedwater then travels into the steam drum (Figure 2.1 No.31) and back into the boiler (Figure 2.1 No. 10), completing the cycle.

The warm water in the condenser tubes is sprayed into cooling towers (Figure 2.1 No. 31), approximately a quarter of the way up (http://www.draxpower.com, viewed 20/04/2007). The water falls through honeycombed plastic packing creating a very fine spray that is cooled by an up draught of air (E.ON UK, 2004). Some of the water evaporates into the atmosphere as steam but most of the water condenses into droplets that fall like rain into the "pond" at the bottom of the towers. From here it is pumped back into the condenser tubing.

2.2.5. Environmental Protection

The combustion of coal releases gases that can potentially harm the environment so care is taken to minimise any detrimental effects. Initially the boiler flue gas is passed through electrostatic precipitators to remove particulates. The flue gas then enters the bottom of the flue gas desulphurisation tower (Figure 2.1 No. 35) and is cooled by water that is added primarily to eliminate any solid material at the inlet. The coarse pulverised fuel ash is cleaned by a recirculating limestone slurry. A convenient by-product of this process is gypsum, which is pumped into a settling pit. The water is removed with a hydrocyclone system (http://www.draxpower.com, viewed 20/04/2007). The final product is sold to the building trade or made into building blocks (E.ON UK 2004).

2.3. Steam Turbine

It is in the steam turbine that useful work is done; energy is captured and transferred to generate electricity (Foster and Parfitt, 1970). Within the turbine high enthalpy steam expands in the stationary blades, called nozzles, which causes a decrease in pressure. There is a corresponding increase in velocity and therefore kinetic energy, which is converted into mechanical energy as the moving blades rotate at 3000rpm. This in turn generates electrical energy as explained in Section 2.2.3 (Kearton, 1964).

The life expectancy of a turbine in the UK is approximately 30 years (Kearton, 1964). In this time a turbine will be subjected to numerous stresses including: thermal due to start up and shut down, rotational and centrifugal due to movement of the blades

attached to the central disc and rotor as well as internal pressure on the casing due to the containment of high pressure steam (Wyatt, 1976). For the first part of a turbine's life it operates continually and for the second part it is shutdown each weekend (Wyatt, 1976). Over the third and longest period it is subject to a two shifting regime in which it is on load during the day and shut down overnight. This continues for approximately 10,000 cycles of 16 h and is therefore where most of the stresses are incurred. For the last part of its life it is used only at times of peak demand (Wyatt, 1976). In the LP turbines the presence of steam combined with the high stresses induced by blade rotation, give the potential for stress corrosion cracking (SCC) problems, which is the focus of this project and will be discussed in more detail in Section 2.11(Wyatt, 1976).

2.3.1. Turbine Types

Turbines that maintain steam pressure throughout are called impulse or back-pressure turbines. If the exit pressure is less than the inlet pressure they are called an impulse-reaction or condensing turbines (Kearton, 1958 and Kiameh 2002).

In impulse turbines, the steam is ejected at the same pressure as it entered so their size is uniform throughout (Kiameh, 2002). In condensing turbines the steam pressure decreases as it passes so they must be bigger at the exhaust end due to a greater volume of steam.

Steam turbines with power ratings of 40-60 MW are most often single-cylinder units whereas power stations such as Ratcliffe-on-Soar and Didcot (E.ON UK, 2004) have power outputs of around 2000 MW so use multiple cylinders, called compound turbines, to extract the most energy from the steam (Kiameh, 2002). Compound turbines consist of one HP turbine with between one and four LP turbines and sometimes an IP turbine; however, there are usually no more than five turbines in total. They can be positioned in groups next to each other on two or more shafts, known as cross compound, or successively along a single shaft, called tandem compound as shown in Figure 2.2 (Wyatt, 1976). The HP and IP turbines experience inlet temperatures around 565°C (Wyatt, 1976) and the exhaust steam of the low pressure turbine is close to 40°C (S. Osgerby Private Communication, 2006).
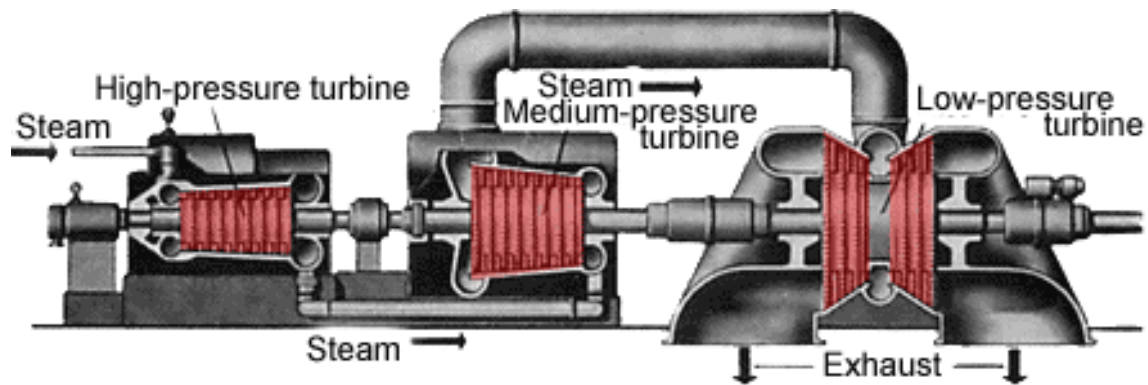
Figure 2.2: Diagram of high, medium and low pressure steam turbines in tandem compound arrangement (http://library.thinkquest.org/C006011/english/sites/dampfturbine.php3?v=2, date viewed 20/05/2007).

2.3.2. Turbine Rotor

Rotors are the largest and highest quality steel products in a turbine. HP and IP turbines operate at high temperature but under moderate stresses, so high temperature strength and creep resistance are important for material selection. The extra stresses induced by the long blades in LP turbines means that the rotor proof stress requirements are greater than for HP or IP turbines (Kearton, 1964). The low operating temperature and high stresses also means that the steel used must have high fracture toughness (Wyatt, 1976). Rotors must also cope with erosion and corrosion from the steam. Built up rotors are often used for low pressure steam turbines. They are unsuitable for HP turbines as the interference fit would disappear if the material was heated into its creep range. The use of "shrunk on discs" can be a problem because two large discs close together can result in stress raisers at the shaft surface. This effect can be accentuated by fabrication defects or pitting from environmental attack (Wyatt, 1976).

The shaft operates at a lower temperature than the working steam so steam condenses on the shaft and evaporates off again. Dissolved impurities that are carried over from the boiler tend to precipitate in crevices and then dissolve in the next cycle of condensed steam. Over many cycles the local concentration of these solids can become very high (Wyatt, 1976). This can lead to the initiation of cracks which can propagate in pure steam. This is called stress corrosion cracking (SCC) which is discussed in detail in Section 2.11(Wyatt, 1976). The material chosen for low pressure rotors must have good corrosion resistance to prevent environmental attack (Kearton 1964).

2.3.3. Turbine Blades

The working part of a turbine blade is a curved aerofoil (10 mm - 1800 mm) that is twisted gradually along the length (Wyatt, 1976). HP and IP turbines contain mainly small blades whereas LP turbines contain much larger blades. Nozzles are normally attached to the turbine casing which is split into two sections that are bolted together. The moving blades are attached to the rotor. Blades are perfectly balanced as any variation in the centre of gravity would induce massive additional stresses in the turbine (Kearton, 1964). A complete ring of nozzles and blades are held together in a diaphragm. Collectively these make up one stage and a turbine consists of multiple stages of varying diameter (Wyatt, 1976).

During service turbine blades experience high temperatures, corrosive environments and cyclic bending stresses so blades must be designed properly to minimise the induced in-service stresses. If the frequency of the vibrations caused by cyclic stresses were to match the fundamental frequency of the turbine blade material, then simple harmonic motion would be set up. In this instance the stresses induced would exceed that of the material's fatigue strength and premature failure would occur (Wyatt, 1976). For this reason turbine blade design is very important.

Minute water droplets are contained in steam from the boiler. Condensation can be caused by expansion of steam in the nozzles (Kearton, 1964) or by parts such as the rotor which may operate below the steam temperature, particularly in the LP turbines (Wyatt, 1976). Water reduces the efficiency of the nozzles and blades. The impact of water droplets at high velocity can induce local stresses enough to erode the blade surface material. This effect becomes more apparent where the steam is wettest, i.e. the last stages of the low pressure turbine. The reheat stage of the steam power plant cycle helps to reduce the overall steam wetness in the LP turbines (Kearton, 1964)

2.3.4. Turbine Blade Manufacture

Historically ingots of steel for steam turbine blades have been produced by either high frequency or consumable arc re-melting and forged into bar stock (Wyatt, 1976). These are then manufactured into blades by a combination of cold drawing, rolling and machining (Kearton, 1958) or are hand forged to a near net shape (Wyatt, 1976). For small blades the final forging stage is achieved with either drop stamping or rolling

through shaped rolls, however, larger blades are often machined using copy milling (Wyatt, 1976).

2.3.5. Turbine Blade Attachment

Turbine reliability is dependent upon successful blade attachment. The stresses in attachment sections can be high, particularly in large LP turbines. It is difficult to accurately calculate the exact values because there is potential for stress concentrations at sharp corners (Kearton, 1964). Turbine blades can be attached to the central rotor by a number of different methods including rivets, circumferential slots, De Laval attachment or inverted T attachment (Wyatt, 1976). The choice of attachment is important because it may alter the shape of the wheel rim, add stresses to the system, or increase the necessary length of the turbine (Kearton, 1964). The favoured technique is the use of "fir tree roots", an example of which is shown in Figure 2.3. The blade root is known as the male end, which fits quite loosely into the corresponding female slot and is secured by riveted pegs or circlips. The roots are designed to be loose fitting to damp the in-service vibrations but the drawback of this is that steam can pass through the gaps and potentially cause problems with stress corrosion cracking.
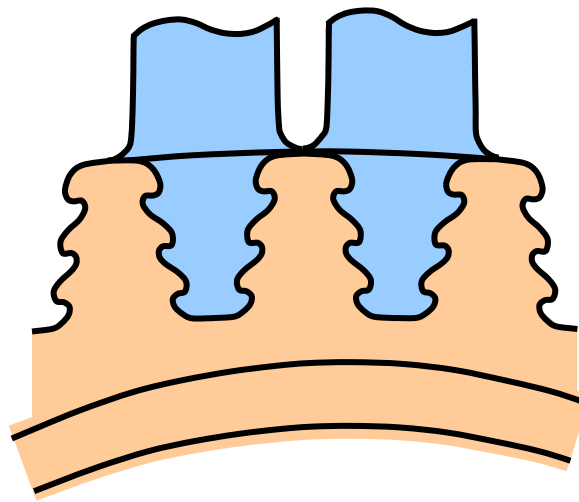
Figure 2.3: Diagram showing the fir tree blade root attachment method for turbine blades (Lyle and Burghard, 1982).

2.3.6. Turbine Blade Materials

All material selections should be made after carefully considering the service conditions that will be experienced. HP and IP turbines operate at the highest temperatures so their material must be chosen accordingly. The LP turbines experience much lower

temperatures: however, the steam condenses and is therefore wet, so the material selected for their manufacture must have sufficient corrosion and erosion resistance (Kearton, 1958).

Most steam turbine blades can be produced from 12 wt% Cr steels. Exceptions to this are the LP exhaust blades, in excess of 1 m length, which require superior strength and the first row HP blades that operate around 565°C, which need better creep strength. The mechanical properties of 12 wt% Cr steels can be improved by the addition of molybdenum and vanadium in combination with well designed heat treatments, however, they are generally chosen for their corrosion resistance to hot steam and moist air (Wyatt, 1976). Additions of nickel hinder the development of δ ferrite, but are normally restricted to 0.6 wt% to prevent any loss of creep strength. To increase the short term properties of stress rupture and creep strength niobium can be added but it has been shown that the strengthening effect of niobium carbides decreases over time making them no better than ordinary 12 wt% Cr, Mo, V in the long term. Additions of 1 wt% tungsten have been shown to give a slight improvement to stress rupture strength (Wyatt, 1976).

2.4. Stainless steel

Stainless steels contain 11-30 wt% chromium, which makes them resistant to staining, pitting and corrosion in atmospheric conditions (Parr and Hanson, 1966). They are utilised in applications that require good surface finish and in high temperature environments where oxidation resistance throughout long time service is necessary. Stainless steels are also used for construction purposes due to their excellent formability and joining capabilities. The major disadvantage of these steels is that they are more expensive than plain carbon steels (Parr and Hanson, 1966).

It is generally accepted that stainless steels can be categorised into six different groups depending on their composition and structure: ferritic, martensitic, austenitic, manganese-substituted austenitic, duplex austenitic-ferritic and precipitation hardening (Lula, 1985).

2.4.1. Ferritic Stainless Steel

Ferritic stainless steels have a body centred cubic (bcc) crystal structure (Bhadeshia and Honeycombe, 2006). They typically contain 11-27 wt% chromium, no nickel and up to 0.2 wt% carbon (Parr and Hanson, 1966). They have good ductility and can be

easily drawn but they have poor toughness. Ferritic stainless steels with 11-14 wt% chromium have the lowest corrosion resistance and are used for structural purposes. Steels from the 17-19 wt% chromium group have better corrosion resistance and are commonly used for automotive trim and applications where aesthetics are important. The steels with 22-27 wt% chromium are used for high temperature applications because they have the best corrosion and oxidation resistance (Lula, 1985).

2.4.2. Martensitic Stainless Steel

Martensite can be formed when a stainless steel with an appropriate composition is quenched to room temperature. It is considered to be a diffusionless, shear transformation from austenite because no atoms diffuse and the carbon is retained in solid solution (Petty, 1970). Martensite can be characterised by thin laths or plates in the microstructure (Bhadeshia and Honeycombe, 2006). Martensitic stainless steels can be classified as either low or high carbon with a threshold set at 0.15 wt% C. Low carbon martensitic steels also have relatively low chromium content or else the steel would be ferritic, whereas high carbon steels can tolerate up to 18 wt% (Lula, 1985).

2.4.3. Austenitic Stainless Steel

Austenitic stainless steels have a face centred cubic (fcc) crystal structure similar to that of high temperature iron (Bhadeshia and Honeycombe, 2006). Alloying additions, usually nickel, are used to stabilise the austenitic structure at room temperature. The most common composition is 18 wt% chromium and 8 wt% nickel (Lula, 1985). These steels are used for many applications because they are easy to form and weld whilst maintaining good corrosion properties. Some austenite transforms to martensite during cold working of metastable 18-8 wt% steels, but additions of 10-13 wt% nickel stabilise austenite further and prevent this. Additions of 2-4 wt% molybdenum produce steels with increased stress rupture strength and high temperature creep resistance as well as providing superior corrosion resistance, particularly to pitting and crevice corrosion in chloride environments (Lula, 1985). Methods to prevent sensitisation include reducing the carbon concentration or adding titanium and niobium. The steels with the most chromium and nickel have the best high temperature strength and oxidation resistance, which is helped by small additions of silicon. Machineability can be improved by the addition of sulphur and selenium but corrosion resistance is reduced (Lula, 1985).

2.4.4. Manganese Substituted Austenitic Stainless Steel

Manganese-substituted austenitic stainless steels are those where approximately 4 wt% of the nickel used to stabilise the austenite is exchanged for 7 wt% manganese and up to 0.25 wt% nitrogen. The resulting steels are less expensive to produce, have reduced density and 40% increased yield strength with no loss of ductility or corrosion resistance (Lula, 1985).

2.4.5. Duplex Austenitic-Ferritic Stainless Steel

Duplex austenitic-ferritic stainless steels have a combination of fcc and bcc crystal structures and have compromised properties, which depend on the proportions of each phase. In general duplex stainless steels are stronger and have better resistance to stress corrosion cracking in chloride environments than austenitic stainless steels and have better toughness than ferritic stainless steels (Lula, 1985).

2.4.6. Precipitation-Hardening Stainless Steel

Precipitation-hardening stainless steels are created when carbides are allowed to form through aging a metastable supercooled solid solution. This low temperature treatment can be carried out on components after fabrication, which results in otherwise unattainable properties. This group of steels can be further categorised as martensitic and austenitic precipitation hardening stainless steels (Lula, 1985).

2.5. Failure Mechanisms

A metal may fracture when it is subject to applied load, whether it be tensile, compressive, shear or torsional. Ductile failure is easily identified by the characteristic "cup and cone" fracture surface produced when small cavities coalesce alongside localised necking (Callister, 2000). Brittle fracture may be transgranular or intergranular and produces a relatively flat fracture surface. Crack propagation is quick, perpendicular to the applied stress and shows little external warning before failure occurs.

Fatigue is the result of a metal being subject to cyclic loading over a substantial time period and failure occurs at stresses lower than the recorded tensile strength (Dieter, 1986). Fatigue is very important because brittle catastrophic failure occurs with little prior warning and reportedly accounts for approximately 90% of all failures in metals

(Callister, 2000). The fracture often initiates from a stress concentration and propagates perpendicular to the applied stress, resulting in a striated characteristic fracture surface of alternate smooth and rough sections. The smooth sections are a result of metal surfaces rubbing together and the rough surfaces are where that section of the metal has failed (Dieter, 1986).

Creep is a time dependent and high temperature failure mechanism that occurs at approximately $0.4T_m$ or above and under constant load, where T_m is the absolute melting temperature of the metal (Callister, 2000). Figure 2.4 shows the three stages of creep: primary, secondary and tertiary before fracture occurs (Dieter, 1986). In the first stage the metal experiences strain hardening as its creep resistance increases. The second stage is a steady state phase where the rate of strain hardening is equal to that of the material's recovery. The final stage is an increase in strain hardening before failure occurs.
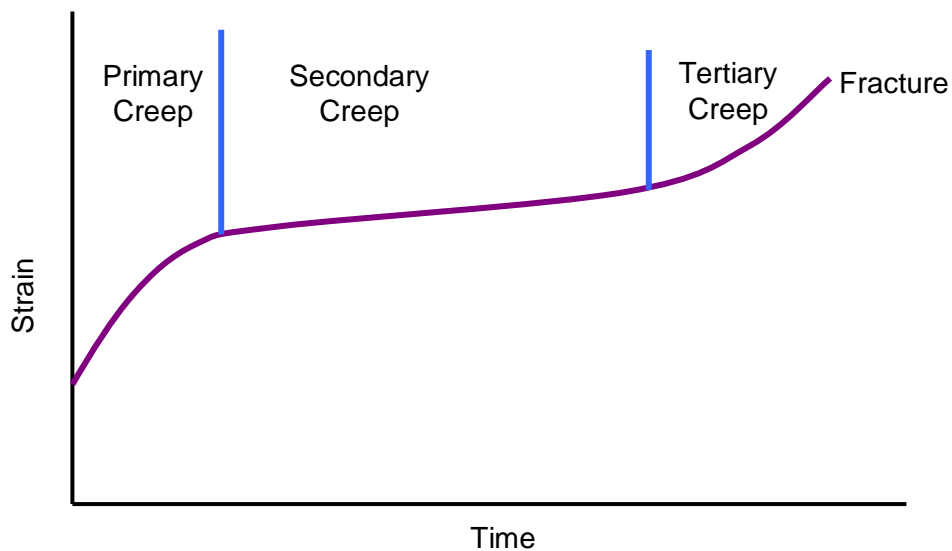
Figure 2.4: Schematic of the three stages of creep: primary, secondary and tertiary (following Dieter, 1986).

All the turbines in power stations suffer from fatigue in one form or another. Thermal fatigue is an increasing problem due to two-shifting power stations that were designed to base load. As mentioned previously, the first rows of the HP and IP turbine blades operate around 565°C which is within the creep regime for many metals. The materials and design of HP and IP turbine blades are carefully chosen to minimise the effect of creep. The LP turbines do not operate in the creep regime. LP turbine blades suffer more from insufficient tensile strength due to the large size of the last row blades but

more importantly they suffer from corrosion and erosion from the water droplets in the wet steam.

2.6. Corrosion

When a material is chemically attacked it is called corrosion. For corrosion to occur there must be two electrochemical reactions (with a flow of electrons), oxidation and reduction, occurring simultaneously and in equilibrium (Talbot and Talbot, 1998).

2.6.1. Types of Corrosion

The main types of corrosion are shown in Figure 2.5 categorised by how easily they can be identified: Group I is under visual inspection, Group II is with special inspection equipment and Group III is by microscopical investigation.
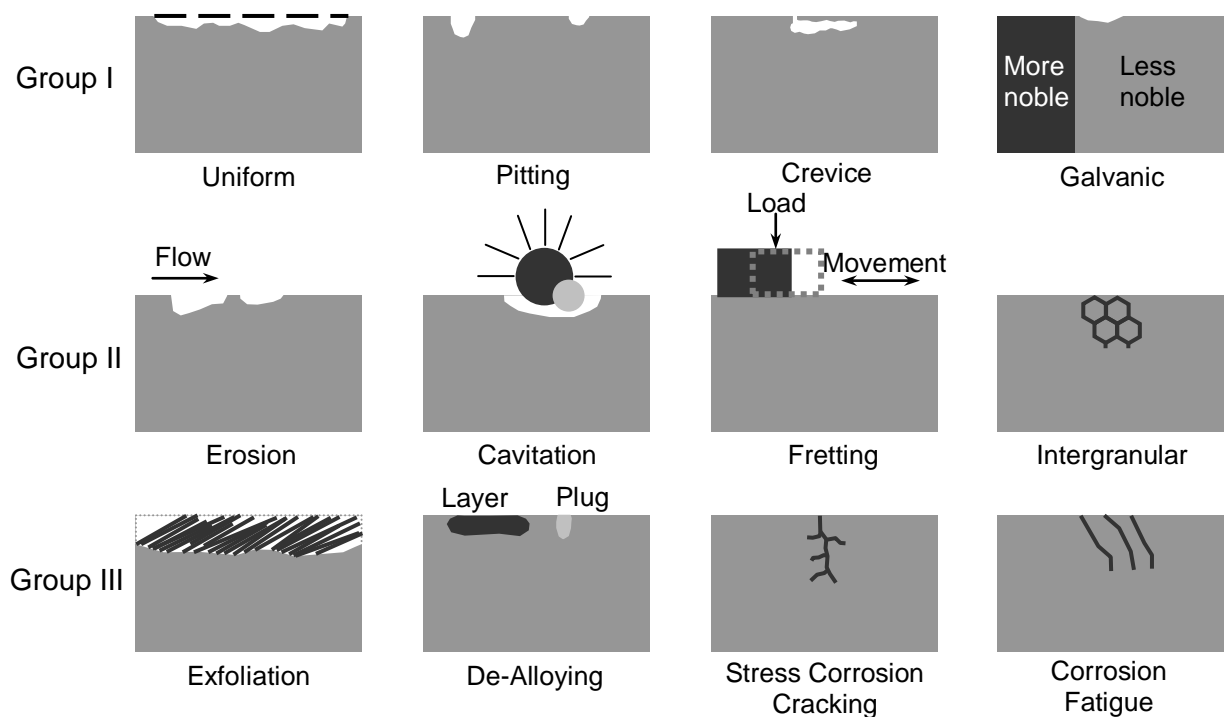
Figure 2.5: Types of corrosion categorised by how easily they can be identified, Group I: identified by visual inspection, Group II: identified with the aid of special inspection equipment and Group III: identified by microscopical investigation (following Roberge, 2000).

Uniform corrosion is that which occurs consistently over the whole surface or a major portion of the surface. Although uniform corrosion depletes the greatest quantity of material it is easily detected and monitored so catastrophic failures are avoided (Roberge, 2000). In pitting corrosion, cavities form when localised regions are

preferentially attacked. This type of corrosion is harder to detect than uniform corrosion because the pits that form often become filled with corrosion products. Small diameter pits can cause catastrophic failure with minimal warning or metal loss as propagation is promoted by the localised corrosive microenvironment (Roberge, 2000).

Crevice corrosion is similar to pitting corrosion, however, it is generally caused when corrosive media remains stationary in a discrete region. The many shapes that crevices can take are shown in Figure 2.6 (Roberge, 2000).

Narrow, deep	Shallow, wide	Subsurface
Undercutting	Horizontal grain attack	Vertical grain attack
Elliptical		
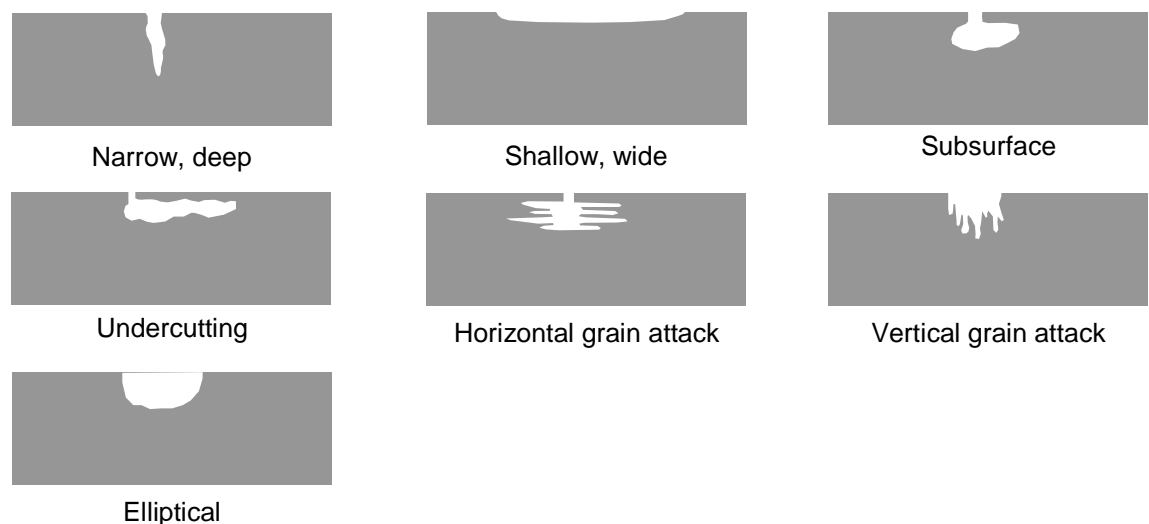
Figure 2.6: The different types of crevice corrosion that can occur (following Roberge, 2000).

Galvanic corrosion can occur when an electrochemical corrosion cell is created between two different metals connected by an electrolyte. The metal with the more noble corrosion potential acts as a cathode and the other becomes an anode, which dissolves into the electrolyte. Erosion corrosion is the combined effect of mechanical wear and electrochemical reactions. Cavitation is a form of erosion corrosion in which surface defects are introduced by unstable vapour bubbles in the electrolyte (Roberge, 2000). Fretting is another type of this corrosion caused by vibrations between the metal surface and the electrolyte. Intergranular corrosion is selective attack along or next to grain boundaries and is often a result of grain boundary segregation or enrichment, which produce regions of vulnerability. Exfoliation is a form of intergranular corrosion linked particularly to high strength aluminium alloys that have flattened elongated grains due to extrusion or rolling. Dealloying occurs when the corrosive media causes a particular element to selectively leach out from an alloy, while the majority of the alloy remains unaffected (Roberge, 2000).

Stress corrosion cracking is a localised form of environmental corrosion in which microscopic intergranular or transgranular cracks penetrate a material under the combined influence of stress and corrosive media (Roberge, 2000). This type of corrosion is explained in greater detail in Section 2.11.

Corrosion fatigue is another form of environmental corrosion that can occur in any metal and results in premature failure due to a combination of cyclic stress and corrosive environment (Talbot and Talbot, 1998).

2.7. Aqueous Corrosion

With regards to a metal in aqueous solution, electrons are removed from the metal surface by chemical species within the aqueous solution (Talbot and Talbot, 1998) i.e. the metal is oxidised and the attacking chemical species are reduced. These reactions generate an electric current at the surface of the metal, which cause an electric potential that facilitates further corrosion (Talbot and Talbot, 1998).

If iron in water is considered, metal ions are dissolved into solution and electrons are released in the anodic reaction:

$$Fe \rightarrow Fe^{2+} + 2e^-$$ ………………………………………………. Equation 2.1

The cathodic reaction is most often the rate controlling step (Roberge, 2000) as it is dependent on the pH of the aqueous solution and increases with acidity:

$$2H^+ + 2e^- \rightarrow H_2$$ …………………………………………………….. Equation 2.2

Depolarisation can occur whereby hydrogen ions reduce dissolved oxygen to create water, which increases the rate of the cathodic reaction because dissolved oxygen reacts with hydrogen regardless of impurities included in the metal (Roberge, 2000):

$$4H^+ + O_2 + 4e^- \rightarrow 2H_2O$$ …………………………………………... Equation 2.3

The half equations 2.1 and 2.3 can be combined, if the reversible reaction for the dissociation of water into hydrogen and hydroxide ions is included, to give:

$$2Fe + 2H_2O + O_2 \rightarrow 2Fe(OH)_2$$ ………………………………………… Equation 2.4

which forms a surface diffusion barrier layer that further oxygen must diffuse through. The same is true for $FeO \cdot nH_2O$ (Roberge, 2000).

A model of these reactions is shown in Figure 2.7.
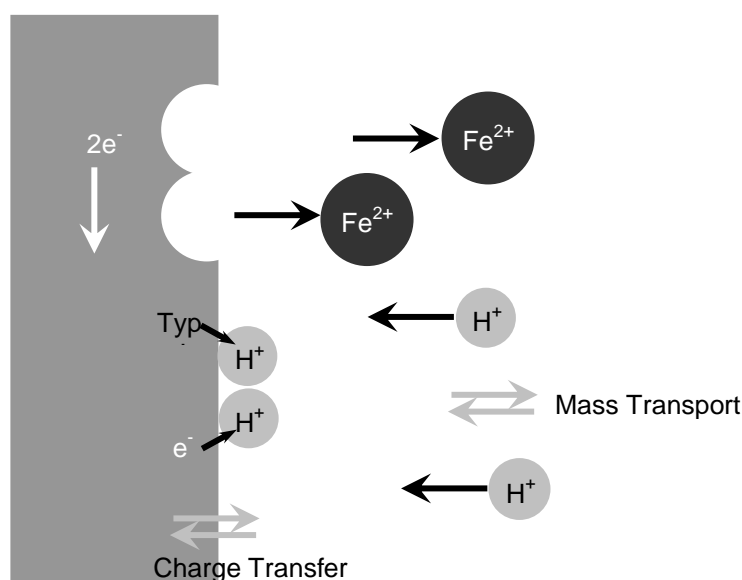
Figure 2.7: Schematic representation of electrochemical reactions occurring when iron is in an aqueous solution (following Roberge, 2000).

There are three main oxidation states in which iron can exist. Ferrous iron, Fe(II), and ferric iron, Fe(III) are capable of forming oxides, hydrous oxides, soluble cations and their salts (Talbot and Talbot, 1998). Fe(VI) is more rare because it is only stable in alkaline environments as the ferrate ion, FeO_4^{2-} (Talbot and Talbot, 1998). In general, "rust" films are found to have three layers of iron oxide where the iron has a different oxidation state (Roberge, 2000). Hydrous ferric oxide is the familiar orange/red/brown colour that can form as nonmagnetic hematite (Fe_2O_3) or as a black magnetic hydrous ferrous ferrite, magnetite ($Fe_3O_4 \cdot nH_2O$), which is often present between the layers of hydrous Fe_2O_3 and wüstite FeO (Roberge, 2000).

This description of iron corrosion is shown as an example with respect to a pure metal, although the use of alloys is more common in everyday life. Similar processes occur that lead to the production of other oxides such as CrO, Cr_2O_3 and Al_2O_3 etc., depending on the composition of the particular alloy.

2.8. Oxidation

Alloys that are designed for service at high temperature or in oxidising environments utilise the phenomena of oxidation for their protection (Kofstad, 1988). They are dependent on the initial formation of a dense, adherent oxide layer, which is more resistant to the oxidising environment than the bulk material. This oxide layer protects the bulk from further rapid deterioration. The oxide is usually formed from an alloying addition, of which there is a smaller proportion than the bulk metal. In steels the most common oxides to form are alumina or chromia (Kofstad, 1988).

The formation of the protective oxide results in a depletion of the constituent element at the surface of the substrate. If the oxide layer were to crack or spall, the substrate would become highly susceptible to oxidation, but at an increased rate due to an insufficient amount of chromium or aluminium at the surface (Evans, Donaldson and Gilmore, 1998).

From the iron-oxygen phase diagram shown in Figure 2.8 it can be seen that three possible oxides may form which are: wüstite ($Fe_{1-y}O$), magnetite (Fe_3O_4) and hematite (Fe_2O_3) (Kubaschewski, 1982).
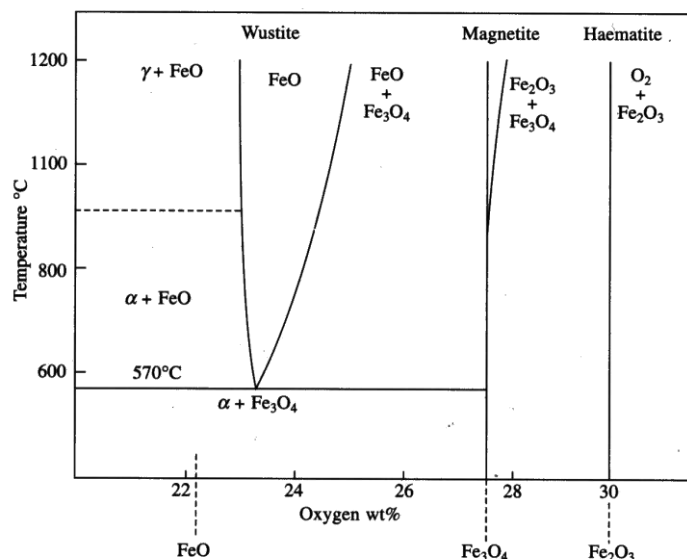

Figure 2.8: Iron-Oxygen phase diagram (reproduced from Kubaschewski, 1982).
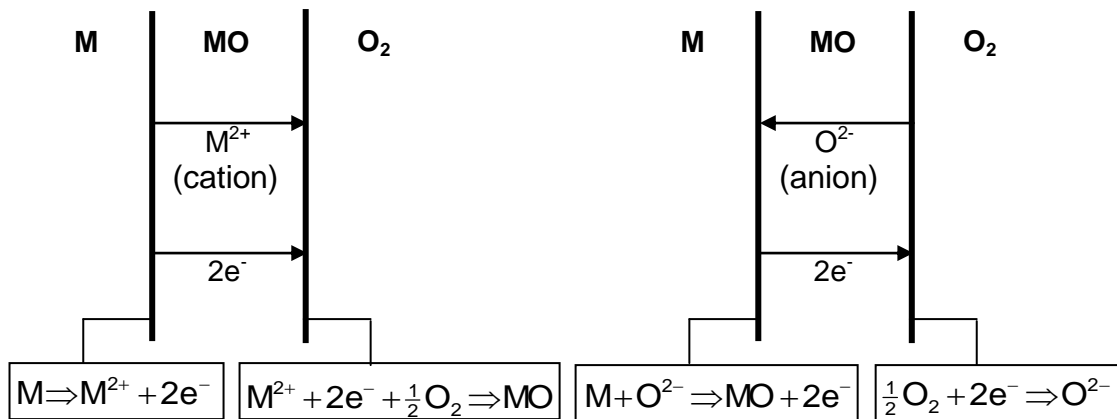
2.8.1. Oxidation Mechanisms

Metal oxides are ionically bonded so it is only necessary to consider the movement of ions though the oxide and not neutral atoms. There are several mechanisms used to

describe ion transport that are separated into categories of stoichiometric crystals and non-stoichiometric crystals. For some compounds this distinction is clear, however, in reality it is more accurate to assume that all types of defects are present with one preferential type that dominates (Birks and Meier, 1983).

The two principal defects present in strongly stoichiometric ionic compounds are Schottky and Frenkel defects (Birks and Meier, 1983). Schottky defects, Figure 2.9 (a), are anion and cation vacancies within the sub-lattices. It is assumed that the concentration of each is equal so that the lattice remains electroneutral. In this mechanism it is thought that both anions and cations are able to move. Frenkel defects, Figure 2.9 (b), are cation vacancies in the sub-lattice, which means that only the cations are mobile. To maintain electroneutrality in this instance it is thought that there are equal concentrations of cation vacancies and cation interstitials (Birks and Meier, 1983).
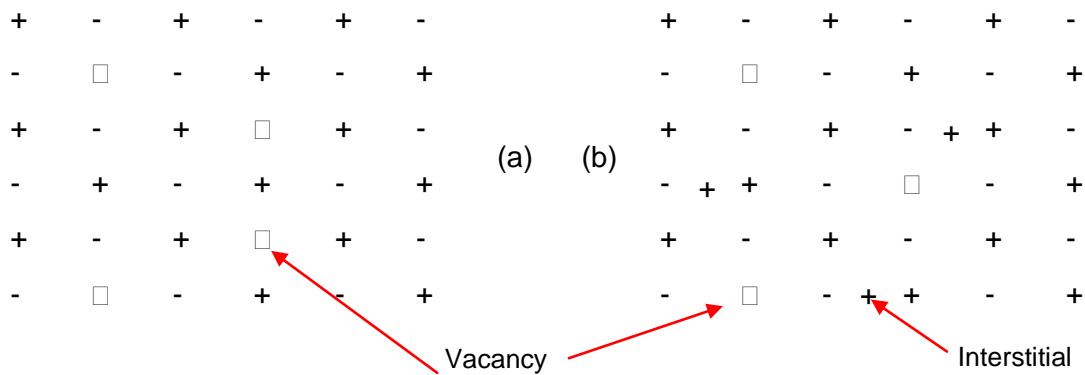
Figure 2.9: (a) Schottky defects and (b) Frenkel defects (following Birks and Meier, 1983).

$$M \Rightarrow M^{2+} + 2e^-$$ $$M^{2+} + 2e^- + \tfrac{1}{2}O_2 \Rightarrow MO$$ $$M + O^{2-} \Rightarrow MO + 2e^-$$ $$\tfrac{1}{2}O_2 + 2e^- \Rightarrow O^{2-}$$

Figure 2.10: Possible oxidation reactions for cation and anion migration (following Birks and Meier, 1983).

Neither of these defects describes a transport mechanism for electrons so cannot be used to explain oxidation. Figure 2.10 shows the two possible oxidation reactions that can take place. In cation migration positive metal ions and negative electrons move through the oxide and react with the oxygen at the oxide-gas interface. In anion migration negative oxygen ions move through the oxide to the metal-oxide interface and react with the metal to form more oxide whilst negative electrons move in the opposite direction through the oxide. The nature of the migrating ions determines the type of oxidation that occurs. Cation migration causes external oxidation whereas anion migration causes internal oxidation (Birks and Meier, 1983).
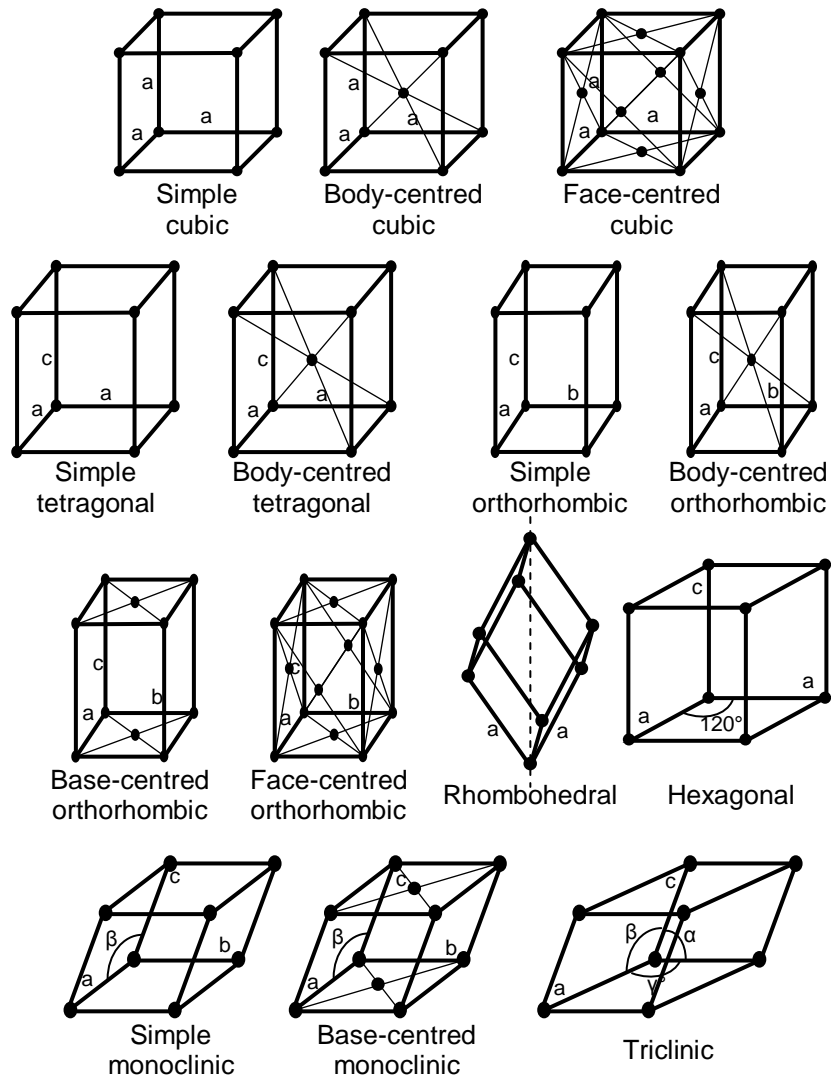
To explain the migration of ions and electrons at the same time it must be assumed that the oxides are in fact non-stoichiometric compounds. This means that although the oxides are electrically neutral their composition is not exactly that which their chemical formulae would suggest. For this to be true it must also be assumed that one of the elements involved exhibits variable valency. In this instance it is assumed that the metal cation exhibits variable valency (Birks and Meier, 1983).

Ionic compounds that are non-stoichiometric are described as semiconductors, which can be N-type or P-type depending on the charge of the particles that are transported through them. N-type semiconductors arise from either an excess of metal or a deficit of non-metal and the charge carriers are negative. P-type semiconductors are the result of either an excess of non-metal or a deficit of metal and the charge carriers are positive (Birks and Meier, 1983).
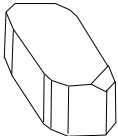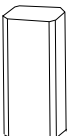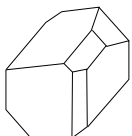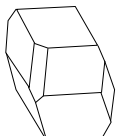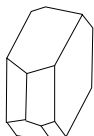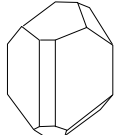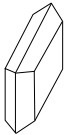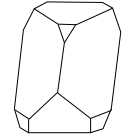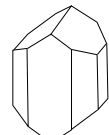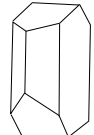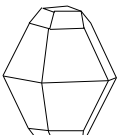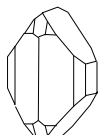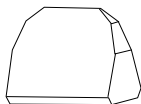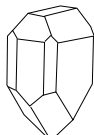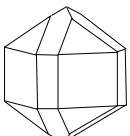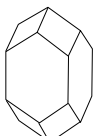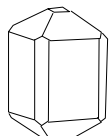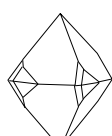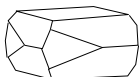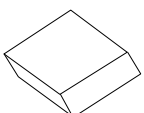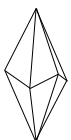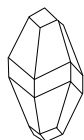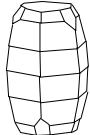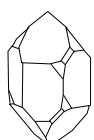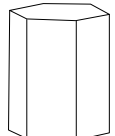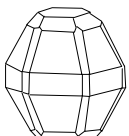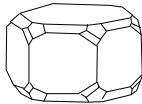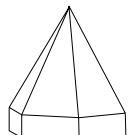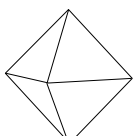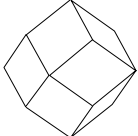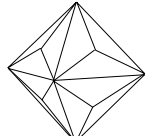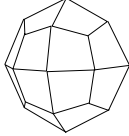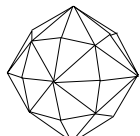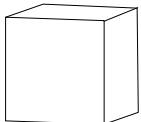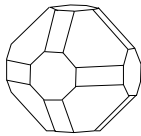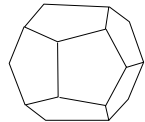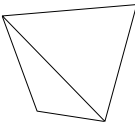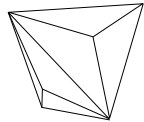
2.9. Crystal Structures

The atoms in crystalline materials are arranged in regular order whereas in amorphous materials the atoms are arranged randomly (Hammond, 2009). A lattice is an array of points in space where each point is in an identical environment to the next. The motif is the arrangement of atoms associated with the lattice points. In three dimensional lattices it is important to consider: a) the plane of symmetry or mirror plane, which is an imaginary line cutting a lattice into two symmetrical halves, b) the axis of symmetry, which is a line that passes through the centre of the lattice and if the lattice were to be rotated 360° about this axis it would return to its original position and c) the centre of symmetry is the point at which parallel opposite faces are identical if rotated 180° (Hammond, 2009). There are fourteen different space lattices which are known as Bravais lattices after the person who determined them (Hammond, 2009). Figure 2.11

shows the unit cells of the fourteen Bravais lattices in terms of their lattice vectors a, b and c and the angles between them α, β and γ. The Bravais lattices are grouped into seven crystal systems based on the shape of the unit cell. The seven systems are called cubic, hexagonal, trigonal, tetragonal, orthorhombic, monoclinic and triclinic. Trigonal includes the rhombahedral unit cells. Examples of the crystal shapes formed within each crystal system are shown in Figure 2.12

Figure 2.11: The fourteen Bravais lattices (following Hammond, 2009).

Triclinic	chalcanthite	kyanite	axinite	rhodonite	albite
Monoclinic	wolframite	gypsum	titanite	augite	Orthoclase
Orthorhombic	sulphur	barytes	olivine	struvite	hemimorphite
Tetragonal	cassiterite	zircon	vesuvianite	scheelite	wulfenite
Trigonal	rhombohedron	scalenohedron	calcite	corundum	quartz
Hexagonal	beryl	pyrrhotite	apatite	zincite	nepheline
Cubic	octahedron	rhombododecahedron	trisoctahedron	icositetrahedron	hexakisoctahedron
	cube	galena	Pentagonal dodecahedron	tetrahedron	tristetrahedron

Figure 2.12: The seven crystal systems with examples of each system (following Bauer, 1987).

26

2.9.1. Crystal Structure of Oxides

The oxides of iron have different structures. Wüstite has a cubic lattice and exists as the halite structure, which is shown in Figure 2.13 (Kofstad, 1988). The O^{2-} anions are arranged as close-packed cubic and the Fe^{2+} cations sit in the octahedral interstices (Hammond, 2009). Most oxides that appear in the form MO have a halite structure, these include: MgO, CaO, SrO, CdO, CoO, NiO, TiO, NbO and VO. The oxides BeO and ZnO are exceptions to the rule in that they have a structure in which the metal ions occupy every other tetrahedral site between the oxygen ions (Kofstad, 1988).
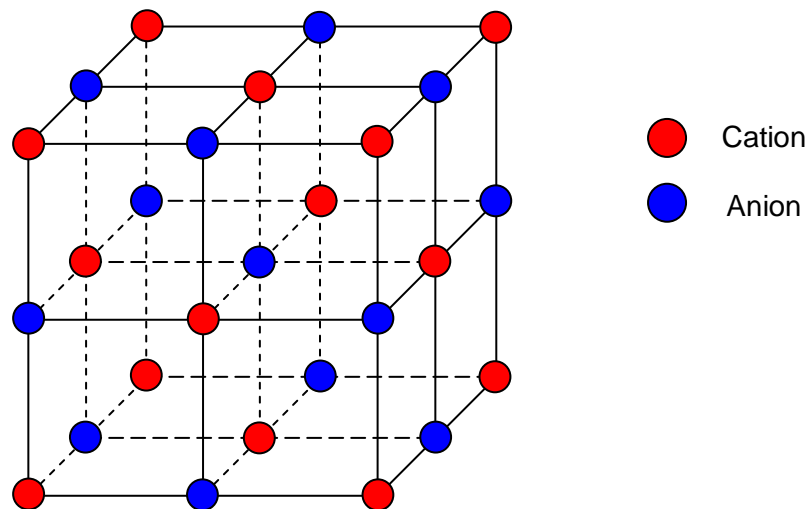
Figure 2.13: Halite crystal structure showing atom positions (following from Kofstad, 1988).

Wüstite oxidises to magnetite, which also has a cubic lattice but exists as an inverse spinel structure shown in Figure 2.14. In the spinel structure, the oxygen ions are cubic close-packed in the same way as the halite structure, however, the unit cell of magnetite is twice the height and 8 times the volume of the halite unit cell (Hammond, 2009). It consists of 32 O^{2-} ions with 8 Fe^{3+} ions occupying the tetrahedral sites with 8 Fe^{2+} ions and 8 Fe^{3+} ions occupying the octahedral sites (Hammond, 2009 and Kofstad, 1988).

In the oxidation of magnetite the 32 O^{2-} ions and 16 Fe^{3+} ions remain, but the 8 Fe^{2+} ions are replaced by an additional 5⅓ Fe^{3+} ions. This gives the formula Fe_2O_3, or more accurately, γ-Fe_2O_3 which is known as maghemite. This structure is not stable so the oxygen ions rearrange into α-Fe_2O_3 called hematite. This has a rhombohedral lattice with corundum structure shown in Figure 2.15 (Kofstad, 1988 and Hammond, 2009).
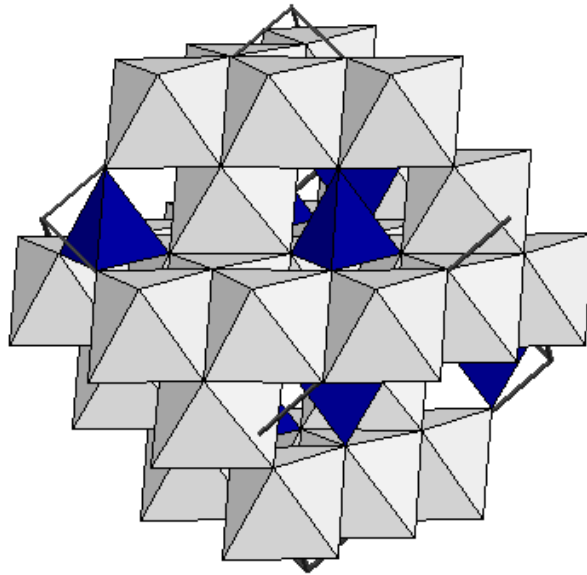
Figure 2.14: Spinel crystal structure (http://ruby.colorado.edu/~smyth/min/spinel.html, viewed 10/01/2006).
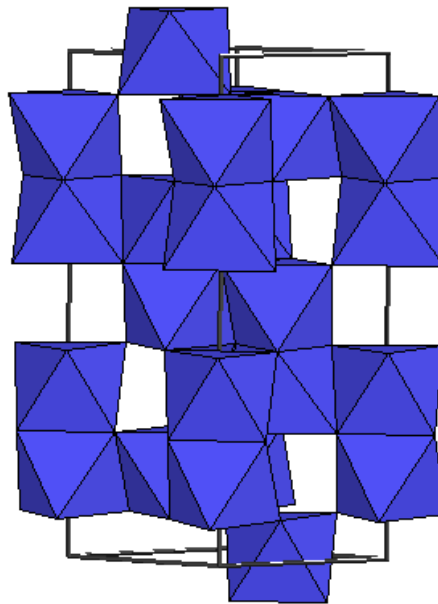
Figure 2.15: Corundum structure (http://ruby.colorado.edu/~smyth/min/corundum.html, viewed 10/01/06).

2.10. Fracture Mechanics

It is important to have an understanding of fracture mechanics when considering the initiation and propagation of cracks. The stress intensity factor, K, is a very important parameter when dealing with fracture mechanics, which can be used when explaining crack growth in situations where the stress field around the crack tip is primarily elastic (Janssen, Zuidema and Wanhill, 2002). Although crack propagation can be quite complicated there are three basic stress systems used to describe it, as illustrated in

Figure 2.16, which depend on the direction of applied load. In mode I, called the opening mode, a tensile load is applied to a sample at the crack initiation, which results in crack propagation perpendicular to the stress. Mode II is called the sliding mode and in this instance a shearing force is applied to the edge of a sample causing a crack to propagate parallel to the applied loads. Mode III is called the tearing mode whereby opposite torsional forces are applied to the edge of a sample causing crack propagation perpendicular to the applied load (Janssen, Zuidema and Wanhill, 2002).

Mode I   Mode II   Mode III
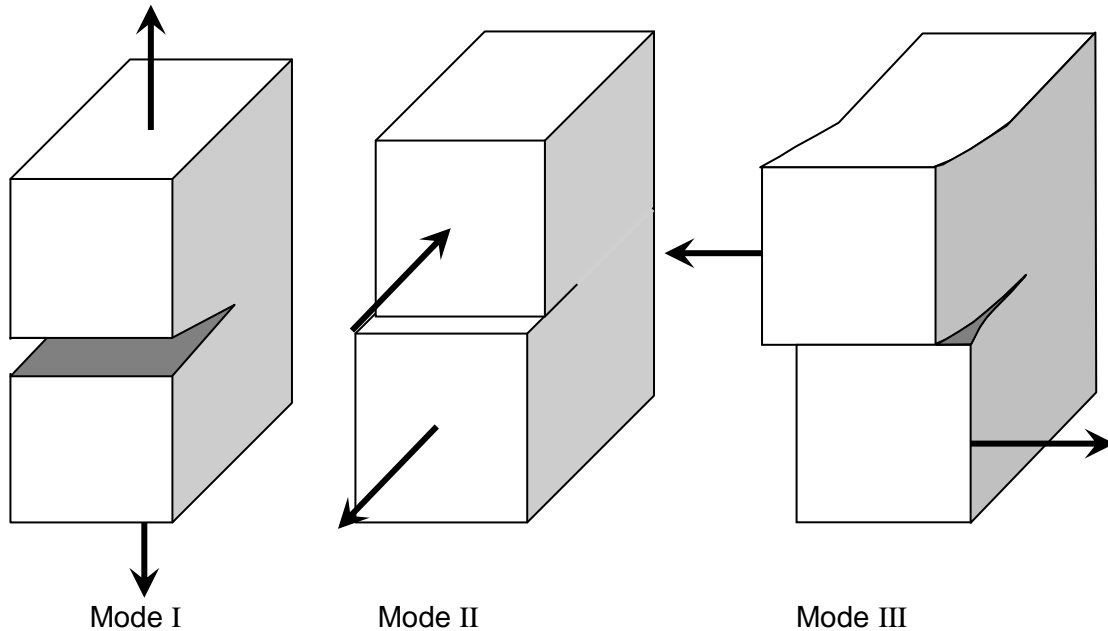
Figure 2.16: Three modes of fracture (following Janssen, Zuidema and Wanhill, 2002)
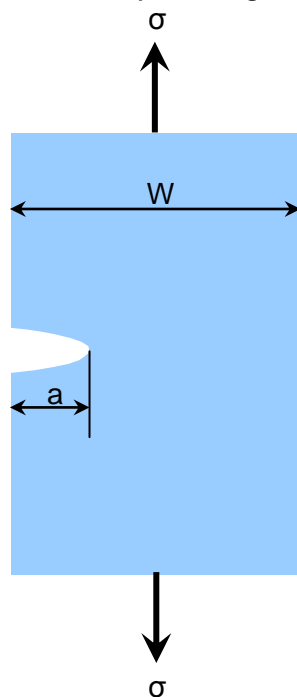
Figure 2.17: Diagram of edge notched specimen for fracture toughness calculation (following Janssen, 2002).

For this work only fracture mode I will be considered as this is directly related to the test method used. Figure 2.17 shows a schematic of a single edge notched specimen under mode I loading, with applied tensile stress, σ, overall width, W, and crack length, a.

Centre cracked samples have compressive stresses acting, which have a closing effect on the crack, however, this is not the case in edge notched samples because the stress, σ_x, acting at the free edge is equal to zero. As a result a centre crack and an edge crack may have equal crack length, a, and stress, σ, however the crack opening at the free periphery of the edge crack will be bigger than that at the middle of the centre crack. It has been calculated that this stress raising effect has a value of 12% so the following equation for the fracture toughness in mode I loading (K_I) can be deduced:

$$K_I = 1.12\sigma\sqrt{\pi a}$$ ....Equation 2.5

As cracks become longer it is also necessary to account for finite geometry so the following equation has been produced to include specific correction factors, which is accurate to 0.5% when a/W < 0.6:

$$K_I = \sigma\sqrt{\pi a}\left\{1.122 - 0.231\left(\frac{a}{W}\right) + 10.550\left(\frac{a}{W}\right)^2 - 21.710\left(\frac{a}{W}\right)^3 + 30.382\left(\frac{a}{W}\right)^4\right\}$$ …

………………………………………………………………………....................Equation 2.6

2.11. Stress Corrosion Cracking

Stress Corrosion Cracking (SCC) is considered to be a delayed failure process that can cause catastrophic failure in all materials under stress, which may be applied or residual (Lula, 1985), and in a corrosive environment. The focus of this thesis is the effect of SCC on the metals used for steam turbine blades, discs and rotors.

There are three stages of SCC: stage 1 is crack initiation, stage 2 is steady-state crack propagation and stage 3 is final failure. However, in reality there is no discernible shift between each stage. SCC cracks initiate perpendicular to the tensile stress and propagate at a slow rate, e.g.10^{-6} ms^{-1} (ASM International Handbook Committee,

1987), until the stress in the metal ahead of the crack exceeds that of its fracture strength, whereupon final failure occurs. Intergranular corrosion in unloaded metals can be as fast as stress corrosion crack growth but without additional force intergranular corrosion eventually ceases, whereas stress corrosion cracking can continue until catastrophic failure occurs (ASM International Handbook Committee, 1987).

2.11.1. SCC Initiation and Propagation

Stress corrosion cracks often initiate at surface flaws. Pre-existing fabrication defects such as grooves, laps, burrs and pits can act as crevices which promote localised corrosion and subsequent SCC. Pits can also be generated in service as a consequence of corrosion or erosion (ASM International Handbook Committee, 1987). They commonly form at surface inclusions or where protective layers become damaged. A pit will only become a crack if the correct conditions are met and these depend on factors including but not limited to: material (composition, yield strength, susceptibility), pit geometry (which in turn affects the stress and strain at the pit base) and localised environment within the pit. Pit geometry is particularly important as the ratio between depth and the surface diameter must exceed ten before the pit initiates a crack (ASM International Handbook Committee, 1987). (A ratio of one represents uniform corrosion whereas a ratio of 1000 is common for a stress corrosion crack. The electrochemistry at the pit base is considered to be even more important than pit geometry as pre-existing pits do not always develop into cracks and crack growth has ceased in samples that were removed from solution, rinsed, dried and reinserted into solution. This suggests that the electrochemistry of a pre-existing pit is different from that of a pit generated in service. If the grain boundaries of a material have a different chemistry from the bulk then SCC can initiate from intergranular corrosion. SCC can also initiate by slip-dissolution whereby the crack travels along slip planes (ASM International Handbook Committee, 1987).

A crack can only propagate if it has first been initiated, but just because a crack initiates it does not mean it will necessarily propagate. For a crack to propagate from a pit, the aspect ratio must be above the critical value, i.e. much longer than it is wide. The bottom of the pit must have the correct pH and potential and be under stress above the threshold for SCC initiation, K_{ISCC}. All of the conditions for crack propagation are most likely somewhat different from those for crack initiation (ASM International Handbook Committee, 1987).

2.11.2. SCC Initiation and Propagation Mechanisms

It is generally thought that stress corrosion cracks can initiate and propagate when localised regions of metal become exposed to the corrosive environment that were previously protected by surface films such as oxides. Rapid oxidation can occur because a large potential difference is set up between the cathodic damaged oxide and the newly created anodic metal surface. The oxide that forms can stop crack propagation until it is damaged again, unless the crack propagation rate is faster than the rate of oxide growth at the crack tip. However, the oxide that forms can also prevent the crack from healing if the stress is relaxed.

There is no definitive explanation for the mechanisms of initiation and propagation of stress corrosion cracks but several theories have been suggested. Karpenko and Vasilenko, 1979, published a book reviewing their own and other authors' investigations into SCC. They determined that there were two main conflicting theories: the mechanical-electrochemical theory and the electrochemical theory. The adsorption theory is only concerned with the propagation of stress corrosion cracks.

a. Mechanical-electrochemical theory

In the mechanical-electrochemical theory it is assumed that stress corrosion cracks are initiated by the formation of microscopic or even submicroscopic brittle edge notches that propagate under the influence of applied stress and the electrochemical action of the corrosive solution reacting with the unprotected metal. In high stress situations it is thought that mechanical processes are dominant, especially in deep stress raisers where induced stresses are high, whereas in low stress situations it is the electrochemical processes that govern the rate of stress corrosion cracking (Karpenko and Vasilenko, 1979).

Figure 2.18 shows a schematic representation of the mechanical-electrochemical theory in which an edge notched sample is stressed in mode I as described in Section 2.10. The combined influence of stress and corrosive media results in crack propagation perpendicular to the applied load.
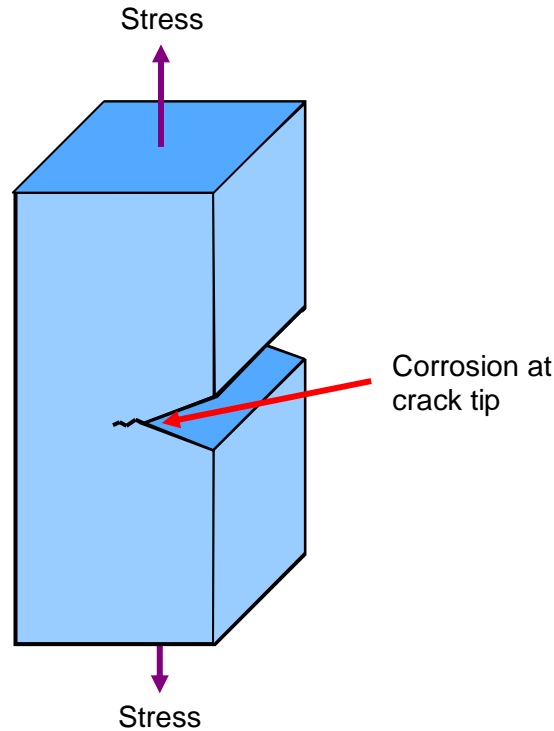
Figure 2.18: Schematic representation of the mechanical-electrochemical theory in which metal corrosion occurs at the tip of a brittle edge notch and crack propagation is perpendicular to the applied tensile stress.

Karpenko and Vasilenko, 1979, found evidence to support this theory experimentally at room temperature by immersing pre-cracked specimens of hardened U8A steel in 6% sodium hydroxide solutions at various stress levels. At 0.95-0.98 times the stress required for a crack of specific length to propagate in air (denoted as P from now on), the crack propagation rate was measured to be between 1 and $2x10^{-4}ms^{-1}$. The applied stress was then progressively reduced, which induced a concurrent reduction in the rate of crack propagation until it terminated at a stress of 0.75-0.80P due to the formation of a protective surface oxide at the crack tip. The load was then increased gradually but crack propagation did not resume until the stress reached 0.90-0.95P whereby the stress was great enough to cause plastic deformation of the metal at the crack tip, which damaged the protective surface oxide revealing fresh metal to the corrosive environment. A further reduction in load showed crack propagation to cease at 0.75-0.80P as it did previously. Similar evidence was found in experiments using hardened steels where the corrosive media comprised of distilled water containing passivators (Karpenko and Vasilenko, 1979).

Further evidence to support this theory was discovered using copper-base alloys in various electrolytes but in particular austenitic steels in chloride solutions (Leu and

Helle, 1958). Samples of austenitic (Kh18N9T) steel were used for two sets of experiments; in the first samples were passivated and deformed before being immersed in boiling chloride with applied load, the second were passivated in air following deformation and then immersed under load in the same electrolyte. Stress corrosion cracks were apparent in the first set of samples after just 15 minutes of immersion whereas it was two hours before any cracks were noticed in the samples tested by the second method (Karpenko and Vasilenko, 1979). It is thought that deformation of the samples caused localised damage to the protective oxide that was sufficient to permit electrochemical dissolution of the fresh metal at the crack tip. However, the second set of samples were passivated in air post deformation so a new protective surface film had formed, which prevented stress corrosion cracks from initiating for much longer. In contradiction Uhlig and Sava, 1963, did not find evidence to support this work during their investigation of Type 310 stainless steels in the same chloride solutions.

Karpenko and Vasilenko, 1979, reported that evidence to support the mechanical theory has been found from acoustic experiments where sound is emitted during fracture in the same way as metals fractured in air. This is particularly true for metals tested with high levels of applied stress. However, similar experiments were conducted where no sounds have been captured, which is evidence to support the electrochemical theory.

b. Electrochemical theory

The electrochemical theory states that stress corrosion cracks are initiated and propagated by the continuous action of the corrosive media causing metal dissolution at the crack tips, which is accelerated by the applied stress. A corrosion cell is created at the crack tip by the potential difference between the damaged oxide, which acts as a cathode, and the fresh metal, which acts as an anode, a schematic of which is shown in Figure 2.19. In experiments conducted by Noev in 1947, involving solutions of highly concentrated sodium hydroxide, the potential difference between two such aforementioned surfaces was reported to be 0.7 V.

It has already been mentioned that intergranular corrosion in unloaded samples can be as fast as corrosion crack propagation but it will eventually cease whereas crack growth in loaded samples can continue throughout the metal. This supports the idea that stress corrosion cracks are merely accelerated by the application of stress and are

not dependent upon it. Flis and Scully, 1968, used electron microscopy to show the initiation of stress corrosion cracks in stressed foils due to dissolution of anodic metal rather than by the formation of a brittle edge notch as described in the mechanical-electrochemical theory. With regards to intergranular cracking, grain boundaries are considered to be anodic regions, whereas in transgranular cracking anodic regions are created either by clustering of dislocations on the slip planes or by the presence of anodic type precipitates.
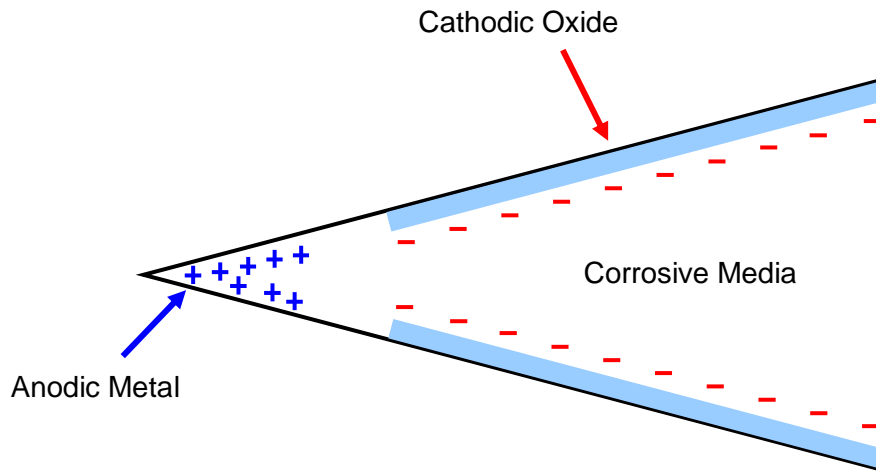
Figure 2.19: Schematic representation of the electrochemical theory in which a corrosion cell is set up between the damaged cathodic oxide and the anodic bare metal.

Rooyen, 1960, carried out acoustic emission experiments on austenitic stainless steels immersed in solutions of magnesium chloride at 421K with a stress of 281 MNm^{-2} in order to investigate the nature of stress corrosion cracking. The conditions used were optimum, however, the acoustic emission equipment picked up no sounds throughout the initiation and propagation of stress corrosion cracks, which presents evidence to show that this type of failure can occur purely by the electrochemical action of the corrosive media and does not rely on any mechanical processes. However, this contradicts the work by Karpenko and Vasilenko in 1979 who found evidence to support the mechanical nature of cracking using similar acoustic emission experiments.

c. *Adsorption theory*

The adsorption theory (Figure 2.20) states that crack propagation can be correlated with a decrease in the metal's surface energy as a result of the adsorption of particular ions from the electrolyte (Karpenko and Vasilenko, 1979).

Experimental conditions have a large effect on the rate of crack propagation, which is commonly reported between 1.8 and 3.6×10^{-6} ms^{-1}, values that are noticeably quicker than those measured from corrosion without the formation of passivating films. Harwood stated that the mechanical-electrochemical theory could explain this crack growth rate, whereas Tomashov used the electrochemical theory (Karpenko and Vasilenko, 1979). Uhlig and Sava, 1963, said that it is due to a combination of the adsorption and electrochemical theories. Several authors agree with the idea that stress corrosion cracking can only be explained by two or more theories. The fact that stress corrosion crack propagation is intermittent can only be explained by the electrochemical theory if the effects of the mechanochemical and chemomechanical processes are included (Karpenko and Vasilenko, 1979).
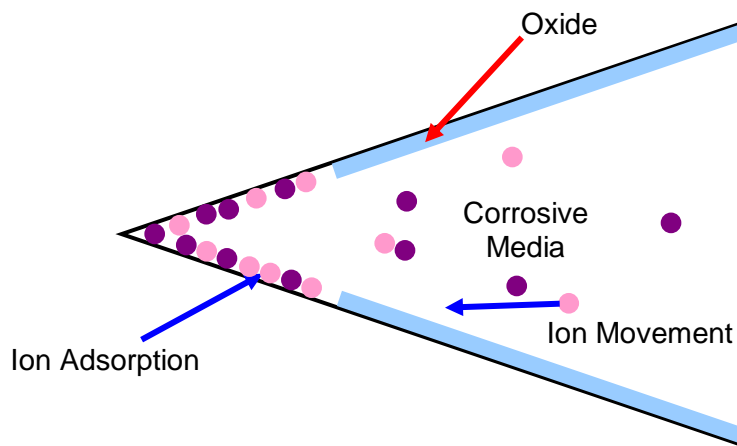
Figure 2.20: Schematic representation of the adsorption theory.

2.11.3. Experiments

There are historically three types of SCC experiments: static loading of smooth samples, static loading of pre-cracked samples and slow strain rate tests.

a. Static loading of smooth samples

In experiments involving smooth samples the time to failure in a consistent environment under various fixed stress levels is measured (ASM International Handbook Committee, 1987).

Figure 2.21 shows an idealised set of results from stress corrosion experiments on statically loaded smooth samples, where the logarithm of time to failure, t_f, is plotted as a function of applied stress, $\sigma_{applied}$. The time to failure decreases dramatically with

increasing applied stress. The threshold stress is established when the time to failure approaches infinity and the fracture stress is determined when the time to failure is instantaneous.
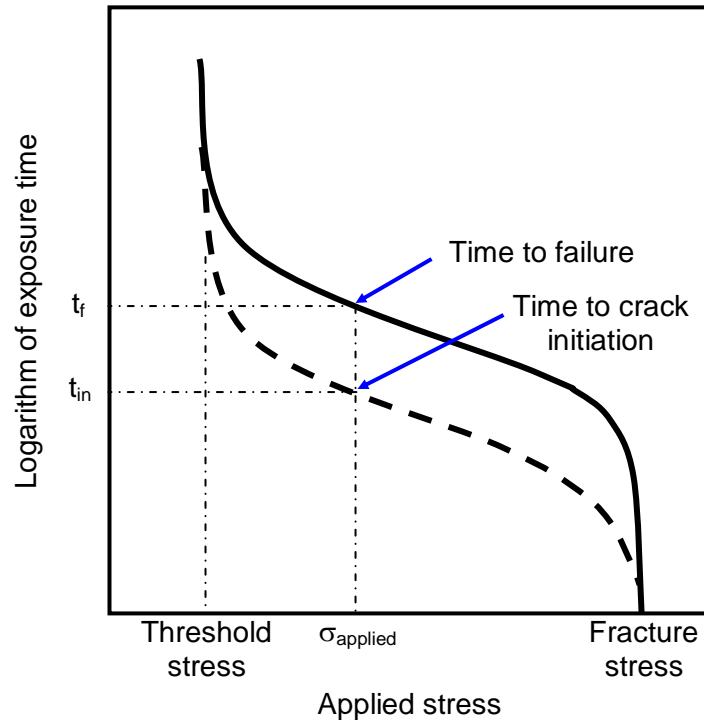
Figure 2.21: Schematic illustrating the effect of applied stress on the time to failure of smooth samples in statically loaded stress corrosion experiments (following ASM International Handbook Committee, 1987).

b. *Static loading of pr-ecracked samples*

In experiments involving pre-cracked samples the crack propagation velocity is measured in a consistent environment with either a set crack opening displacement or a fixed applied load (ASM International Handbook Committee, 1987). SCC tests of this nature can be constructed in three ways: under constant applied load the stress intensity factor, K, increases with crack length; using fixed crack mouth opening displacement K decreases with increasing crack length and by using special tapered samples K remains unchanged with increasing crack length.

Three distinct regions are identified in Figure 2.22, which shows typical results from a plot of crack propagation velocity, v, as a function of the stress intensity factor, K. There is no crack propagation below a certain threshold stress intensity, K_{ISCC}, the value of which is dependent upon several factors including the alloy composition and environment. Stage 1 crack propagation occurs at low stress intensity levels and within

this region the crack growth rate is very sensitive to small changes in stress intensity. In stage 2 the crack propagation velocity remains constant regardless of increased stress intensity. This is known as the plateau velocity, the value of which is specific to the alloy in its environment and is controlled by the rate limiting step in the corrosion process. Stage 3 is similar to stage 1 in that the crack growth rate increases quickly for small increases in stress intensity. This continues until the velocity approaches infinity, which is defined as the critical stress intensity required to cause mechanical fracture in an inert environment. (ASM International Handbook Committee, 1987)
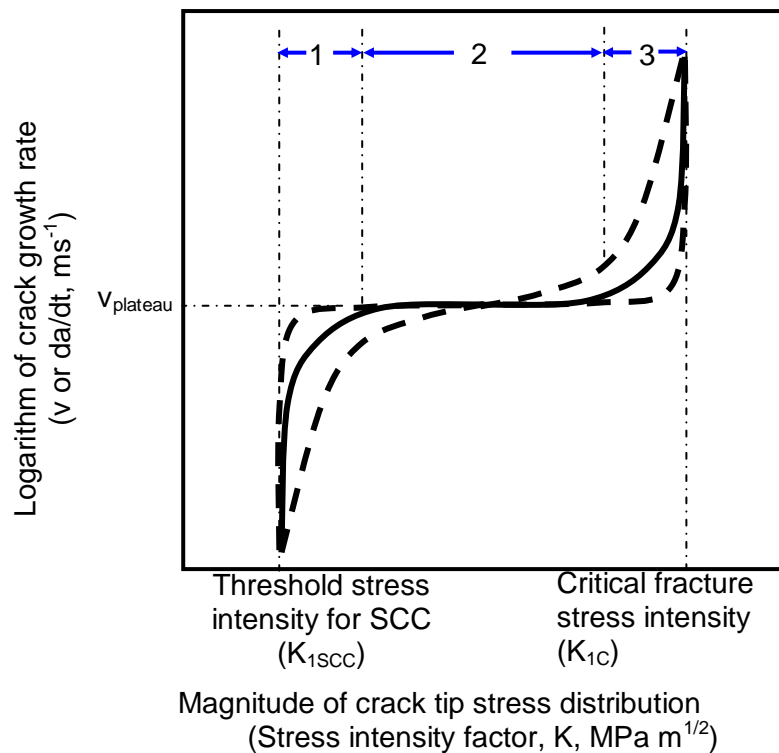
Figure 2.22: Schematic illustrating static loading of pre-cracked samples, (following ASM International Handbook Committee, 1987).

c.   *Slow strain rate tests*

Slow strain rate experiments can be carried out on both smooth and pre-cracked samples and involve gradually increasing the load applied to a sample in a constant environment. This is usually done using a tensile testing machine with a slow crosshead speed, for example 10^{-5} to 10^{-9} ms^{-1}, on samples in an inert atmosphere and a corrosive environment (ASM International Handbook Committee, 1987). The strain to failure in both environments can then be plotted against the strain rate shown in Figure 2.23.
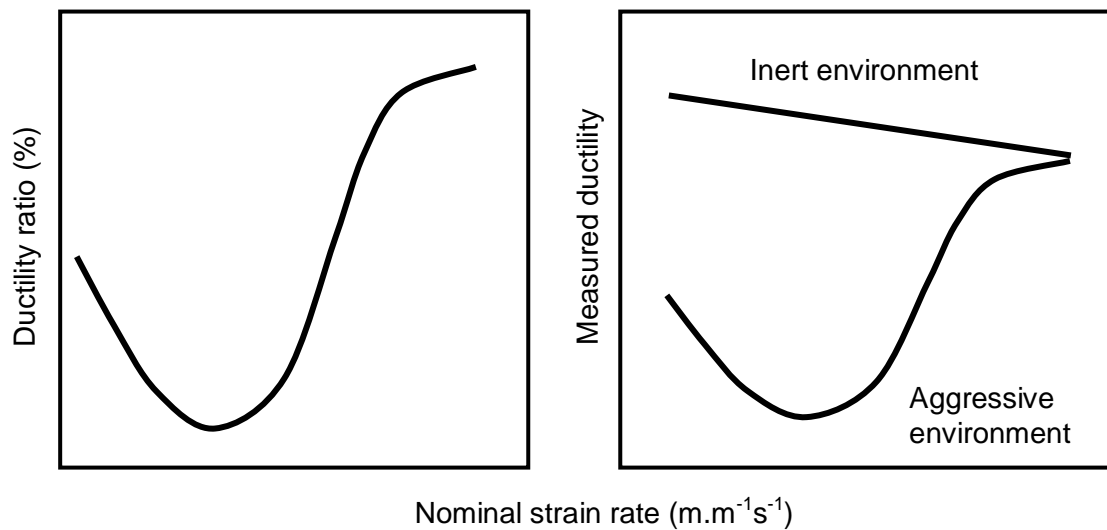
Figure 2.23: Schematic illustrating ductility measurements from slow strain rate experiments (following ASM International Handbook Committee, 1987).

2.11.4. Stress Corrosion Cracking vs. Corrosion Fatigue

Corrosion fatigue (CF) is a process that occurs in metals that are subject to cyclic loading whilst in a corrosive atmosphere. CF is common in turbine blades due to the vibrations induced by blade rotation. It is also common for cracks in LP turbine blades and rotors to be a result of a combination of SCC and CF due to the various operating conditions experienced by turbines throughout service.

Table 2.2 gives the main similarities and differences between SCC and CF. The most important difference is that for CF to initiate a crack there must be a surface stress raiser, whereas SCC can initiate from smooth surfaces as a result of pitting as described previously. Another difference is that although SCC initiation may be transgranular, propagation is usually intergranular with respect to the prior austenite grain boundaries, whereas initiation and propagation of CF is normally transgranular, with the striations expected of fatigue failures in inert atmospheres. Due to the method of crack propagation, SCC is often branched, whereas CF is one crack (Richman, McNaughton and Paterson, 1989).

Table 2.2: Similarities and differences between SCC and CF (Richman, McNaughton and Paterson, 1989)

	Stress Corrosion Cracking	Corrosion Fatigue
Similarities	Surface Initiated	
	Brittle Appearance	
Differences	Initiation can be from smooth surfaces	Initiation from stress concentrations
	Intergranular or transgranular initiation relative to prior austenite grain boundaries. Intergranular initiation in martensitic and low carbon steels	Transgranular initiation and propagation
	Intergranular propagation in martensitic and low carbon steels	Transgranular propagation. Intergranular propagation is only possible over a small stress intensity range.
	Fracture surfaces appears rougher than CF	Fracture surface is not as rough as SCC
	Extensive crack branching	Little to no crack branching
	No striations on the fracture surface	Striations on the fracture surface
	Crack propagation only occurs if the stress intensity is above the threshold value	Crack propagation related to frequency and stress wave shape.

2.11.5. Stress Corrosion Cracking in Stainless Steel

Stress Corrosion cracking in steels used for turbine blades and discs has been studied for over 30 years (Turnbull and Zhou, 2003). The cracks can propagate in an intergranular or transgranular manner along stacking faults or slip planes, sometimes a combination of both (Wyatt, 1976), with little or no external evidence of damage, even in metals that are generally ductile. Many stress corrosion cracks and their propagation damage are so small that they can only be detected with special non-destructive testing techniques (Karpenko and Vasilenko, 1979).

Most stress corrosion cracking experiments on stainless steel and other alloys have been carried out in various corrosive media such as ammonia, magnesium chloride or sodium hydroxide solutions. Although there is some work on high temperature water, there is limited information available for condensing steam at around 95°C, which is the area of interest for this project. It is reported that pure metals do not suffer from stress corrosion cracking but any level of impurity increases the likelihood of damage in this way (Karpenko and Vasilenko, 1979).

Austenitic stainless steels are far more susceptible to stress corrosion cracking than ferritic and martensitic stainless steels (Lula, 1985). Evidence to support this has been shown in experiments on several ferritic-martensitic, austenitic and nickel-base alloys in supercritical water at temperatures up to approximately 600°C (Was, Ampornrat, Gupta, Teysseyre, West, Allen, Sridharan, Tan, Chen, Ren, and Pister, 2007). Ferritic stainless steels have been found to crack in acid chlorides, but this can be avoided if nickel and copper additions are minimised (Lula, 1985).

It has been suggested that the susceptibility of austenitic stainless steels to transgranular cracking can be explained because the cubic structure has low stacking fault energy, which means that dislocation clusters collect along the initial slip planes when deformed. A similar connection to intergranular cracking has not yet been discovered, however, it is thought to be connected to grain boundary segregation of impurities (Karpenko and Vasilenko, 1979).

2.11.6. Stress Corrosion Cracking at Disc Rim Blade Attachments

Whilst stress corrosion cracking can occur in turbine blades it is more often found in rotors and discs. Figure 2.24 shows a diagram of a cross section through a shaft and disc with indication of the locations most susceptible to SCC. These include axial – circumferential and axial radial cracking in the rim and through the web, in addition to axial radial cracking of the keyway and bore surface. Axial circumferential cracking is Type I and axial radial cracking is Type II (Lyle and Burghard, 1982).

Figure 2.25 shows a cross-section of a fir tree blade attachment marked with the most common locations where axial circumferential and axial radial SCC occurs.

SCC in LP discs is normally intergranular along the prior austenite grain boundaries. The fracture surfaces normally appear brittle, without the striations typical of corrosion

fatigue. The cracks often contain iron oxide corrosion products but Na_2CO_3, NaOH and sulphides have also been present in LP rotors. Impurities in the steam such as chlorides, sodium and sulphates, which carry over into the LP turbine, assist SCC. Most sources quote SCC to consist of 3 stages: initiation, propagation and final failure. This can be broken down into a further 2 stages to give: incubation, initiation, stable crack growth, accelerated crack growth by SCC, HCF or LCF and unstable crack growth or fracture.

Rim – circumferential and radial cracking

Web – circumferential and radial cracking

Keyway – radial cracking

Bore Surface – radial cracking
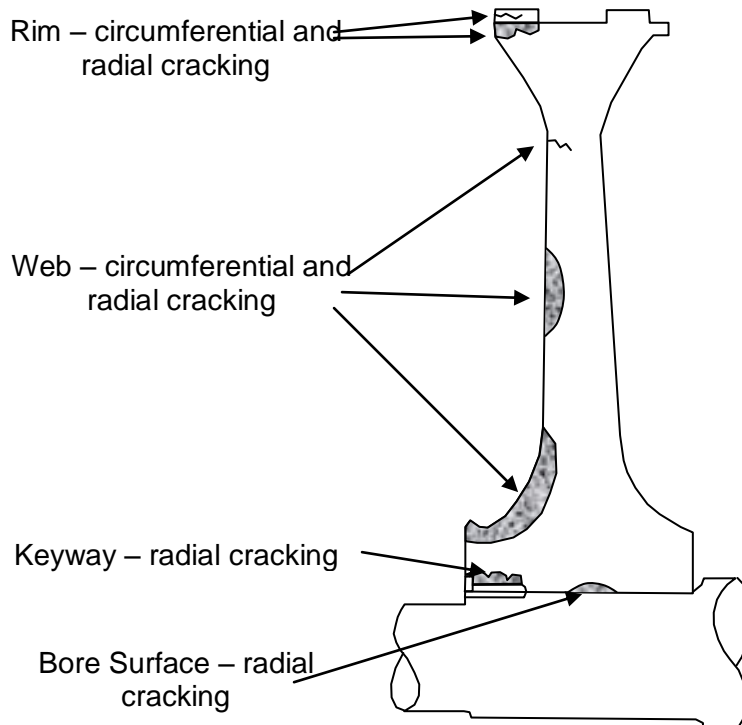
Figure 2.24: Diagram of an LP turbine disc with indications of the locations most susceptible to SCC (Lyle and Burghard, 1982).

Blade

Root

Type I

Dovetail

Rim Line

Type II
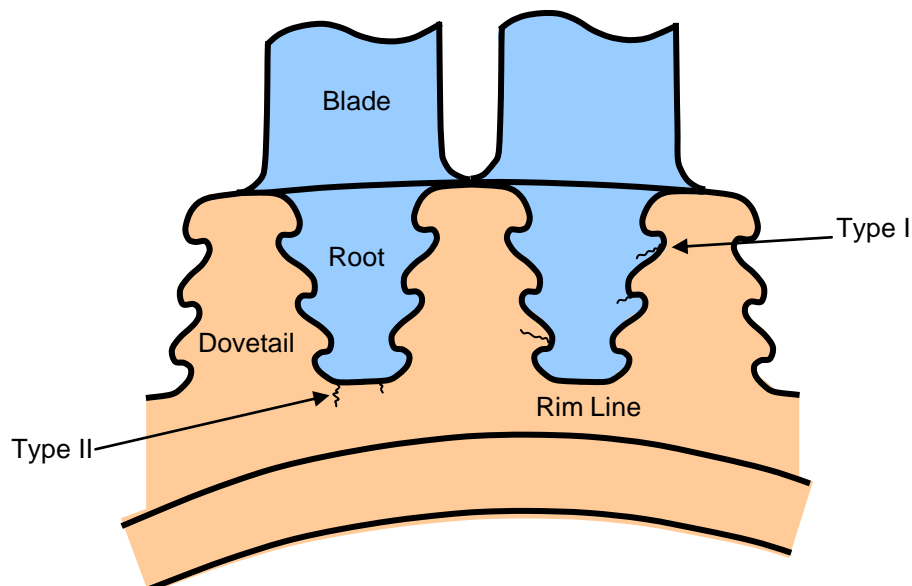
Figure 2.25: Diagram showing fir tree blade root attachment with common crack locations identified (Lyle and Burghard, 1982).

2.12. Summary

In summary, power can be generated in numerous ways, however, in the UK coal fired steam power plant are most commonly used to generate electricity. Turbine blades encounter various conditions depending on position their position within the system, as described in Section 2.3, although this work concentrates on low pressure turbine blades where the temperature range is 40 – 230°C. In Section 2.5 it is shown that there are many ways in which a metal may fail, however, this work will focus on possible stress corrosion cracking under mode I loaded samples.

SCC has been studied in various materials for many years but little investigation has been done using such mildly corrosive environments as condensing steam at 95°C. Understanding stress corrosion cracking is industrially very important because it is considered to be a delayed failure process, whereby microscopic cracks can potentially propagate through a metal undetected until catastrophic failure occurs. The aim of this work is to recreate the conditions experienced by low pressure steam turbine blades to establish links between crack length and external factors such as exposure time in order to devise a method of dating stress corrosion cracks and therefore predicting their possible occurrence in-service.

3. Experimental Procedure

Three types of specimen were produced for the investigation of Stress Corrosion Cracking (SCC): Wedge Opening Loading (WOL), Single Edge Notched Bend (SENB) and Free Surfaces. In this chapter the methods used for the production of these specimens will be described together with an introduction to the analytical techniques used including: scanning and transmission electron microscopy, focused ion beam sample preparation and synchrotron X-ray analysis techniques.

3.1. Wedge Opening Loading

A set of 16 WOL specimens (Figure 3.1) were provided by the project sponsors, Alstom Power Materials Research, Rugby. They were machined from FV520B, which is a precipitation hardened martensitic stainless steel, used in the power industry for low pressure steam turbine blades and rotors. The composition of the steel is detailed in Table 3.1. The steel was subject to a heat treatment regime of two hours at 990 – 1050°C, air cooled then four hours at 750 – 950°C, air cooled then four hours above 500°C and air cooling. Specimens were provided with four different proof strengths of 1018, 1024, 1061 and 1072 MPa. The specimens were exposed to condensing steam at 95°C with controlled water chemistry (e.g. oxygen content, pH and conductivity) to recreate the conditions experienced by low pressure steam turbines in service.
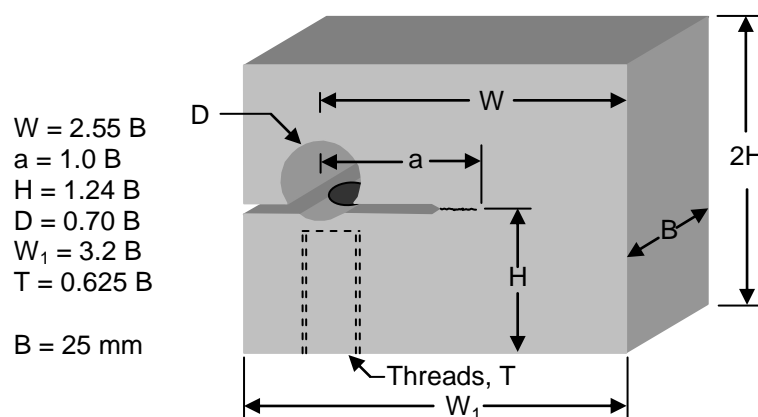
Figure 3.1: "T" type wedge opening loading (WOL) specimen with relative dimensions (Brown, 1970).

Table 3.1: Compositional tolerances of the FV520B used for the WOL specimens (Osgerby, Private Communication, 2006).

Element	C	Si	Mn	P	S	Ni	Cr	Mo	Nb	Cu
Wt%	<0.07	<0.7	<1.0	<0.025	<0.015	5.0-6.0	13.0-15.0	1.2-2.0	0.15-0.30	1.4-2.1

Table 3.2: Data for the 16 WOL specimens prior to exposure to condensing steam at 95°C.

Specimen Number	Proof Stress / MPa	Exposure Time / h	Initial Stress Intensity / MPa m$^{1/2}$	Fatigue Pre-cracked?
799	1061	98284	10	Yes
800		12960	8	No
801		9792	30.3	No
802		7536	62.5	No
803	1024	98284	5	Yes
804		12960	16.5	No
805		9792	32	No
806		7536	65.3	No
807	1018	98284	5	Yes
808		12960	15.5	No
809		9792	30.9	No
810		7536	62.3	No
811	1072	98284	5	Yes
812		12960	15.9	No
813		9792	31.2	No
814		7536	62.6	No

For each proof strength there were four exposure times: 7536, 9792, 12960 and 98284 h, which have been rounded to 7.5, 9.8, 13.0 and 98.3 kh throughout this thesis. The specimens tested for 98.3 kh were fatigue pre-cracked prior to exposure to condensing steam at 95°C. The remaining specimens were stressed in the as-notched state. The stress was applied by tightening a bolt onto a perpendicular cylindrical wedge, which created a mode I (opening) force. The initial stress intensity at the pre-crack/notch tip ranged between 5 and 62.6 MPam$^{1/2}$. Table 3.2 contains the aforementioned specimen details.

After exposure the specimens were fully separated into two pieces to reveal the surfaces of the stress corrosion crack as shown schematically in Figure 3.2. It should be noted that only one section of each WOL specimen was provided for examination.
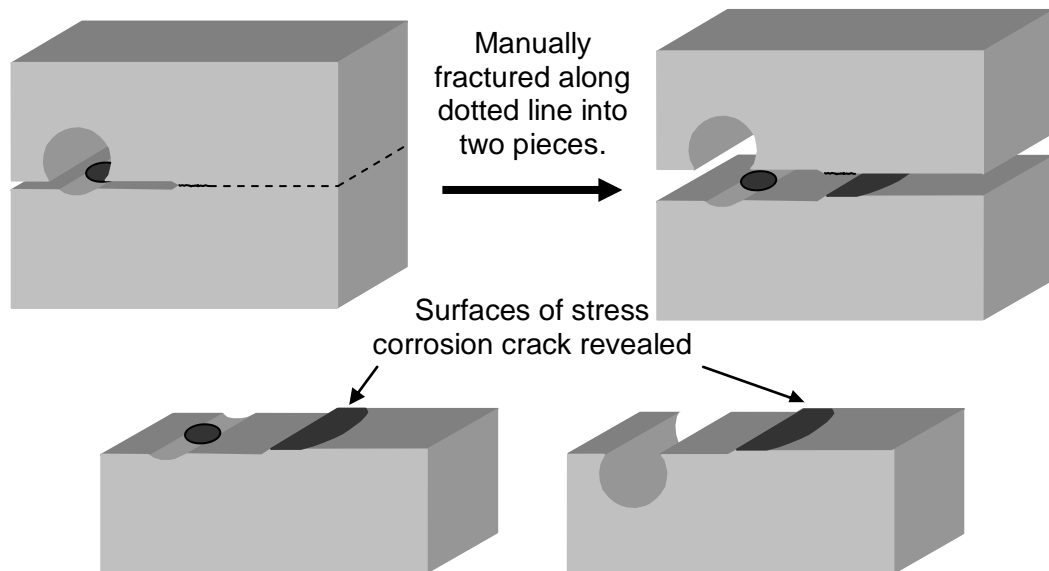
Figure 3.2: Schematic showing how the WOL specimens were fractured into two pieces to facilitate examination of the stress corrosion crack surface.
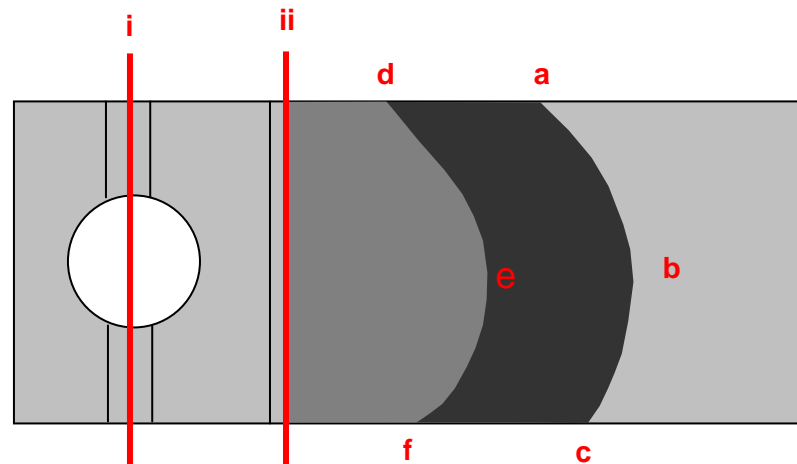
Figure 3.3: Schematic showing the positions from which crack length measurements were taken: "i" = centre of the threaded hole, "ii" = crack initiation and "a - f" = maximum length.

Initial examination involved taking detailed measurements of the crack lengths, using a digital vernier calliper. Measurements were taken from the centre of the screw thread hole, i, and from the crack initiation edge, ii, to the maximum crack length points along the sample sides, a and c, and the overall maximum crack length, b, for all 16 specimens. A schematic of these points is shown in Figure 3.3. As specimens 799 (1061 MPa, 98.3 kh), 803 (1024 MPa, 98.3 kh), 807 (1018 MPa, 98.3 kh) and 811 (1072 MPa, 98.3 kh) were fatigue pre-cracked prior to exposure to condensing steam at 95°C, additional measurements to d, e and f were also made.

In order to examine the surfaces of the stress corrosion cracks the specimens had to be reduced to a size that could be accommodated by the analysing equipment. This

was accomplished using a Struers Labatom with an aluminium oxide cut-off wheel. Figure 3.4 shows how the specimens were reduced in size from their as-received condition. For consistency each specimen was cut 2 mm before the start of the notch and 2 mm further than the crack tip. The total height of the specimens was reduced to 10 mm. Care was taken to protect the crack surface at all times using appropriate sized pieces of cork sheet. For cross-section examination a slice of approximately 5 mm thickness was cut from the crack section of each specimen, using a Struers Accutom with an aluminium oxide cut-off wheel, mounted in edge retaining conductive Bakelite and metallographically prepared to a 1 µm finish.
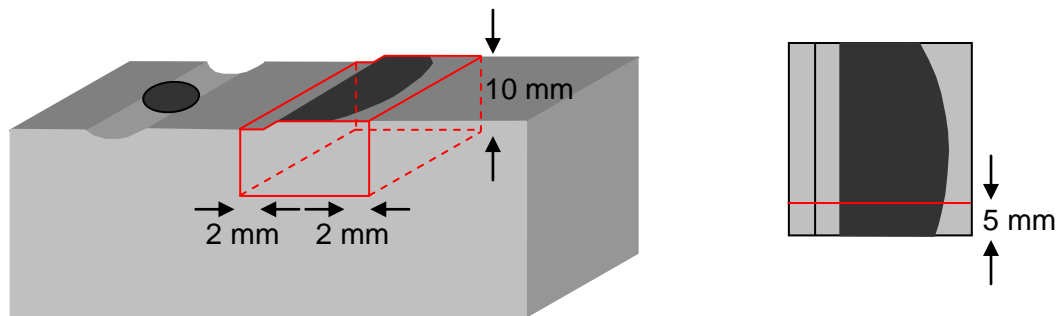
Figure 3.4: Schematic illustrating how the WOL specimens were reduced to an appropriate size for the analysing equipment. They were trimmed to 2 mm ahead of the notch and 2 mm after the crack tip with a maximum height of 10 mm. For cross section examination a 5 mm slice was cut from one edge.

3.2. Single Edge Notched Bend

Single edge notched bend (SENB) specimens, based on ASTM E 399-90 dimensions (Janssen, Zuidema and Wanhill, 2002), (Figure 3.5) with a chevron notch crack starter (Figure 3.6), were machined from a hot rolled slab of FV520B. The composition of the slab is shown in Table 3.1.

Experiments have confirmed that it is not possible to machine a sufficiently sharp, narrow notch to simulate natural crack growth so the chevron notch tip acts as an initiation point for fatigue pre-cracking (Janssen, Zuidema and Wanhill, 2002). The required notch depth was calculated such that the fatigue pre-crack length, a, should not exceed half the specimen width, W, to allow for stress corrosion crack growth during the testing period. The front and back surfaces were metallographically prepared with successively finer silicon carbide papers to 1200 grit to remove any machining marks and unwanted stress raisers prior to being fatigue pre-cracked.

Element	C	Si	Mn	P	S	Ni	Cr	Mo	Nb	Cu
Wt%	0.031	0.226	0.48	0.025	0.009	5.32	13.27	1.33	0.227	1.32

$B = 0.5\ W$
$S = 4\ W$
$a = 0.45\text{-}0.55\ W$
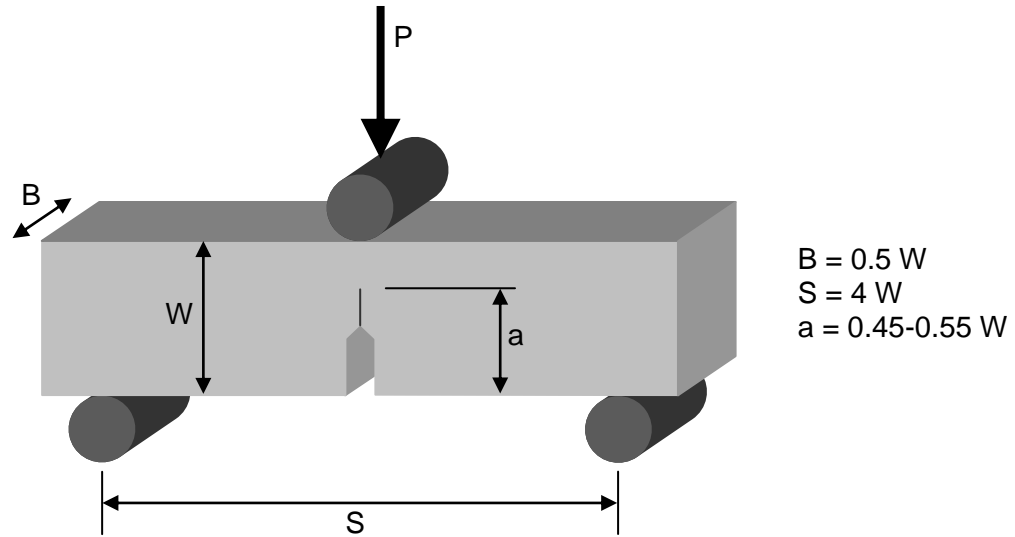
Figure 3.5: ASTM single edge notched bend (SENB) specimen with relative dimensions (following Janssen, Zuidema and Wanhill, 2002).
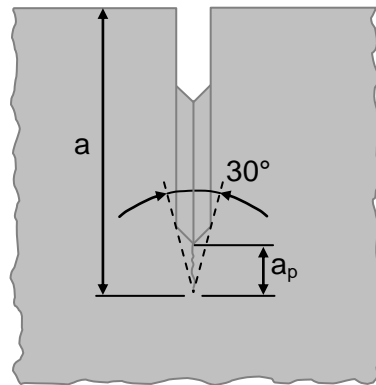
Figure 3.6: Chevron notch crack starter (following Janssen, Zuidema and Wanhill, 2002)

The samples were fatigue pre-cracked using a three-point bend fixture attached to an Instron Dartec 9610, which is a servohydraulic mechanical testing machine. S-N curve fatigue data, for stainless steels with similar composition to FV520B (Figure 3.7), were analysed to estimate the fatigue limit of the SENB specimens and the threshold stress intensity, K_c, for fatigue crack growth. By combining Equations 3.1 and 3.2 it was possible to calculate the load required to achieve a specific initial stress intensity, K_c, at the notch tip. K_I = fracture toughness under mode I loading, P = load, S = distance between supports, B = breadth of specimen, W = width of specimen and a = chevron notch plus fatigue crack growth.

If K = 10 MPam$^{\frac{1}{2}}$ then the crack growth rate is ~4 x 10^{-5} and therefore 25,000 cycles are required to propagate a crack ~1 mm.
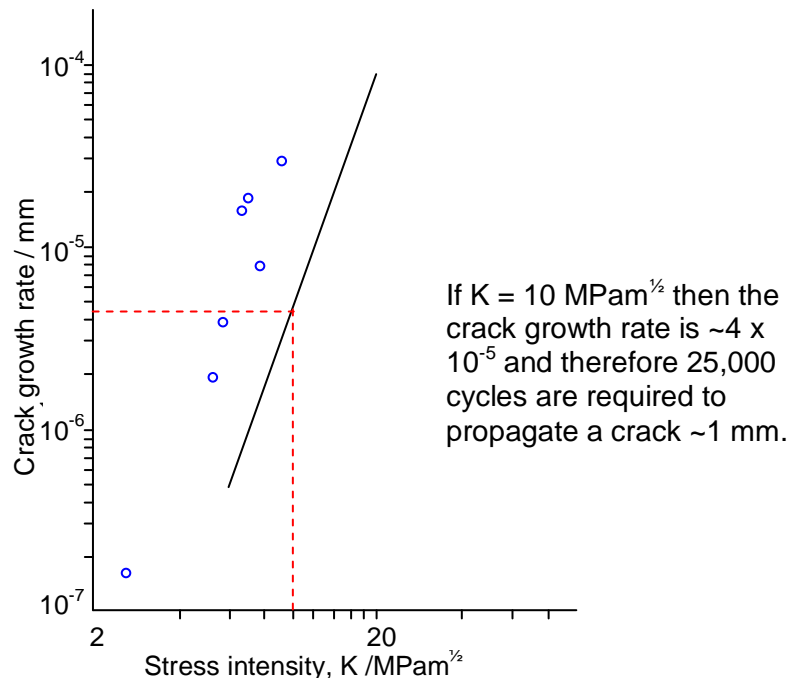
Figure 3.7: Fatigue crack growth data for a turbine blade steel in air (Zhou, 2007).

Preliminary tests were carried out on one SENB specimen to confirm the conditions required for the remaining specimens. The optimum conditions were determined to be 40,000 cycles at 5 Hz with a calculated load of 15 kN to achieve an initial K of 30 MPam$^{\frac{1}{2}}$. Specimens were stressed in a custom made three-point bend jig (Figure 3.8) and placed in a oven maintained with condensing steam at 95°C for times of 730, 1460, 2920, 4380, 5840, 7300 and 8760 h, which equate to 1, 2, 4, 6, 8, 10 and 12 months.

After exposure the specimens were reduced in size, using a Struers Labatom with aluminium oxide cut-off wheel, to approximately 5 mm from either side of the notch to conform to the dimensional constraints of the analysis equipment, shown schematically in Figure 3.9 (a). The cracks were protected with appropriate sized pieces of cork sheet during the preparation. After all cross sectional examination was complete, the samples were carefully cut into two pieces to reveal the surfaces of the stress corrosion crack, shown in Figure 3.9 (b).

$$K_I = \frac{PS}{BW^{\frac{3}{2}}} \bullet f\left(\frac{a}{W}\right)$$ .... ……………………...…..... ***Equation 3.1***

$$f\left(\frac{a}{W}\right) = \frac{3\left(\frac{a}{W}\right)^{\frac{1}{2}}\left[1.99 - \frac{a}{W}\left(1 - \frac{a}{W}\right)\left\{2.15 - 3.93\left(\frac{a}{W}\right) + 2.7\left(\frac{a}{W}\right)^2\right\}\right]}{2\left(1 + 2\frac{a}{W}\right)\left(1 - \frac{a}{W}\right)^{\frac{3}{2}}} \quad ....Equation\ 3.2$$

Figure 3.8: Three point bending jig used to stress SENB specimens whilst exposed to condensing steam at 95°C.
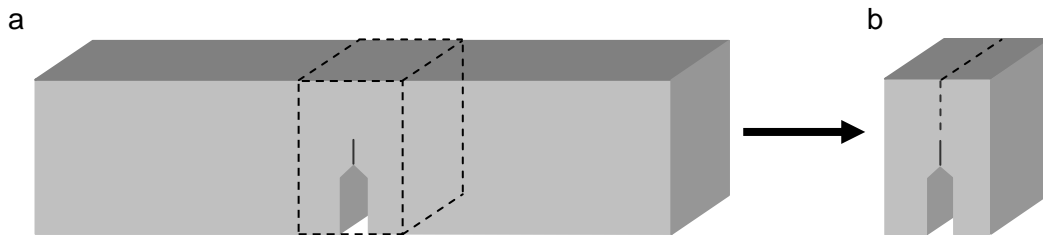
Figure 3.9: Area of SENB specimens cut out prior to cross-sectional examination (a) and to reveal the stress corrosion crack surfaces (b)

3.3. Free Surfaces

Specimens with approximate dimensions 20 x 20 x 10 mm were cut from the same hot rolled slab of FV520B, detailed in Table 3.3, using a Struers Labatom with aluminium oxide cut-off wheel. One 20 x 20 mm surface of each specimen was metallographically prepared to either 220 grit or 1 µm finish and subjected to condensing steam at 95°C for 730, 1460, 2920, 4380, 5840, 7300, 8760 and 10220 h (1, 2, 4, 6, 8, 10, 12 or 14 months). After exposure the surfaces were examined and compared to the WOL and SENB specimens.

3.4. Substrate Microstructure

Samples with approximate dimensions 5 x 5 x 10 mm, were produced from both the WOL specimens and the hot rolled slab of FV520B that was used to make the SENB and Free Surface specimens. They were mounted in edge retaining conductive Bakelite and metallographically prepared to 1 µm finish. These polished samples were etched in Kallings I reagent (33 ml distilled water, 33 ml ethanol 96%, 33 ml

hydrochloric acid 32% and 1.5 g copper(II) chloride) (Lee, Kim, Jung, Pyoun and Shin, 2009) to examine the substrate microstructure and establish what effect this might have on SCC.

3.5. Hardness Testing

A Mitutoyo AVK-C2 Macro Vickers hardness testing machine with 30 kg load was used to measure the substrate hardness of the WOL specimens. Five measurements per sample were recorded and an average value was calculated. Hardness testing gives an indication of the strength of a metal (Callister, 2000).

3.6. Optical Microscopy

The WOL and SENB specimens were observed in bright field Köhler illumination using a Reichert MEF3 reflective light optical microscope with attached digital camera. In bright field mode, light that is reflected perpendicular to the sample surface is detected so the etched grain boundaries, where light rays are scattered, appear dark (Haynes, 1984).

3.7. Scanning Electron Microscopy

The WOL, SENB and Free Surface specimens were examined using a Leo 1530 VP Field Emission Gun Scanning Electron Microscope (FEGSEM). Secondary electron micrographs of the crack surfaces were acquired using accelerating voltages of 5 or 10 kV with a 30 μm aperture. When using the Everhart Thornley detector the working distance was around 12 mm and ≤ 5 mm with the in lens detector. The in lens detector was used to collect higher resolution secondary electron micrographs. Cross sections through the main crack were imaged using the backscattered electron detector with 10-20 kV accelerating voltage, 30-60 μm aperture and 10-12 mm working distance. The backscattered electron detector was chosen because higher atomic mass elements appear brighter so it was possible to visually distinguish between substrate and oxide.

3.8. Focused Ion Beam Scanning Electron Microscopy

A focused ion beam scanning electron microscope is similar to a normal scanning electron microscope but it has an additional ion column mounted at 52° from vertical. Gallium is currently the preferred ion source and is used primarily to sputter material from the sample under examination (Giannuzzi and Stevie, 2005).

A FEI Nova 600 Nanolab dual beam Focussed Ion Beam FEGSEM (FIB FEGSEM) was used to acquire secondary electron micrographs at 10 kV/2.1 nA and ion induced secondary electron images at 30 kV/10 pA. It was also used to produce site-specific electron transparent samples for analysis using Transmission Electron Microscopy (TEM).
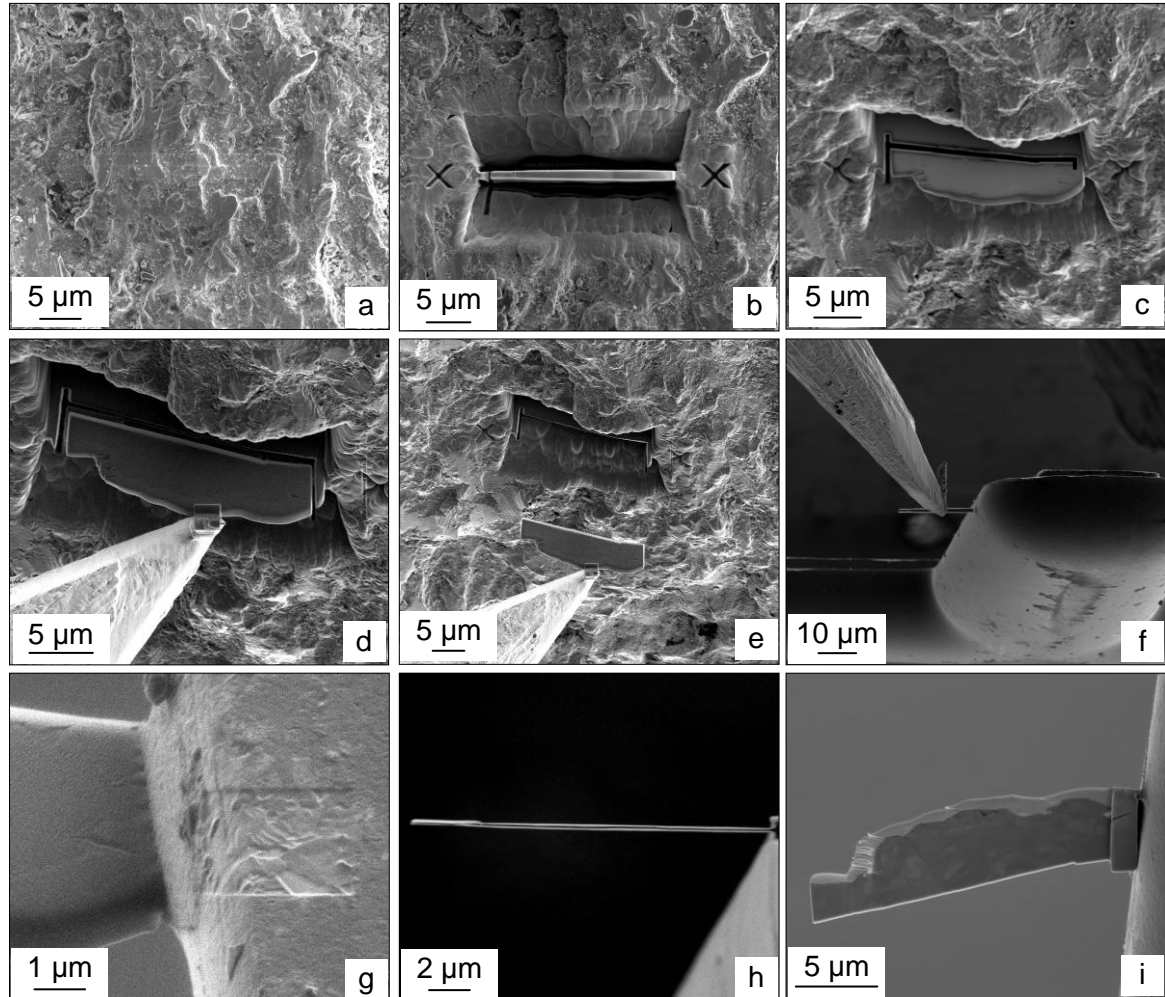
Figure 3.10: Successive stages of site specific TEM preparation using the dual beam FIB FEGSEM: a) area selection and protective platinum deposition, b) sample isolated by digging trenches on either side, c) "u-shaped" cut, d) micromanipulator attached to sample and final ligament milled away, e) sample lifted out of the bulk specimen, f) sample aligned with copper grid, g) sample attached to copper grid with platinum and the micromanipulator is detached, h) middle section of sample thinned to ~200 nm and i) finished sample.

The procedure for TEM sample preparation is shown in Figure 3.10. The first step was to choose an area and deposit a layer of protective platinum (a). The first few atomic layers of the sample were preserved by depositing an initial 500 nm thick layer of electron beam platinum at 0° tilt before a 2 µm layer of ion beam platinum was deposited at 52° tilt on top of the electron beam platinum. The next stage (b) was to

use the ion beam to mill trenches either side of the area of interest to whatever depth is appropriate for the sample being produced. For the majority of samples prepared, a depth of 7 μm was sufficient. The remaining material was milled away using successively smaller ion beam currents at 50.5° and 53.5° tilt until both sides of the platinum layer were clean and the sample was approximately 2 μm thick. At 7° tilt, the ion beam was used to mill a "u-shape" through the sample (c). At 0° tilt the micromanipulator was carefully inserted until it touched the sample. A layer of platinum was deposited which attached the micromanipulator to the sample (d) and then the ion beam was used to mill away the final ligament. Using 1 μm stage movements the sample was lifted out of the bulk specimen (e). The sample was aligned with a prong of a copper TEM grid (f). The sample was attached to the grid by depositing a connecting layer of platinum (g) and the ion beam was used to detach the micromanipulator by milling away the original platinum join. The middle section of each sample was thinned to electron transparency, approximately 200 nm, using successively smaller ion beam currents (h). The final sample (i) was then ready for TEM analysis. In this example the sample was attached along one side to the "I" prong of the copper grid, however, in many instances the samples were attached by two corners to the centre of the "V" prong as this provided better stability.

3.9. Transmission Electron Microscopy

The site specific thin foil samples produced in the dual beam FIB FEGSEM were examined using a Jeol JEM 2000FX TEM. The accelerating voltage used was 200 kV. Images were collected with a Gatan Erlangshen ES500W digital camera. A double tilt sample holder was employed for convergent beam and selected area diffraction.

The first step for collecting electron diffraction patterns was to select an area of interest. Then the sample holder was rotated through the range of alpha tilt angles until the area of interest became dark as this indicated the diffraction contrast was greatest. Then the convergent beam diffraction pattern was generated. The aim was to find a low order zone axis, which is where lots of planes intersect. Small adjustments were made to the alpha tilt until the low order zone axis convergent beam diffraction pattern was centred on the phosphorous screen. The sample holder was then rotated in the beta tilt direction until the convergent beam diffraction pattern was symmetrical. Once this was achieved a Selected Area Diffraction (SAD) pattern was generated, focused and centred on the phosphorous screen. The selected area

diffraction patterns were collected on photographic film and developed conventionally. A schematic representation of a diffraction pattern is shown in Figure 3.11.
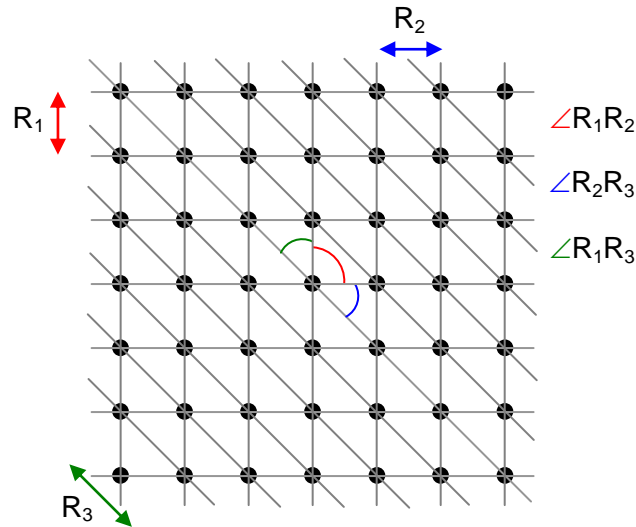
Figure 3.11: Schematic representation of a selected area diffraction pattern.

$$Rd = L\lambda = camera\,constant$$ ....Equation 3.3

To analyse the SAD patterns it was necessary to measure the spacing between the spots, R_1 R_2 and R_3, and the angle between the spots, $\angle R_1 R_2$, $\angle R_1 R_2$ and $\angle R_1 R_2$. The values for R_1, R_2 and R_3 were converted into "d" values using Equation 3.3, where R = real values measured from the diffraction pattern, d = interplanar spacing, L = camera length and λ = wavelength of electrons at 200 kV (2.5×10^{-12} m) (Thomas and Goringe, 1797). The camera constant for the TEM used to collect the SAD patterns analysed in this thesis was calculated to be 2.472×10^{-12} m. The SAD patterns were analysed using a computer program called CRYSTAL which calculated the possible crystal planes and zone axis by comparing information from the SAD pattern to data for known materials. In this instance the SAD patterns were compared to magnetite (Fe_3O_4) , maghemite (γ-Fe_2O_3), hematite (Fe_2O_3), goethite ($FeO(OH)$, chromia (Cr_2O_3), chromite (Cr_2O_4) and nickel chromium oxide ($NiCr_2O_4$). First the software required the crystal structure and lattice parameter, a, for the element or compound to which the SAD pattern was compared. Then it was necessary to input two interplanar spacings and the angle between them, as acquired from the SAD pattern. The software then calculated the possible crystal planes and zone axis by comparing the information with that of the known element or compound. This process was repeated with each of the compounds listed previously until all options were exhausted.

3.10. Energy Dispersive X-ray Spectroscopy

Energy Dispersive X-ray Spectroscopy (EDS) was used with SEM, FIBSEM and TEM to establish which elements were present within the stress corrosion crack. In bulk samples the spatial resolution of the technique is limited by the sampling volume, which is 1 μm^3 (Goodhew, 2001) at 20 kV accelerating voltage. EDS can be confidently used as a qualitative technique and as a quantitative technique if the relevant standards are available. Thick sections used in SEM suffer from a high interaction/excitation volume, plus the possibility of fluorescence of neighbouring atoms with lower binding energy (Goodhew, 2001). Therefore it is important to consider possible sources of errors when reporting quantified data (Haynes, 1984). The interaction/excitation volume is reduced for thin sections examined with TEM (Goodhew, 2001) so the errors associated with quantified data are less. SEM point spectra and maps were collected at 20 kV with 60 µm aperture and the largest possible working distance ~20 mm. TEM point spectra were collected at 200 kV.

3.11. Electron Backscatter Diffraction

EBSD is a technique that has been developed for use with SEM and is now used with FIB FEGSEM. Amongst other things it is used for phase identification. For the technique to work the sample must have a highly polished surface and be positioned so that the incident electron beam makes an angle no greater that 20° with the sample surface. This increases the proportion of backscattered electrons that are diffracted out of the sample, which can be captured and converted into a diffraction pattern by complex computer software (Randle, 2000).

3.12. X-ray Absorption Fine Structure

An atom absorbs X-rays most strongly at wavelengths around the binding energy of the first shell electrons (Newville, 2004). The scientific theory behind this phenomenon is known as X-ray Absorption Fine Structure (XAFS). By collecting data over a range of photon energies it is possible to determine the particular energy at which atoms absorb most strongly, called the absorption edge (Newville, 2004). The spectra produced show the X-ray absorption coefficient, µ, with respect to energy, based on Beer's Law shown in Equation 3.4 where "I" is the intensity of the X-ray transmitted through the sample, "I_0" is the intensity of the incident X-ray and "t" is the thickness of the sample.

$$I = I_0 \, e^{-ut}$$ ....*Equation 3.4*

The spectra collected in this way can be analysed in two ways. The first part of an XAFS spectrum, up to 30 eV past the absorption edge, is called X-ray Absorption Near Edge Structure (XANES) and from this it is possible to determine information about the absorbing atom. The remainder of the spectrum is called Extended X-ray Absorption Fine Structure (EXAFS) and this gives information about the atoms in the immediate vicinity of the absorbing atom (Newville, 2004). It is possible to determine the oxidation state, coordination chemistry and coordination number of the absorbing atom and immediately adjacent atoms plus the distances between the absorbing and adjacent atoms (Newville, 2004).

The I18 microfocus spectroscopy beamline at Diamond Light Source synchrotron on the Harwell Science and Innovation Campus in South Oxfordshire was used to examine the oxide on the stress corrosion cracks. XANES and EXAFS data were collected from site-specific samples produced in the dual beam FIB FEGSEM that had not been thinned to electron transparency, the crack surface of bulk samples, reference oxide samples and reference metal foil samples of iron, chromium and nickel. Data were collected at energies around the iron, chromium and nickel adsorption edges. The absorption edge for iron is 7112 eV, chromium is 5989 eV and nickel is 8333 eV. The beam size during the experiments was 4 x 4 μm.
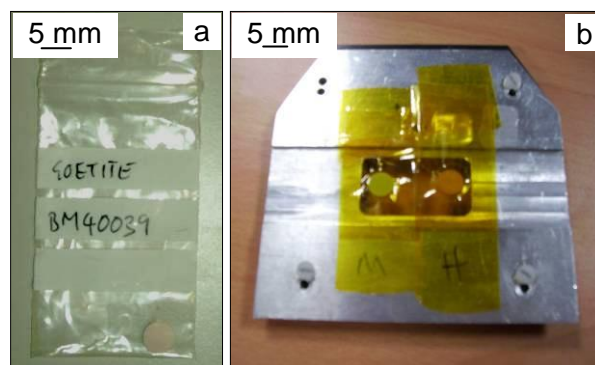
Figure 3.12: (a) Reference pellet of goethite mixed with boron nitride and (b) arrangement of pellets for use in the synchrotron.

Reference oxide samples of magnetite (Fe_3O_4), synthetic hematite (Fe_2O_3), maghemite (γ-Fe_2O_3), amorphous iron oxide, goethite (FeO(OH)), synthetic goethite (FeO(OH), chromite (Cr_2O_4), nickel (II) oxide (NiO) and nickel chromium oxide ($NiCr_2O_4$) were donated by the Natural History Museum. These samples were made into pellets for use in the synchrotron. The total pellet mass was 1 g, with 5% reference sample and

the balance of boron nitride. The mixture was ground in a pestle and mortar for a minimum of five minutes and then pressed in a 5 mm die under a load of five tons. An example of a pellet produced from goethite is shown in Figure 3.12 (a). The pellets were secured between two layers of X-ray transparent Kapton tape and attached to a mounting block as shown in Figure 3.12 (b).
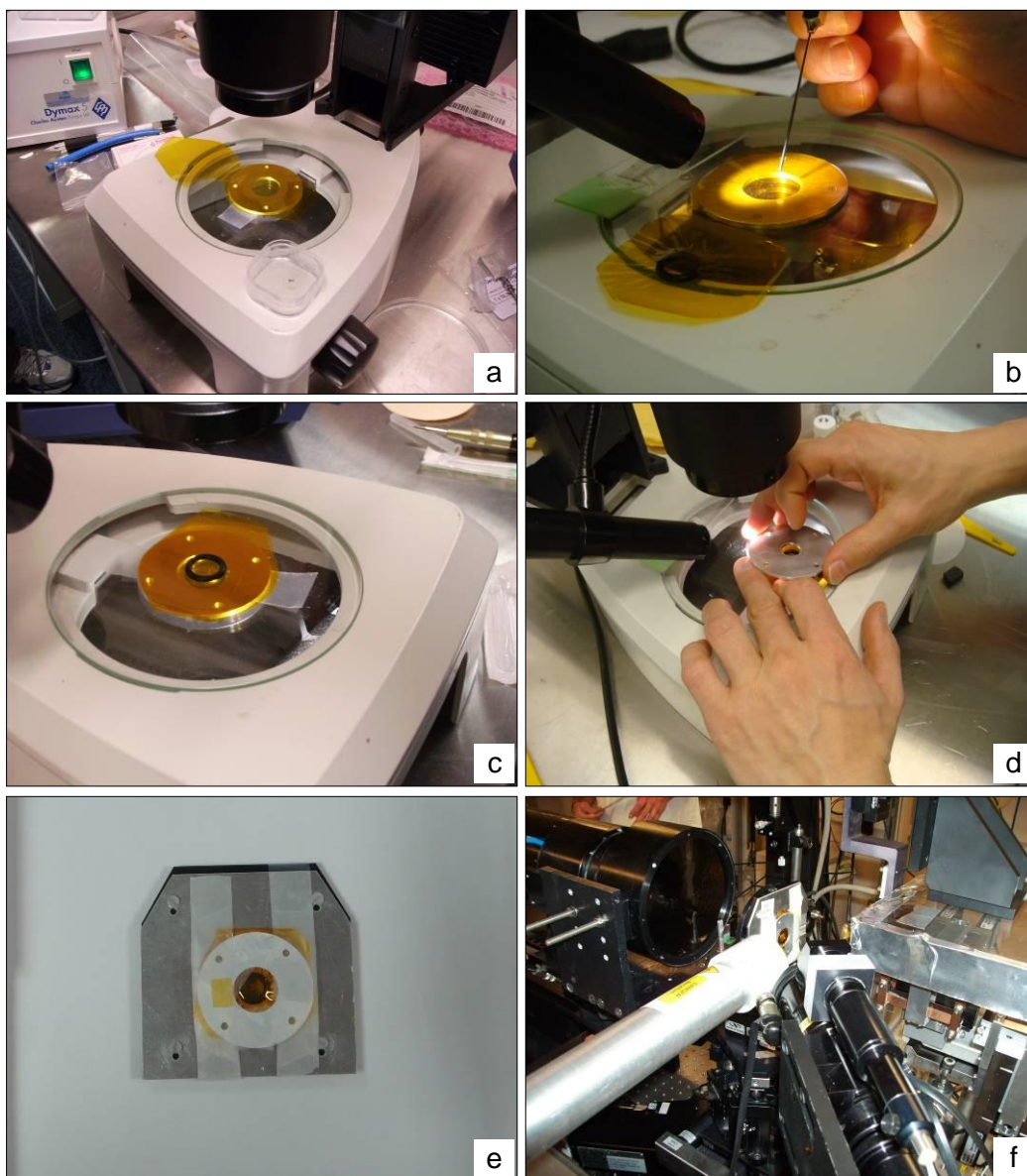
Figure 3.13: Photographs showing the successive stages of mounting site specific samples for examination in the synchrotron: a) sheet of Kapton film cut to an appropriate size and placed over back plate, b) site-specific sample placed on the Kapton film in the centre of the back plate ring, c) Kapton film folded over to contain sample and o-ring centrally aligned on top, d) top plate placed centrally and secured with adhesive tape, e) sample holder attached to mounting block with adhesive tape and f) mounting block aligned with synchrotron beam.

The site specific samples produced in the dual beam FIB FEGSEM were very small and fragile. Unlike the pellets, they could not be held between two layers of Kapton

tape as this would have rendered them unsuitable for subsequent examination with TEM. Instead the following method of securing the samples was devised which is shown pictorially in Figure 3.13. A sheet of Kapton film was folded in half and trimmed to the outer size of the ring-shaped back plate (ø ~ 55 mm) and then opened up (a). The site specific sample was placed onto the film at the centre of the inner ring (ø ~ 21 mm) of the back plate (b). The sheet of Kapton film was folded again so that the sample was between the two layers (c). An o-ring with diameter slightly smaller (ø ~ 14 mm) than the inner ring of the back plate was placed centrally on top of the film (c). A ring-shaped top plate ($\varnothing_{outer}$ ~ 55 mm, $\varnothing_{inner}$ ~ 12 mm) was then put on top and secured with adhesive tape (d). The hole in the top plate was smaller than the hole in the back plate so it pushed down on the o-ring, creating tension in the film which kept the sample level with the back plate. This arrangement was then attached to a mounting block with adhesive tape (e) and aligned with the synchrotron beam (f).

Unidentified XANES spectra collected from the site specific and bulk samples were analysed using software called Athena (version 0.8.059). The program has the capability of fitting a linear combination of standard spectra to an unknown spectrum. The data were fitted to the metal foils and the reference oxide samples provided by the National History Museum. The software calculates all the possible combinations of standards and returns a list containing the best matches to the unknown compound and the statistical accuracy of each result. Where multiple solutions were found the best match was chosen by considering the statistical accuracy for each solution.

3.13. X-ray Diffraction

Each WOL crack surface was examined using X-ray diffraction (XRD). Initial experiments were carried out using a copper, chromium and cobalt tube to determine which X-ray source produced the best results. Data were collected by a Bruker D8 X-ray diffractometer using a copper X-ray tube, solex energy dispersive detector and Huber quarter circle Eulerian cradle with a 1 mm divergence slit, 1 mm receiving slit and 0.2mm detector slit. Data were collected in continuous mode from 2-140° with a step size of 0.02° and 8 s counting time. For the 13.0 kh samples additional data were collected using the same equipment but the 2 theta range was reduced to 20-70°. The patterns were analysed by comparing peak positions (d-spacings) with those of known compounds until all the peaks were accounted for.

The Diamond light source synchrotron was used to collect μXRD data from two site specific samples, one from a line of oxide with mixed morphology on the crack surface of specimen 799 (1061 MPa, 98.3 kh) and one through oxide on the crack surface of specimen 801 (1061 MPa, 9.8 kh). XRD data was collected at 10 keV with an area detector. Patterns collected in this way present as rings of spots which are converted into peaks of d-spacings and analysed in a similar way to conventional XRD.
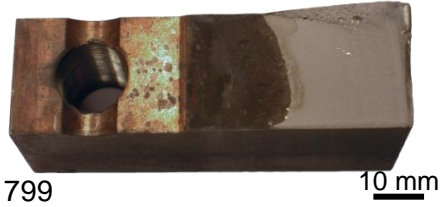
4. Results and Discussion: Wedge Opening Loading

A set of 16 WOL SCC specimens of FV520B with proof strengths of 1018, 1024, 1061 and 1072 MPa were produced by Alstom Power Materials Research, Rugby. One specimen of each proof strength was exposed to condensing steam at 95°C for 7.5, 9.8, 13.0 and 98.3 kh. After exposure the specimens were fully separated into two pieces to reveal the surfaces of the cracks and one section of each specimen was provided for examination. Results from the examination of these specimens are presented and discussed in this Chapter. Evidence is shown which links exposure time to variables including crack length, proof strength, stress intensity and oxide development.

4.1. As-Received Specimens

Photographs of the WOL specimens in their as-received condition are shown in Figure 4.1. They are displayed in a grid with respect to exposure time (columns) and proof strength of the steel (rows). Of the 16 WOL specimens, 15 bottom sections and one top section were provided; however, this inconsistency is not thought to have affected the results. The bottom sections contain a threaded cylindrical hole which housed the bolt throughout the experiments whereas the top section contains a smooth incomplete cylinder where the wedge fitted during the experiments. Figure 3.1 shows the WOL specimen configuration during the experiments. The photographs in Figure 4.1 can be compared to the schematic representation of the crack surfaces (Figure 3.3) which shows the stress corrosion crack initiation from the tip of the chevron notch starter and the arced crack front that meets the manually fractured surface.

Figure 4.1: Half WOL specimens in the as-received condition after exposure to condensing steam at 95°C and subsequent fracture into two pieces (The exposure time and proof strengths are labelled).

4.2. Substrate Microstructure

The substrate microstructure of each specimen was examined using reflective light optical microscopy as described in Section 3.6. Figure 4.2 shows optical micrographs of the substrate microstructure for one specimen of each proof strength that had been exposed to condensing steam for the same time of 98.3 kh. The micrographs show that the samples have a martensitic microstructure interspersed with precipitates; this is consistent with information provided about FV520B which states that it is a precipitation hardened martensitic stainless steel.

The proof strengths of specimen 799 (1061 MPa, 98.3 kh) and 811 (1072 MPa, 98.3 kh) are similar to each other but the microstructures are quite different in appearance. Specimens 803 (1024 MPa, 98.3 kh) and 807 (1018 MPa, 98.3 kh) also have similar proof strengths but different substrate microstructures. The microstructures of specimens 799 (1061 MPa, 98.3 kh) and 803 (1024 MPa, 98.3 kh) are similar and specimen 807 (1018 MPa, 98.3 kh) has a similar appearance to specimen 811 (1018 MPa, 98.3 kh). There is no obvious trend in the substrate microstructure relative to the reported proof strengths of the specimens.

Hardness testing was carried out as described in Section 3.5 and used as a crude method to ascertain whether the proof strength information provided for the specimens was accurate. The hardness testing results are presented in Table 4.1. Specimen 811 (1072 MPa, 98.3 kh) had the highest average hardness of 387 HV30, which suggests it should also have the highest proof strength, which is consistent with the reported data. Specimen 799 (1061 MPa, 98.3 kh) had a slightly lower average hardness of 381 HV30 which is also consistent with the reported proof strength. If the individual results are considered, both specimen 799 (1061 MPa, 98.3 kh) and 811 (1072 MPa, 98.3 kh) had values of 385 and 390 HV30, which reflects the small difference in proof strength between the two specimens. Specimen 803 (1024 MPa, 98.3 kh) had an average hardness of 346 HV30, which was lower than the average hardness of specimen 807 (1018 MPa, 98.3 kh) 351 HV30. These results contradict the reported values of proof strength, however, the hardness values are very close to each other, which reflects the small difference between the reported proof strengths of specimens 803 (1024 MPa, 98.3 kh) and 807 (1018 MPa, 98.3 kh).

799
1061 MPa,
98.3 kh

100 µm

20 µm

803
1024 MPa,
98.3 kh

100 µm

20 µm

807
1018 MPa,
98.3 kh

100 µm

20 µm

811
1072 MPa,
98.3 kh

100 µm

20 µm
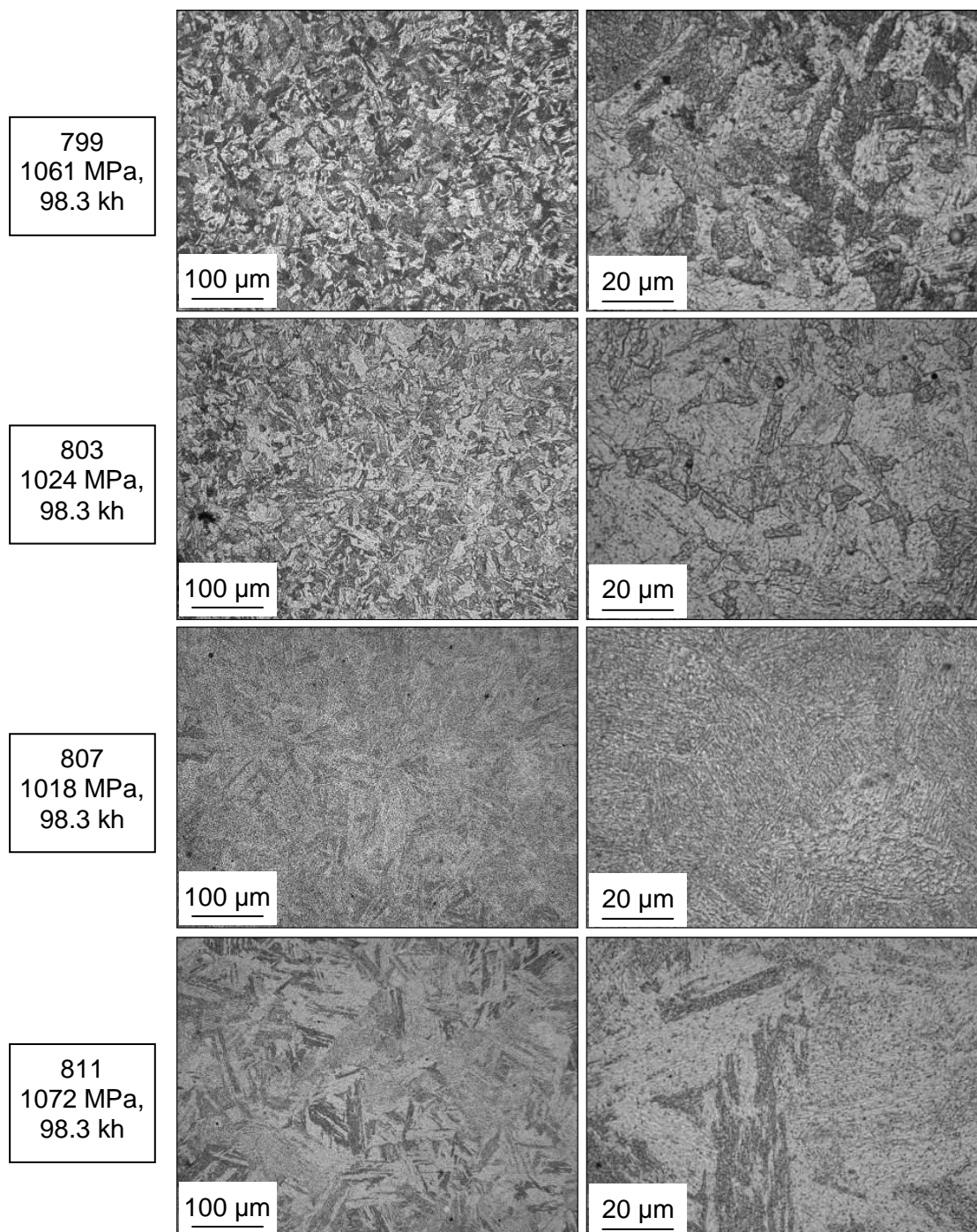
Figure 4.2: Optical micrographs showing the substrate microstructure at two magnifications for one specimen of each proof strength: 799 (1061 MPa, 98.3 kh), 803 (1024 MPa, 98.3 kh), 807 (1018 MPa, 98.3 kh) and 811 (1072 MPa, 98.3 kh).

Table 4.1: Substrate hardness values for specimens 799 (1061 MPa, 98.3 kh), 803 (1024 MPa, 98.3 kh), 807 (1018 MPa, 98.3 kh) and 811 (1072 MPa, 98.3 kh).

Specimen Number	Hardness / HV30					
	1	2	3	4	5	Average
799 (1061 MPa, 98.3 kh)	374	385	390	375	379	381
803 (1024 MPa, 98.3 kh)	342	345	345	349	350	346
807 (1018 MPa, 98.3 kh)	355	352	346	351	352	351
811 (1072 MPa, 98.3 kh)	389	385	390	386	386	387

4.3. Analysis of Crack Length

The crack length of each specimen was measured using the method described in Section 3.1 and these data are shown in Table 4.2. The most important values to note are the maximum crack lengths measured from the crack initiation, which are highlighted in column bii. Specimens 799 (1061 MPa), 803 (1024 MPa), 807 (1018 MPa) and 811 (1071 MPa) were fatigue pre-cracked prior to exposure to condensing steam at 95° for 98.3 kh. Column eii contains the maximum fatigue pre-crack lengths measured from the crack initiation edge. The total crack growth of the specimens exposed for 98.3 kh is equal to the total crack length minus the fatigue pre-crack length (bii – eii). The total crack growth for specimen 799 (1061 MPa, 98.3 kh) was therefore 11.5 mm. During the 98.3 kh exposure, specimens 803 (1024 MPa), 807 (1024 MPa) and 811 (1018 MPa) did not propagate past the fatigue pre-crack so have the same values for total crack length and fatigue pre-crack length, and therefore zero crack growth. For the samples that were not fatigue pre-cracked prior to testing, the total crack length is the same as the total crack growth.

Crack length has been analysed with respect to exposure time, proof strength of the steel and initial stress intensity at the crack tip.

Table 4.2: Total crack length and fatigue pre-crack length of each WOL specimen. Measurements were taken from the centre of the screw thread hole, i, and the initiation edge, ii, to the maximum crack propagation at the edges of the specimens, a and c, and the maximum crack length, b. This is shown schematically in Figure 3.3.

Specimen	Total Crack Length / mm						Fatigue Pre-crack Length / mm					
	ai	aii	bi	**bii**	ci	cii	di	dii	ei	eii	fi	fii
799	35.6	15.7	40.8	**21.1**	36.3	17.7	23.8	4.2	30.5	9.6	24.7	4.7
800	22.6	3.6	22.8	**4.8**	23.1	3.6						
801	23.2	3.6	26.2	**6.5**	23.1	3.1						
802	23.7	4.0	25.2	**5.3**	24.0	4.2						
803	22.7	3.1	23.7	**4.1**	22.4	2.7	22.7	3.1	23.7	4.1	22.4	2.7
804	22.7	2.8	24.4	**4.5**	23.2	3.4						
805	22.8	3.1	24.7	**5.1**	23.2	3.6						
806	22.6	2.9	24.0	**4.4**	22.5	2.9						
807	20.9	3.4	21.4	**4.0**	20.4	2.9	20.9	3.4	21.4	4.0	20.4	2.9
808	20.0	2.2	22.0	**4.2**	21.0	3.3						
809	20.4	2.5	21.6	**3.8**	20.3	2.8						
810	20.0	2.4	21.1	**3.4**	20.2	2.4						
811	28.7	2.7	29.9	**4.0**	28.9	3.1	28.7	2.7	29.9	4.0	28.9	3.1
812	20.8	2.9	21.8	**4.1**	20.1	2.5						
813	21.1	3.2	22.5	**4.7**	20.3	2.6						
814	20.7	2.8	21.8	**4.0**	20.1	2.7						

4.3.1. Effect of Exposure Time on Crack Length

It would be natural to assume that for the same proof strength steel, longer exposure times would result in longer crack lengths. Specimens 803 (1024 MPa), 807 (1018 MPa) and 811 (1072 MPa) did not propagate during the 98.3 kh exposure so do not fit this assumption. Specimen 799 (1061 MPa, 98.3 kh) had a longer crack than the other specimens in the same proof stress group, however, specimen 801 (1061 MPa, 9.8 kh) was the second longest and specimen 802 (1061 MPa, 7.5 kh) had a longer crack than specimen 800 (1061 MPa, 13.0 kh). Specimens 806 (1024 MPa), 810 (1018 MPa) and 814 (1072 MPa) were exposed for 7.5 kh and they had shorter cracks than the specimens in the same proof stress groups exposed for 9.8 kh and 13.0 kh. Specimen 805 (1024 MPa, 9.8 kh) had a longer crack than specimen 804 (1024 MPa,

13.0 kh). The same pattern was true for the equivalent specimens from the 1072 MPa proof stress group: specimen 813 (1072 MPa, 9.8 kh) had a longer crack than 812 (1072 MPa, 13.0 kh). The opposite result was shown for the 1018 MPa proof strength group: specimen 808 (1018 MPa, 13.0) had a longer crack than specimen 809 (1018 MPa, 9.8 kh). These inconsistencies suggest that a variable other than exposure time affected the crack length.

4.3.2. Effect of Proof Strength on Crack Length

Table 3.2 shows that specimens 811-814 had the highest proof strength of 1072 MPa, specimens 799-802 had a proof strength of 1061 MPa, specimens 803-806 had a proof strength of 1024 MPa and 807-810 had a proof strength of 1018 MPa. There is some debate in the literature about the effect of yield strength on SCC susceptibility. Speidel *et al* reported that the higher the yield strength of the steel the more susceptible it will be to SCC, however McMinn *et al* found no such correlation.

Of the specimens exposed for 7.5 kh, 802 (1061 MPa) had a longer crack than 806 (1024 MPa) and 806 (1024 MPa) had a longer crack than 810 (1018 MPa) which is consistent with the findings of Speidel *et al*. However, whilst specimen 814 (1072 MPa) had a longer crack length than 810 (1018 MPa) it had a shorter crack length than 802 (1061 MPa) and 806 (1024 MPa), which contradicts Speidel *et al* but supports McMinn *et al*. The specimens exposed for 9.8 kh showed the same pattern as the specimens exposed for 7.5 kh. The longest crack length was in specimen 801 (1061 MPa) followed by 805 (1024 MPa), 813 (1072 MPa) and 809 (1018 MPa). Similarly, of the specimens exposed for 13.0 kh the crack in specimen 800 (1061 MPa) was longer than 804 (1024 MPa), which was longer than 808 (1018 MPa). The shortest crack was in specimen 812 (1072 MPa). The results from this investigation were consistent with Speidel *et al* for proof strengths of 1018 MPa, 1024 MPa and 1061 MPa but the results for 1072 MPa proof strength contradicts Speidel *et al* and support McMinn *et al*. The crack lengths of specimens 799 (1061 MPa), 803 (1024 MPa), 807 (1018 MPa) and 811 (1072 MPa) exposed for 98.3 kh were not consistent with Speidel *et al* as the only crack growth was in specimen 799 (1061 MPa).

The crack length results for theses specimens show that the role of proof strength on SCC is inconclusive. Some of the results are consistent with the findings of Speidel *et al*, who wrote that materials with higher proof strength are more susceptible to SCC

whereas some of the results are consistent with the work of McMinn *et al* who found no such correlation between SCC and proof strength.

4.3.3. Effect of Initial Stress Intensity on Crack Length

The initial stress intensity at the notch tip for specimens 803 (1024 MPa, 98.3 kh), 807 (1018 MPa, 98.3 kh) and 811 (1072 MPa, 98.3 kh) was 5 MPam$^{\frac{1}{2}}$ and there was no crack growth, whereas the stress intensity of specimen 799 (1061 MPa, 98.3 kh) was 10 MPam$^{\frac{1}{2}}$ and the crack grew 11.5 mm. It can be deduced that there was a threshold stress intensity somewhere between 5 MPam$^{\frac{1}{2}}$ and 10 MPam$^{\frac{1}{2}}$. Specimen 800 (1061 MPa, 13.0 kh) had an initial stress intensity at the notch tip of 8 MPam$^{\frac{1}{2}}$ and the results showed that a crack initiated and propagated, which indicated that the threshold stress intensity was more precisely between 5 MPam$^{\frac{1}{2}}$ and 8 MPam$^{\frac{1}{2}}$. Obviously, this is an approximation as the threshold stress intensity would be specific to the proof stress of the steel.

Specimen 800 (1061 MPa, 13.0 kh) had a shorter crack than specimens 801 (1061 MPa, 9.8 kh) and 802 (1061 MPa, 7.5 kh) that were exposed for shorter times. The initial stress intensity of specimens 802 (1061 MPa, 7.5 kh), 806 (1024 MPa, 7.5 kh), 810 (1018 MPa, 7.5 kh) and 814 (1072 MPa, 7.5 kh) varied between 62.5 MPam$^{\frac{1}{2}}$ and 65.3 MPam$^{\frac{1}{2}}$. The stress intensity of specimens 804 (1024 MPa, 13.0 kh), 808 (1018 MPa, 13.0 kh) and 812 (1072 MPa, 13.0 kh) was around 16 MPam$^{\frac{1}{2}}$, which was double that of specimen 800 (1061 MPa – 13.0 kh). It is possible that the near-threshold stress intensity of specimen 800 (1061 MPa, 13.0 kh, 8 MPam$^{\frac{1}{2}}$) meant that the crack in specimen 802 (1061 MPa, 7.5 kh, 62.5 MPam$^{\frac{1}{2}}$) initiated earlier and therefore propagate further in a shorter time. This also explains why the cracks in specimens 804 (1024 MPa, 13.0 kh, 16.5 MPam$^{\frac{1}{2}}$), 808 (1018 MPa, 13.0 kh, 16.5 MPam$^{\frac{1}{2}}$) and 812 (1072 MPa, 13.0 kh, 16.5 MPam$^{\frac{1}{2}}$) were longer than (or very similar in length to) the specimens exposed for 7.5 kh in their respective proof strength groups.

The specimens exposed for 9.8 kh had initial stress intensities of 30.3 – 32 MPam$^{\frac{1}{2}}$. Specimens 801 (1061 MPa, 9.8 kh, 30.3 MPam$^{\frac{1}{2}}$), 805 (1024 MPa, 9.8 kh, 32 MPam$^{\frac{1}{2}}$) and 813 (1072 MPa, 9.8 kh, 30.3 MPam$^{\frac{1}{2}}$) had longer cracks than the specimens exposed for 7.5 kh and 13.0 kh in their respective proof strength groups. In these instances it is possible that the higher initial stress intensity in the specimens exposed for 9.8 kh caused the cracks to initiate earlier than in the specimens exposed for

13.0 kh and therefore propagated further in a shorter exposure time. The results indicated that exposure time and initial stress intensity are two competing variables that affect the stress corrosion crack length and that there is a delicate balance between which dominates.

4.4. Cross-Section Analysis

The stress corrosion cracks were examined in backscattered electron mode using a Leo 1530 VP FEGSEM. The crack propagation direction relative to the page is left to right in all images presented in this Section.

4.4.1. Exposure Time: 98.3 kh

Figure 4.3 shows a composite of micrographs which make up the full stress corrosion crack length through specimen 799 (1061 MPa). An oxide layer of a few microns covers the whole crack length. It is probable that some of the oxide was lost when the WOL specimens were separated into two pieces and during the preparation of cross-section samples due to cutting, grinding and polishing. It is also probable that the other sections of the WOL specimens (not provided for examination) have similar amounts of oxide, possibly in places corresponding to bare sections of the WOL specimens examined. In some discrete locations there is oxide measuring around 20 μm. Crack branching into the substrate can be seen on numerous occasions throughout Figure 4.3.

The full fatigue pre-crack length of specimens 803 (1024 MPa), 807 (1018 MPa) and 811 (1072 MPa) are shown with a series of micrographs in Figure 4.4, Figure 4.5 and Figure 4.6 respectively. Similar to specimen 799 (1061 MPa), there is a thin layer of oxide on the crack surfaces of specimens 803 (1024 MPa), 807 (1018 MPa) and 811 (1072 MPa). There is also substantial crack branching into the substrate in specimens 803 (1024 MPa) and 811 (1072 MPa), which is unlikely to have been a result of fatigue pre-cracking, therefore it must have occurred during exposure to condensing steam at 95°C. There is some crack branching into the substrate of specimen 807 (1018 MPa), but it is wider and shallower than in the other specimens exposed for 98.3 kh. Specimen 807 (1018 MPa) had the lowest original proof strength and the least amount of crack branching into the substrate. This supports the work of Speidel *et al* who said that higher strength steels are more susceptible to SCC as the cross section examination of specimens exposed to condensing steam for the same 98.3 kh duration show that stronger steels suffer from deeper crack branching into the substrate.

100 µm
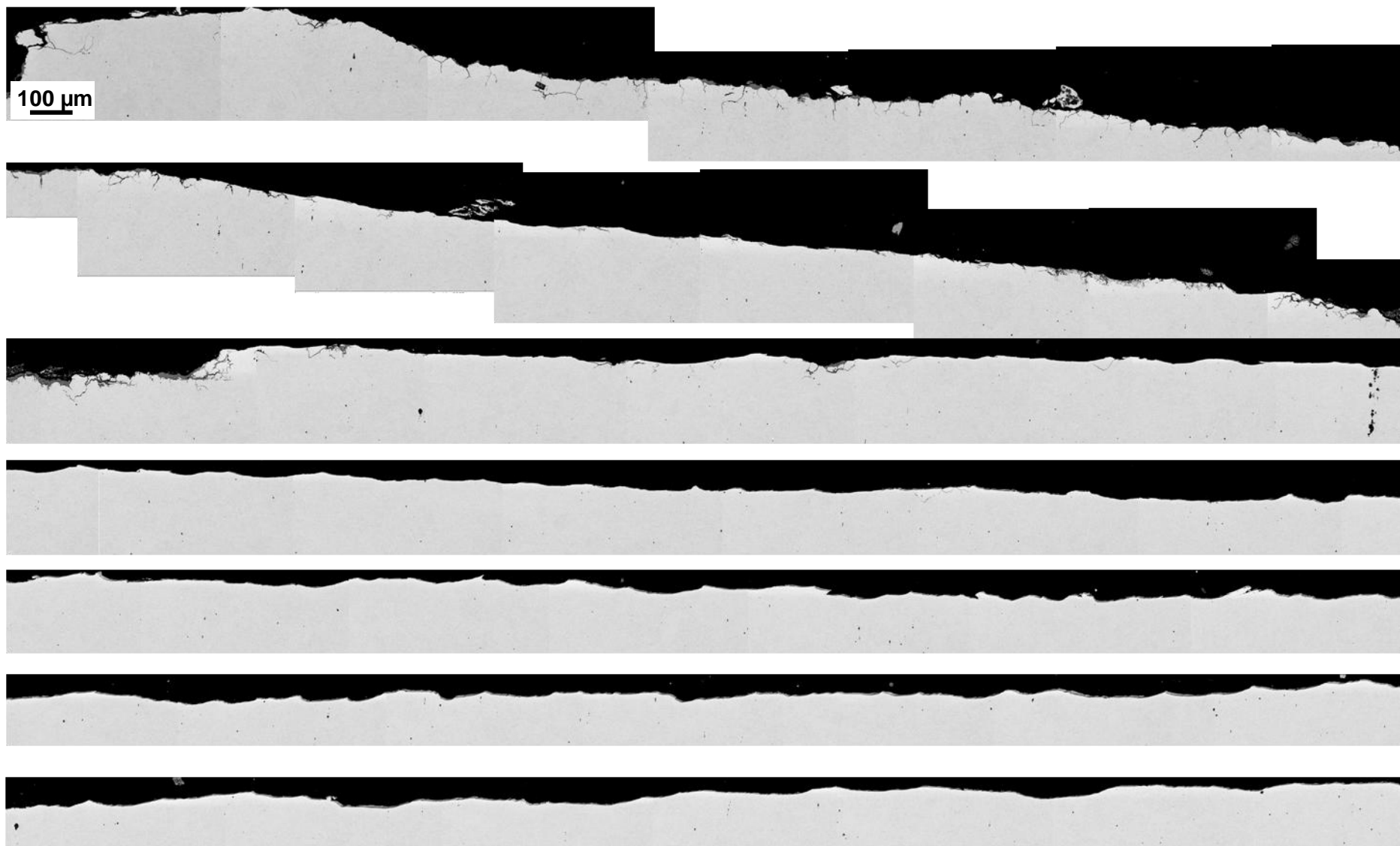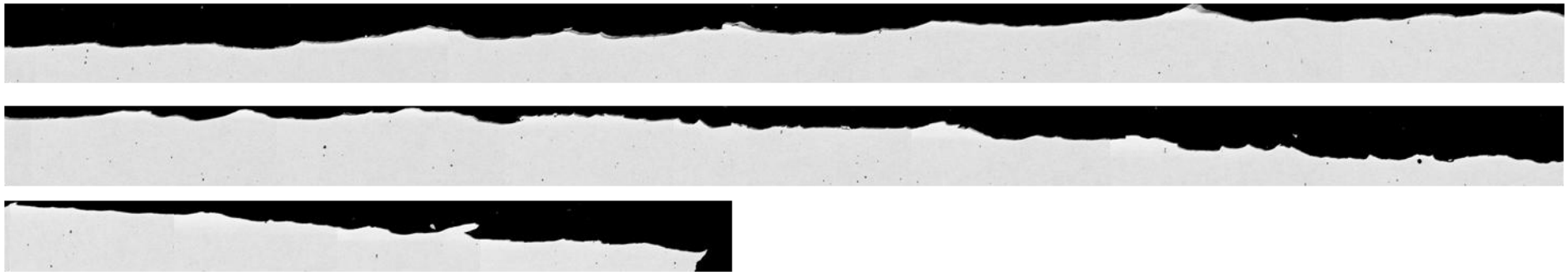
Figure 4.3: Composite of backscattered electron micrographs showing the full length of the stress corrosion crack through specimen 799 (1061 MPa, 98.3 kh)

100 µm
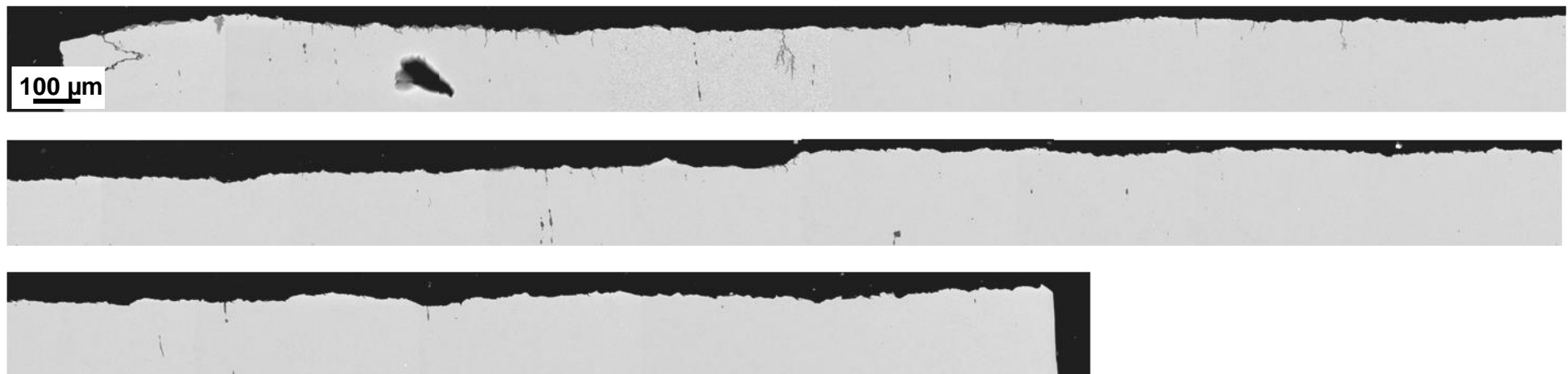
Figure 4.4: Composite of backscattered electron micrographs showing the full length of the stress corrosion crack through specimen 803 (1024 MPa, 98.3 kh)
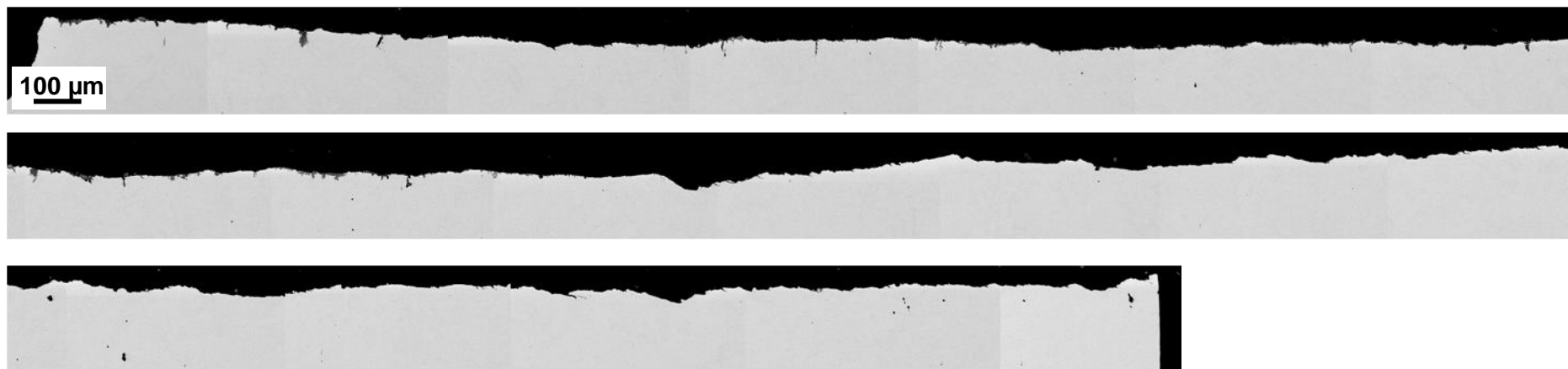
Figure 4.5: Composite of backscattered electron micrographs showing the full length of the stress corrosion crack through specimen 807 (1018 MPa, 98.3 kh)
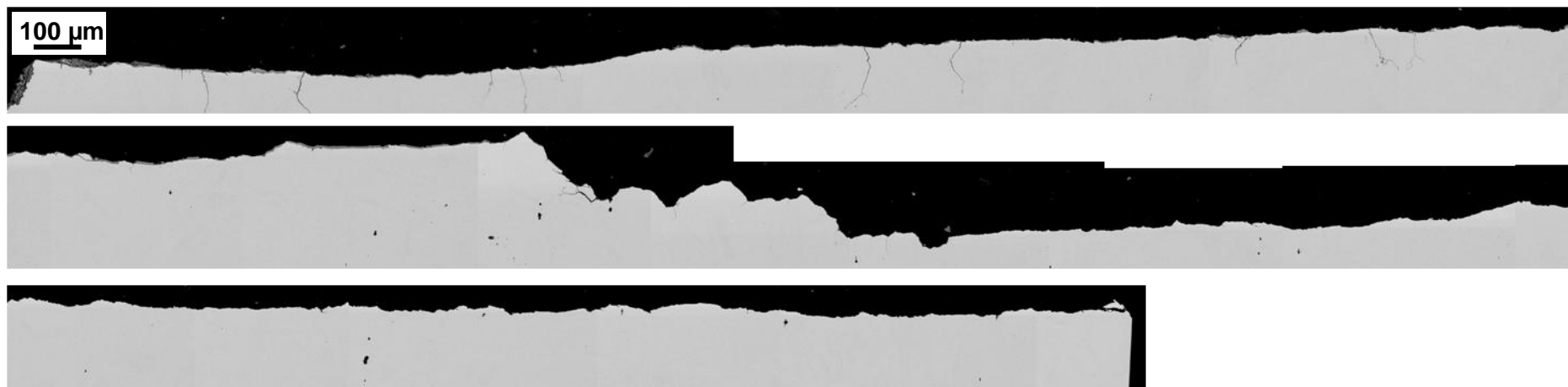
Figure 4.6: Composite of backscattered electron micrographs showing the full length of the stress corrosion crack through specimen 811 (1072 MPa, 98.3 kh)

Figure 4.7 (a) shows a backscattered electron micrograph of a cross section through specimen 799 (1061 MPa). It shows a solid block section of oxide along the surface of the main stress corrosion crack that measures ~ 8 µm thick and 30 µm long. The oxide consists of three layers, which are indicated by the different shades labelled i, ii and iii. In this micrograph there are also cracks penetrating the substrate between 10 µm and 20 µm, the majority of which point down and to the right, coinciding with the direction of the main crack growth. Figure 4.7 (b) shows a region of the sample where there is a continuous layer of oxide varying in thickness between 2 µm and 5 µm. There are multiple cracks that extend ≤ 50 µm into the substrate, some of which appear to trace grain boundaries.
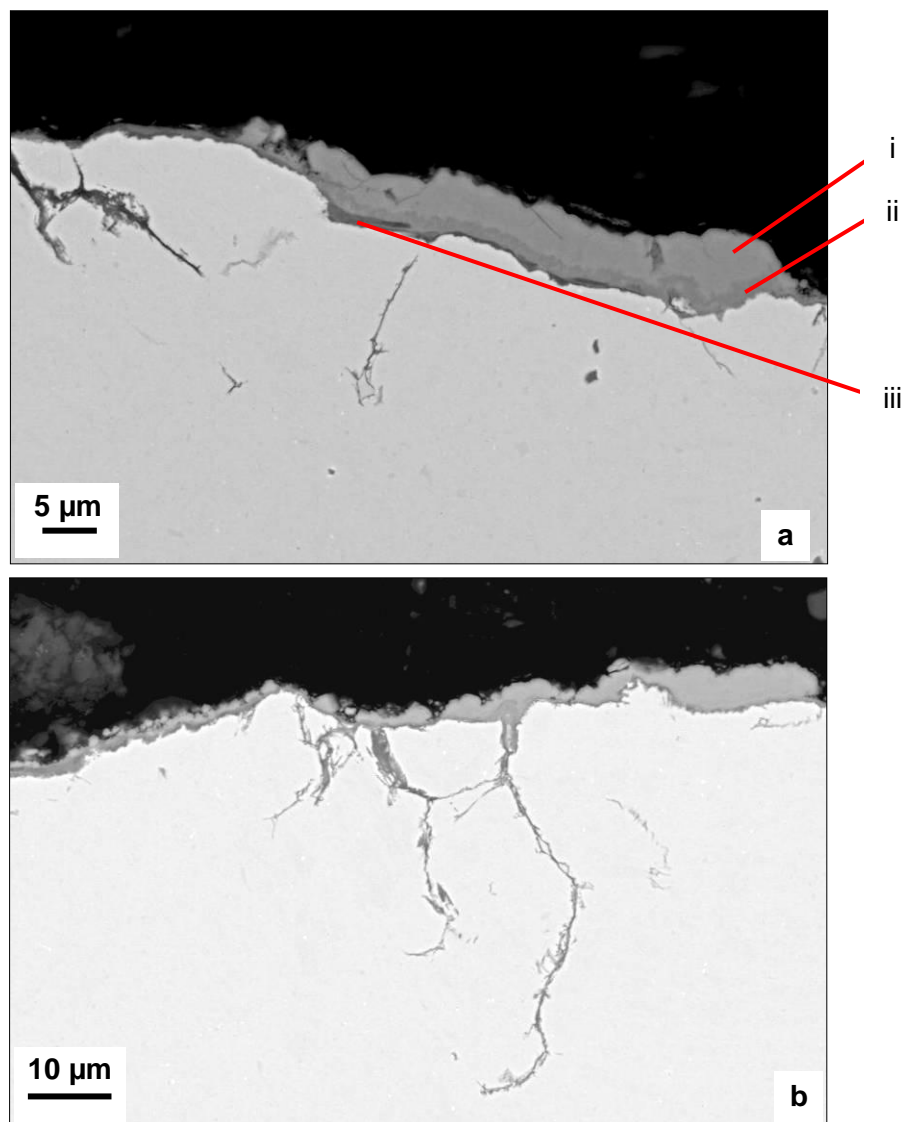
Figure 4.7: Backscattered electron micrographs showing cross sections of oxide (a) and crack branching into the substrate of specimen 799 (1061 MPa, 98.3 kh).
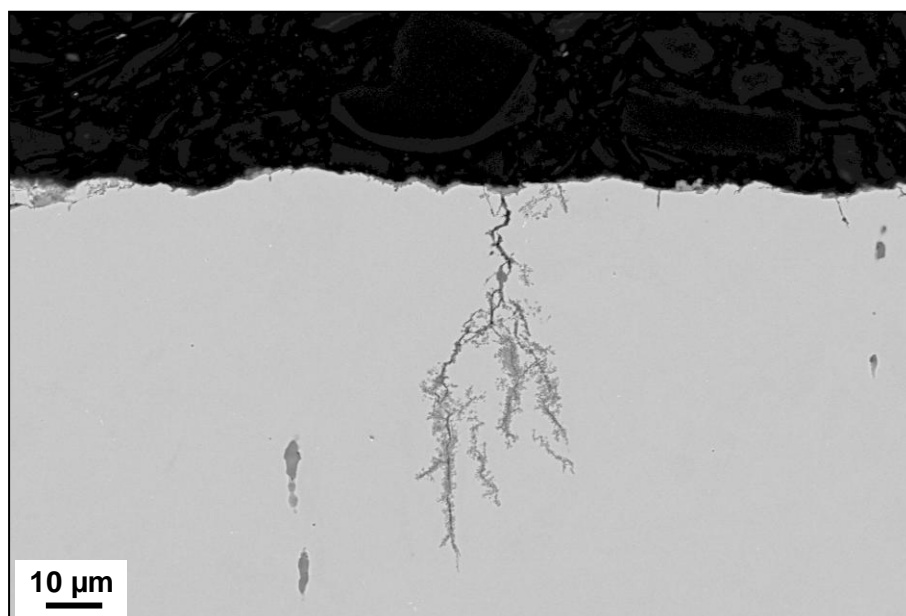
Figure 4.8: Backscattered electron micrograph showing substrate crack branching in specimen 803 (1024 MPa, 98.3 kh).

Figure 4.8 shows severe crack branching in specimen 803 (1024 MPa) which penetrates ~70 μm into the substrate. The appearance can be likened to that of plant roots as the branching increases with depth.

Figure 4.9 is a micrograph that illustrates several features of the stress corrosion crack. There are two blocks of oxide, which vary in thickness up to 20 μm and consist of light grey particles within a matrix of darker grey oxide. The EDS maps in Figure 4.9 (b) show that the oxide is iron rich with some particles also rich in chromium and manganese. There is a bright region in Figure 4.9 that is of similar contrast to the substrate metal, which suggests it is a section of metal that did not oxidise. There is a dark void, which may be grain pull-out due to sample preparation. Below these oxide regions is a dark void line where the oxide has spalled from the substrate, creating a crack surface. The absence of all the selected elements from the EDS maps in Figure 4.9 (b) indicates the dark line is a void, which supports the suggestion that it represents one surface of the main stress corrosion crack. It is therefore possible that the free edge of the oxide traces the opposing crack surface, which is not displayed in this micrograph. Beneath the void line in Figure 4.9 there is ~ 10 μm thick substrate oxide consisting of two or more layers that can be identified by the variation in contrast, which is similar to that shown in Figure 4.7 (a). The EDS maps in Figure 4.9 (b) show the upper region is an iron-rich oxide whereas the lower oxide layer contains no iron but is rich in chromium and manganese. In places the lower oxide layer penetrates the

73

substrate a further 10 µm with the exception of the oxide on the right of the micrograph which continues deeper and may trace grain boundaries.
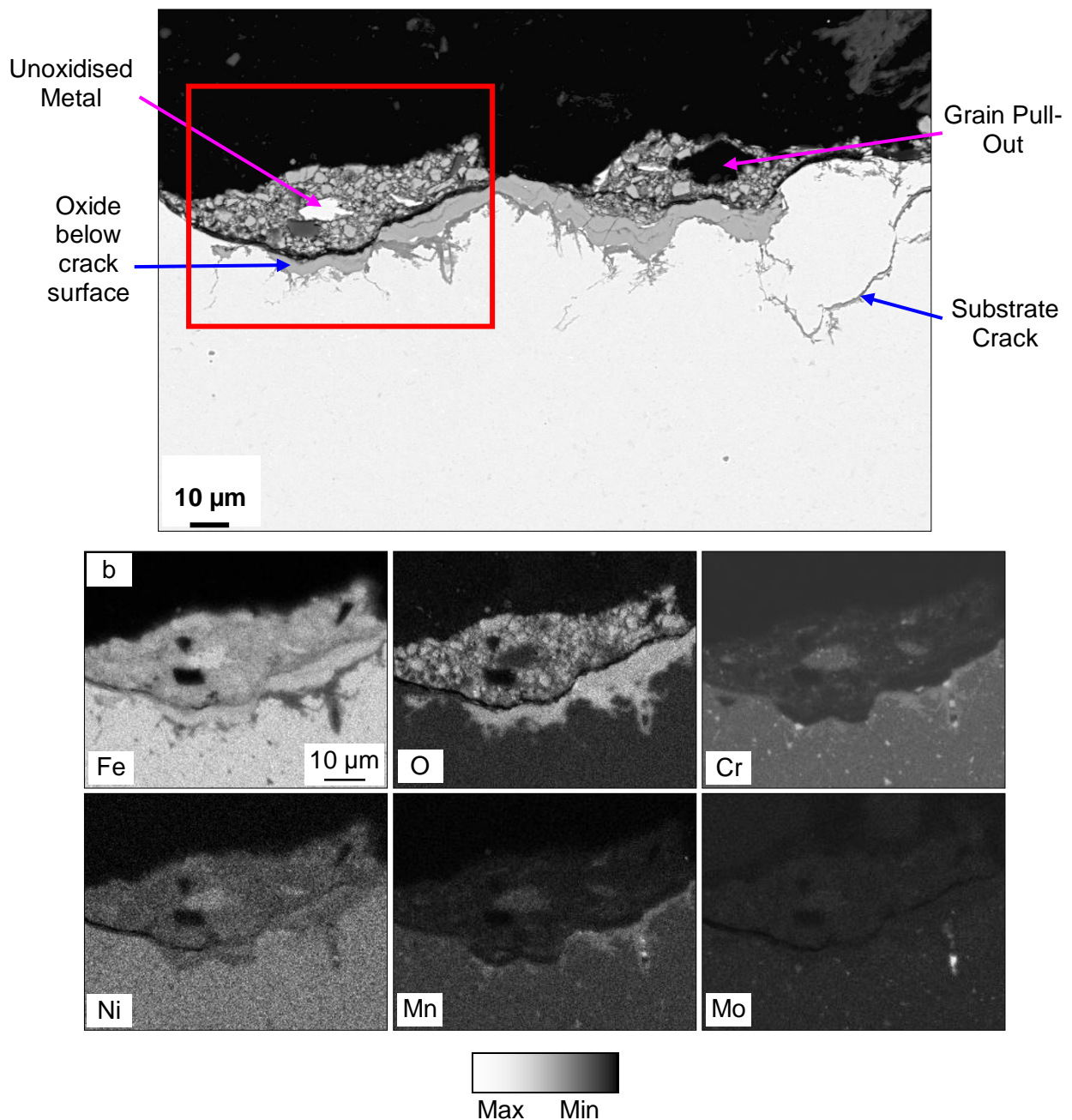
Figure 4.9: Backscattered electron micrograph of oxide above and below the crack surface of specimen 799 (1061 MPa, 98.3 kh).

Simultaneous EBSD and EDS data was collected for a cross sectioned area of the specimen 799 (1061 MPa). The selected area has a layer of surface oxide along the main stress corrosion crack and a significant substrate crack. The IQ map in Figure 4.10 clearly shows the martensitic substrate microstructure identified using optical microscopy in Figure 4.2 and the substrate cracking/oxide traces prior austenite grain

boundaries. The EDS maps show the crack to contain a chromium-manganese rich oxide, with a corresponding depletion in iron.
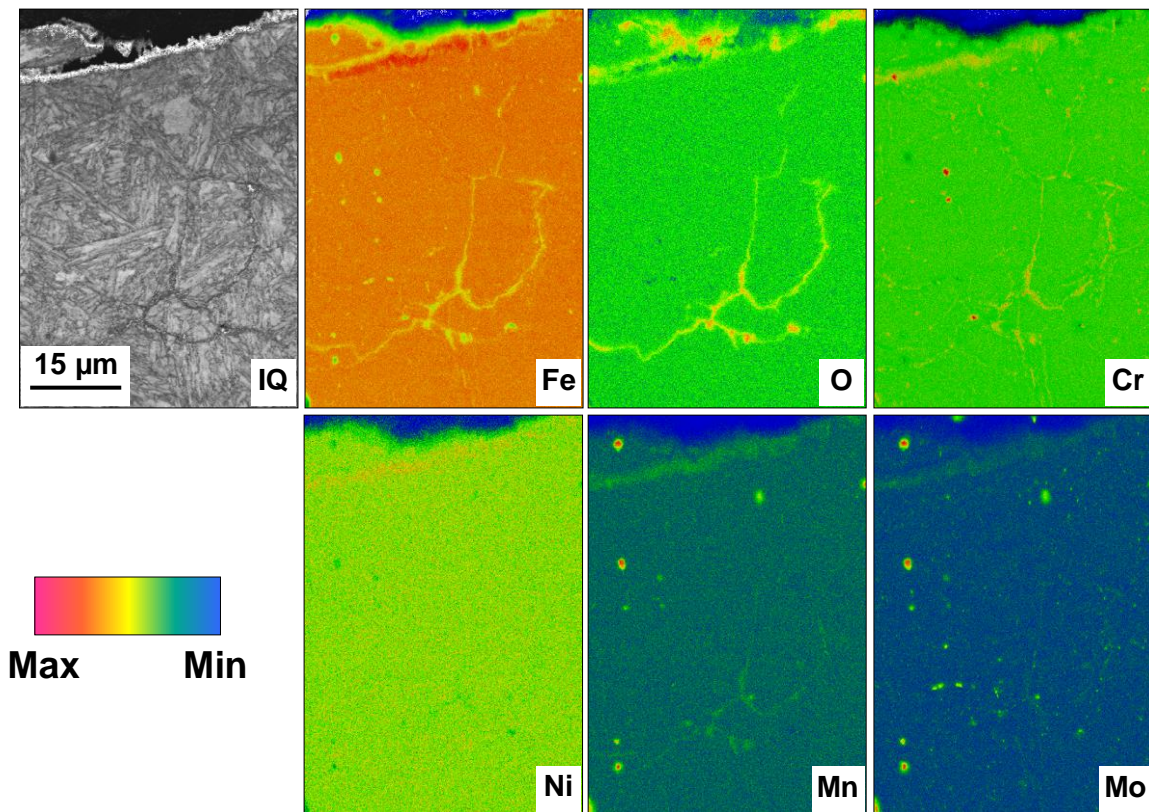
Figure 4.10: Image Quality map with accompanying rainbow EDS maps showing the chemical distribution within substrate crack branching in specimen 799 (1061 MPa, 98.3 kh).

4.4.2. Exposure Time: 13.0 kh

Figure 4.11 shows a composite image of micrographs spanning the full crack length of specimen 800 (1061 MPa, 13.0 kh). Unlike the micrographs shown for the specimens exposed to condensing steam at 95°C for 98.3 kh (Figure 4.3 to Figure 4.6), there is no oxide visible along any of the crack length of specimen 800 (1061 MPa, 13.0 kh), even though the magnification of the specimens is the same for all the micrographs. Some crack branching into the substrate can be identified from the composite image in Figure 4.11, but the cracks are much shorter than those seen in the micrographs for the specimens exposed to condensing steam at 95°C for 98.3 kh.
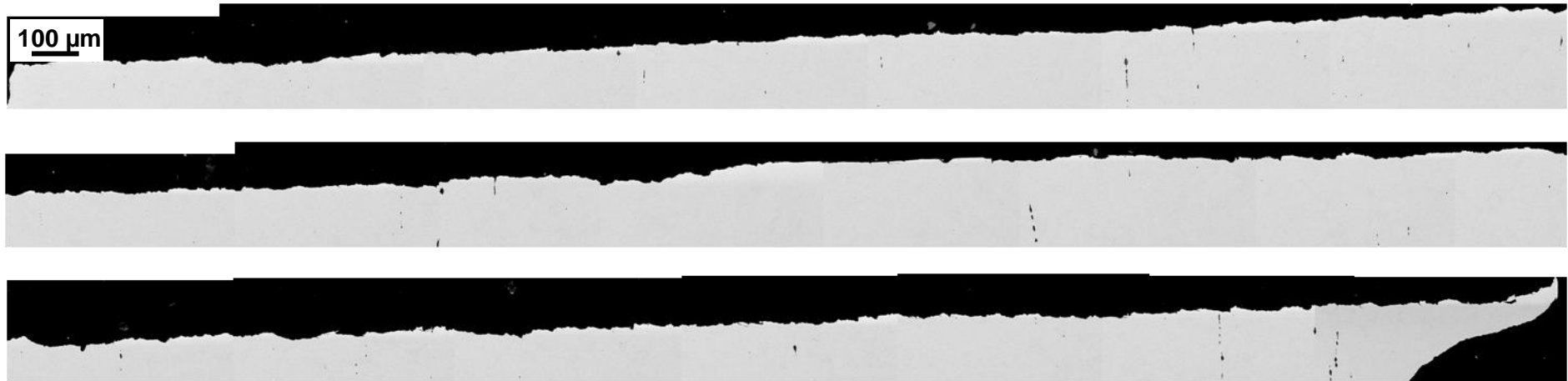
Figure 4.11: Composite of backscattered electron micrographs showing the full length of the stress corrosion crack through specimen 800 (1061 MPa, 13.0 kh)

Figure 4.12 is a backscattered electron micrograph showing a cross section of the stress corrosion crack through a sample exposed to condensing steam at 95°C for 13.0 kh. There are several cracks visible that penetrate approximately 2 µm into the substrate occurring at around 10 µm intervals. The direction of these cracks from initiation to tip is generally diagonally down and to the right of the micrograph, which coincides with the growth direction of the main crack. These cracks are much shorter than those identified in the substrate of the specimens exposed to condensing steam at 95°C for 98.3 kh, which is why they could not been seen in the composite image shown in Figure 4.11.
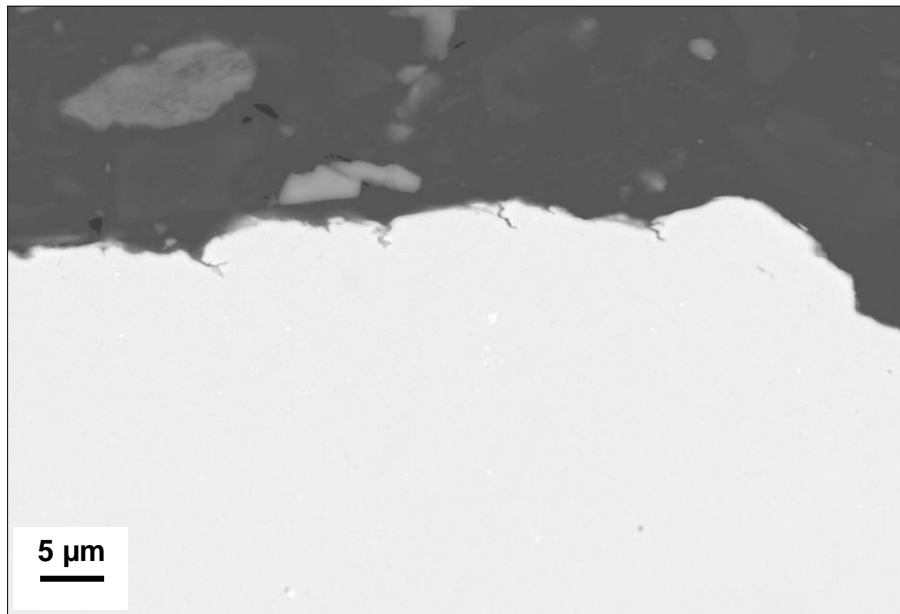
Figure 4.12: Backscattered electron micrograph showing a cross section of a stress corrosion crack with substrate cracks in a sample exposed to condensing steam at 95°C for 13.0 kh.

4.4.3. Exposure Time: 7.5 kh

Figure 4.13 shows a composite image of secondary electron micrographs showing the full crack length of specimen 802 (1061 MPa, 7.5 kh). Similar to Figure 4.11, no oxide is visible along the crack length at this magnification. There are some visible cracks penetrating the substrate but, similar to the cracks seen in Figure 4.11, they are much shorter than those identified in the composite micrographs of the specimens exposed to condensing steam at 95°C for 98.3 kh.

Figure 4.13: Composite of backscattered electron micrographs showing the full length of the stress corrosion crack through specimen 802 (1061 MPa, 7.5 kh)

Figure 4.14: Backscattered electron micrograph showing substrate cracks along a stress corrosion crack through a sample exposed to condensing steam at 95°C for 7.5 kh.

A typical region of the cross section through the 7.5 kh sample is shown in Figure 4.14. In this micrograph there is little oxide visible along the crack surface, however, there are numerous cracks penetrating the substrate some of which are branched, with lengths that vary between 5 µm and 25 µm. The general direction of the cracks from initiation to tip is diagonally down and to the right, which is consistent with the growth direction of the main crack.
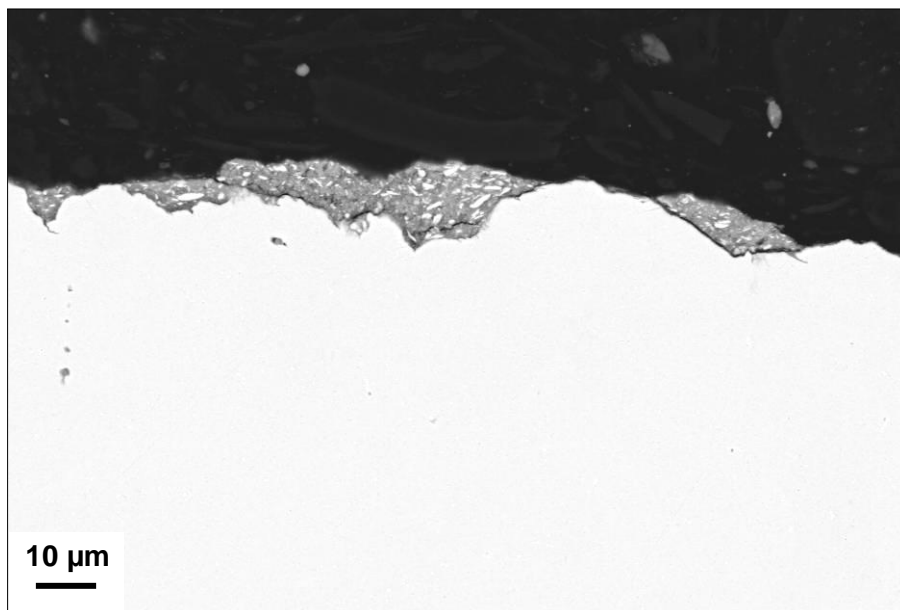
Figure 4.15: Backscattered electron micrograph showing a cross section of oxide along a stress corrosion crack through a sample exposed to condensing steam at 95°C for 7.5 kh.
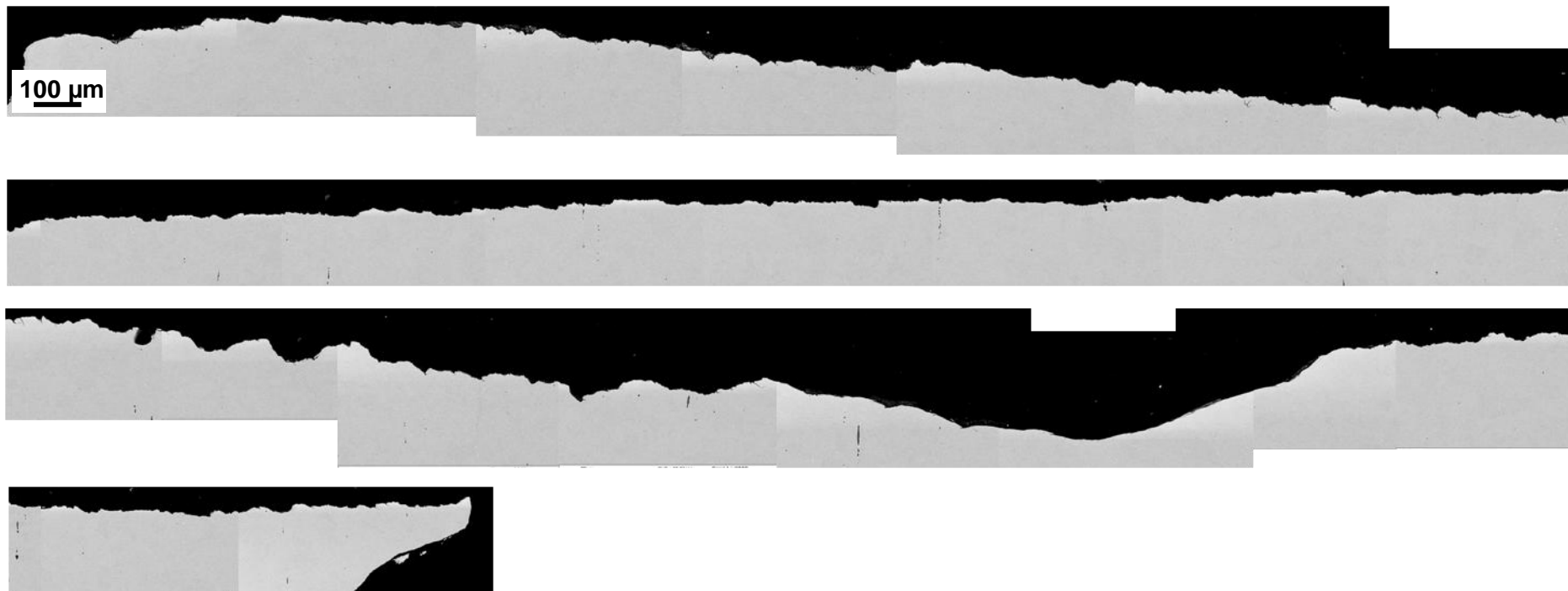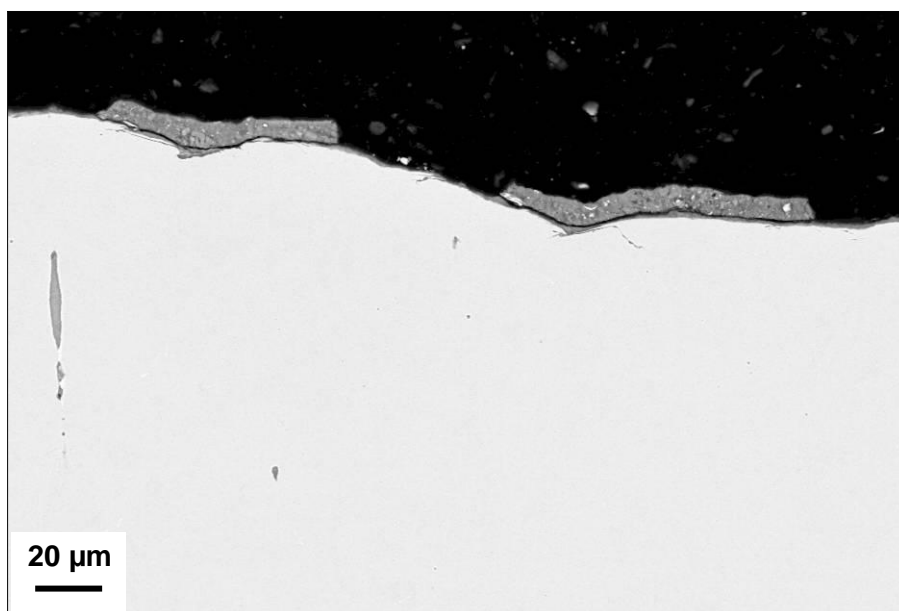
Figure 4.16: Backscattered electron micrograph showing a cross section of oxide along a stress corrosion crack through a sample exposed to condensing steam at 95°C for 7.5 kh.

Figure 4.15 is an electron micrograph of a cross section through a stress corrosion crack in a sample exposed to condensing steam at 95°C for 7.5 kh, showing oxide at the surface. This oxide varies in thickness up to approximately 10 µm and is present repeatedly along the crack length but is not constant throughout the length. Multiple bright elliptical spots of around 2 µm in length are visible within the oxide and there are dark lines that appear to be voids. Figure 4.16 shows two sections of oxide on the substrate surface. They are similar to the oxide in Figure 4.15 in that they contain several bright spots, however, these differ because their thickness is nearly uniform throughout at around 10 µm. Also these oxide sections have a black void line between them and the substrate where the oxide has spalled at the newly created crack surface. In addition to the oxide, this micrograph shows a substrate inclusion that measures up to 4 µm wide and has a total length of around 40 µm.

4.4.4. Oxide Development

It has already been shown in Section 4.3 that in general the longer exposure time resulted in longer stress corrosion crack growth in the specimens examined. It was also shown that initial stress intensity at the notch/pre-crack tip plays an important role in initiating or "re-initiating" a crack. By examining the specimens in cross section, it is possible to identify other effects of exposure time.

In the composite micrographs for the specimens exposed to condensing steam for 98.3 kh, there are regions along the crack where oxide is visible, particularly in specimen 799 (1061 MPa, 98.3 kh). Figure 4.7 and Figure 4.9 show sections of oxide on the surface of specimen 799 (1061 MPa, 98.3 kh) which are representative of areas throughout the length of the crack. In the composite micrographs covering the full length of specimens exposed to condensing steam at 95°C for 13.0 kh (Figure 4.11) and 7.5 kh (Figure 4.13**Error! Reference source not found.**) there was no visible oxide on the crack surface. Figure 4.15 and Figure 4.16 show the few areas along the crack length of specimen 802 (1061 MPa, 7.5 kh) where oxide was found and there were no such areas observed in specimen 802 (1061 MPa, 13.0 kh). For the remaining specimens exposed to condensing steam at 95°C for both 13.0 kh and 7.5 kh there were no sections with retained oxide present.

The results show that there is far more oxide present inside the cracks exposed for 98.3 kh than those exposed for 13.0 kh and 7.5 kh, which is consistent with previous comments that longer exposure time results in more SCC. However, it has also been observed that specimen 802 (1061 MPa, 7.5 kh) had more oxide visible along the crack than specimen 800 (1061 MPa, 13.0 kh). This shows that exposure time is not the only contributing factor in SCC growth.

As both specimens were from the same proof strength group, it is possible to rule out that variable as a contributing factor. In Table 4.2 it was shown that specimen 802 (1061 MPa, 7.5 kh) had a crack length of 5.3 mm whereas specimen 800 (1061 MPa, 13.0 kh) had a shorter crack length of 4.8 mm. This was attributed to the fact that specimen 800 (1061 MPa, 13.0 kh) had an initial stress intensity at the notch tip of 8 MPa $m^{\frac{1}{2}}$ whereas the equivalent value for specimen 802 (1061 MPa, 7.5 kh) was 62.5 MPa $m^{\frac{1}{2}}$. It is likely that the crack in specimen 802 (1061 MPa, 7.5 kh) initiated after a shorter exposure time than the crack in specimen 800 (1061 MPa, 13.0 kh), which explains the additional oxide in the specimen exposed for a shorter total time.

The remaining specimens exposed to condensing steam at 95°C for 13.0 kh had values of initial stress intensity at the notch tip around 16 MPa $m^{\frac{1}{2}}$. All the specimens exposed for 7.5 kh had initial stress intensity values of around 62.5 MPa $m^{\frac{1}{2}}$. In these instances, the specimens exposed for 13.0 kh had longer cracks than those exposed for 7.5 kh. This further supports the idea that SCC is worse for longer exposure time but that initial stress intensity is an important variable to consider with regards to when a crack might initiate.

4.4.5. Crack Branching

The visual results of the depth and frequency of cracks which branch from the main stress corrosion crack and penetrate the substrate tell a similar story to that of the observed differences in oxide development. The specimens exposed to condensing steam at 95°C for 98.3 kh had many cracks that penetrated the substrate, several of which were estimated to measure ≤ 50 µm. There were several substrate penetrating cracks observed in the specimens exposed for 13.0 kh and 7.5 kh but none of them reached the lengths observed in the specimens exposed for 98.3 kh.

These results show that the level of crack branching from the main stress corrosion crack is worse with increased exposure time. However, similar to the results for oxide development observed in cross section, the substrate penetrating cracks in specimen 802 (1061 MPa, 7.5 kh) generally appeared to be longer than those in specimen 800 (1061 MPa, 13.0 kh). If the initial stress intensity at the notch tip is considered again, then there is more evidence to suggest that the crack in specimen 802 (1061 MPa, 7.5 kh) initiated earlier in the total exposure time than the crack in specimen 800 (1061 MPa, 13.0 kh). This would mean that although the total exposure time was less for specimen 802 (1061 MPa, 7.5 kh) than specimen 800 (1061 MPa, 13.0 kh), the length of time that the crack was growing was greater for specimen 802 (1061 MPa, 7.5 kh). If this is true, then the idea that SCC is worse for longer exposure time is still true, it is just that exposure time from when the crack initiates may be more important than the total exposure time, because other factors such as initial stress intensity are important to consider.

4.5. Crack Surface Morphology

The surfaces of the stress corrosion cracks were examined using the secondary electron detector of the Leo 1530 VP FEGSEM. The crack propagation direction relative to the page is left to right in all images presented in this Section.

4.5.1. Exposure Time: 98.3 kh

Specimens 803 (1024 MPa, 5 MPam$^{\frac{1}{2}}$), 807 (1018 MPa, 5 MPam$^{\frac{1}{2}}$) and 811 (1072 MPa, 5 MPam$^{\frac{1}{2}}$) were fatigue pre-cracked prior to exposure to condensing steam and it has been deduced that the initial stress intensity at the pre-crack tip of these specimens was below the threshold for crack propagation during the experiment. Figure 4.17 shows the surface of specimen 803 (1024 MPa) leading up to the pre-crack
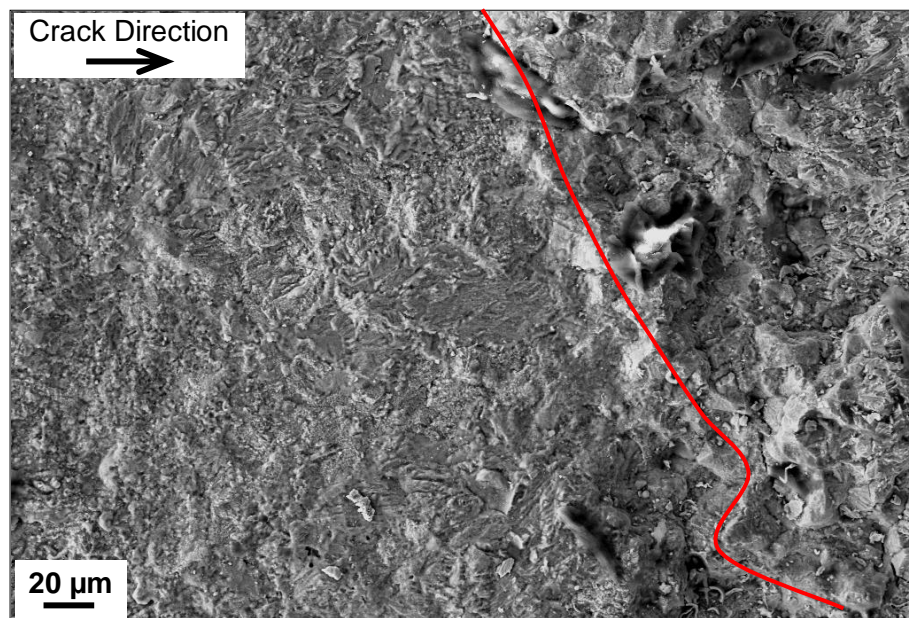
tip, which is highlighted by the solid red line, and the manually fractured surface after the crack tip. It is representative of the same region in specimens 807 (1018 MPa) and 811 (1072 MPa). The fatigue pre-crack surface is covered with oxide all the way to the crack tip. At this magnification the oxide may not be obviously visible; however, the surface is much rougher than that of an un-corroded fatigue fracture surface.

Specimen 799 (1061 MPa, 10 MPam$^{\frac{1}{2}}$) was also fatigue pre-cracked prior to exposure to condensing steam but the initial stress intensity at the pre-crack tip was sufficient to promote crack propagation during the experimental time. Figure 4.18 shows the surface of specimen 799 (1061 MPa) around the crack tip, which is indicated by the solid red line. Although Figure 4.17 and Figure 4.18 are at slightly different magnifications the crack tip region of specimen 799 (1061 MPa) is very different from the fatigue pre-crack tip of specimens 803 (1024 MPa), 807 (1018 MPa) and 811 (1072 MPa). The crack surface leading up to the crack tip of specimen 799 (1061 MPa) is intergranular with very little visible oxide present.

The fatigue pre-crack region of specimen 799 (1061 MPa) is shown in Figure 4.19, which is comparable to specimens 803 (1024 MPa), 807 (1018 MPa) and 811 (1072 MPa). There is a thin layer of oxide throughout the pre-crack regions of all the specimens exposed for 98.3 kh and the full crack length of specimen 799 (1061 MPa). This oxide exhibits various morphologies, some of which are shown in Figure 4.20 and Figure 4.21.

Figure 4.20 shows three micrographs of needle-like oxide structures on the crack surface of specimen 799 (1061 MPa), illustrating a progressive oxide development. In Figure 4.20 (a) the needles measure approximately 1 µm in length with minimal width, however, within the area of the micrograph highlighted by a blue dashed ellipse there is a needle that has an estimated width of 0.8 µm. This is similar to the oxide morphology shown in Figure 4.20 (b) where the needles are significantly wider than in Figure 4.20 (a) with flat faces measuring between 0.5 µm and 1 µm. From the needle faces there are sets of multiple parallel lines, which look like needle growth similar to that shown in Figure 4.20 (a). Figure 4.20 (c) shows clusters of needle-like oxide morphologies that emanate from central points. The sizes of the structures are a combination of those shown in Figure 4.20 (a) and (b). This suggests that the growth develops from fine needles into flat-faced needles from which new fine needles grow. Eventually this structure grows up from the crack surface into cone-shaped structures.

Figure 4.21 shows three micrographs of the crack surface of specimen 799 (1061 MPa) where the oxide morphology presents as randomly orientated, intertwined hexagonal platelets. In Figure 4.21 (a) mainly the faces of the platelets are visible whereas in Figure 4.21 (b) only the edges of the platelets can be seen. In Figure 4.21 (a) and (b) the platelets are essentially regular hexagons that measure approximately 2 µm on any diagonal passing through the centre. In Figure 4.21 (c) the hexagons have alternate long and short sides and measure approximately 1 µm on any diagonal passing through the centre.

Figure 4.17: Secondary electron micrograph showing the surface of the stress corrosion crack in specimen 803 (1024 MPa, 98.3 kh) leading up to the fatigue pre-crack tip, which is highlighted by the solid red line.
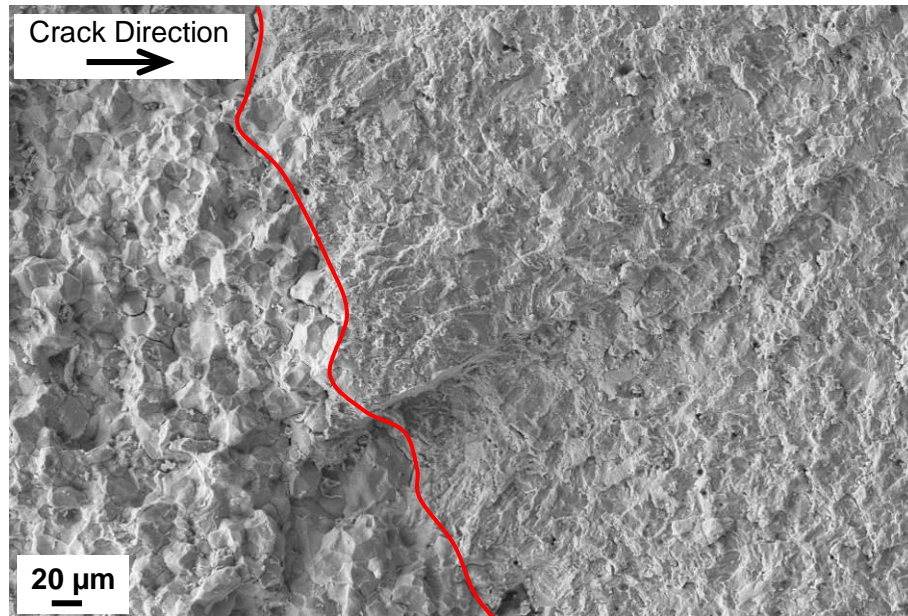
Figure 4.18: Secondary electron micrograph showing the surface of the stress corrosion crack in specimen 799 (1061 MPa, 98.3 kh) leading up to the crack tip, which is highlighted by the solid red line.
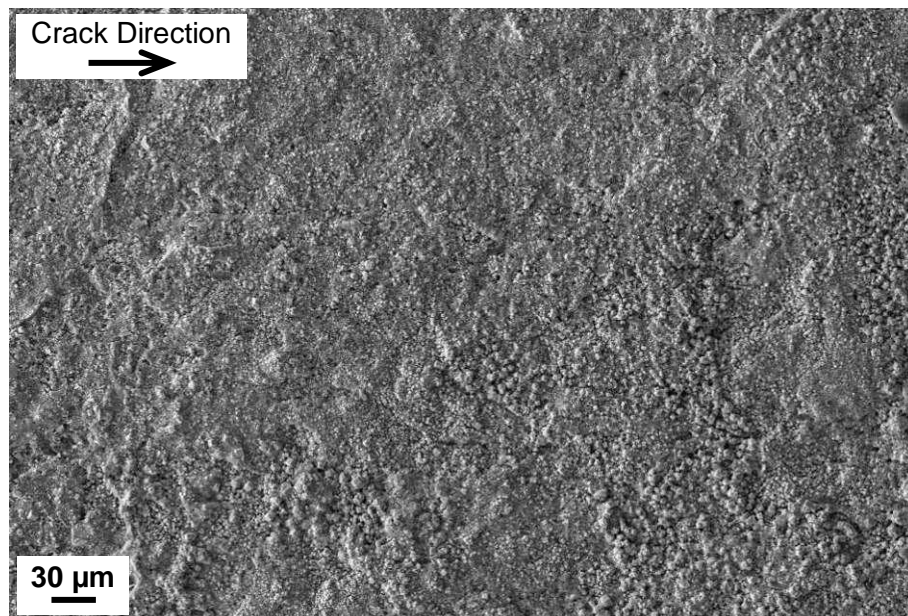
Figure 4.19: Secondary electron micrograph showing the fatigue pre-crack region of specimen 799 (1061 MPa, 98.3 kh).
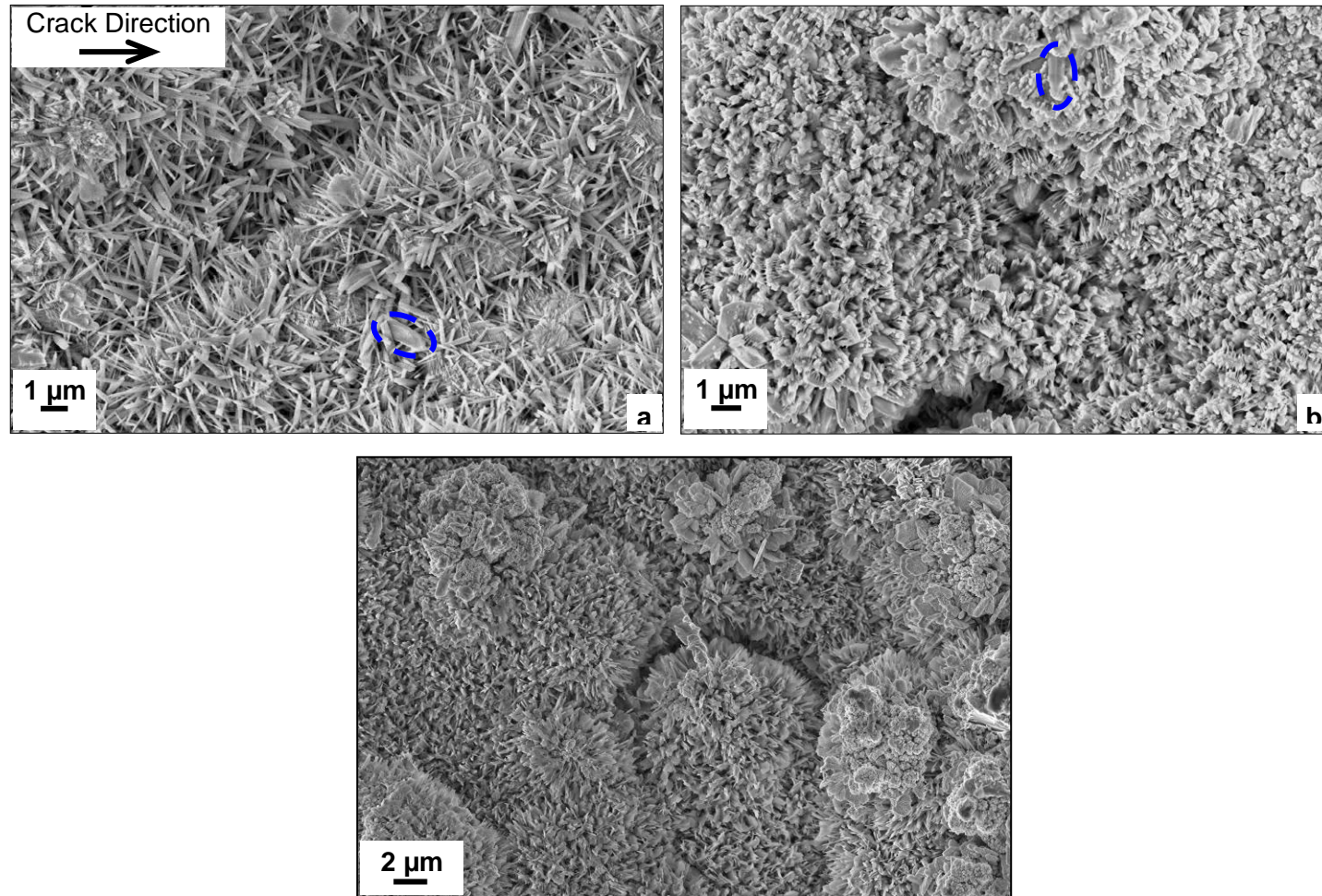
Figure 4.20: Secondary electron micrographs showing the surface of specimen 799 with (a and b) randomly orientated needle-like oxide morphologies and (c) clusters of needle-like oxide morphologies radiating from central points.
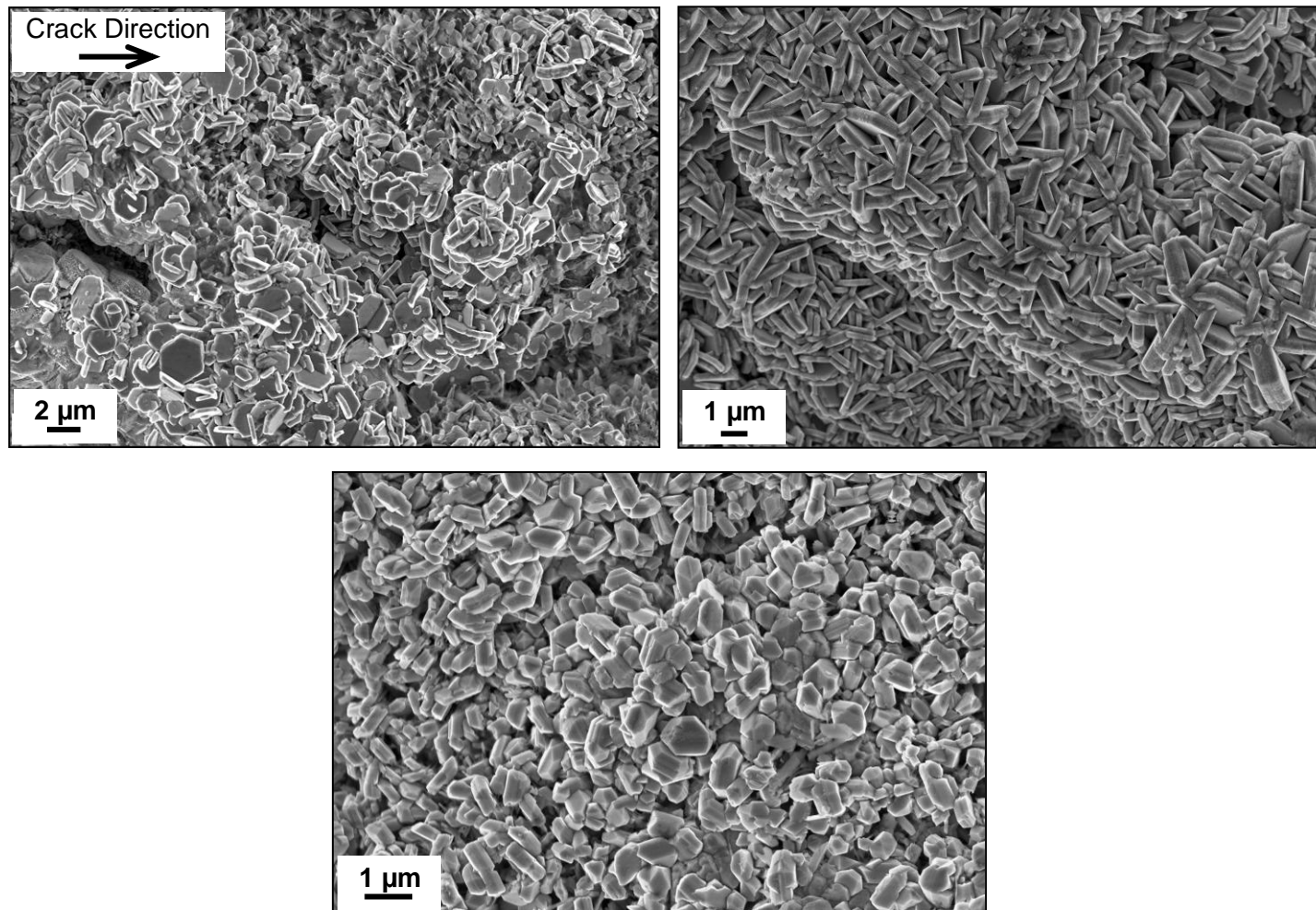
Figure 4.21: Secondary electron micrographs showing (a) faces, (b) edges and (c) misshapen hexagonal platelet oxide morphologies on the surface of specimen 799.

In some locations throughout the crack surface of the specimens exposed for 98.3 kh there are bigger features on top of the thin layer of oxide shown in Figure 4.20 and Figure 4.21.

Figure 4.22 (a) exhibits an isolated octahedral oxide crystal measuring ~ 6 μm from apex to apex and nearly 4 μm vertically. Figure 4.22 (b) shows a cluster of intertwined octahedral oxide crystals. The individual oxide crystals range from approximately 2 μm to 6 μm in size and vary in orientation. Regions with this oxide morphology appear repeatedly along the crack surface.
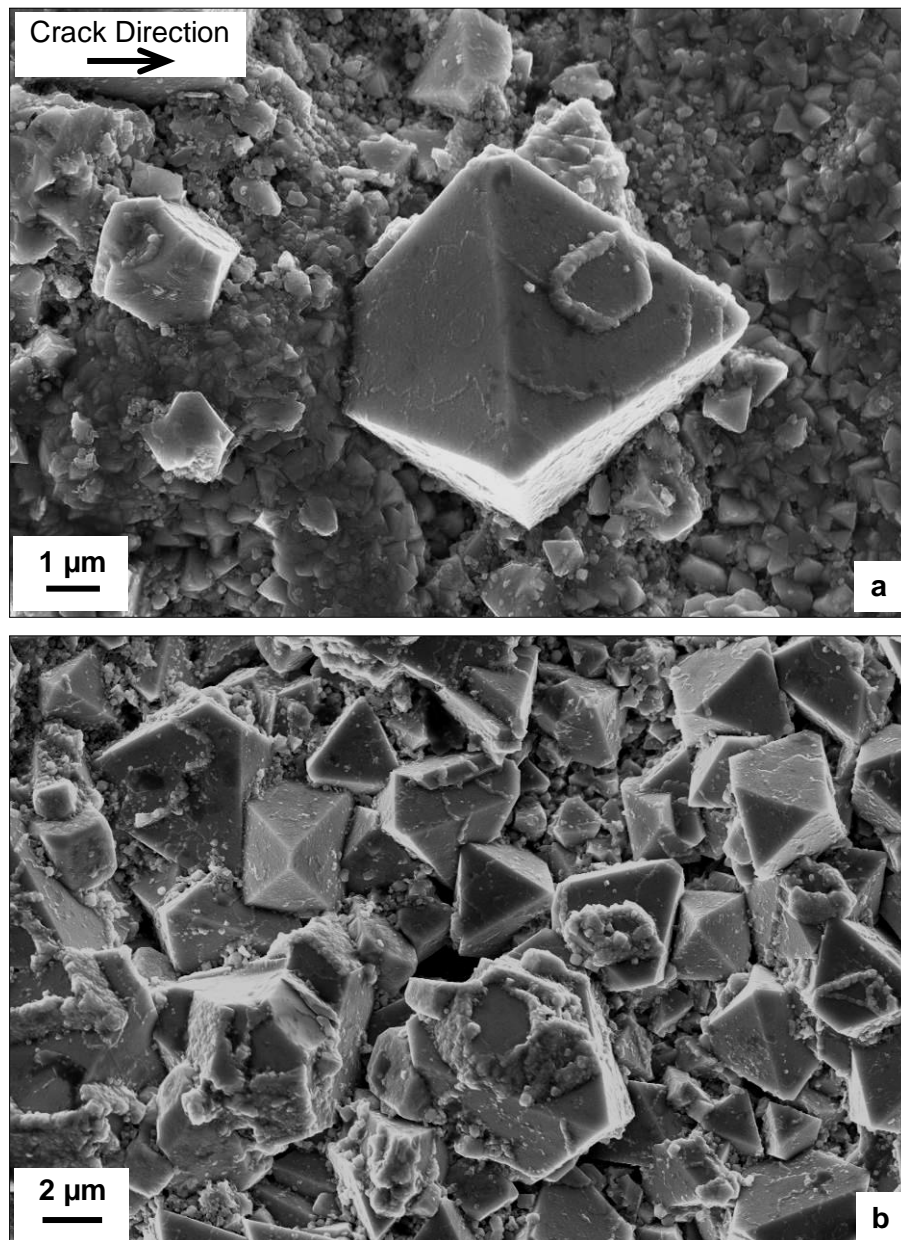
Figure 4.22: Secondary electron micrographs showing (a) an individual octahedron oxide crystal and (b) octahedral oxide crystals over a region of the crack surface of specimen 799 (1061 MPa, 98.3 kh).
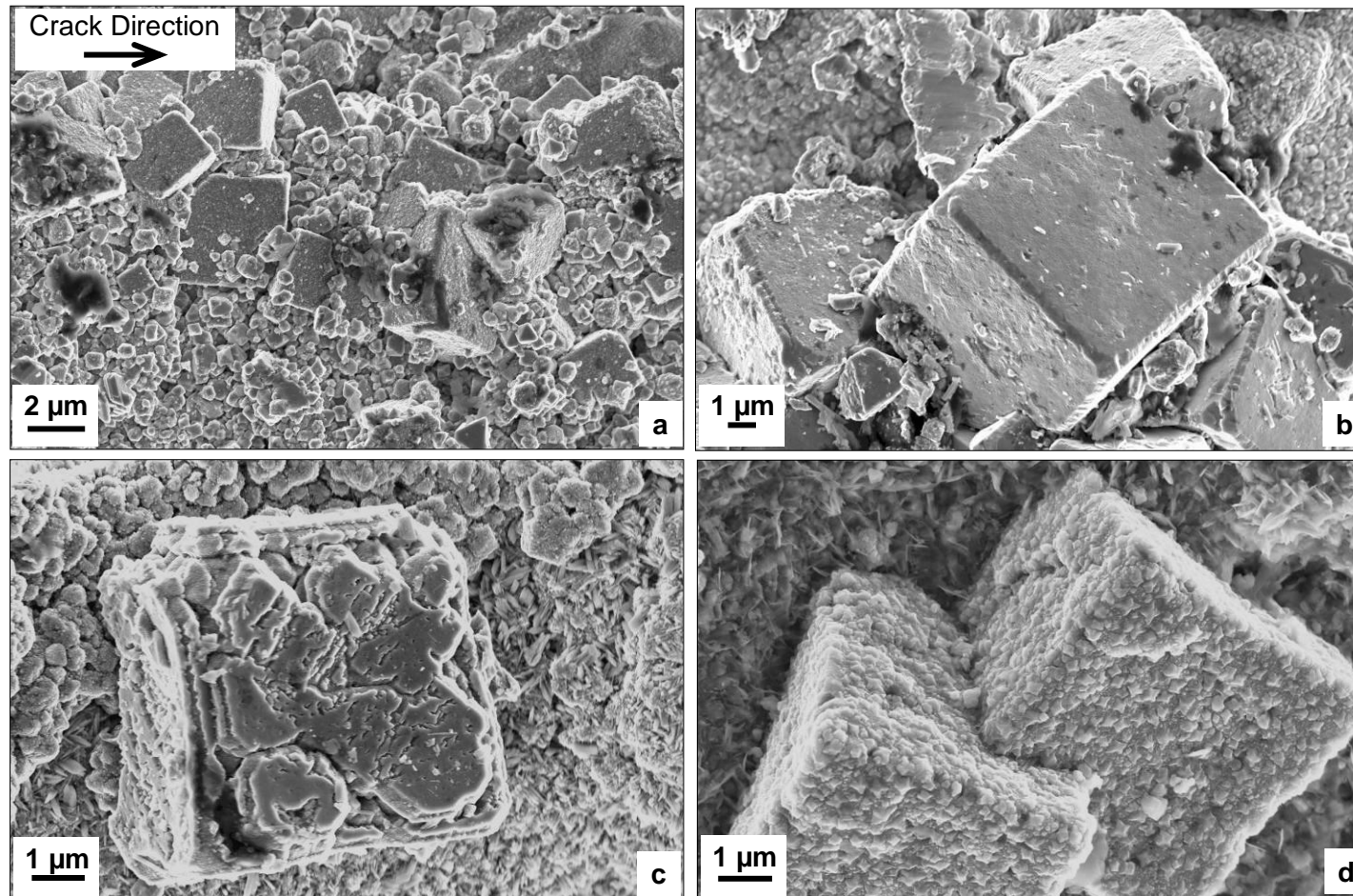
Figure 4.23: Secondary electron micrographs showing cubic oxide crystals on the crack surface of specimens exposed to condensing steam at 95°C for 98.3 kh; (a) densely packed region of cubic oxide grains, (b) oxide crystals with relatively smooth faces, (c) oxide crystal within complete surfaces and (d) oxide crystals with raised surfaces.

Figure 4.23 shows some of the many regions on the crack surface of specimen 799 (1061 MPa) where the oxide morphology is cubic. Figure 4.23 (a) shows clusters of overlaid cubic structures, which vary in size between 1 µm and 10 µm. These cubes are highlighted in Figure 4.23 (b). In this instance the central cube measures approximately 5 µm, has smooth surfaces with crisp edges and is surrounded by other cubes of similar appearance. Figure 4.23 (c) shows an isolated cube which also measures approximately 5 µm with defined edges but the surfaces are rough and incomplete, which is the opposite of the cubes in Figure 4.23 (a) and (b). Figure 4.23 (d) shows a pair of overlapping cubes that have different surface appearance from the examples in Figure 4.23 (a, b and c) because they are covered in raised "bumps" of smaller tetrahedral-shaped oxide.

A cuboctahedron oxide crystal is shown in Figure 4.24, which has alternate triangle and square faces. The triangle faces have flattened points that make them irregular hexagons with alternate long and short sides measuring an average of 4 µm and 1 µm respectively. However, when considering the microscopic scale on which they are being measured, it is possible to assume them to be triangular. The square faces are solid whereas the triangular faces are missing oxide at their centres. Several of these shapes are found within the crack surface although the occurrences are either isolated or a few closely packed together. Also, the majority of cuboctahedra did not have voids at the centres of the triangular faces.
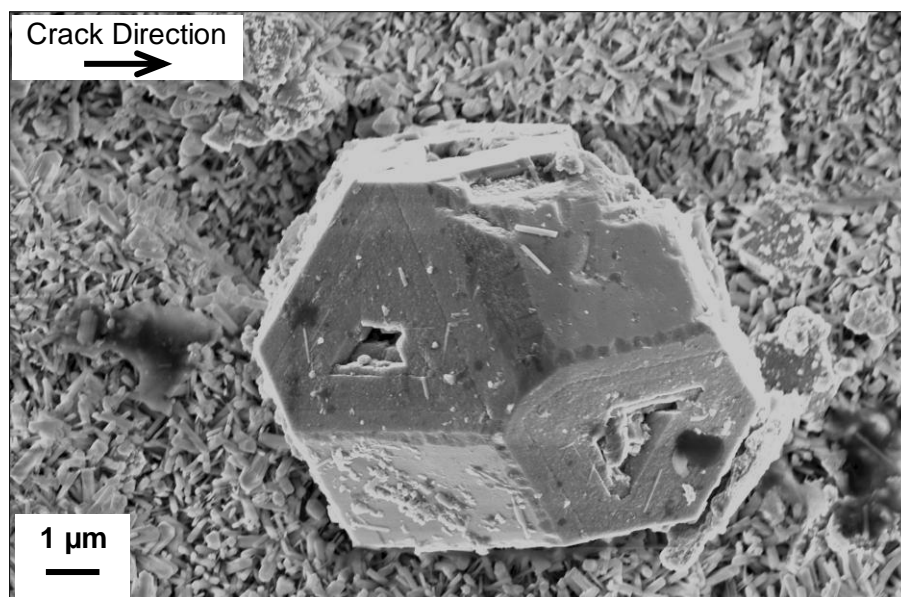
Figure 4.24: Secondary electron micrograph showing an isolated cuboctahedron oxide crystal on the crack surface of specimen 799.
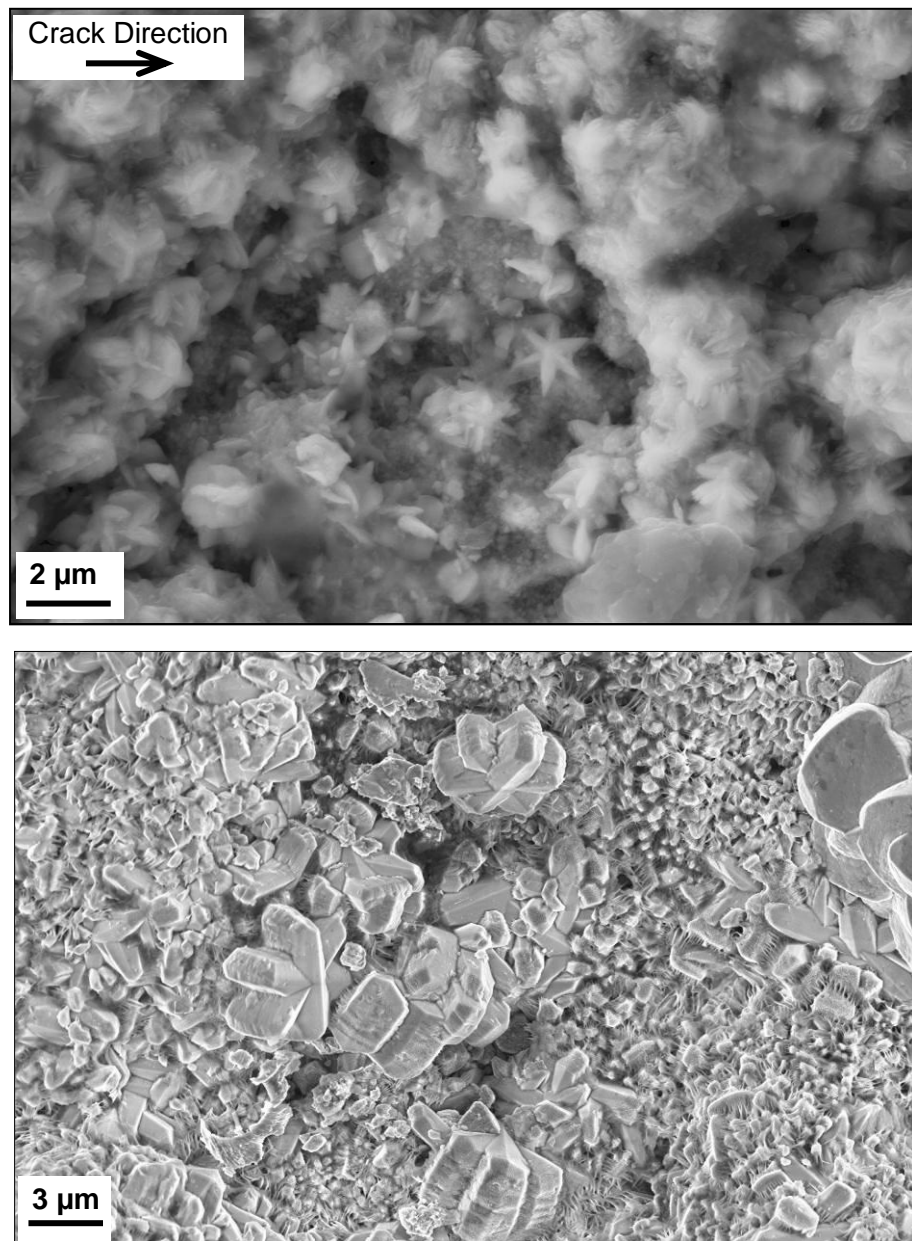
Figure 4.25: Secondary electron micrograph of asterisk oxide morphology on the crack surface of (a) specimen 803 (1024 MPa) and (b) specimen 799 (1061 MPa).

Figure 4.25 shows the crack surface of specimens 803 (1024 MPa) (a) and 799 (1061 MPa) (b) where the oxide exhibits an asterisk morphology. In specimen 803 (1024 MPa) the asterisks are approximately 1 µm in diameter with submicron thickness. In specimen 799 (1061 MPa) they are approximately 4 µm in diameter with a thickness of 2 µm. This difference suggests that the oxide is more developed in Figure 4.25 (b) than Figure 4.25 (a).

4.5.2. Exposure Time: 13.0 kh

The specimens exposed to condensing steam at 95°C for 13.0 kh were not fatigue pre-cracked. The initial stress intensity at the notch tip was above the threshold value which meant that cracks initiated and propagated during the experiment time in all specimens exposed for 13.0 kh. Figure 4.26 shows the crack initiation of specimen 804 (1024 MPa) and Figure 4.27 shows a region of the crack through specimen 800 (1061 MPa). The appearance of the fracture surfaces in the two micrographs is similar.

The area of Figure 4.27 inside the blue dashed ellipse exhibits transgranular fracture, but otherwise it is unclear as to the mode of crack propagation in either specimen. The surfaces are littered with very small oxide particles but there are no recognisable features similar to those seen in the specimens exposed for 98.3 kh. This is not unexpected as the exposure time was much less than the specimens exposed for 98.3 kh. Figure 4.28 shows the crack surface of specimen 800 (1061 MPa) leading up to the crack tip, which is indicated by the solid red line. The area inside the blue dashed ellipse immediately adjacent to the crack tip exhibits intergranular fracture as do several other areas on the crack surface. In contrast the area inside the blue dotted ellipse is very flat and does not show intergranular fracture. The crack tip region of specimen 800 (1061 MPa) in Figure 4.28 is similar in appearance to the crack tip region of specimen 799 (1061 MPa) in Figure 4.18.
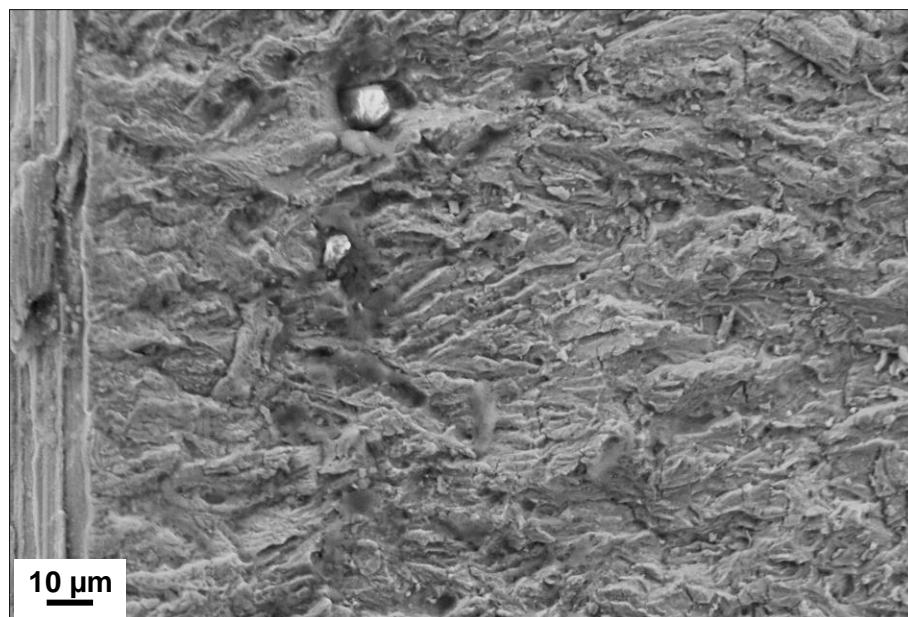
Figure 4.26: Secondary electron micrograph showing the crack initiation region of specimen 804.
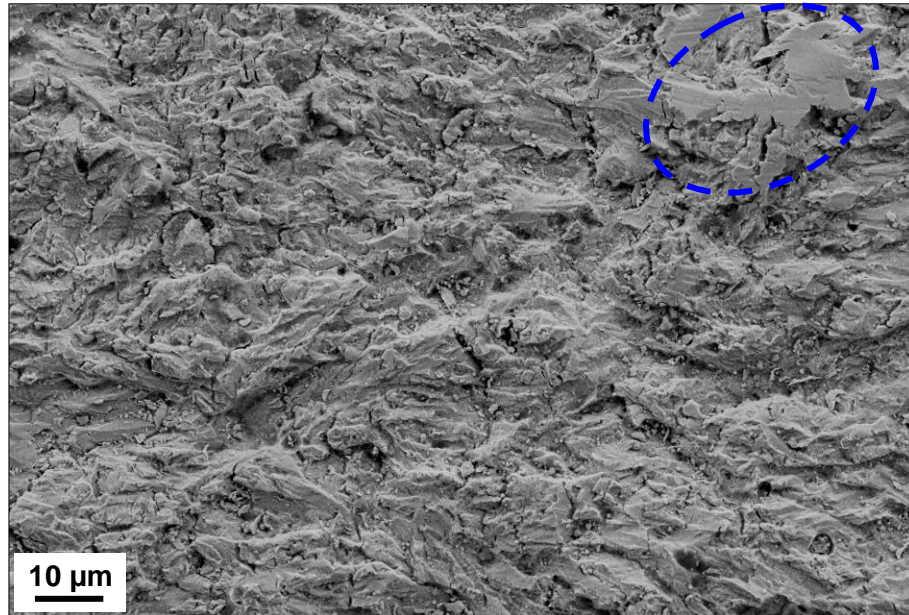
Figure 4.27: Secondary electron micrograph showing the surface of the crack through specimen 800 (1061 MPa, 13.0 kh).
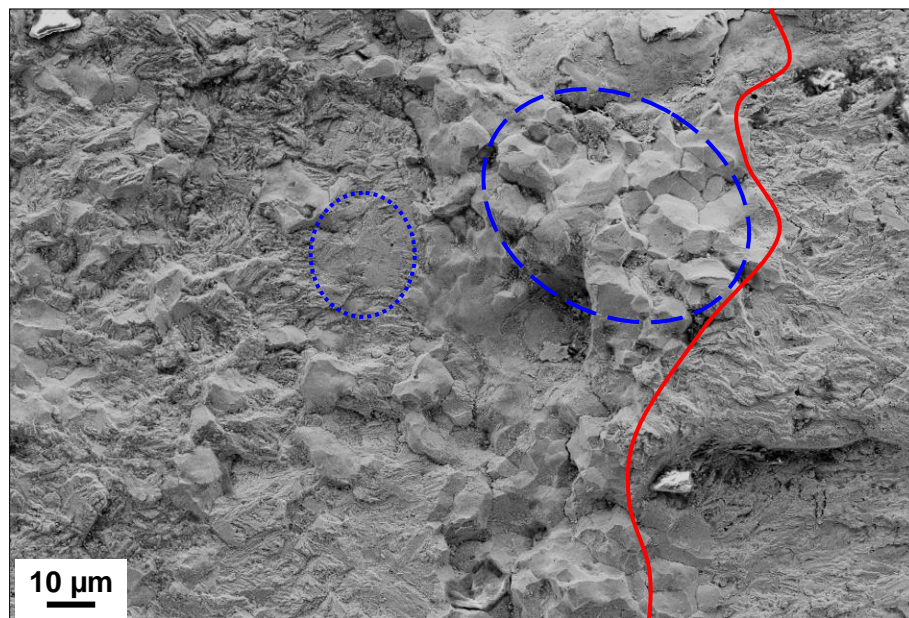
Figure 4.28: Secondary electron micrograph showing the crack tip region of specimen 800 (1061 MPa, 13.0 kh).

4.5.3. Exposure Time: 9.8 kh

Micrographs of the crack surface of specimens exposed to condensing steam at 95°C for 9.8 kh are shown in Figure 4.29, Figure 4.30 and Figure 4.31. Although specimen 801 (1061 MPa) is shown, the micrographs are representative of all specimens exposed for 9.8 kh. Figure 4.29 shows a typical region of the crack surface, which is covered with dots of oxide, similar to the crack surfaces shown in Figure 4.19 and

Figure 4.27. Much of the fracture surface is intergranular, which is highlighted within the dashed red ellipses.   Figure 4.30 shows oxide particles of random size and orientation at the crack initiation region of specimen 801 (1061 MPa).   The biggest particle in Figure 4.30 measures ~10 x 10 µm and is shown within the dashed red ellipse. There is far more oxide covering the surfaces of specimens exposed for 9.8 kh than 13.0 kh, but the oxide does not exhibit any of the specific structures seen on the surfaces of the specimens exposed for 98.3 kh. At very high magnification Figure 4.31 shows that the oxide consists of various size spheres.
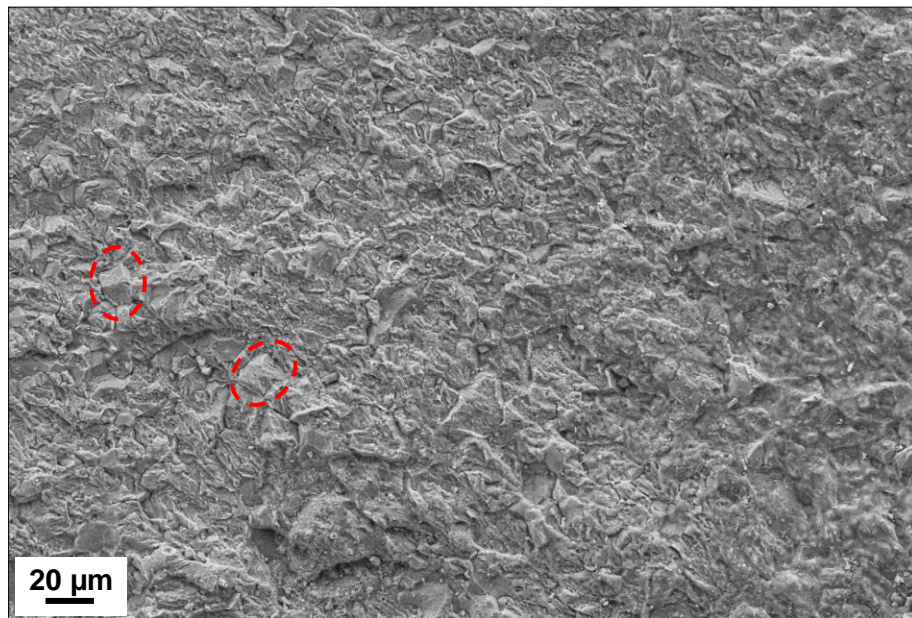
Figure 4.29: Secondary electron micrograph showing a typical region of the crack surface of specimen 801 (1061 MPa, 9.8 kh).

Figure 4.30: Secondary electron micrograph showing the oxide at the crack initiation of specimen 801 (1061 MPa, 9.8 kh).

94
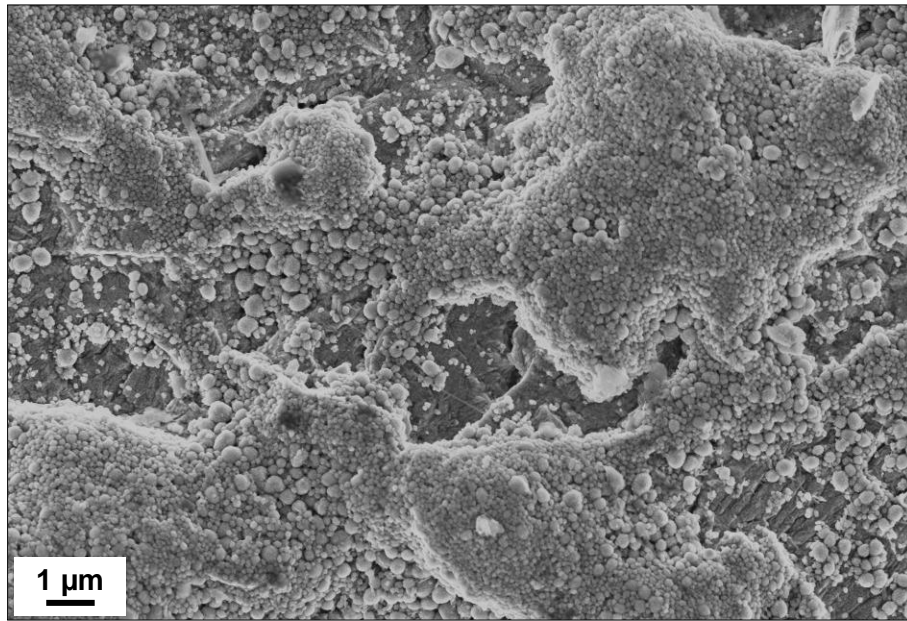
Figure 4.31: Secondary electron micrograph showing balls of oxide on the crack surface of specimen 801 (1061 MPa, 9.8 kh).

4.5.4. Exposure Time: 7.5 kh

Figure 4.32 shows the crack surface of specimen 802 (1061 MPa, 7.5 kh), near to the crack tip. This micrograph is representative of the same region in all the specimens exposed to condensing steam for 7.5 kh and also represents the majority of all the crack surfaces, not just the tip. The surface is a mixture of intergranular transgranular fracture with little to no oxide visible. Figure 4.33 shows the crack through specimen 810 (1018 MPa) from the initiation, which is covered with oxide particles. This result is not typical of the specimens exposed for 7.5 kh and is present only on this specimen and only up to the solid red line. To the right of this line the crack surface is similar to that of specimen 804 (1024 MPa) shown in Figure 4.26.
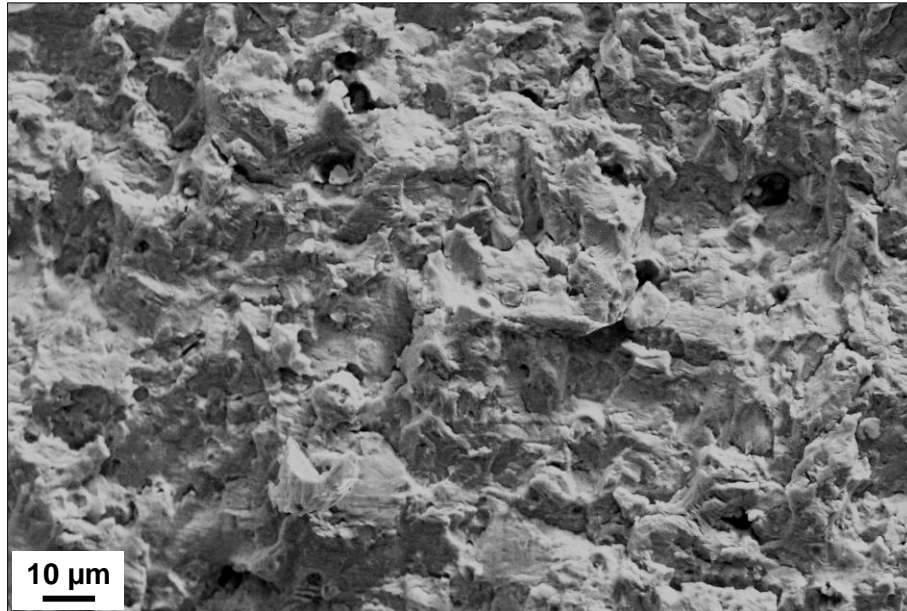
Figure 4.32: Secondary electron micrograph showing the crack surface near the crack tip of specimen 802 (1061 MPa, 7.5 kh).
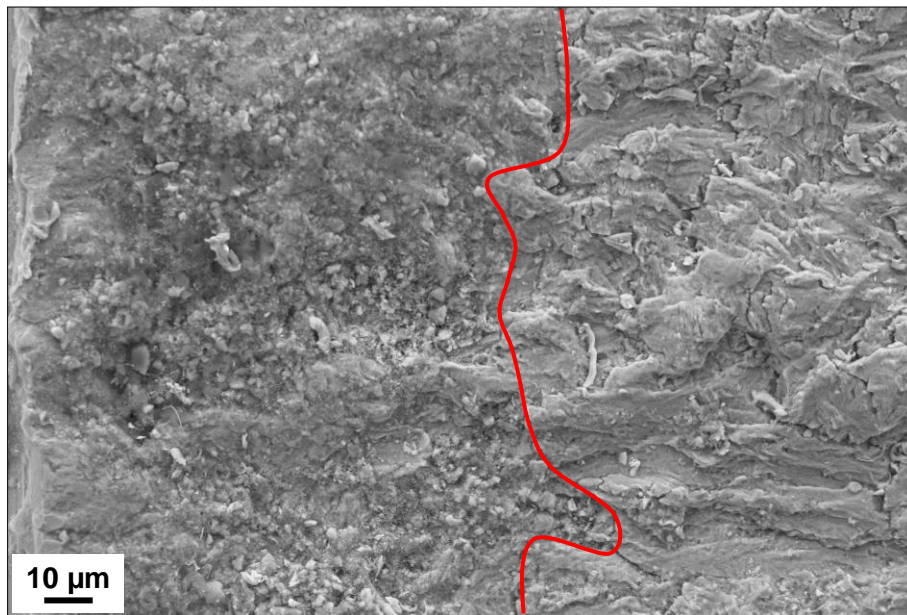
Figure 4.33: Secondary electron micrograph showing the crack initiation of specimen 810 (1018 MPa, 7.5 kh).

4.5.5. Oxide Development

The specimens exposed to condensing steam at 95°C for 98.3 kh had substantial oxide visible within the crack, much more than the specimens exposed for 13.0, 9.8 and 7.5 kh. Similar to the previous results discussed, the additional oxide present in the specimens exposed for 98.3 kh shows that increased exposure time leads to more severe SCC. The initial stress intensity at the pre-crack tip of specimens 803 (1024 MPa, 98.3 kh), 807 (1018 MPa, 98.3 kh) and 811 (1072 MPa, 98.3 kh) was

below the threshold value for SCC to occur. This is reflected in the oxide present on the crack surfaces of the specimens. Whilst oxide was present through the surfaces of the specimens exposed for 98.3 kh, there were only a few descrete locations on the surfaces of specimen 803 (1024 MPa, 98.3 kh), 807 (1018 MPa, 98.3 kh) and 811 (1072 MPa, 98.3 kh) where the build up was severe. The surface of specimen 799 (1061 MPa, 98.3 kh) was covered with areas of highly developed large oxide crystals with distinctly geometric morphologies. This suggests that the level of corrosion inside the crack of specimen 799 (1061 MPa, 98.3 kh) was increased by the extra opening force at the crack tip.

The specimens exposed to condensing steam at 95° for 9.8 kh were not fatigue pre-cracked so the cracks shown are those which initiated and propagated during the experiment time. The initial stress intensity at the notch tip was around twice that of the specimens exposed for 13.0 kh. It has already been shown in Section 4.3.3 that specimens 801 (1061 MPa), 805 (1024 MPa) and 813 (1072 MPa) that were exposed for 9.8 kh had longer cracks than the specimens exposed for 13.0 kh in the respective proof strength groups. It has been suggested in Section 4.3.3 that this was because the specimens exposed for 9.8 kh had substantially higher initial stress intensity at the notch tip than those exposed for the longer time of 13.0 kh. It is possible that this extra opening force allowed the corrosive medium to penetrate the cracks more easily, which resulted in more visible oxide on examination of the crack surfaces, even though the exposure time was less.

It has been shown that there were several large oxide features on the crack surface of specimen 799 (1061 MPa, 98.3 kh). These included cubes, octahedrons and cuboctahedra. Figure 2.12 showed examples of crystal morphologies as part of the seven crystal systems (Bauer, 1987). This shows that cube and octahedron morphologies are part of the cubic system. The cuboctahedron morphology present on the surface of specimen 799 (1061 MPa, 98.3 kh) is not included in the examples shown in Figure 2.12, but it is similar to the galena shape, which is also part of the cubic system.

4.6. X-ray Diffraction Characterisation of Crack Surface

The surfaces of the stress corrosion cracks were examined using X-ray diffraction to try to identify what phases were present, the results of which are presented and discussed in this Section.

4.6.1. Exposure Time: 98.3 kh

Figure 4.34 (a) shows the full 2θ (2-140°) XRD traces for specimens 799 (1061 MPa), 803 (1024 MPa), 807 (1018 MPa) and 811 (1072 MPa) that were exposed to condensing steam at 95°C for 98.3 kh. A comparison to a trace for pure iron confirmed that the biggest peaks belong to the substrate. The substrate is stainless steel so the alignment with the trace for pure iron is not perfect because alloying additions alter the interplanar spacing and therefore the peak positions, however, the match is sufficient to identify the substrate peaks. The remaining peaks are shown more clearly in Figure 4.34 (b) over the 2θ range 20-70°. This range was chosen to include two substrate peaks, at approximately 45° and 65°, for reference purposes. There are possibly some more non-substrate peaks outside of this range, but the most defined peaks are within the chosen range.

All the peaks in the reduced range can be accounted for by comparison with traces of three compounds: magnetite Fe_3O_4, hematite Fe_2O_3 and goethite $FeO(OH)$. Peaks that can be associated with magnetite are at approximately 30°, 35.5°, 43°, 53.5°, 57° and 63°. Peaks that coincide with hematite are at approximately 24°, 33°, 35.5°, 41°, 43°, 54°, 57° and 63°. Peaks that can be matched with goethite are at approximately 21°, 33°, 34.5°, 36.5°, 40°, 41°, 43°, 51°, 53.5°, 54°, 57°, 59, 61° and 64°. Peaks for magnetite, hematite and goethite are close around 43° and 57°. Magnetite and hematite peaks are very close around 35.5° and 63°; magnetite and goethite peaks are very close around 53.5° and 57° and similarly for hematite and goethite at 33°, 41° and 54°.

Figure 4.35 (a) shows the XRD traces over the full 2θ range for specimens 800 (1061 MPa), 804 (1024 MPa), 808 (1018 MPa) and 812 (1072 MPa) that were exposed to condensing steam at 95°C for 13.0 kh. The substrate peak positions have been identified by a comparison to the same trace for pure iron that was used for the specimens exposed for 98.3 kh. Over this range it is not possible to identify any peaks other than substrate so the same specimens are shown in Figure 4.35 (b), but over the

reduced 2θ range of 20-70°. There are far fewer non-substrate peaks than in the traces for the specimens exposed for 98.3 kh and those which are present are very small, approximately 20 counts above the background noise. Peak positions for magnetite, hematite and goethite have been overlaid onto the XRD traces, which account for all the non-substrate peaks. There are no definitive magnetite peaks in any of the traces. At 35.5° there is a peak that may be linked to magnetite or hematite. There is a peak matching hematite peak at 24° and peaks at 33°, 41° and 54° that may be linked to hematite or goethite. Peaks matching goethite are at 26°, 34.5°, 36.5°, and 59°.

Figure 4.36 (a) shows the XRD results for specimens 801 (1061 MPa), 805 (1024 MPa), 809 (1018 MPa) and 813 (1072 MPa) exposed to condensing steam for 9.8 kh over the full 2θ range (2-140°) and Figure 4.36 (b) shows the same specimens over the range 20-70°. Again, the substrate peaks have been identified by comparison with an XRD trace for pure iron. There are more non-substrate peaks than in the specimens exposed for 13.0 kh but fewer than the specimens exposed for 98.3 kh. The majority of non-substrate peaks are bigger than those for specimens exposed for 13.0 kh.

There are no definitive peaks that match those of magnetite. There are small peaks at 35.5° and 63° which can be accounted for by magnetite or hematite due to the overlap in the traces. Peaks that coincide with hematite, that are also present the specimens exposed for 98.3 kh, are at approximately 33°, 35.5°, 41° and 57°. There are possibly peaks at 43°, 54° and 63° but there are no peaks at 24°. Peaks associated with goethite, which are also present in the specimens exposed for 98.3 kh, are at approximately 33°, 34.5, 36.5°, 51°, 53.5° and 57°. The 100 count peak at 21° in the specimens exposed for 98.3 kh is not present in the specimens exposed for 9.8 kh, neither are the peaks at 40°, 41°, 43°, 59, 61° and 64°. There is, however, a peak matching goethite at 47.5° that is not present in the specimens exposed for 98.3 kh. There is a peak of 97 counts at approximately 32° and a peak of 48 counts at approximately 68° that are unaccounted for. An extensive search of the powder diffraction file database revealed no substance that identified these peaks. It has already been mentioned that and there were no definitive peaks that matched magnetite, however, these remaining peaks can be accommodated by shifting the magnetite trace 2° to the right.

XRD traces of specimens 802 (1061 MPa), 806 (1024 MPa), 810 (1018 MPa) and 814 (1072 MPa) that were exposed to condensing steam for the shortest time of 7.5 kh are shown over the full 2θ range in Figure 4.37 (a) and over the range 20-70°C in Figure 4.37 (b). The substrate peaks have been identified using the same trace for pure iron as the other specimens.   Traces for magnetite, hematite and goethite have been overlaid on Figure 4.37 (b). The traces for these specimens have the fewest and smallest distinguishable non-substrate peaks of all the exposure times. Similar to the results for specimens exposed for 13.0 kh and 9.8 kh, there are no definitive peaks that match magnetite in the specimens exposed for 7.5 kh. There are small peaks at 35.5°, but these can be accounted for by both magnetite and hematite. There are possibly peaks at 24° and 49° that match hematite and peaks at 33° that can be accounted for by hematite and goethite. In specimen 802 (1061 MPa, 7.5 kh) there is a peak of 58 counts at approximately 26° that matches goethite. This peak was not present in any of the specimens exposed for 98.3 kh or 9.8 kh but was present in the specimens exposed for 13.0 kh.

At this point it is important to note that powder diffraction files of various combinations of iron, chromium, nickel and manganese were compared to the XRD traces for each WOL specimen but none matched perfectly.   When using XRD as an analysis technique it is not possible to accurately distinguish between elements of similar size. As the substrate is mainly iron, it was decided that for the purposes of this investigation, comparisons with magnetite, hematite and goethite were acceptable. However, the matches are more accurately identified as M_3O_4, M_2O_3, and $MO(OH)$ where M represents iron, chromium, nickel or possibly manganese. To identify the exact elemental composition of the oxides present within the stress corrosion cracks another analysis technique is required, such as EDS.

Definitive magnetite peaks were only present in the specimens exposed for the longest time of 98.3 kh. Figure 4.36 showed the XRD results for the specimens exposed to condensing steam at 95°C for 13.0 kh. There was a selection of peaks that could be accounted for by magnetite with a 2° shift. It is possible that the crack surfaces contained oxide where some of the iron in the magnetite (or rather M_3O_4) had been substituted for elements of a similar size, such as chromium or nickel. Any substitution would alter the interplanar spacing of the crystals and therefore shift the XRD peak positions.
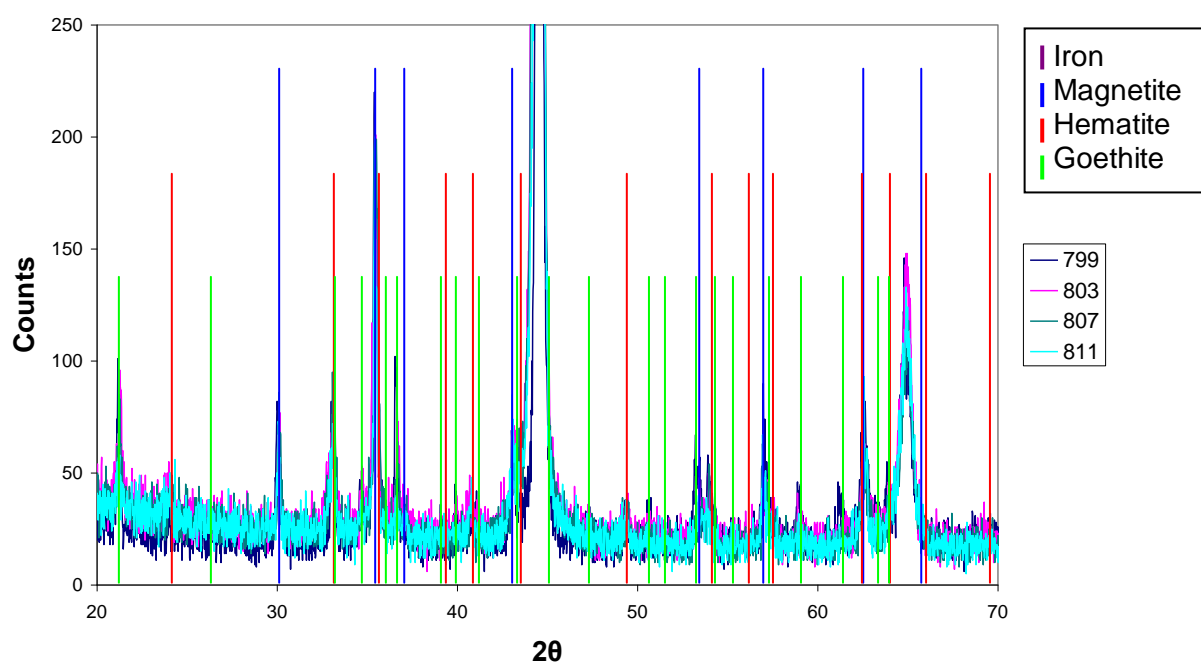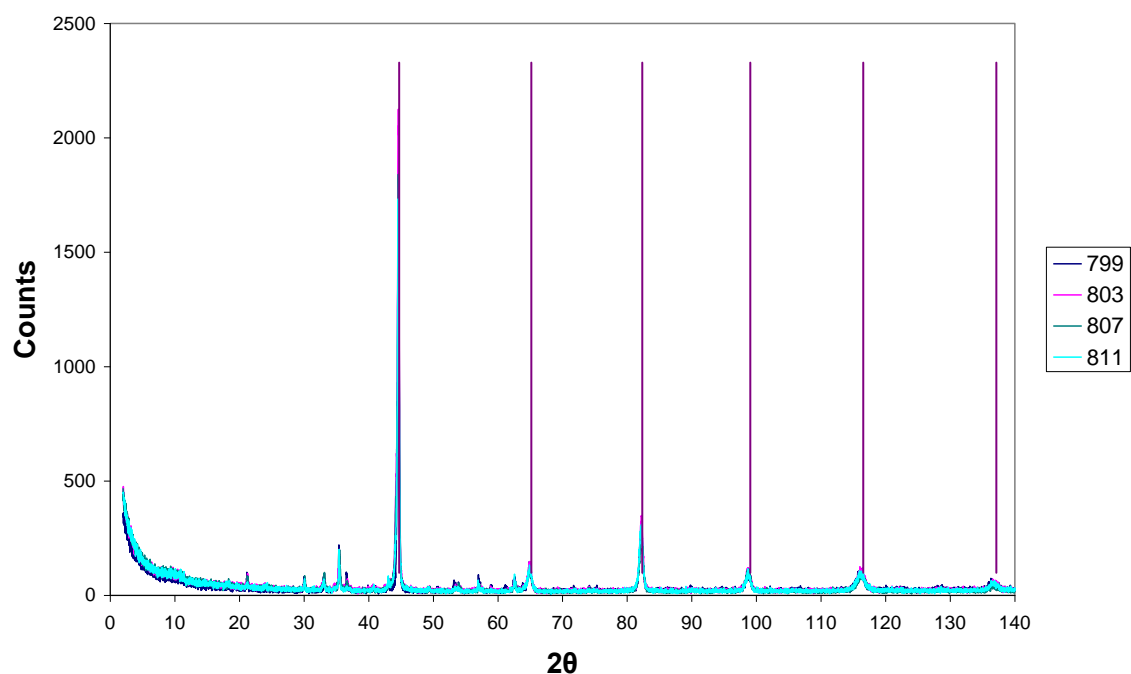
Figure 4.34: XRD data for samples 799, 803, 807 and 811 exposed to condensing steam at 95°C for 98.3 kh showing (a) all the peaks between 2 and140° and (b) 20-70° focusing on the peaks not accounted for by the substrate.
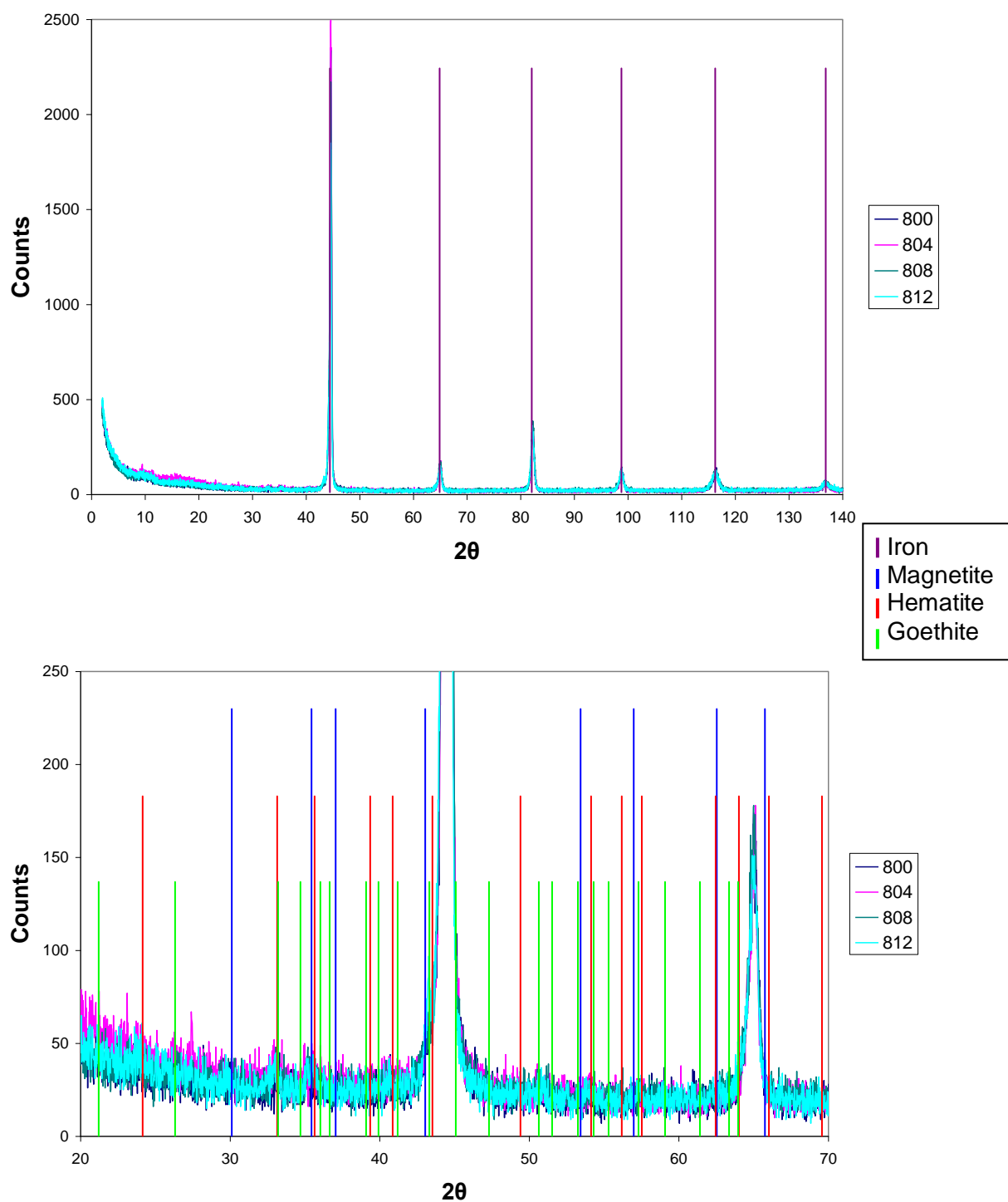
Figure 4.35: XRD data for samples 800, 804, 808 and 812 exposed to condensing steam at 95°C for 13.0 kh showing (a) all the peaks between 2 and140° and (b) 20-70° focusing on the peaks not accounted for by the substrate.
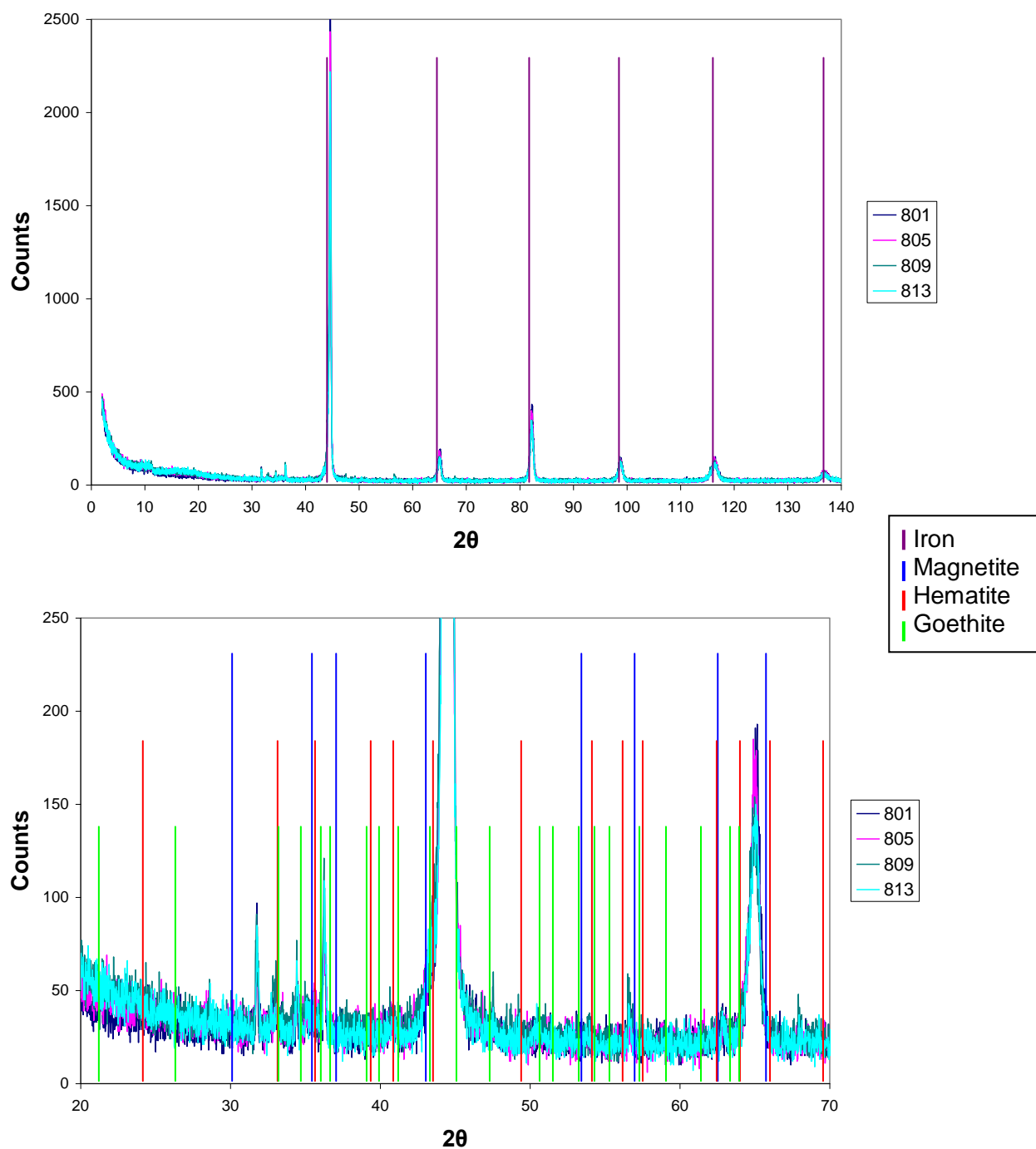
Figure 4.36: XRD data for samples 801, 805, 809 and 813 exposed to condensing steam at 95°C for 9.8 kh showing (a) all the peaks between 2 and140° and (b) 20-70° focusing on the peaks not accounted for by the substrate.
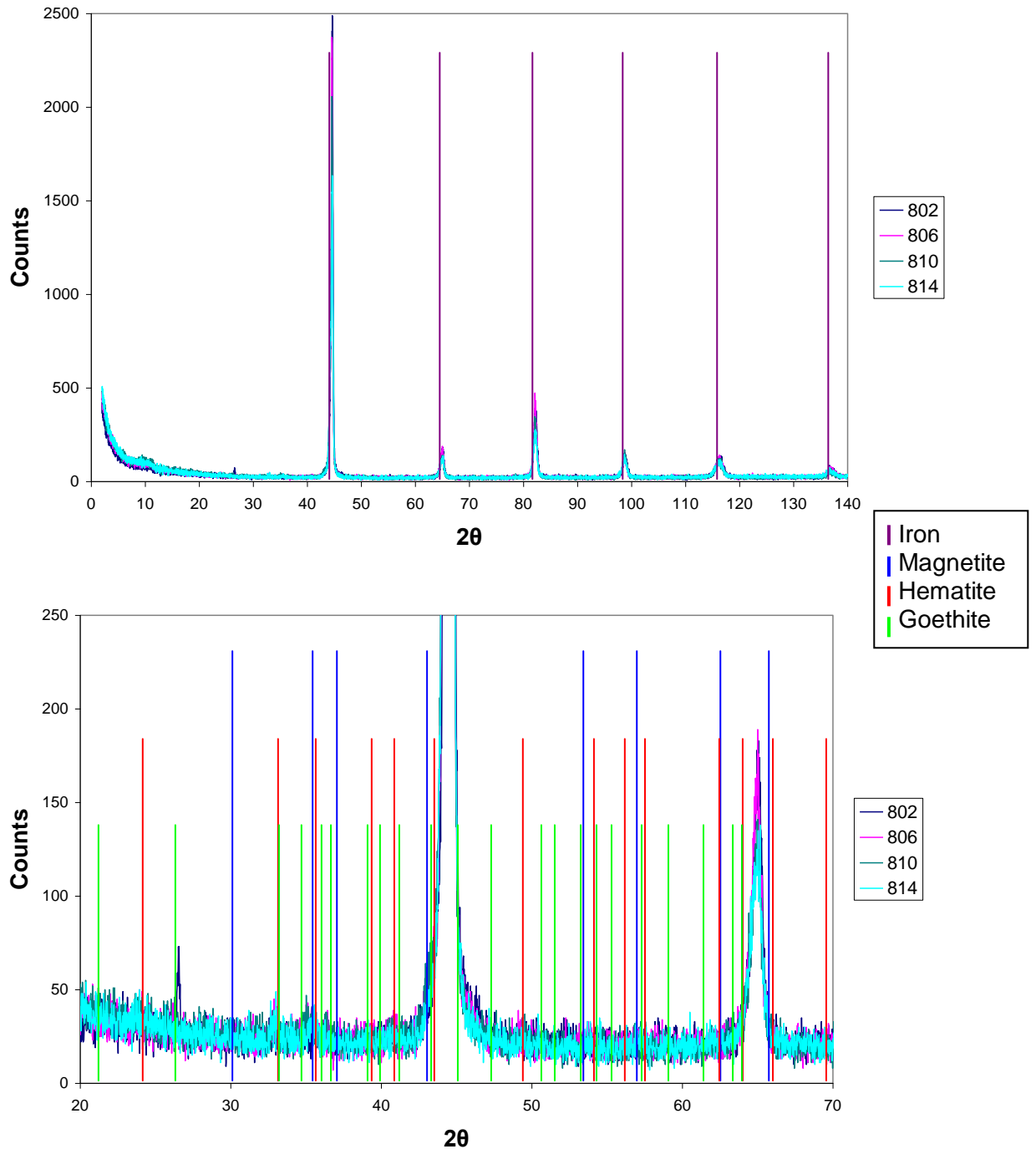
Figure 4.37: XRD data for samples 802, 806, 810 and 814 exposed to condensing steam at 95°C for 7.5 kh showing (a) all the peaks between 2 and140° and (b) 20-70° focusing on the peaks not accounted for by the substrate.

4.7. Microstructural Characterisation of Specific Morphologies

Ion induced secondary electron imaging and TEM was used to examine some of the oxide morphologies including cubes, cuboctahedra and octahedrons that were observed on the surfaces of the stress corrosion cracks. Site specific samples were

made using the dual beam FIB FEGSEM as described in Section 3.8. EDS spectra and SAD patterns have been collected and analysed, the results of which are presented and discussed in this section.

4.7.1. Analysis of Cuboctahedra

Figure 4.38 shows a secondary electron micrograph of a cuboctahedron on the crack surface of specimen 799 (1061 MPa, 98.3 kh). Figure 4.20 showed that the entire crack surfaces of specimens exposed to condensing steam at 95° for 98.3 kh were covered with a layer of oxide exhibiting a needle-like or hexagonal platelet structure. This fine structured oxide layer can also be seen in Figure 4.38, however, it is not possible to determine the exact morphology. Around the cuboctahedron of interest in Figure 4.38, there are several smaller, less developed structures protruding from the crack surface. This cuboctahedron was cross-sectioned using the dual beam FIB FEGSEM as shown by the ion induced secondary electron micrograph in Figure 4.39. The top two layers (~ 3 μm) should be disregarded as these are the protective platinum. The prior austenite grains in the substrate can be distinguished by the variation in contrast, whereas the cuboctahedron is monotone which suggests it is a single grain. Beneath the platinum on both sides of the cuboctahedron it is just possible to see the layer of fine-grained structure covering the entire crack surface.

The cross-section of the cuboctahedron was thinned to electron transparency and examined with TEM as shown in Figure 4.40. There are dark lines on the cuboctahedron in Figure 4.40 (a) which could be confused with grain boundaries, however, they move across the grain when the sample is tilted, which suggests they are actually bend contours, i.e. minor variations in thickness. Examination with ion induced secondary electron imaging and TEM suggest that the cuboctahedron is a single crystal. The fine-grained layer can be seen more clearly in Figure 4.40 than Figure 4.39. Figure 4.40 (b) shows that the layer is approximately 1 μm thick consisting of mainly columnar grains perpendicular to the crack surface, which is consistent with the needle-like and hexagonal platelet structures seen in Figure 4.20. The layer of fine grains continues between the cuboctahedron and the substrate. Figure 4.40 (a) shows some bigger grains that are consistent with the growth of other features shown in Figure 4.38.
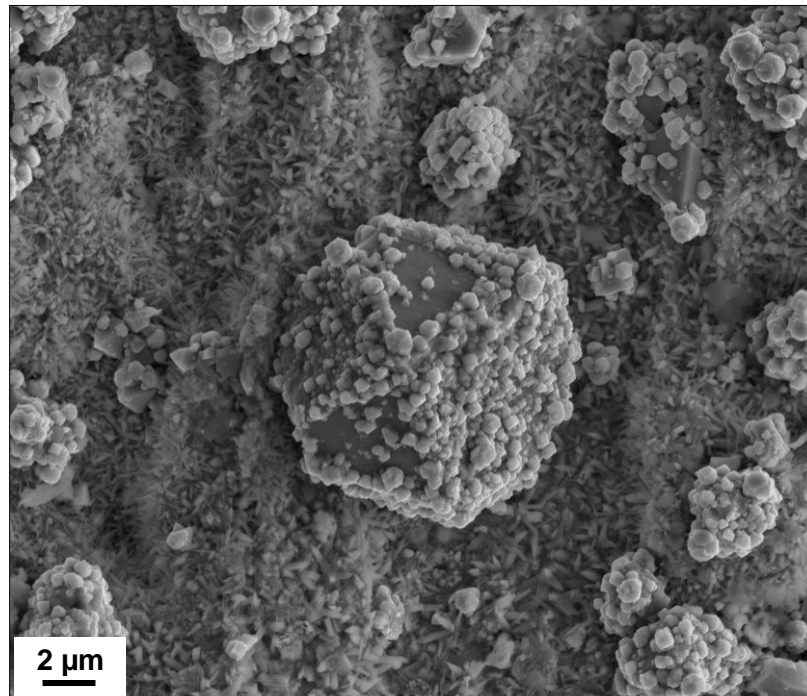
Figure 4.38: Secondary electron micrograph of a cuboctahedron on the crack surface of specimen 799 (1061 MPa, 98.3 kh)
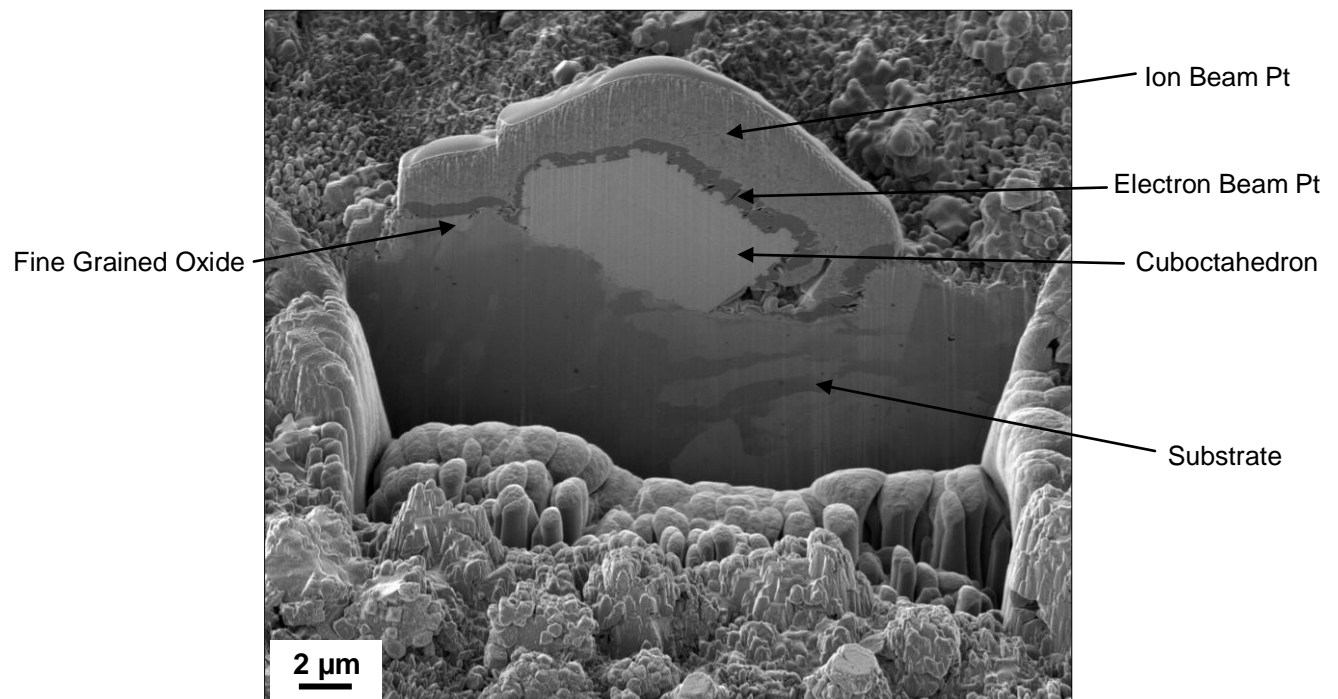
Figure 4.39: Ion induced secondary electron micrograph showing the cross-section of the cuboctahedron from Figure 4.38.

106
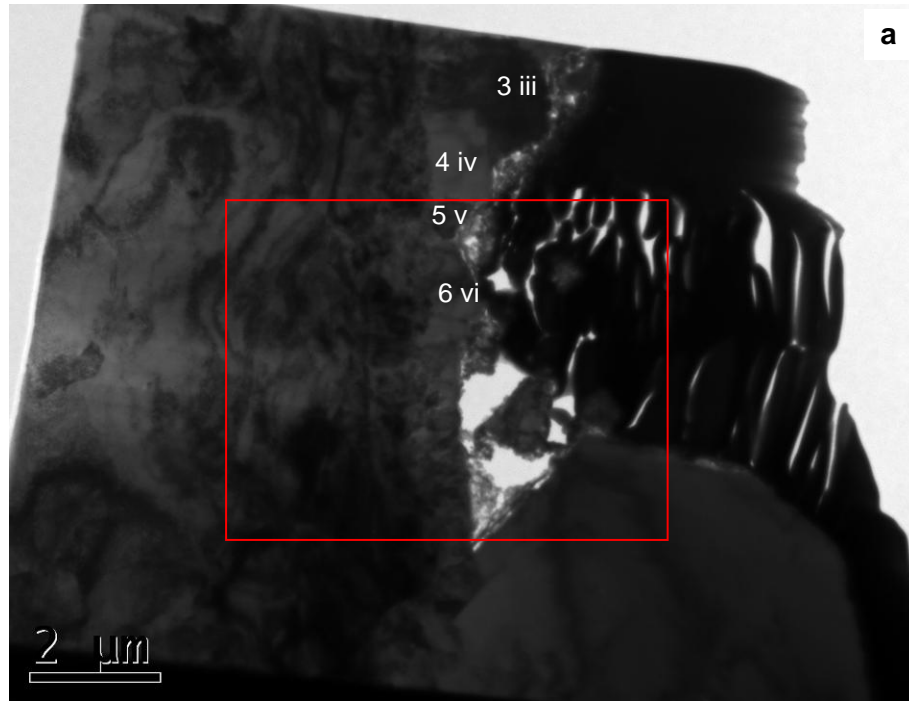
Substrate   Fine Grained Oxide   Cuboctahedron
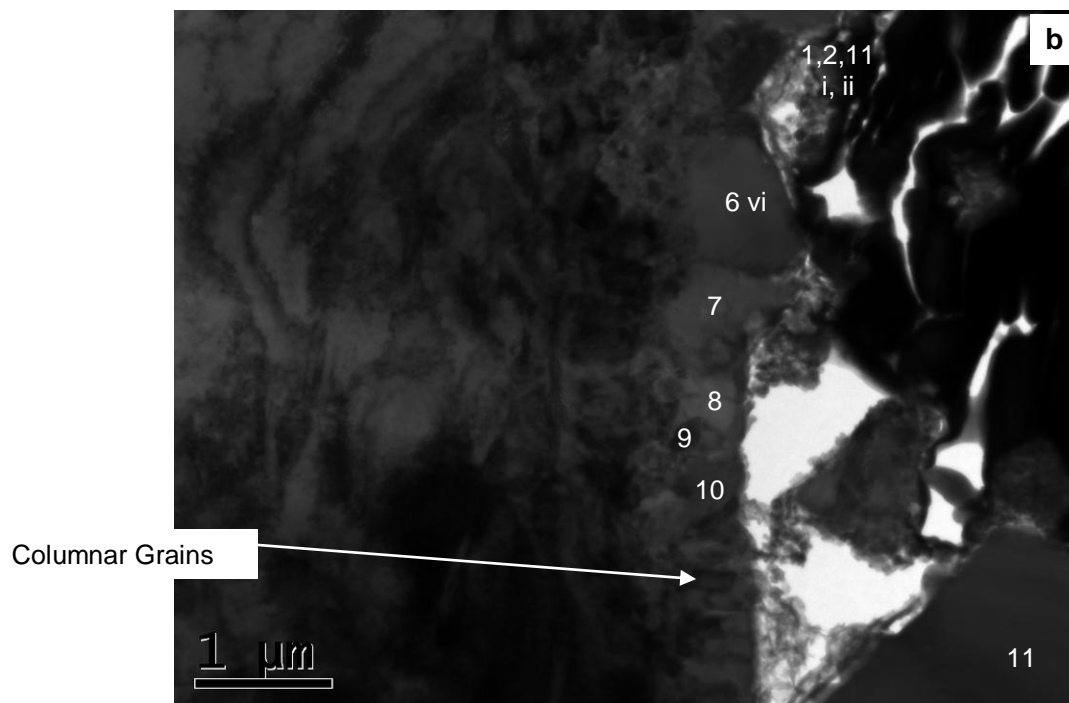
Figure 4.40: (a) Transmission electron micrograph showing a site-specific cross-section through the cuboctahedron on the surface of specimen 799 (1061 MPa, 98.3 kh) from Figure 4.38 and (b) a higher magnification micrograph of the boxed area highlighted in Figure 4.40 (a). The letters i – vi refer to SAD patterns shown in Figure 4.41 - Figure 4.46 and numbers 1-6 and 11 correspond to EDS point spectra detailed in Table 4.3.

SAD patterns were collected from the cross-section of the cuboctahedron and surrounding areas as indicated by the annotations i – vi in Figure 4.40 (a). EDS spectra were also collected from the cross section at the points indicated by the numbers 1-11 in Figure 4.40. Two diffraction patterns (i and ii) were collected from the cuboctahedron at two zone axes so that analysis of both patterns could provide consistently accurate solutions. Analysis of pattern i gave solutions for maghemite (γ-Fe_2O_3), magnetite (Fe_3O_4), goethite ($FeO(OH)$) and nickel chromium oxide ($NiCr_2O_4$). Analysis of pattern ii gave solutions for maghemite (γ-Fe_2O_3), magnetite (Fe_3O_4) and nickel chromium oxide ($NiCr_2O_4$) but not goethite ($FeO(OH)$). The quantitative EDS data for corresponding points 1, 2 and 11 show negligible chromium. This suggests that the cuboctohdedron is either maghemite (γ-Fe_2O_3) or magnetite (Fe_3O_4). For both diffraction patterns i and ii, the measured d_1 value is closest to the magnetite (Fe_3O_4) solution and the measured d_2 value is closest to the maghemite (γ-Fe_2O_3) solution so it is not possible to determine which oxide is the most probable. The EDS data for points 1 and 11 show significant amounts of nickel present, but not enough to match the stoichiometry of an iron nickel oxide. Nickel is only slightly bigger than iron, so it is possible that the some of the iron atoms in primarily maghemite (γ-Fe_2O_3) or magnetite (Fe_3O_4) cuboctahedron have been substituted for nickel.

	h	k	l	d_1	h	k	l	d_2	u	v	w	Angle
Measured				2.966				2.514				32°
γ-Fe_2O_3	0	$\bar{2}$	$\bar{2}$	2.9483	1	$\bar{3}$	$\bar{1}$	2.5143	$\bar{2}$	$\bar{1}$	1	31.5°
Fe_3O_4	0	$\bar{2}$	$\bar{2}$	2.9684	1	$\bar{3}$	$\bar{1}$	2.5315	$\bar{2}$	$\bar{1}$	1	31.5°
Fe_2O_3												
$FeO(OH)$	0	$\bar{2}$	$\bar{1}$	2.5833	0	0	$\bar{1}$	3.0220	1	0	0	31.3°
$FeO (OH)$	0	$\bar{1}$	1	2.8917	1	$\bar{1}$	$\bar{1}$	2.4494	0	$\bar{1}$	1	32.1°
Cr_2O_3												
FeO												
$NiCr_2O_4$	0	$\bar{2}$	$\bar{2}$	2.9402	1	$\bar{3}$	$\bar{1}$	2.5074	$\bar{2}$	$\bar{1}$	1	31.5°
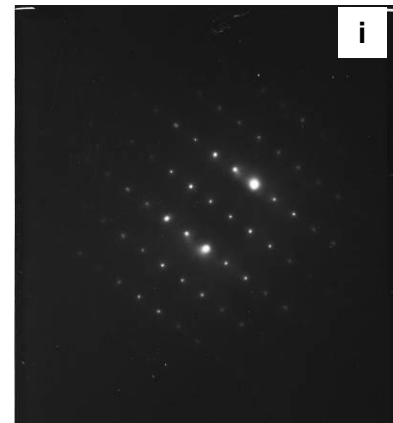
Figure 4.41: Selected area diffraction pattern collected from point i in Figure 4.40.

	h	k	l	d_1	h	k	l	d_2	u	v	w	Angle
Measured				4.220				4.823				55°
γ maghemite	0	$\bar{2}$	0	4.1695	1	$\bar{1}$	$\bar{1}$	4.8145	1	0	1	54.7°
magnetite	0	2	0	4.1980	1	$\bar{1}$	$\bar{1}$	4.8474	1	0	1	54.7°
hematite												
goethite												
chromia												
wustite												
nickel chromium oxide	0	$\bar{2}$	0	4.1580	1	$\bar{1}$	$\bar{1}$	4.8012	1	0	0	54.7°
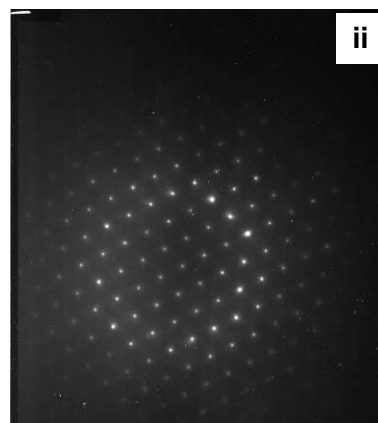
Figure 4.42: Selected area diffraction pattern collected from point ii in Figure 4.40.

	h	k	l	d_1	h	k	l	d_2	u	v	w	Angle
Measured				2.966				2.514				31°
γ-Fe_2O_3	0	$\bar{2}$	$\bar{2}$	2.9483	1	$\bar{3}$	$\bar{1}$	2.5143	$\bar{2}$	$\bar{1}$	1	31.5°
Fe_3O_4	0	$\bar{2}$	$\bar{2}$	2.9684	1	$\bar{3}$	$\bar{1}$	2.5315	$\bar{2}$	$\bar{1}$	1	31.5°
Fe_2O_3												
FeO(OH)	0	0	$\bar{1}$	3.0220	0	$\bar{2}$	$\bar{1}$	2.5833	1	0	0	31.3°
FeO(OH)	0	$\bar{1}$	1	2.8917	1	$\bar{1}$	$\bar{1}$	2.4494	0	$\bar{1}$	1	32.1°
Cr_2O_3												
FeO												
$NiCr_2O_4$	0	$\bar{2}$	$\bar{2}$	2.9402	1	$\bar{3}$	$\bar{1}$	2.5074	$\bar{2}$	$\bar{1}$	1	31.5°

Figure 4.43: Selected area diffraction pattern collected from point iii in Figure 4.40.

	h	k	l	d_1	h	k	l	d_2	u	v	w	Angle
Measured				4.12				4.785				55°
γ-Fe_2O_3	0	$\bar{2}$	0	4.1695	1	$\bar{1}$	$\bar{1}$	4.8145	1	0	1	54.7°
Fe_3O_4	0	$\bar{2}$	0	4.1980	1	$\bar{1}$	$\bar{1}$	4.8474	1	0	1	54.7°
Fe_2O_3												
FeO(OH)												
Cr_2O_3												
FeO												
$NiCr_2O_4$	0	$\bar{2}$	0	4.1580	1	$\bar{1}$	$\bar{1}$	4.8012	1	0	1	54.7°

Figure 4.44: Selected area diffraction pattern collected from point iv in Figure 4.40.

109

	h	k	l	d_1	h	k	l	d_2	u	v	w	Angle
Measured				4.190				4.863				55°
γ-Fe$_2$O$_3$	0	$\bar{2}$	0	4.1695	1	$\bar{1}$	$\bar{1}$	4.8145	1	0	1	54.7°
Fe$_3$O$_4$	0	$\bar{2}$	0	4.1980	1	$\bar{1}$	$\bar{1}$	4.8474	1	0	1	54.7°
Fe$_2$O$_3$												
FeO(OH)												
Cr$_2$O$_3$												
FeO												
NiCr$_2$O$_4$	0	$\bar{2}$	0	4.1580	1	$\bar{1}$	$\bar{1}$	4.8012	1	0	1	54.7°

Figure 4.45: Selected area diffraction pattern collected from point v in Figure 4.40.

	h	k	l	d_1	h	k	l	d_2	u	v	w	Angle
Measured				2.966				2.966				60°
γ-Fe$_2$O$_3$	0	$\bar{2}$	$\bar{2}$	2.9483	2	$\bar{2}$	0	2.9483	$\bar{1}$	$\bar{1}$	1	60°
Fe$_3$O$_4$	0	$\bar{2}$	$\bar{2}$	2.9684	2	$\bar{2}$	0	2.9684	$\bar{1}$	$\bar{1}$	1	60°
Fe$_2$O$_3$												
FeO(OH)												
Cr$_2$O$_3$												
FeO												
NiCr$_2$O$_4$	0	$\bar{2}$	$\bar{2}$	2.9402	2	$\bar{2}$	0	2.9402	$\bar{1}$	$\bar{1}$	1	60°

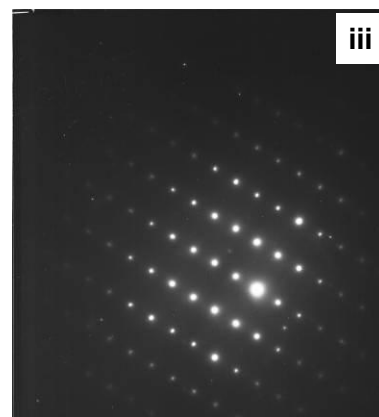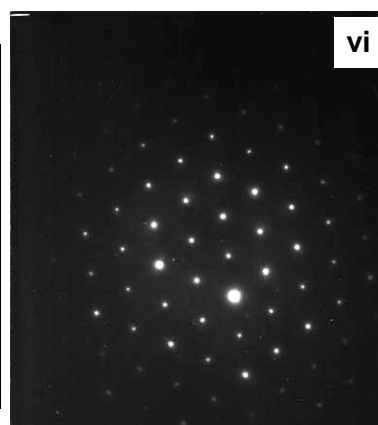*Figure 4.46: Selected area diffraction pattern collected from point vi in Figure 4.40.*

Analysis of SAD pattern iii also had solutions for maghemite (γ-Fe$_2$O$_3$), magnetite (Fe$_3$O$_4$), goethite (FeO(OH)) and nickel chromium oxide (NiCr$_2$O$_4$). EDS spectrum number 3 had insufficient chromium for the solution of nickel chromium oxide (NiCr$_2$O$_4$) to be correct. Goethite (FeO(OH)) can also be eliminated as the solutions for d_1 and d_2 are the furthest from the measured d values. This suggests that the grain with diffraction pattern iii is either maghemite (γ-Fe$_2$O$_3$) or magnetite (Fe$_3$O$_4$). The measured d_1 value is closest to the magnetite (Fe$_3$O$_4$) solution and the measured d_2 value is closest to the maghemite (γ-Fe$_2$O$_3$) solution so it is not possible to determine which oxide is the most probable, as with diffraction patterns i and ii.

Diffraction patterns iv – vi all had solutions for maghemite (γ-Fe$_2$O$_3$), magnetite (Fe$_3$O$_4$) and nickel chromium oxide (NiCr$_2$O$_4$). The corresponding EDS point spectra all showed that there was insufficient chromium for the grains to be nickel chromium oxide (NiCr$_2$O$_4$). For diffraction pattern iv the measured d_1 value was closest to the magnetite (Fe$_3$O$_4$) solution whereas the measured d_2 value was closest to the maghemite (γ-Fe$_2$O$_3$) solution, which means that it is not possible to determine which oxide is most

probable. For diffraction patterns v and vi, both the measured d_1 and d_2 values are closest to the magnetite solution, which suggests that the grains are most probably magnetite.

Table 4.3: Quantified EDS data from a site-specific cross-section through a cuboctahedron on the crack surface of specimen 799 (1061 MPa, 98.3 kh). The spectrum numbers correspond to the numbers 1-11 in Figure 4.40 (a and b).

Spectrum Number		Element				
		O	Cr	Mn	Fe	Ni
1	Wt%	6.0 (3.7)	0.3 (0.4)	0.4 (0.5)	86.4 (3.5)	6.8 (0.6)
	At%	18.3	0.3	0.3	75.4	5.7
2	Wt%	23.6 (3.9)	1.1 (0.6)	0.8 (0.7)	73.8 (3.8)	0.7 (0.4)
	At%	51.9	0.8	0.5	46.4	0.4
3	Wt%	15.6 (3.9)	0.1 (0.5)	0.9 (0.6)	79.0 (3.7)	4.4 (0.6)
	At%	39.3	0.1	0.7	57.0	3.0
4	Wt%	19.2 (3.6)	0.4 (0.5)	0.2 (0.6)	75.9 (3.4)	4.2 (0.6)
	At%	45.4	0.3	0.2	51.4	2.7
5	Wt%	22.2 (3.8)	1.8 (0.6)	0.7 (0.6)	72.6 (3.6)	2.7 (0.5)
	At%	49.8	1.3	0.5	46.8	1.7
6	Wt%	21.6 (3.7)	0.9 (0.5)	0.4 (0.6)	73.6 (3.5)	3.6 (0.6)
	At%	49.0	0.6	0.3	47.9	2.2
7	Wt%	14.7 (4.0)	0.7 (0.5)	1.3 (0.7)	78.8 (3.8)	4.6 (0.6)
	At%	37.6	0.5	1.0	57.7	3.2
8	Wt%	21.3 (4.1)	0.6 (0.6)	0	79.0 (4.2)	0.1 (0.5)
	At%	48.5	0.4	0	51.6	0.1
9	Wt%	15.0 (4.4)	2.1 (0.6)	4.3 (0.8)	74.8 (4.0)	3.8 (0.6)
	At%	38.2	1.6	3.2	54.4	2.6
10	Wt%	15.7 (3.9)	1.1 (0.5)	0	76.0 (3.6)	7.5 (0.7)
	At%	39.6	0.8	0	55.0	4.8
11	Wt%	2.8 (3.6)	0.5 (0.4)	0.7 (0.6)	88.4 (3.3)	7.6 (0.6)
	At%	9.1	0.5	0.7	82.9	6.8

Small proportions of nickel were present in all the EDS spectra corresponding to the diffraction patterns, which suggests there may be some nickel substitution in the magnetite (Fe_3O_4) / maghemite (γ-Fe_2O_3). EDS spectra 7-11 all suggest the grains to be iron oxides with some nickel substitution and trace amounts of chromium.

4.7.2. Analysis of Octahedrons

Figure 4.47 shows a secondary electron micrograph of three octahedrons on the crack surface of specimen 799 (1061 MPa, 98.3 kh). Similar to Figure 4.38, the crack surface surrounding the octahedrons is covered with a layer of fine-structured oxide.

The central octahedron is the area of interest and it can be identified by the protective layer of electron beam platinum 20 x 1.5 µm. This octahedron was cross-sectioned using the dual beam FIB FEGSEM and examined with the aid of ion induced secondary electron microscopy (Figure 4.48). The top two layers are the protective platinum deposited to preserve the area of interest. Figure 4.48 shows that the octahedron is a single crystal sitting on a layer of smaller grained oxide. This is confirmed in the transmission electron micrograph in Figure 4.49. Similar to the cuboctahedron in Figure 4.40, tilting the sample confirmed that the dark lines on the octahedron in Figure 4.49 are bend contours rather than grain boundaries.

Analysis of diffraction pattern i showed solutions for maghemite (γ-Fe_2O_3), magnetite (Fe_3O_4) and nickel chromium oxide ($NiCr_2O_4$), which is the same as the cuboctahedron in Figure 4.38. EDS spectrum number one shows iron and oxygen present with a small amount of nickel and trace amounts of chromium and manganese. This data eliminates nickel chromium oxide as a possible solution for diffraction pattern i, despite the solution values of d_1 and d_2 being closer to the measured d values than the iron oxides. The solution d values of maghemite (γ-Fe_2O_3) are closer to the measured d values than those of magnetite (Fe_3O_4). This suggests that the octahedron is maghemite (γ-Fe_2O_3).
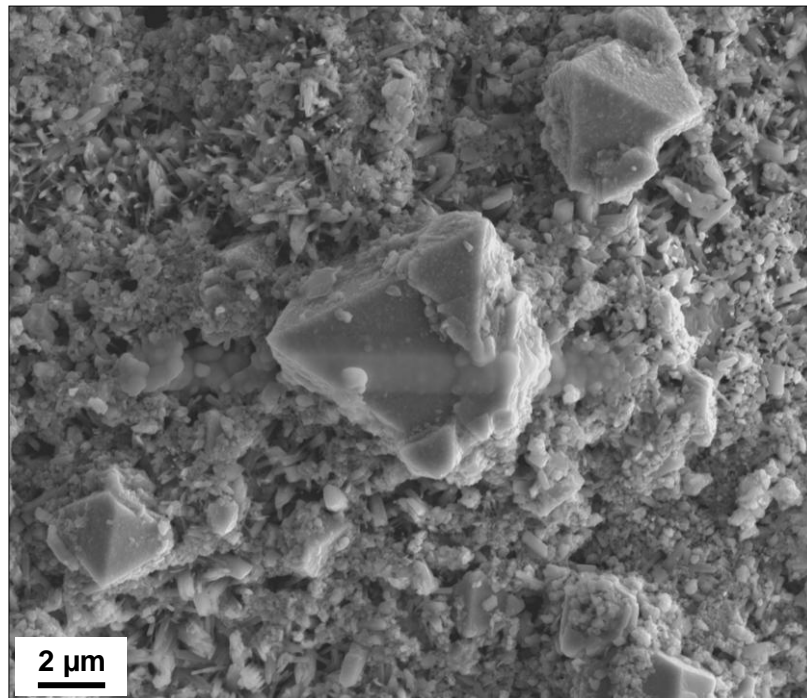
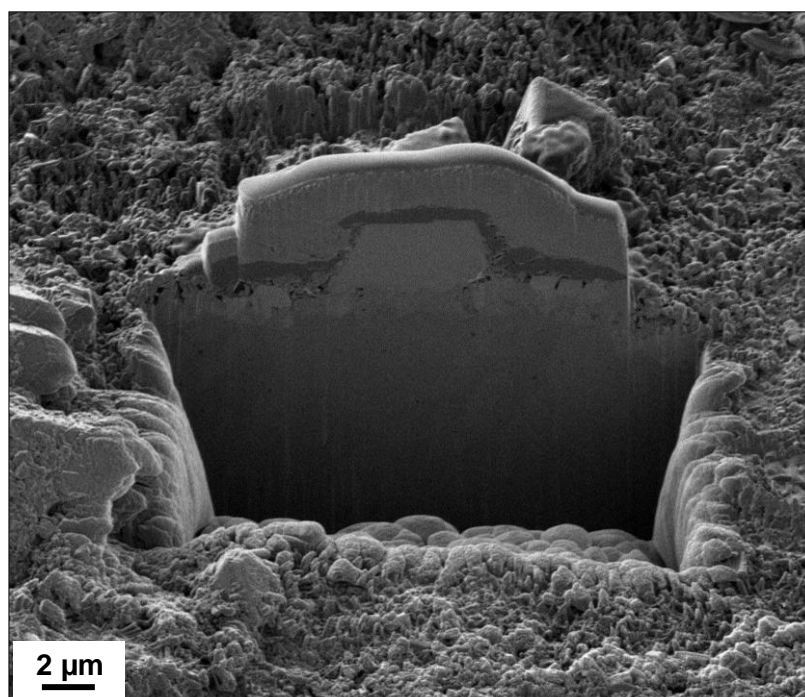**Figure 4.47: Secondary electron micrograph showing an octahedron on the crack surface of specimen 799 (1061 MPa, 98.3 kh)**

Figure 4.48: Ion induced secondary electron micrograph showing the cross-section of the octahedron in Figure 4.47.
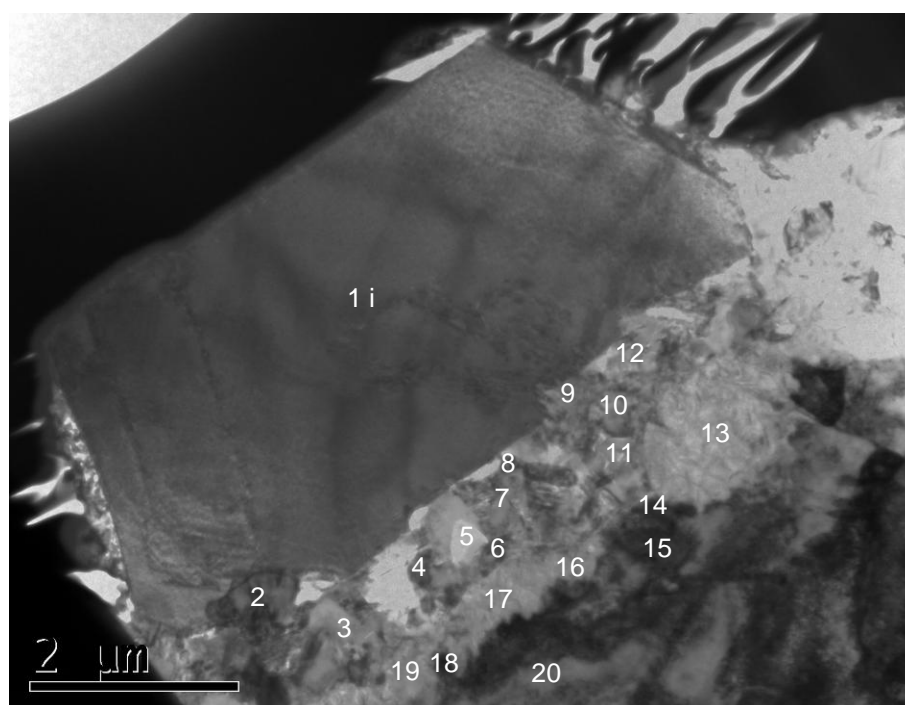
Figure 4.49: Transmission electron micrograph showing a site-specific cross-section through the octahedron from Figure 4.47. The letter i corresponds to a selected area diffraction pattern from the octahedron and the numbers 1 – 20 refer to EDS point spectra detailed in Table 4.4.

	h	k	l	d_1	h	k	l	d_2	u	v	w	Angle
Measured				4.12				4.785				54
γ-Fe$_2$O$_3$	0	$\bar{2}$	0	4.1695	1	$\bar{1}$	$\bar{1}$	4.8145	1	0	1	54.7°
Fe$_3$O$_4$	0	$\bar{2}$	0	4.1980	1	$\bar{1}$	$\bar{1}$	4.8474	1	0	1	54.7°
Fe$_2$O$_3$												
FeO(OH)												
Cr$_2$O$_3$												
FeO												
NiCr$_2$O$_4$	0	$\bar{2}$	0	4.1580	1	$\bar{1}$	$\bar{1}$	4.8012	1	0	1	54.7°

Figure 4.50: Selected area diffraction pattern collected from point i on Figure 4.49.

EDS point spectra 14, 15, 18 and 20 show iron, chromium and nickel but no oxygen, which illustrates the transition between the substrate and the layer of fine-grained oxide. Spectra for points 13, 16, 17 and 19 contain iron, oxygen, some nickel and substantial chromium (equal or greater than the quantity of iron), which suggests that much of the fine-grained structure is either chromia (Cr$_2$O$_3$) or an iron chromium oxide. Spectra 3 and 10 contained iron and oxygen with traces of nickel, chromium and manganese. The remaining spectra contain iron and oxygen with slightly higher values of nickel and chromium than spectra 3 and 10, which suggests that these grains are iron oxide but that some of the iron atoms have been substituted for nickel and chromium.

Table 4.4: Quantitative EDS point data from a site-specific sample through an octahedron oxide particle in Figure 4.49.

| Spectrum Number		Element				
		O	Cr	Mn	Fe	Ni
1	Wt%	13.8 (4.7)	0.8 (0.6)	0.9 (0.6)	80.9 (4.5)	3.6 (0.7)
	At%	35.9	0.7	0.7	60.3	2.6
2	Wt%	23.5 (4.2)	3.8 (0.7)	0	70.2 (4.0)	2.8 (0.7)
	At%	51.7	2.6	0	44.3	1.7
3	Wt%	18.6 (4.1)	0.1 (0.5)	0.6 (0.6)	79.6 (4.1)	1.1 (0.5)
	At%	44.4	0.1	0.4	54.4	0.7
4	Wt%	15.2 (5.1)	2.0 (0.7)	0.4 (0.8)	80.3 (4.9)	2.1 (0.7)
	At%	38.5	1.6	0.3	58.2	1.5
5	Wt%	22.5 (4.2)	0.9 (0.6)	0.2 (0.7)	74.7 (4.1)	1.7 (0.6)
	At%	50.4	0.6	0.1	47.9	1.0
6	Wt%	22.3 (4.3)	3.7 (0.7)	0	72.4 (4.1)	2.2 (0.6)
	At%	50.0	2.5	0	46.5	1.4
7	Wt%	23.7 (4.3)	0.2 (0.6)	0	75.3 (4.3)	1.6 (0.6)
	At%	52.0	0.1	0	47.4	1.0
8	Wt%	24.7 (4.4)	3.4 (0.7)	0.5 (0.7)	69.1 (4.1)	24 (0.7)
	At%	53.3	2.3	0.3	42.8	1.4
9	Wt%	32.4 (3.9)	4.2 (0.7)	0	59.9 (3.5)	3.8 (0.7)
	At%	62.5	2.5	0	33.1	2.0
10	Wt%	22.3 (4.1)	0.4 (0.4)	0	76.3 (4.0)	1.4 (0.6)
	At%	50.0	0.3	0	49.1	0.8
11	Wt%	16.4 (4.7)	3.2 (0.7)	0	78.7 (4.6)	2.1 (0.6)
	At%	40.6	2.5	0	55.9	1.4
12	Wt%	21.5 (4.2)	2.6 (0.7)	0.2 (0.7)	73.7 (4.0)	2.0 (0.6)
	At%	48.9	1.8	0.1	47.9	1.2
13	Wt%	24.5 (5.1)	35.0 (2.7)	0.4 (1.0)	36.1 (2.8)	4.0 (0.9)
	At%	52.3	23.0	0.3	22.1	2.3
14	Wt%	0	16.1(0.9)	1.4 (0.6)	80.0 (2.5)	5.1 (0.6)
	At%	0	18.2	1.5	84.4	5.1
15	Wt%	0	15.7 (0.8)	0	80.1 (2.4)	5.7 (0.5)
	At%	0	17.1	0	81.4	5.3
16	Wt%	25.6 (5.0)	30.8 (2.4)	1.1 (1.0)	38.1 (2.9)	4.4 (0.9)
	At%	53.9	19.9	0.7	23.0	2.5
17	Wt%	29.4 (5.1)	31.5 (2.7)	1.1 (1.0)	33.0 (2.8)	5.0 (1.1)
	At%	58.6	19.3	0.7	18.8	2.7
18	Wt%	0	19.6 (1.1)	1.0 (0.7)	74.6 (3.0)	6.6 (0.7)
	At%	0	21.7	1.0	77.1	6.5
19	Wt%	23.8 (5.3)	39.0 (3.0)	0.1 (1.0)	32.6 (2.6)	4.5 (1.0)
	At%	51.3	25.8	0.1	20.2	2.7
20	Wt%	0	15.4 (0.9)	0.8 (0.6)	79.3 (2.5)	4.7 (0.6)
	At%	0	16.5	0.8	78.9	4.4

4.7.3. Analysis of Cubes

Figure 4.51 shows a secondary electron micrograph of several cubes on the crack surface of specimen 799 (1061 MPa, 98.3 kh). The area of interest is the three incomplete, intertwined cubes in the centre of Figure 4.51 that can be identified by the 20 x 1.5 µm layer of protective electron beam platinum. Using the dual beam FIB FEGSEM these three cubes were cross-sectioned and examined using TEM. Figure 4.52 shows a transmission electron micrograph of the one of the three cubes in cross-section with accompanying SAD patterns in Figure 4.53 - Figure 4.55 and EDS point spectra in Table 4.5. Figure 4.52 shows again that there is a layer of fine-grained oxide ~ 1 µm thick covering the substrate, including beneath the cube. The cube itself appears quite distorted as a result of the thinning process.

SAD patterns i and ii were collected from the cube at two different zone axes. Analysis of said patterns produced solutions for maghemite (γ-Fe_2O_3), magnetite (Fe_3O_4) and nickel chromium oxide ($NiCr_2O_4$). The accompanying EDS point spectrum shows that there is iron and oxygen but insufficient nickel or chromium to substantiate the solution for nickel chromium oxide ($NiCr_2O_4$). The solution d values for maghemite (γ-Fe_2O_3) are closer to the measured d values for diffraction pattern i than the solutions for magnetite (Fe_3O_4), however, the opposite is true for diffraction pattern ii. The difference between the magnetite (Fe_3O_4) solution and measured d values for diffraction pattern ii is 0.0035 Å and the solution angle is only 0.5° different from the measured angle. The difference between the maghemite (γ-Fe_2O_3) solution and measured d values for diffraction pattern i is 0.0423 Å, which is a factor of 10 times more inaccurate than the solution for diffraction pattern ii. The solution angle for diffraction pattern i is 1.1° different from the measured angle, which is twice as inaccurate as the solution for diffraction pattern ii. It is therefore more probable that the cube is magnetite (Fe_3O_4) rather than maghemite (γ-Fe_2O_3).
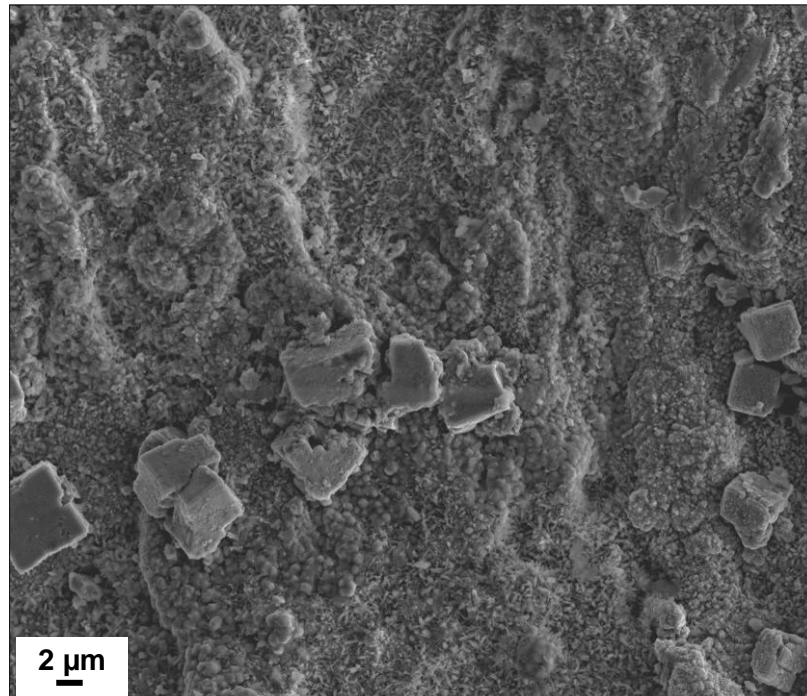
Figure 4.51: Secondary electron micrograph showing three intertwined imperfect cubes on the crack surface of specimen 799 (1061 MPa, 98.3 kh).
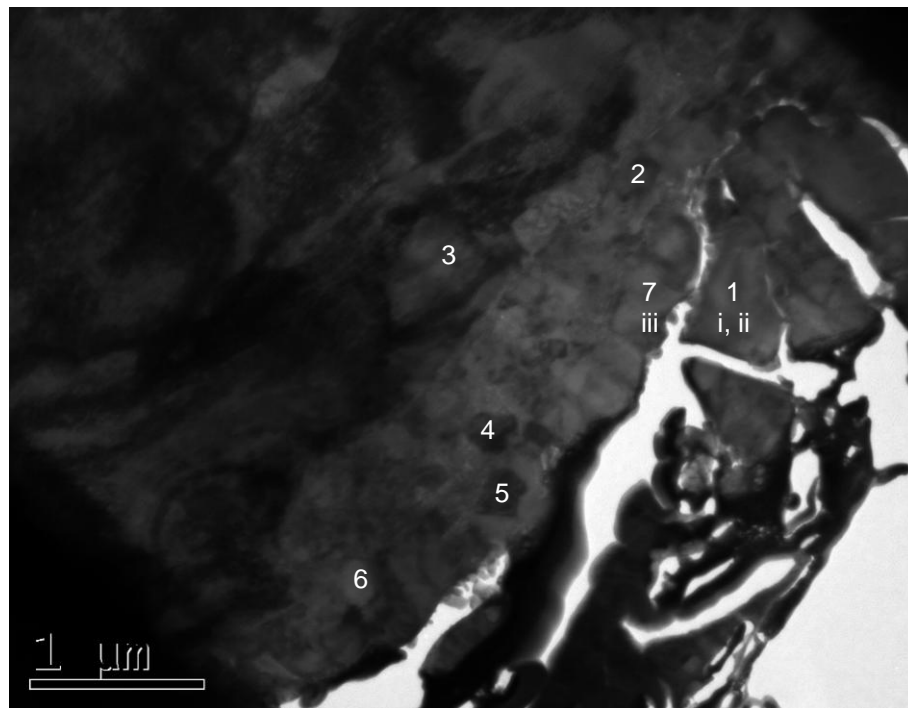
Figure 4.52: Transmission electron micrograph showing a cross-section through the three cubes on the crack surface of specimen 799 (1061 MPa, 98.3 kh) shown in Figure 4.51. The letters i-iii correspond to the selected area diffraction patterns Figure 4.53 - Figure 4.55 and the numbers 1-6 refer to the EDS data in Table 4.5.

	h	k	l	d_1	h	k	l	d_2	u	v	w	Angle
Measured				2.472				2.472				34°
γ-Fe$_2$O$_3$	1	$\bar{3}$	$\bar{1}$	2.5143	1	$\bar{3}$	1	2.5143	$\bar{3}$	$\bar{1}$	0	35.1°
Fe$_3$O$_4$	1	$\bar{3}$	$\bar{1}$	2.5315	1	$\bar{3}$	1	2.5315	$\bar{3}$	$\bar{1}$	0	35.1°
Fe$_2$O$_3$												
FeO(OH)												
Cr$_2$O$_3$												
FeO												
NiCr$_2$O$_4$	1	$\bar{3}$	$\bar{1}$	2.5074	1	$\bar{3}$	1	2.5074	$\bar{3}$	$\bar{1}$	0	35.1°
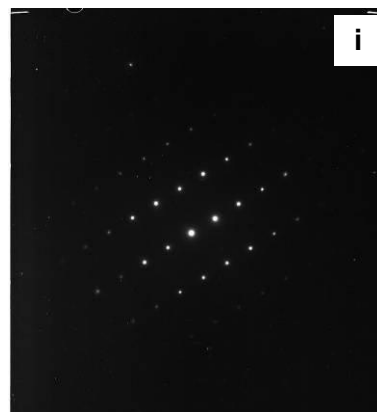
Figure 4.53: Selected area diffraction pattern collected from point i on Figure 4.52

	h	k	l	d_1	h	k	l	d_2	u	v	w	Angle
Measured				2.535				2.535				51°
γ-Fe$_2$O$_3$	1	$\bar{3}$	$\bar{1}$	2.5143	1	$\bar{1}$	3	2.5143	4	1	1	50.5°
Fe$_3$O$_4$	1	$\bar{3}$	$\bar{1}$	2.5315	1	$\bar{1}$	3	2.5312	4	1	1	50.5°
Fe$_2$O$_3$												
FeO(OH)												
Cr$_2$O$_3$												
FeO												
NiCr$_2$O$_4$	1	$\bar{3}$	$\bar{1}$	2.5074	1	-1	-3	2.5074	4	1	1	50.5°

Figure 4.54: Selected area diffraction pattern collected from point ii on Figure 4.52.

Analysis of diffraction pattern iii suggests that the grain is goethite (FeO(OH)). This may be correct, however, the solution angle is 3.1° different from the measured angle. The difference between the measured and solution d_1 values is 0.0167 Å and the difference between the measured and solution d_2 values is 0.0185 Å. Also, it is possible that the high energy beam used in TEM would evaporate any water present in goethite, which could prevent its identification. The accompanying EDS spectrum 7 shows only iron and oxygen in almost equal quantity, which is consistent with a solution of goethite.

EDS point spectrum number 3 highlights the transition between substrate and oxide. Spectrum 4 has a substantial amount of chromium in addition to iron and oxygen, which suggests the grain may be chromia (Cr$_2$O$_3$) or an iron chromium oxide. The remaining spectra are iron oxide with varying amounts of nickel.

	h	k	l	d_1	h	k	l	d_2	u	v	w	Angle
Measured				1.301				1.701				29°
γ-Fe_2O_3												
Fe_3O_4												
Fe_2O_3												
FeO(OH)	1	$\bar{3}$	$\bar{2}$	1.3177	2	$\bar{2}$	$\bar{1}$	1.7195	$\bar{1}$	$\bar{3}$	4	32.1°
Cr_2O_3												
FeO												
$NiCr_2O_4$												
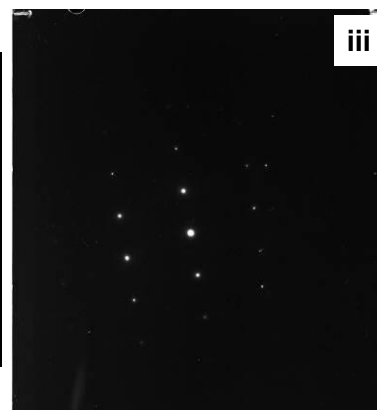
Figure 4.55: Selected area diffraction pattern collected from point iii on Figure 4.52

Table 4.5: Quantitative EDS data from points 1-7 on the site-specific cross-section through three cubes on the surface of specimen 799 (1061 MPa, 98.3 kh) shown in Figure 4.52.

Spectrum Number		Element				
		O	Cr	Mn	Fe	Ni
1	Wt%	13.4 (3.0)	1.2 (0.6)	0	81.6 (3.0)	3.7 (0.7)
	At%	35.1	1.0	0	61.2	2.6
2	Wt%	11.8 (2.7)	5.1 (0.7)	1.2 (0.7)	69.2 (2.4)	12.8 (0.9)
	At%	31.8	4.2	0.9	53.6	9.4
3	Wt%	1.3 (2.0)	15.8 (0.8)	0.5 (0.6)	77.1 (1.8)	5.4 (0.6)
	At%	4.3	16.3	0.5	74.0	4.9
4	Wt%	8.2 (2.5)	22.1 (1.0)	1.2 (0.7)	64.3 (2.0)	4.1 (0.6)
	At%	23.5	19.5	1.0	52.8	3.2
5	Wt%	10.7 (2.8)	0.4 (0.4)	0.5 (0.6)	73.0 (2.5)	15.4 (0.9)
	At%	29.7	0.4	0.4	58.0	11.6
6	Wt%	11.0 (3.1)	1.8 (0.6)	1.3 (0.6)	77.0 (2.8)	8.9 (0.8)
	At%	30.2	1.5	1.1	60.6	6.7
7	Wt%	21.2 (3.7)	0.4 (0.6)	0	78.2 (3.8)	0.3 (0.6)
	At%	48.5	0.3	0	51.1	0.2

4.8. Synchrotron Analysis of Oxides

XANES, EXAFS and µXRD data were collected from four samples using the Diamond Light Source synchrotron. Analysis of XANES data are detailed in Section 4.8.1. Results from µXRD were insufficient to analyse, which is shown in Section 4.8.2. Analysis of EXAFS data is part of the further work section of this thesis.

4.8.1. X-ray Absorption Near Edge Structure

XANES data were collected around the iron, chromium and nickel absorption energy edges from the crack surface of specimen 799 (1061 MPa, 98.3 kh) and for three site

specific cross-section samples; two from specimen 799 (1061 MPa, 98.3 kh) and one from specimen 801 (1061 MPa, 9.8 kh). The spectra were analysed using the linear fitting method described in Section 3.11 and the results are reported in tables in this section. The x, y coordinates are I18 beamline stage positions relative to 0, 0.

In several instances spectra were collected around the iron, chromium and nickel absorption edges for the same coordinates (on the same sample). It is important to understand the basic principles of the technique explained in Section 3.11. Solutions for spectra at the same coordinates that were collected around the specific absorption energies of different elements cannot be directly compared to each other. The iron absorption edge is 7112 eV and the chromium absorption edge is 5989 eV so it is not possible to excite both iron and chromium atoms at the same time. It is therefore inappropriate to directly compare the percentages of iron oxides and chromium oxides in two spectra that were collected at the same coordinates. However, it is possible to qualitatively compare the results for the spectra at the same coordinates. It is also important to note that the percentages of oxides reported to be present are not absolute values but give an indication of the ratio of oxides.

Linear fitting analysis of the crack surface of specimen 799 (1061 MPa, 98.3 kh) showed no matches for any combinations of iron oxide reference samples of magnetite (Fe_3O_4), hematite (Fe_2O_3), maghemite (γ-Fe_2O_3), goethite ($FeO(OH)$) and amorphous iron oxide. Analysis of the chromium absorption edge XANES spectra collected from the crack surface of specimen 799 (1061 MPa, 98.3 kh) is displayed in Table 4.6. The unidentified spectra were compared to spectra from a chromium foil and reference samples of chromia (Cr_2O_3), chromite (Cr_2O_4) and nickel chromium oxide ($NiCr_2O_4$). Spectra 1-3 were collected in a line from the crack initiation towards the tip of the fatigue pre-crack region. Spectra 4-7 were collected in a line parallel to the crack propagation direction from the portion of crack that grew during exposure to condensing steam. The results of the fatigue pre-crack region show matches for chromia (Cr_2O_3). Analysis of the spectra from the stress corrosion crack also show matches for chromia (Cr_2O_3) but with traces of nickel chromium oxide ($NiCr_2O_4$) in the second best solutions. As an example of the linear fitting, Figure 4.56 shows spectrum 5 with the fitted curve overlaid. The remaining spectra are presented in Appendix 1.

Table 4.6: Linear fitting analysis for XANES data collected around the chromium absorption edge from the crack surface of specimen 799 (1061 MPa, 98.3 kh). Where multiple results are shown they are in order of the best match. Figures in brackets are the percentage error in the results.

Spectrum Number	Coordinates x, y	Percentage of Reference Spectra Fitted to Unknown Spectra			
		Chromium (Cr)	Chromia (Cr_2O_3)	Chromite (Cr_2O_4)	Nickel chromium oxide ($NiCr_2O_4$)
1	x: 0.05 y: 12.35	92.4 (1.3)	7.3 (2.9)		
2	x: 0.05 y: 7.45	83.1 (1.5)	17.7 (1.5)		
3	x: 0.05 y: 3.3	70.8 (1.8) 72.6 (1.3)	34.1 (1.8) 27.4 (1.3)		
4	x: 2.551 y: -7.1	95.9 (1.6)	5.3 (1.6)		
5	x: 2.551 y: -5.05	90.5 90.6 (1.3)	10.7 4.9 (2)		4.5 (2.4)
6	x: 2.551 y: -2.65	86.7 (1.2)	13.9 (1.2)		
7	x: 2.551 y: 1.2	74.8 (1.2) 75.4 (1.2)	26.9 (1.2) 16.2 (2)		8.4 (2.3)
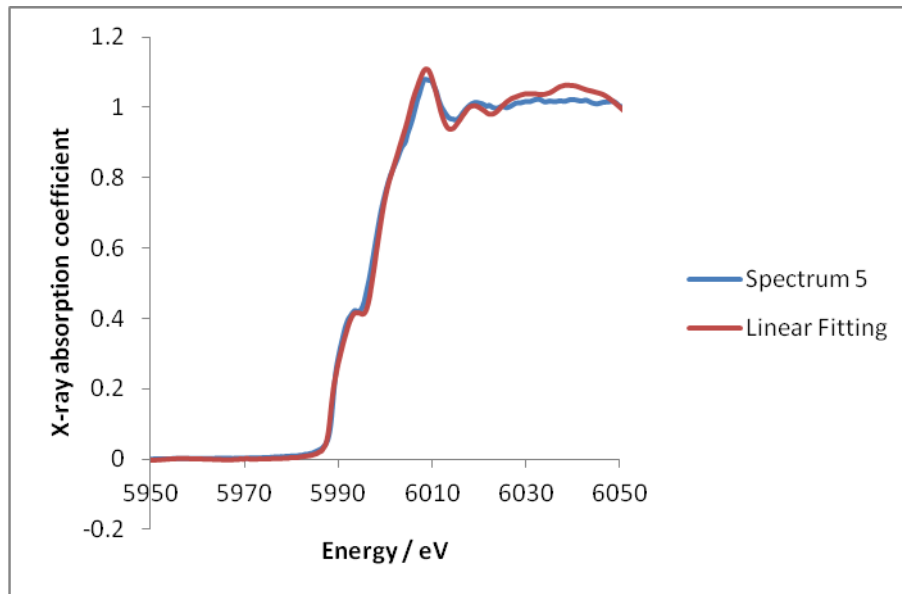
Figure 4.56: Linear fitting analysis of spectrum 5, collected around the chromium absorption edge from the crack surface of specimen 799 (1061 MPa, 98.3 kh).

One of the site-specific samples was a cross-section lifted from a region of the crack surface of specimen 799 (1061 MPa, 98.3 kh) where the oxide morphology presented as three intertwined cubes. The TEM analysis in Section 4.7 showed that the large single crystal features were possibly iron-nickel oxide sitting in a layer of small grained, possibly iron-chromium oxide. It was assumed that the same would be true for the sample through three oxide cubes, so XANES spectra were collected accordingly.

Figure 4.57 shows a schematic representation of the coordinates at which XANES spectra were collected. The red dashed line represents the data collected around the iron absorption edge and the blue dotted line represents the data collected around the chromium absorption edge.
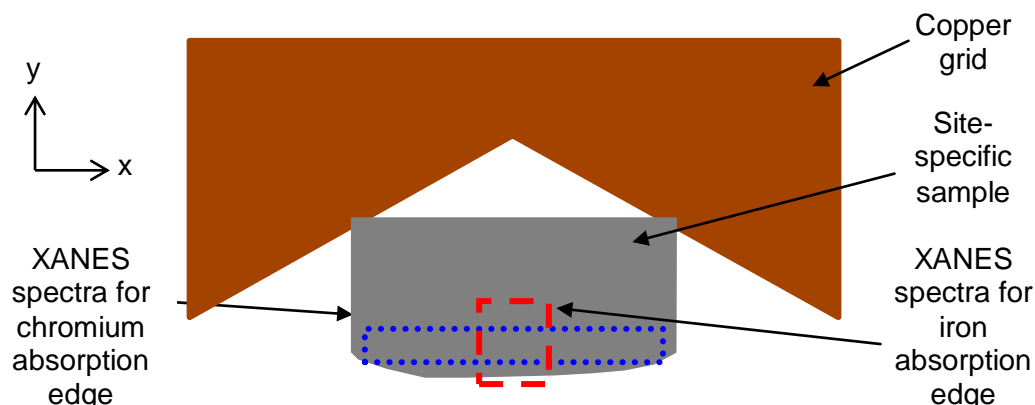

Figure 4.57: Schematic representation of the XANES spectra collected from a site-specific cross-section sample of three oxide cubes from the surface of specimen 799 (1061 MPa, 98.3 kh). The red dashed line represents the coordinates shown in Table 4.7 for the XANES spectra collected around the iron absorption edge. The blue dotted line represents the coordinates shown in Table 4.8 for the XANES spectra collected around the chromium absorption edge.

Analysis of the XANES spectra are displayed in Table 4.7 for energies around the iron absorption edge. The results show up to 34.9 ± 0.9% maghemite (γ-Fe_2O_3) present in the best solution for all the spectra except number 1 where it is in the second best solution. Spectra 1-4 and 7 show varying amounts of magnetite (Fe_3O_4) present up to 23.5% in the best fitting solutions and up to 25% in the second best solution for spectrum 2. Spectrum 1 shows 2.5% hematite present in the third best fitting solution and there is 4% hematite in the second best solution for spectrum 6. The third best solution for spectrum 2 shows 12.8% goethite. From these results it is most probable that the spectra match to iron, maghemite (γ-Fe_2O_3) and magnetite (Fe_3O_4). The presence of hematite (Fe_2O_3) and goethite ($FeO(OH)$) is inconclusive.   Figure 4.58 shows spectrum 3 with the fitted curve overlaid. The remaining spectra are presented in Appendix 1.

Table 4.7: Linear fitting analysis for XANES data collected around the iron absorption edge from a site-specific sample produced from specimen 799 (1061 MPa, 98.3 kh). The sample was a cross section through three cubes on the crack surface. Where multiple results are shown they are in order of the best match. Figures in brackets are the percentage error in the results.

Spectrum Number	Coordinates x, y	Percentage of Reference Spectra Fitted to Unknown Spectra					
		Iron (Fe)	Magnetite (Fe_3O_4)	Hematite (Fe_2O_3)	Goethite (FeO(OH))	Maghemite (γ-Fe_2O_3)	Amorphous Iron Oxide
1	x: 2.248 y: 11.909	94-96 96.5 97.5	3.5	2.5		3.5	
2	x: 2.24 y: 11.909	74.9 75 78.1	23.5 25 9.1		12.8	1.6	
3	x: 2.24 y: 11.917	64.6 (0.9) 65.1 (0.9)	12.6 (3.4)			22.8 (3.5) 34.9 (0.9)	
4	x: 2.236 y: 11.917	81.9 82	1.5			16.6 18	
5	x: 2.232 y: 11.917	87 (1.2)				13 (1.2)	
6	x: 2.228 y: 11.929	94.4 (1.1) 96		4		5.6 (1.1)	
7	x: -2.73 y: 13.635	78.6 (2.1) 79.8 (2.3)	10.6 (7) 16.8 (6.7)			10.8 (7.4)	
8	x: -2.73 y: 13.64	84.2				15.8	
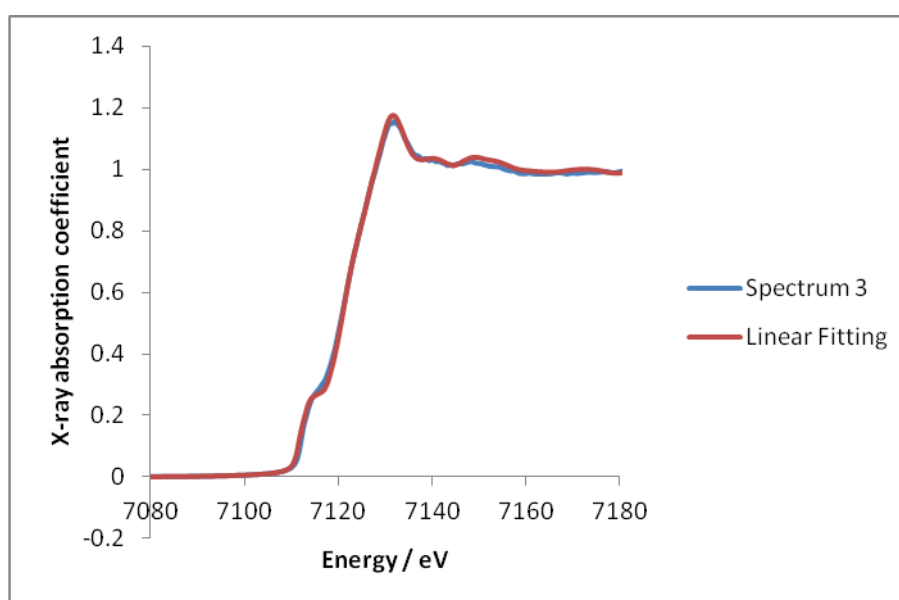
Figure 4.58: Linear fitting analysis of spectrum 3, collected around the iron absorption edge from a site-specific cross-section through three oxide cubes on the crack surface of specimen 799 (1061 MPa, 98.3 kh).

Analysis of the XANES spectra for energies around the chromium absorption edge is shown in Table 4.8. The results show up to 27.9 ± 0.9% chromia (Cr_2O_3) present in the best solution for all the spectra and 28 ± 2.9% in the second best solution for spectrum 11. Spectra 13 and 15 show 3.7 ± 2.5% and 3.8 ± 2.6% chromite (Cr_2O_4) respectively in the best solutions and up to 17.9 ± 2.4% in the second or third best solutions for spectra 2, 4, 5, 7-9, 11-13 and 15-17. There is up to 32.5 ± 2.8% nickel chromium oxide ($NiCr_2O_4$) in the best solutions for spectra 4, 5, 9, 11, 18 and 19. The second and third best solutions for spectra 2, 5, 8-10 and 12 have up to 5.3 ± 1.6% nickel chromium oxide ($NiCr_2O_4$). If all the spectra are considered together these results suggest that the small grained oxide consists of chromia (Cr_2O_3) mixed with some chromite (Cr_2O_4) and nickel chromium oxide ($NiCr_2O_4$).

Figure 4.59 shows spectrum 7 with the fitted curve overlaid. The remaining spectra are presented in Appendix 1.

Table 4.8: Linear fitting analysis for XANES data collected around the chromium absorption edge from a site-specific sample produced from specimen 799 (1061 MPa, 98.3 kh). The sample was a cross section through three cubes on the crack surface. Where multiple results are shown they are in order of the best match. Figures in brackets are the percentage error in the results.

Spectrum Number	Coordinates x, y	Percentage of Reference Spectra Fitted to Unknown Spectra			
		Chromium (Cr)	Chromia (Cr_2O_3)	Chromite (Cr_2O_4)	Nickel chromium oxide ($NiCr_2O_4$)
1	x: 2.244 y: 11.913	87.1 (1) 87.2 (1.3)	14 (1) 10 (2.5)		
2	x: 2.224 y: 11.917	77.8 (0.8) 78.1 (0.8) 78.5 (1.1)	23.1 (0.8) 16.6 (1.3	 17.8 (2.2)	5.3 (1.6) 3.7 (2.5)
3	x: 2.228 y: 11.917	79.1 (1.1)	22 (1.1)		
4	x: 2.232 y: 11.917	68.9 66.5 (1.3)	24.3 23.3 (2.9)	10.2 (3.2)	6.8
5	x: 2.236 y: 11.917	71.3 (1.1) 68.7 (1.2)	20.1 (1.7) 20.8 (2.7)	10.5 (3)	8.6 (2)
6	x: 2.24 y: 11.917	85.9 (1.1)	15.5 (1.1)		
7	x: 2.244 y: 11.917	89 (1.1) 89.1 (1.3)	9.2 (1.7)	10.1 (2.5)	
8	x: 2.248 y: 11.917	90.6 (1.1) 91 (1.3)	10.7 (1.1)	5.5 (2.6)	3.5 (2.9)
9	x: 2.224 y: 11.921	77 (0.9) 76.2 (1) 77.3 (1.2)	16.7 (1.5) 23.8 (1)	 17.9 (2.4)	6.3 (1.7) 4.8 (2.7)
10	x: 2.228 y: 11.921	76 (1.3) 76.5 (1.1)	16.9 (2.5) 18.3 (1.7)		5.2 (2)
11	x: 2.232 y: 11.921	65.6 (1.2) 63.5 (1.3)	27.9 (1.9) 28 (2.9)	8.5 (3.2)	6.5 (2.2)
12	x: 2.236 y: 11.921	75.2 (1.2) 76.4 (1.2)	18 (2.6) 19.8 (1.9)	7.9 (2.7)	3.8 (2.2)
13	x: 2.24 y: 11.921	84.6 (1.1)	12.9 (2.4)	3.7 (2.5)	
14	x: 2.244 y: 11.921	88.2 (1.1)	12.9 (1.1)		
15	x: 2.248 y: 11.921	88.2 (1.2) 87.8 (1.2)	8.7 (2.5) 7.5 (2.6)	3.8 (2.6) 4.7 (2.8)	
16	x: 2.2441 y: 11.917	88.5 (1.1) 87.4 (1.2)	12.3 (1.1) 7.3 (2.5)	5.3 (2.8)	
17	x: 2.24 y: 11.917	84.8 (1) 83.6 (1.1)	15.9 (1) 9.8 (2.4)	6.6 (2.6)	
18	x: 2.236 y: 11.917	70.2 (0.9)	16.1 (1.4)		13.7 (1.7)
19	x: 2.232 y: 11.917	58.6 (1.5)	8.9 (2.4)		32.5 (2.8)
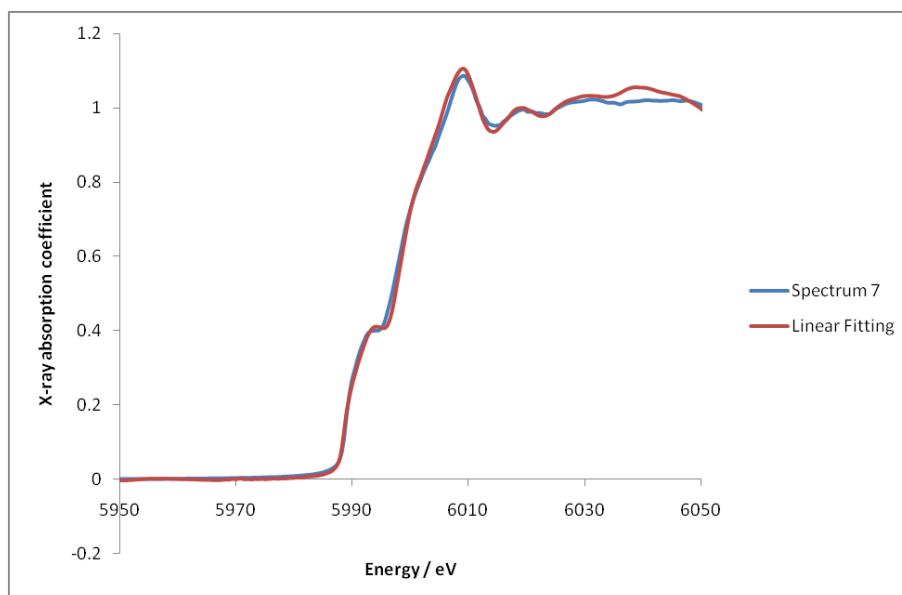
Figure 4.59: Linear fitting analysis of spectrum 7, collected around the chromium absorption edge from a site-specific cross-section through three oxide cubes on the crack surface of specimen 799 (1061 MPa, 98.3 kh).

A site specific sample was taken from a line of oxide on the surface of specimen 799 (1061 MPa, 98.3 kh) that had a mixed morphology. XANES spectra around the iron and chromium absorption edges were taken for the same coordinates covering a rectangle of the sample. The analysis of the spectra collected around the iron absorption edge is shown in Table 4.9 and the spectra collected around the chromium absorption edge are shown in Table 4.10. Figure 4.60 and Figure 4.61 show spectrum 1 with the fitted curve overlaid for the iron absorption edge and chromium absorption edge respectively. The remaining spectra are presented in Appendix 1. The results from Table 4.9 show up to $32.8 \pm 4.7\%$ magnetite (Fe_3O_4) in the best solutions for spectra 2-4 and $4.8 \pm 1.1\%$ in the second best solution for spectrum 1. There is up to $12.2 \pm 4.9\%$ hematite (Fe_2O_3) in the best solutions for spectra 1, 3 and 4 but none in spectrum 2. No goethite (FeO(OH)) is present in any spectra and maghemite (γ-Fe_2O_3) is only present in spectrum 2 at $11.6 \pm 2.6\%$ or 13.1 ± 2.4. Amorphous iron oxide is present up to 9.6% but only in the second or third best solutions. Chromia (Cr_2O_3) is present in the best solutions for all the spectra in Table 4.10 up to $21.8 \pm 2.8\%$ and up to $25.6 \pm 1.2\%$ in the second best solutions. Chromite (Cr_2O_4) is present at $4.3 \pm 2.9\%$ in the best solution for spectrum 3 and up to $9.9 \pm 4.4\%$ in the second best solutions for spectra 2 and 4. There is no chromite (Cr_2O_4) present in any solution for spectrum 1. Nickel chromium oxide ($NiCr_2O_4$) is present up to $7.5 \pm 3.1\%$ in the best solutions for spectra 2 and 4 but there is none present in spectra 1 and 3.

A qualitative comparison of the results for spectra collected at the same coordinates reveals that spectrum 1 is probably mainly substrate as the iron and chromium percentages are both over 90%. There is possibly a little chromia (Cr_2O_3) and hematite (Fe_2O_3) present. Spectrum 2 is probably a mixture of chomia (Cr_2O_3) and maghemite (γ-Fe_2O_3) with traces of nickel chromium oxide ($NiCr_2O_4$) and magnetite (Fe_3O_4). Spectrum 3 is probably magnetite (Fe_3O_4) and chromia (Cr_2O_3) with some hematite (Fe_2O_3) and chromite (Cr_2O_4). Spectrum 4 is probably magnetite (Fe_3O_4) and chromia (Cr_2O_3) with some hematite (Fe_2O_3) and nickel chromium oxide ($NiCr_2O_4$).

Table 4.9: Linear fitting analysis for XANES data collected around the iron absorption edge from a site-specific sample produced from specimen 799 (1061 MPa, 98.3 kh). The sample was a cross-section through a line of oxide on the crack surface with mixed morphology. Where multiple results are shown they are in order of the best match. Figures in brackets are the percentage error in the results.

Spectrum Number	Coordinates x,y	Percentage of Reference Spectra Fitted to Unknown Spectra					
		Iron (Fe)	Magnetite (Fe_3O_4)	Hematite (Fe_2O_3)	Goethite (FeO(OH))	Maghemite (γ-Fe_2O_3)	Amorphous Iron Oxide
1	x: 1.684 y: 3.4	96.1 95.1 (1.1) 96.4 (0.8)	4.8 (1.1)	3.9			3.6 (0.8)
2	x: 1.684 y: 3.402	84.4 (1) 85.5 (0.7)	4 (2.4)			11.6 (2.6) 13.1 (2.4)	
3	x: 1.684 y: 3.404	61.9 (0.9) 61	27 (2.7) 29	9.3 (4.8)			9.6
4	x: 1.684 y: 3.406	55 (1.5) 53.8 (1.4)	32.8 (4.7) 38.1 (4.4)	12.2 (4.9)			8.1 (4.6)

Table 4.10: Linear fitting analysis for XANES data collected around the chromium absorption edge from a site-specific sample produced from specimen 799 (1061 MPa, 98.3 kh). The sample was a cross-section through a line of oxide on the crack surface with mixed morphology. Where multiple results are shown they are in order of the best match. Figures in brackets are the percentage error in the results.

Spectrum Number	Coordinates x, y	Percentage of Reference Spectra Fitted to Unknown Spectra			
		Chromium (Cr)	Chromia (Cr_2O_3)	Chromite (Cr_2O_4)	Nickel chromium oxide ($NiCr_2O_4$)
1	x: 1.684 y: 3.4	93.9 (1.2)	7.4 (1.2)		
2	x: 1.684 y: 3.402	72 (1.7) 69.4 (1.8)	20.6 (2.7) 20.7 (4)	9.9 (4.4)	7.5 (3.1)
3	x: 1.684 y: 3.404	74.5 (1.3) 75.2 (1.2)	21.8 (2.8) 25.6 (1.2)	4.3 (2.9)	
4	x: 1.684 y: 3.406	73.3 (1.2) 71.8 (1.3)	21.6 (1.9) 22.7 (2.8)	5.5 (3.1)	5.1 (2.2)
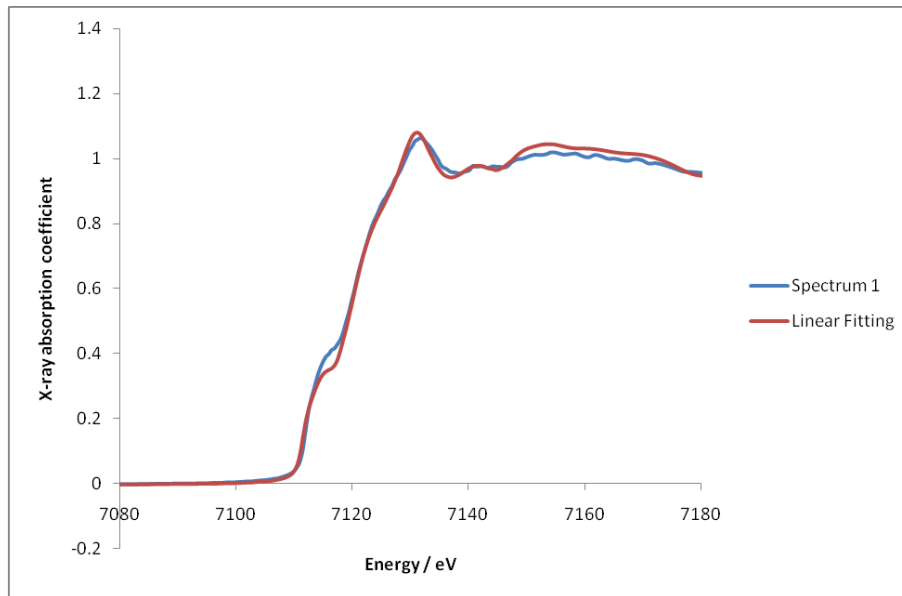
Figure 4.60: Linear fitting analysis of spectrum 1, collected around the iron absorption edge from a site-specific cross-section through a line of oxide with mixed morphology on the crack surface of specimen 799 (1061 MPa, 98.3 kh).
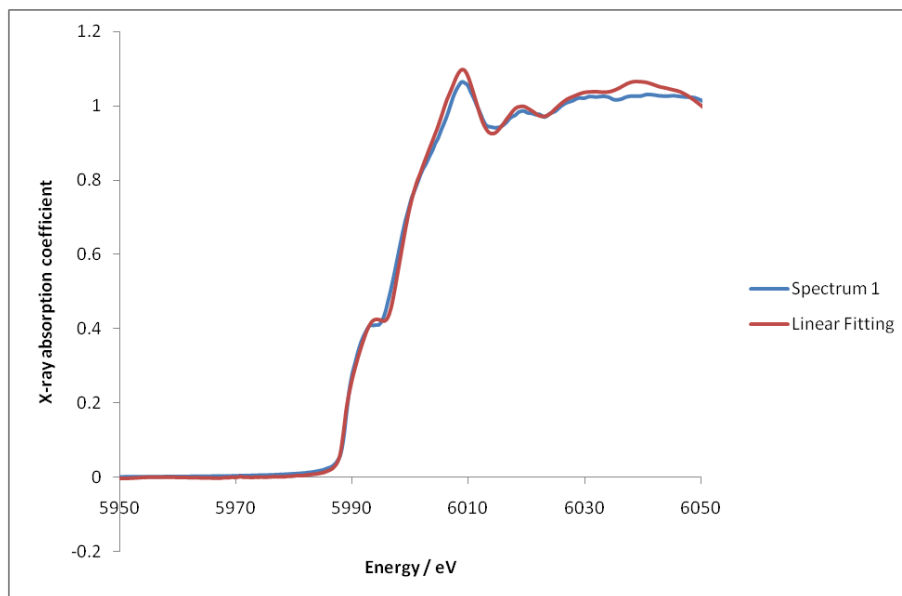
Figure 4.61: Linear fitting analysis of spectrum 1, collected around the chromium absorption edge from a site-specific cross-section through a line of oxide with mixed morphology on the crack surface of specimen 799 (1061 MPa, 98.3 kh).

Linear fitting analysis of the spectra collected around the nickel absorption edge could not be fitted with any of the reference spectra currently available. The spectra for the site-specific sample taken from specimen 801 (1061 MPa, 9.8 kh) collected around the iron, chromium and nickel absorption edges could not be fitted to any of the reference data currently available.

128

The results of the site specific samples from specimen 799 (1061 MPa, 98.3 kh) show matches for both iron oxides and chromium oxides whereas analysis of the spectra from the bulk crack surface sample showed only matches with chromium oxides. At first glance this may seem like an odd result, however, it is consistent with the SEM and XRD results shown in earlier Sections 4.4 and 4.6.

Large oxide features were only present in select locations throughout the crack surface of specimen 799 (1061 MPa, 98.3 kh) but the entire crack surface was covered with a thin layer of oxide with morphologies shown in Figure 4.20 and Figure 4.21. This layer of oxide is the small-grained oxide seen in the site-specific cross-section samples. EDS analysis of the small-grained oxide in the TEM showed it was rich in chromium and the larger features consisted of iron-rich oxide. This result has been supported by the XANES spectra analysis.

The XRD results for the entire surface of specimen 799 (1061 MPa, 98.3 kh) showed peaks matching magnetite (Fe_2O_3), hematite (Fe_2O_3) and goethite ($FeO(OH)$). In Section 4.6 it was explained that it is not possible to distinguish between atoms of similar size using XRD, so the results of magnetite (Fe_3O_4), hematite (Fe_2O_3) and goethite ($FeO(OH)$) were more accurately described as M_3O_4, M_2O_3 and $MO(OH)$ where M represents any combination of iron, chromium and nickel. The XANES results from the crack surface of specimen 799 (1061 MPa, 98.3 kh) showed that the thin layer of oxide is mainly chromia (Cr_2O_3), which suggests that the XRD results for M_2O_3 are probably Cr_2O_3.

4.8.2. µX-ray Diffraction

µXRD data were collected from two site specific samples, one from a line of oxide with mixed morphology on the crack surface of specimen 799 (1061 MPa, 98.3 kh) and one through oxide on the crack surface of specimen 801 (1061 MPa, 9.8 kh). Figure 4.62 and Figure 4.63 show patterns that are representative of the majority of results collected from specimen 799 (1061 MPa, 98.3 kh) and specimen 801 (1061 MPa, 9.8 kh) respectively. Successful results would present as ring patterns that can be converted into patterns similar to those seen in Section 4.6, however these results have insufficient signal for analysis. In all images there are several spots forming part of a ring, which suggests that the data may be from a single crystal.
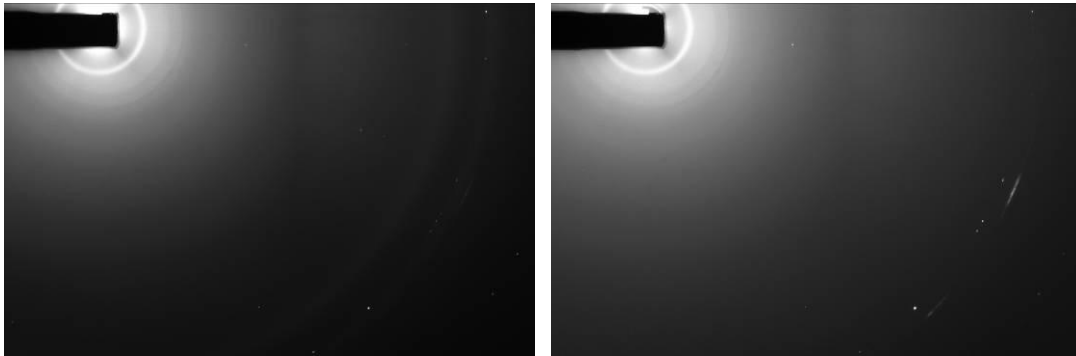
Figure 4.62: µXRD spot patterns from a site specific sample through a line of oxide with mixed morphology on the surface of specimen 799 (1061 MPa, 98.3 kh).
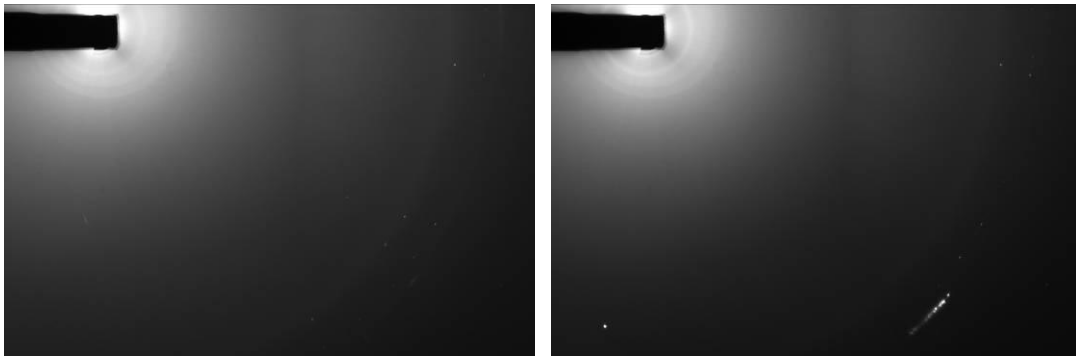
Figure 4.63: µXRD spot patterns from a site specific sample through oxide on the surface of specimen 801 (1061 MPa, 9.8 kh).

4.9. Crack Dating

The information collected from examining the WOL specimens was used to devise a method of estimating the age of a stress corrosion crack. It has already been shown in Section 4.3 that crack length is a good indication of the relative exposure time but only if initial stress intensity at the notch tip is considered. If the proof strength of the steel and the initial stress intensity was the same (above K_{ISCC}) value for two specimens exposed for different times, then it is likely that the resulting crack length would be longer in the specimen exposed for the longer time. In a real industrial situation, two components may be exposed for the same time, but the initial stress intensity would be different. In this instance a crack is likely to initiate earlier in the component that experienced the higher initial stress intensity and the resulting crack would be longer in this component for the same exposure time.

4.9.1. Crack Branching

When the specimens were examined in cross-section it was seen that there were cracks in the substrate that had branched from the main stress corrosion crack. Attempts were made to correlate the penetration depth of the cracks branching into the

substrate with position along the length of the main crack. It was hoped that the position along the crack length could then be linked with the relative exposure time.

For all the specimens it was assumed that the crack tip of the main stress corrosion crack had been exposed for approximately 0 h at the end of the experiment and that the crack opening had been exposed for the whole experiment time. The penetration depth of the crack branching from the main crack was therefore measured relative to the distance away from the crack tip (towards the crack opening). Specimens measured were 799 (1061 MPa, 98.3 kh), 800 (1061 MPa, 13.0 kh) and 802 (1061 MPa, 7.5 kh). The resulting plot of crack branching penetration depth versus exposure time is shown in Figure 4.64.
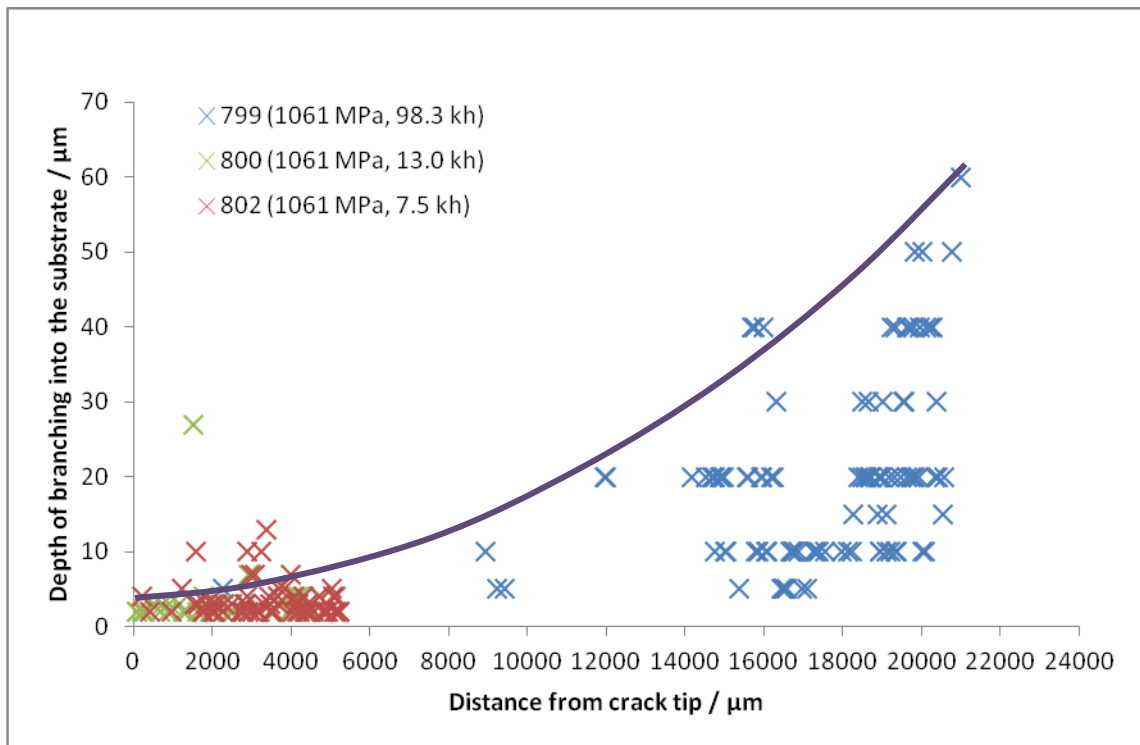
Figure 4.64: Penetration depth of crack branching into the substrate versus the distance along the main crack from the crack tip for specimens 799 (1061 MPa, 98.3 kh), 800 (1061 MPa, 13.0 kh) and 802 (1061 MPa, 7.5 kh)

For specimen 799 (1061 MPa, 98.3 kh) the results show a trend in the penetration depth of branching cracks relative to the position along the main stress corrosion crack. Although there are many shallower branching cracks near the crack tip, the deepest penetrating cracks are closest to the crack initiation and the penetration depth increases with distance away from the crack tip of the main stress corrosion crack. Also, the number of cracks in the substrate increases with distance away from the

131

crack tip of the main stress corrosion crack. Close to the crack tip of specimen 799 (1061 MPa, 98.3 kh) there are few cracks in the substrate. The results for specimen 800 (1061 MPa, 13.0 kh) and 802 (1061 MPa, 7.5 kh) show a lot of short cracks penetrating the substrate.

There is a definite trend in the results for specimen 799 (1061 MPa, 98.3 kh). Figure 4.64 shows that crack branching penetration depth increases with distance away from the crack tip along the main stress corrosion crack. A solid curved line has been overlaid onto the graph in Figure 4.64. The line was not based upon any mathematical formula, but was merely to highlight the trend in the length of the cracks penetrating the substrate. For specimen 799 (1061 MPa, 98.3 kh), the lengths of the majority of the cracks fall along or below the line.

The results from specimens 800 (1024 MPa, 13.0 kh) and 802 (1061 MPa, 7.5 kh) are inconclusive. While the majority of the branching cracks penetrate the substrate up to the same depth as those in specimen 799 (1061 MPa, 98.3 kh) for the same position along the main stress corrosion crack, there are too many that lie above the line for a definite relationship to be established. It has already been mentioned that the crack initiation time was unknown so it is probable that the assumption of linear crack growth is inaccurate. This could explain why the results for specimens 802 (1061 MPa, 7.5 kh) and 800 (1061 MPa, 13.0 kh), which were not pre-cracked do not correlate perfectly with the trend for specimen 799 (1061 MPa, 98.3 kh) that was pre-cracked.

Figure 4.65 shows the depths of the branching cracks for specimens 803 (1024 MPa, 98.3 kh), 807 (1018 MPa, 98.3 kh) and 811 (1072 MPa, 98.3 kh) with distance away from the crack tip. The depth of the cracks increases with distance away from the crack tip, similar to the results shown in Figure 4.64. The maximum and minimum depths of the brached cracks are similar to those measured for specimen 799 (1061 MPa, 98.3 kh), however, for specimens 803 (1024 MPa, 98.3 kh), 807 (1018 MPa, 98.3 kh) and 811 (1072 MPa, 98.3 kh) the main stress corrosion crack did not grow during the exposure to condensing steam so the gradient of the results is steeper.

The penetration depth of branching cracks into the substrate decreases with distance along the main crack for specimens 803 (1024 MPa, 98.3 kh), 807 (1018 MPa, 98.3 kh) and 811 (1072 MPa, 98.3 kh). The rate of decrease is greater than the results shown for specimen 799 (1061 MPa, 98.3 kh). This could be due to the inaccuracy of the

relative positions as they were based on the crack growth of specimen 799 (1061 MPa, 98.3 kh). However, the branching cracks penetrate deeper in specimens 803 (1024 MPa, 98.3 kh) and 811 (1072 MPa, 98.3 kh) than specimens 799 (1061 MPa, 98.3 kh) and 807 (1018 MPa, 98.3 kh), so this may be the reason for the steeper decrease in crack penetration depth and the relative positions may be correct. It is clear that longer exposure time results in deeper branching penetration into the substrate. Further work in this area should be carried out to determine if this could be a viable method for estimating the age of stress corrosion cracks.
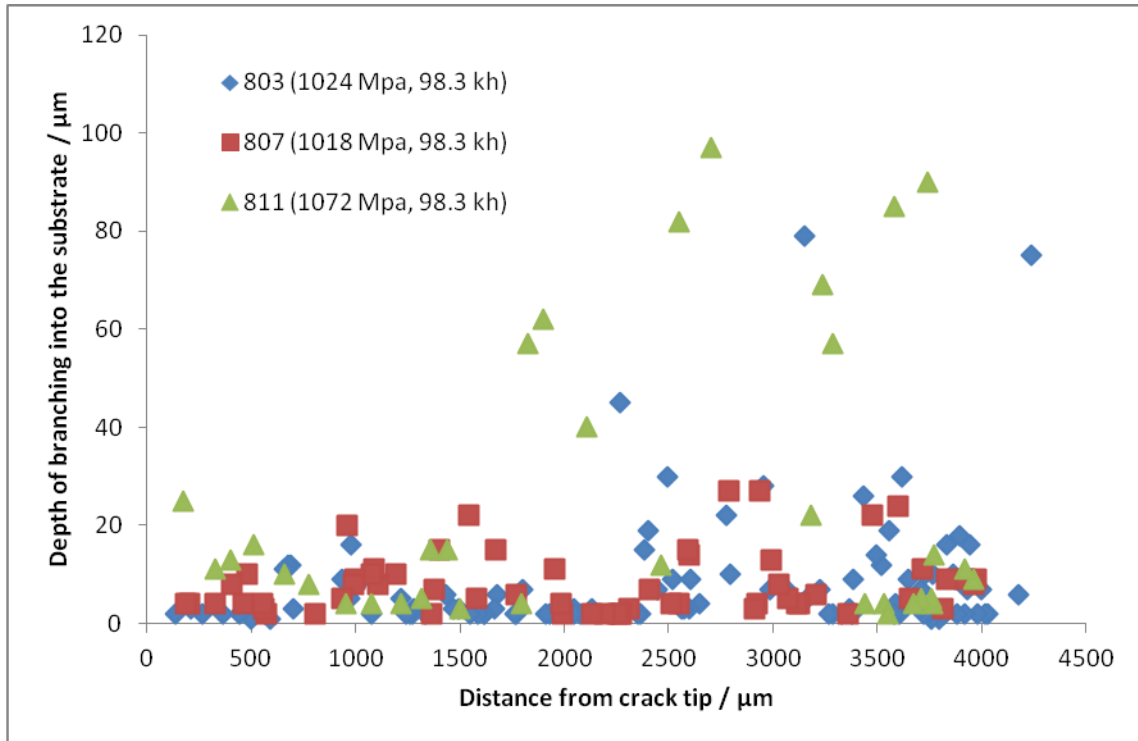
Figure 4.65: Penetration depth of crack branching into the substrate versus distance along the main crack from the crack tip for specimens 803 (1024 MPa, 98.3 kh), 807 (1018 MPa, 98.3 kh) and 811 (1072 MPa, 98.3 kh).

4.9.2. Surface Oxide Appearance

With a few exceptions, the groups of specimens within each exposure time have crack surfaces with similar appearance to each other, but look different to specimens with other exposure times. It is expected that longer exposure to condensing steam at 95°C would result in more oxide development. Visual evidence to support this theory has been shown in Section 4.4. The difference between the specimens exposed for 98.3 kh and the remaining specimens is the most dramatic, whereas distinguishing between the 13.0 kh, 9.8 kh and 7.5 kh specimens is more difficult. This is

understandable as 98.3 kh is 7.6 times 13.0 kh, 10.0 times 9.8 kh and 13.1 times 7.5 kh, whereas 13.0 kh is only 1.7 times 7.5 kh.

Evidence to support the idea that higher stress intensities promote earlier crack initiation has been shown in the crack surface oxide morphology micrographs. The specimens exposed for 9.8 kh had more oxide development than the specimens exposed for 13.0 kh but less than the specimens exposed for 98.3 kh. Generally, the specimens exposed for 13.0 kh show more oxide development than the specimens exposed for 7.5 kh.

Specimens 803 (1024 MPa, 5 MPam$^{\frac{1}{2}}$), 807 (1018 MPa, 5 MPam$^{\frac{1}{2}}$) and 811 (1072 MPa, 5 MPam$^{\frac{1}{2}}$) were fatigue pre-cracked prior to exposure to condensing steam at 95°C for 98.3 kh and showed no crack propagation during the experimental time as the stress intensity was below the threshold value for SCC. Figure 4.19 and Figure 4.27 (a) show that there is oxide present all the way to the pre-crack tip but it is more developed closer to crack initiation. As the steam entered the crack it would corrode the first metal it encountered. The oxide that developed would narrow the crack opening, reducing the flow of steam into the rest of the crack. This process would occur all the way to the crack tip, which is why the oxide is more developed at the crack initiation than at the crack tip even though there is oxide present across the pre-crack length. If the oxide near the initiation developed so much that it completely closed the crack opening, then further oxidation of the crack length would depend on diffusion of oxygen through the oxide into the crack or diffusion of metal ions through the oxide. The below threshold stress intensity would have exacerbated this effect, as the stress would be too low to propagate the crack (ASM International Handbook Committee, 1987).

SCC has three main stages: initiation, propagation and final failure (ASM International Handbook Committee, 1987). From the graph in Figure 2.21 it can be seen that the propagation stage of SCC is assumed to be linear. As specimen 799 (1061 MPa, 98.3 kh) was fatigue pre-cracked prior to exposure to condensing steam at 95°C the initiation stage was removed. During the 98.3 kh experiment specimen 799 (1061 MPa) did not experience final failure, so this stage can be ignored. It can therefore be assumed that oxidation of the crack and crack propagation was approximately linear during the exposure time. The crack initiation was effectively exposed for the full 98.3 kh whereas the crack tip was exposed for 0 h. Using this

assumption is has been possible to build up a map of oxide development with exposure time based on specimen 799 (1061 MPa, 98.3 kh).

Figure 4.66 shows a series of micrographs from the crack initiation (a) to the crack tip (d) of specimen 799 (1061 MPa, 98.3 kh). The crack tip (d) has an intergranular fracture surface with no apparent oxide; however, EDS point spectra confirmed the presence of oxide across the entire crack surface. Moving away from the crack tip (c) the surface is littered with sub-micron particles which are the first visible signs of oxide. These particles increase in size with exposure time (b) and agglomerate at particular sites. Further growth produces intertwined cubic oxide structures with smooth surfaces (a). This series of micrographs relative to crack length shows oxide development with time. The majority of the specimens exposed for 13.0 kh have similar surface appearance to Figure 4.66 (c), and the majority of the specimens exposed for 7.5 kh have similar surface appearance to Figure 4.66 (d). In the specimens that were not pre-cracked prior to the experiment the initiation times are unknown but it can be assumed that the stress corrosion cracks did not initiate the instant the specimens were exposed to condensing steam. It can be deduced that the portion of the crack surface shown in Figure 4.66 (c) has been exposed to condensing steam at 95°C for no more than 13.0 kh ($K = 16 - 32$ MPam$^{\frac{1}{2}}$) and the portion shown in Figure 4.66 (d) has been exposed for no more than 7.5 kh ($K \approx 62$ MPam$^{\frac{1}{2}}$).
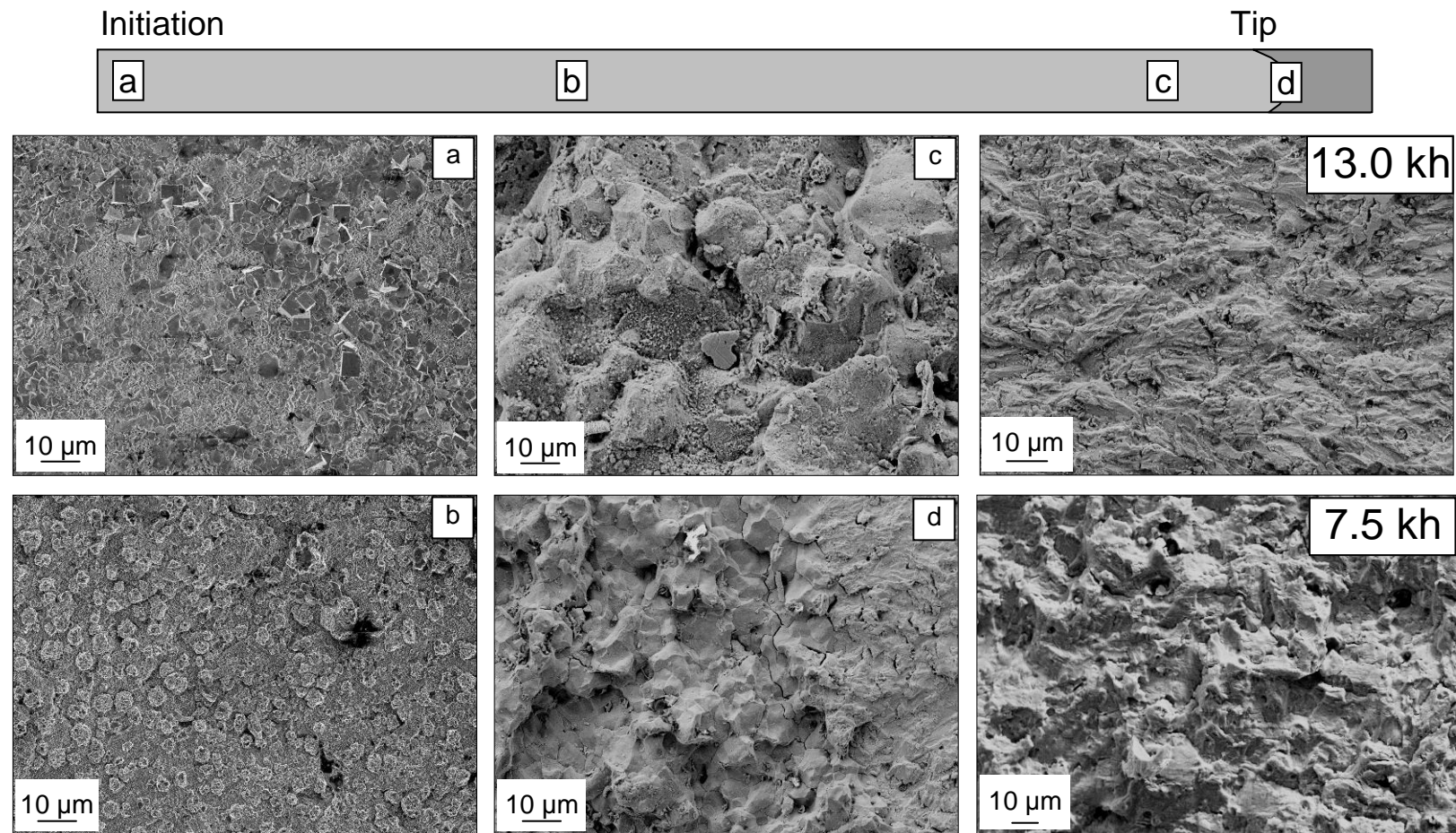
Figure 4.66: Series of secondary electron micrographs (a-d) showing oxide development with time based on linear crack growth of specimen 799 (1061 MPa, 98.3 kh). The surface and oxide morphology of positions c and d correspond to surface micrographs of specimens exposed for 13.0 kh and 7.5 kh respectively.

4.9.3. X-Ray Diffraction

The XRD data are consistent with the visual results collected from the crack surfaces of all the specimens. The strongest peaks were present in the XRD patterns for the specimens exposed for 98.3 kh. It was in these specimens that large oxide features, such as cubes, cuboctahedra and octahedrons were visible on the stress corrosion crack. It was difficult to determine any oxide peaks from the XRD patterns collected from the crack surfaces of the specimens exposed for 7.5 kh. This is consistent with SEM micrographs that show little visual evidence of oxidation. The first visible signs of oxidation were found on the crack surfaces of the specimens exposed for 13.0 kh. This is reflected in the XRD patterns as there are some peaks which can be matched to magnetite, hematite or goethite. There are oxide peaks in the XRD patterns for the specimens exposed for 9.8 kh that are bigger than those seen in the XRD patterns for the specimens exposed for 13.0 kh but smaller than those for the specimens exposed for 98.3 kh. This is also consistent with the visual oxide evidence collected from the crack surfaces of the specimens exposed for 9.8 kh.

Using XRD it is possible to distinguish between the specimens exposed for 98.3 kh and the specimens exposed for 13.0, 9.8 and 7.5 kh. It is not possible to accurately differentiate the XRD patterns from the specimens exposed for 13.0 kh and 7.5 kh, but it is possible to distinguish them from the specimens exposed for 9.8 kh. With some further work it is possible that XRD could be used as a comparative tool to identify the exposure time of a stress corrosion crack.

4.10. Summary

In this Chapter, the results from the WOL specimens provided by Alstom Power Materials have been presented and discussed. Various analysis techniques have been used, including optical and electron microscopy, EDS, X-ray diffraction and X-ray absorption near edge structure. The aim was to identify evidence which could be linked to the age of a stress corrosion crack by studying variables such as exposure time, crack length and initial stress intensity.

The results show that the depth that cracks branch into the substrate increases with longer exposure times and that the oxide development can be correlated with exposure time based on visual examination and XRD peak strength.

5. Results and Discussion: Single Edge Notched Bend

Single Edge Notched Bend (SENB) specimens were machined from a hot rolled slab of FV520B and fatigue pre-cracked as described in Section 3.2. The specimens were then stressed and exposed to condensing steam at 95°C for 0.7, 1.5, 2.9, 4.4, 5.8, 7.3 and 8.8 kh. After exposure the specimens were examined in cross section. They were then fully separated into two pieces to reveal the surfaces of the cracks. Results from the examination of these specimens are presented and discussed in this Chapter.

5.1. As-Received Specimens

Photographs of the SENB specimens after exposure to condensing steam at 95°C are shown in
Figure 5.1. The specimens have been trimmed to approximately 10 mm either side of the notch as described in Section 3.2. Various amounts of oxidation can be seen on all the specimens. Much of the external surface visible in the specimen exposed for 5.8 kh has dark brown oxidation around roughly elliptical voids. This suggests that water droplets from the condensing steam settled on the surface during the exposure time and oxidation has occurred around their edges. A dark brown coloured crack can be seen in most of the specimens, however, in some specimens the crack is masked by shadowing. The dark brown colour of the crack is due to oxidation within the crack. Prior to exposure to condensing steam the cracks were not visible in photographs at the same magnification.

8.8 kh	7.3 kh	5.8 kh	4.4 kh
2.9 kh	1.5 kh	0.7 kh	
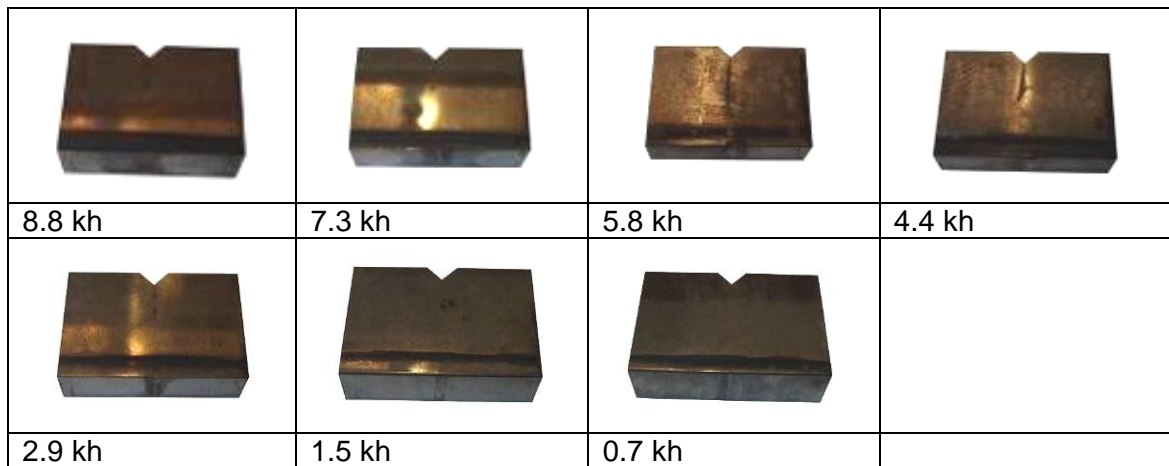
Figure 5.1: Photographs of SENB after exposure to condensing steam at 95°C for 8.8, 7.3, 5.8, 4.4, 2.9, 1.5 and 0.7 kh trimmed to approximately 10 mm either side of the crack.

5.2. Substrate Microstructure

Figure 5.2 shows the microstructure of the hot rolled slab of FV520B from which the SENB specimens were made. The microstructure is martensitic, similar to that of the FV520B from which the WOL specimens were made. All the SENB specimens were machined from the same slab of FV520B so there was no variation in yield strength, unlike the WOL specimens which were made from four batches of steel with different yield strengths.
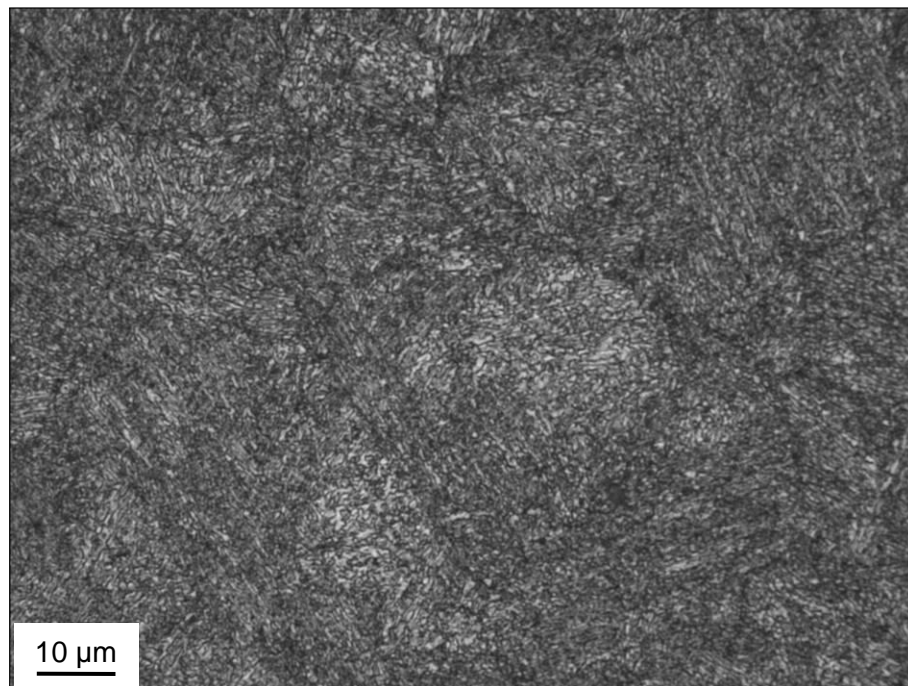
Figure 5.2: Optical micrograph showing the microstructure of the hot rolled slab of FV520B from which the SENB specimens were made.

139

5.3. Cross Section Analysis of Closed Cracks

The SENB specimens were examined using optical microscopy as described in Section 3.6. Each specimen was examined twice: first after the fatigue pre-crack was generated and then after it was stressed and exposure to condensing steam at 95°C for 0.7, 1.5, 2.9, 4.4, 5.8, 7.3 or 8.8 kh.

5.3.1. Exposure Time: 8.8 kh

Figure 5.3 shows optical micrographs of a SENB specimen (a) containing a fatigue crack and (b) after exposure to condensing steam at 95°C for 8.8 kh. There is no obvious change in the length of the crack after exposure; however, it is significantly wider, particularly over the first 500 µm from the initiation. The external surface of the specimen is discoloured which is evidence of corrosion and staining from water droplets. The area adjacent to the crack is the darkest brown, which suggests it is the most heavily corroded. There is a network of dark brown lines which emanate from the crack, which are also evidence of corrosion. The blue areas are likely to be a result of staining caused by the drying of water droplets.
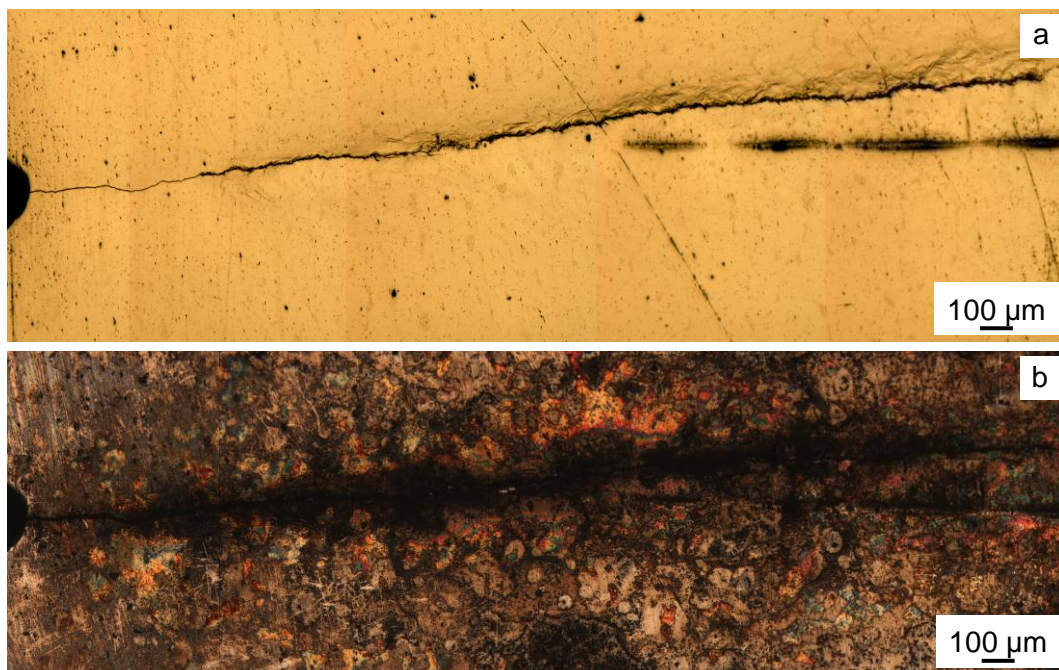
Figure 5.3: Optical micrographs showing the same specimen (a) with a fatigue pre-crack and (b) after exposure to condensing steam at 95°C for 8.8 kh.
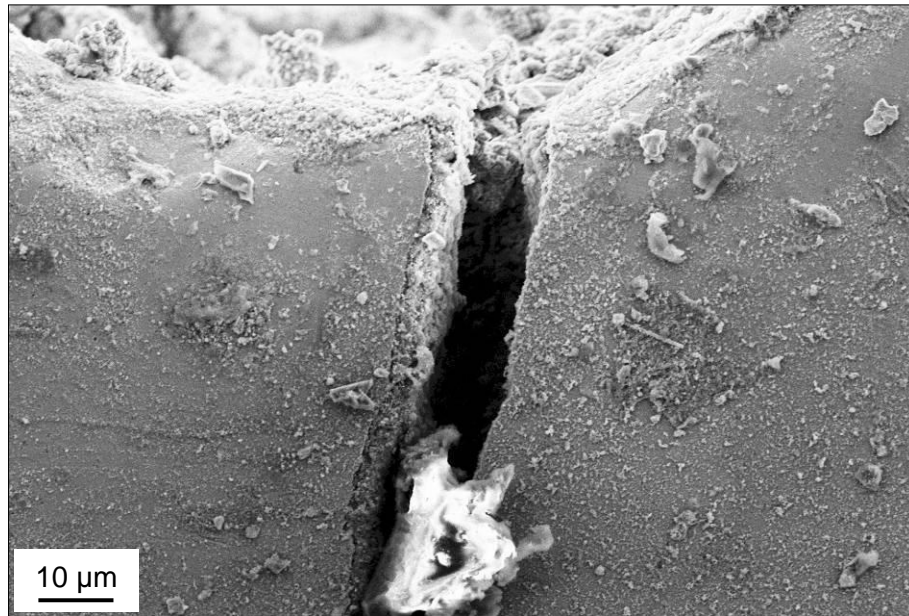
Figure 5.4: Secondary electron micrograph showing the crack initiation of a SENB specimen exposed to condensing steam at 95°C for 8.8 kh.

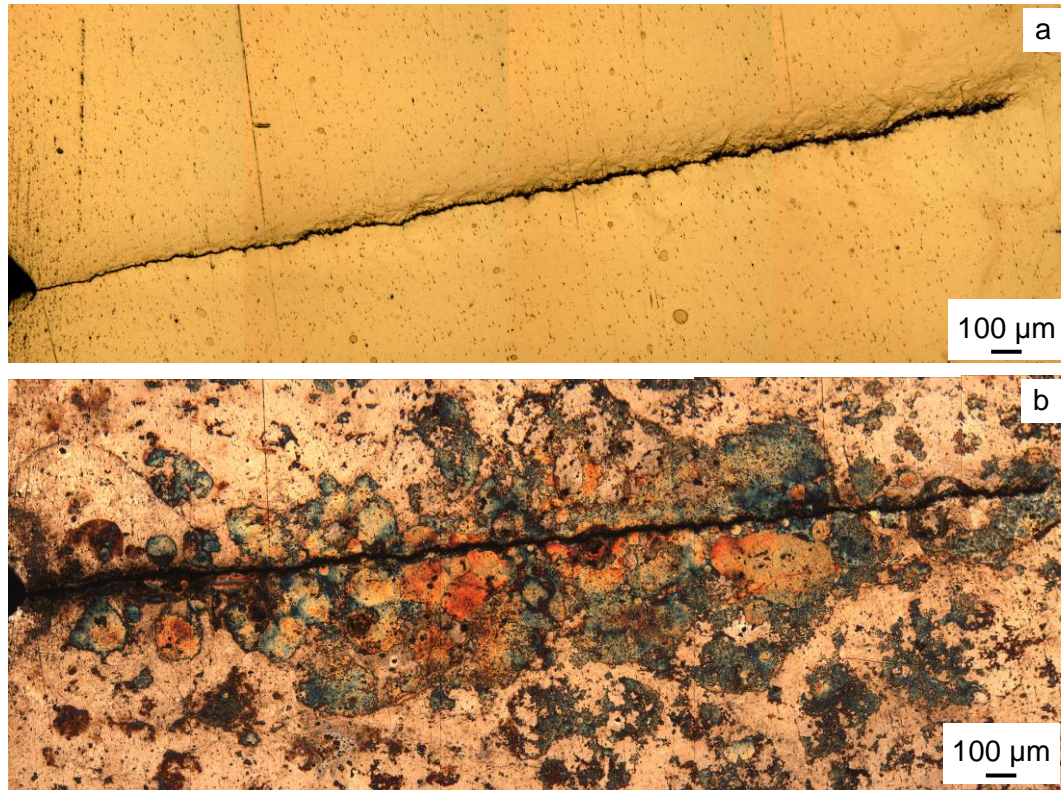Figure 5.4 shows a secondary electron micrograph of the crack initiation region of the SENB specimen exposed to condensing steam at 95°C for 8.8 kh. In the micrograph it is possible to see the notch tip and that the crack initiated slightly off-centre. The crack is approximately 10 µm wide throughout the area shown in Figure 5.4. The left-hand crack surface shown in Figure 5.4 is covered with a layer of oxide approximately 4 µm thick. It is also possible to see oxide within the open crack and particles dispersed across the external SENB surface.
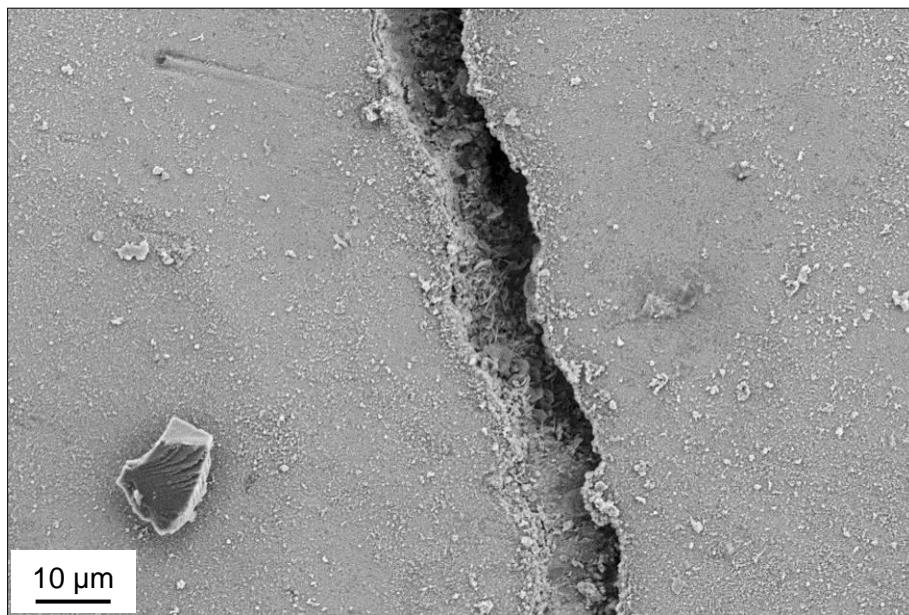
Figure 5.5: Secondary electron micrograph showing the crack through a SENB specimen exposed to condensing steam at 95°C for 8.8 kh.

Figure 5.5 shows an optical micrograph of a portion of the crack in a SENB specimen exposed to condensing steam at 95°C for approximately 8.8 kh. The edges of the crack surfaces shown in the micrograph mirror each other almost perfectly, which is evidence that they are the fatigue crack surfaces. As in Figure 5.4, oxide can be seen within the crack in Figure 5.5.
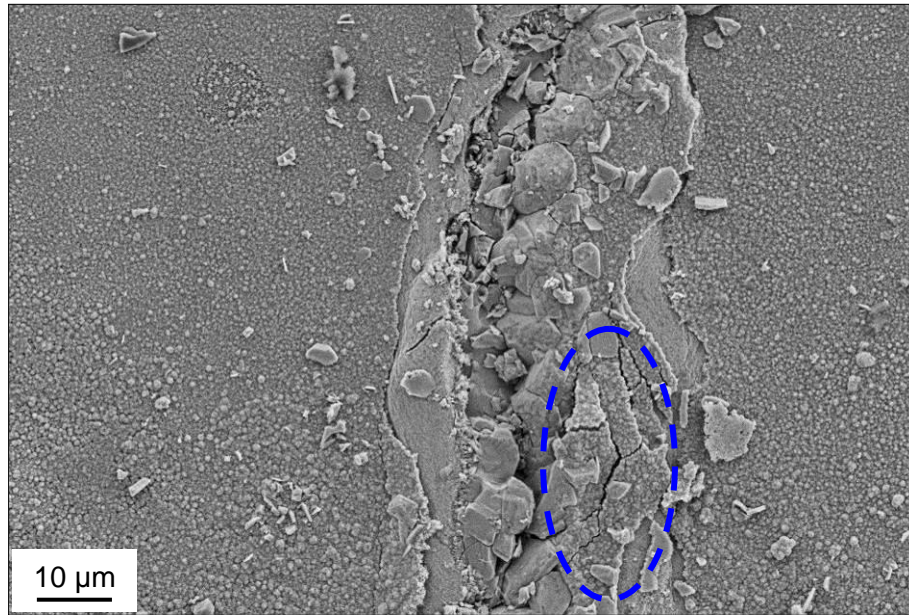
Figure 5.6: Secondary electron micrograph showing oxide in the crack through a SENB specimen exposed to condensing steam at 95°C for 8.8 kh.

Figure 5.6 shows a secondary electron micrograph of the crack through a SENB specimen exposed to condensing steam at 95°C for 8.8 kh. It is not possible to identify the original fatigue crack surfaces because the crack is filled with oxide, unlike the section of the crack shown in Figure 5.5. This is an example where the fatigue crack surfaces have corroded in the condensing steam and the crack has filled with oxide. The oxide within the crack would make further oxidation more difficult as diffusion paths would be blocked with oxide. The crack could be opened further by the stress intensity at the crack tip. The external surface is covered with oxide particles. Within the blue dashed ellipse there is evidence of spalled oxide which suggests that the oxide layer once covered the crack edge.

5.3.2. Exposure Time: 7.3 kh

Figure 5.7 (a) shows an optical micrograph of a fatigue pre-crack in a SENB specimen. Figure 5.7 (b) shows an optical micrograph of the same specimen after exposure to condensing steam at 95°C for 7.3 kh. There is no visible increase in crack length but the crack is more open. There is oxidation on the external surface of the specimen but the discolouration is significantly less than seen in Figure 5.3 (b). This is possibly

because the specimen shown in Figure 5.7 (b) was exposed to condensing steam at 95°C for 7.3 kh whereas the specimen shown in Figure 5.3 (b) was exposed for the longer time of 8.8 kh. The blue-coloured area surrounding the crack is a result of water seeping out of the crack once the specimen was removed from the experimental environment.
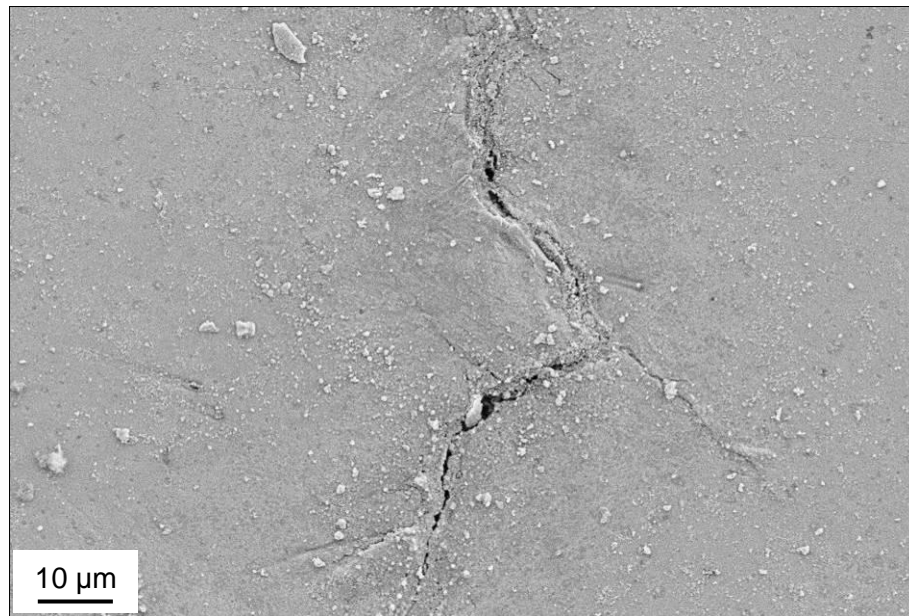

Figure 5.7: Optical micrographs showing the same specimen (a) with a fatigue pre-crack and (b) after exposure to condensing steam at 95°C for 7.3 kh.

Figure 5.8: **Secondary electron micrograph showing the crack initiation of a SENB specimen exposed to condensing steam at 95°C for 7.3 kh.**

Figure 5.8 shows a secondary electron micrograph of the crack initiation region of a SENB specimen exposed to condensing steam at 95°C for 7.3 kh. In this SENB specimen the fatigue pre-crack initiated almost centrally to the notch tip. The fatigue crack is filled with oxide and the original fatigue crack surfaces are difficult to identify due to the level of corrosion. There is a crack running through the oxide in the same direction as the original pre-crack, which would provide a path for steam to travel down and for corrosion to occur further along the crack.
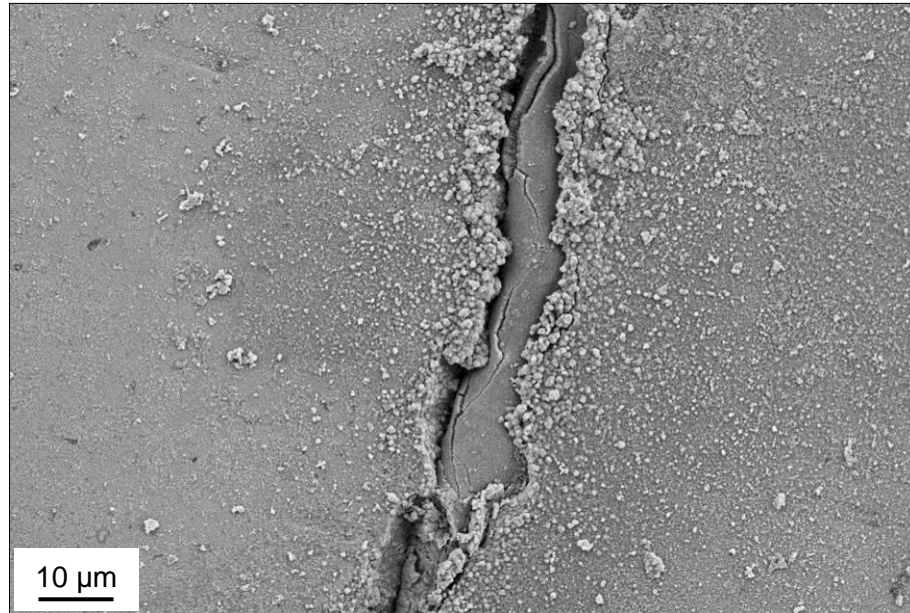
Figure 5.9: Secondary electron micrograph showing the crack through a SENB specimen exposed to condensing steam at 95°C for 7.3 kh.
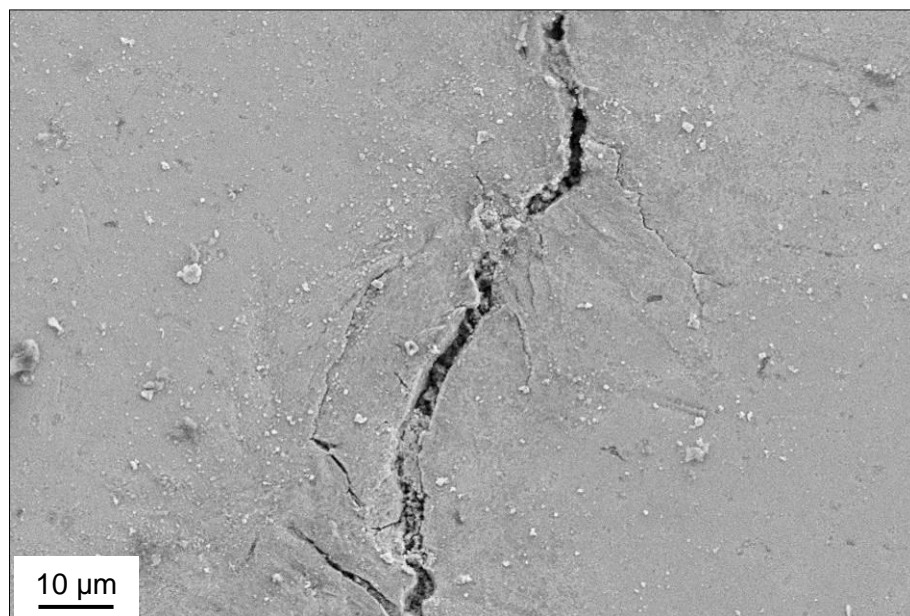
Figure 5.10: Secondary electron micrograph of crack branching in a SENB specimen exposed to condensing steam at 95°C for 7.3 kh.

Figure 5.9 shows a secondary electron micrograph of the crack through a SENB specimen exposed to condensing steam at 95°C for 7.3 kh. The external surface of the specimen is littered with oxide particles. The area immediately adjacent to the crack is most densely populated with a gradient towards sparsely populated at increasing distance from the crack. This suggests that more corrosion occurred on the external surface closest to the crack. The crack is filled with oxide similar to the initiation region, however, the visible surface is very smooth, whereas the initiation area had particles of oxide within the crack.

Figure 5.11: Secondary electron micrograph of crack branching in a SENB specimen exposed to condensing steam at 95°C for 7.3 kh.

Figure 5.10 and Figure 5.11 show secondary electron micrographs of a SENB specimen exposed to condensing steam at 95°C for 7.3 kh. Figure 5.11 shows the crack tip and Figure 5.10 shows a region just behind the crack tip. Both figures show evidence of crack branching. The cracks are mostly filled with oxide but there are some darker areas where there is no oxide at the external surface of the specimen.

5.3.3. Exposure Time: 5.8 kh

Figure 5.12 shows optical micrographs of a SENB specimen (a) containing a fatigue crack and (b) after exposure to condensing steam at 95°C for 5.8 kh. Whilst there is no obvious increase in crack length, the crack is approximately twice as wide after the exposure time. The external surface of the specimen is discoloured, but not as much as the specimens exposed for longer times of 7.3 and 8.8 kh. The external surface of

the specimen exposed for 5.8 kh is most oxidised in the area immediately adjacent to the crack from half way along the crack to the crack tip.
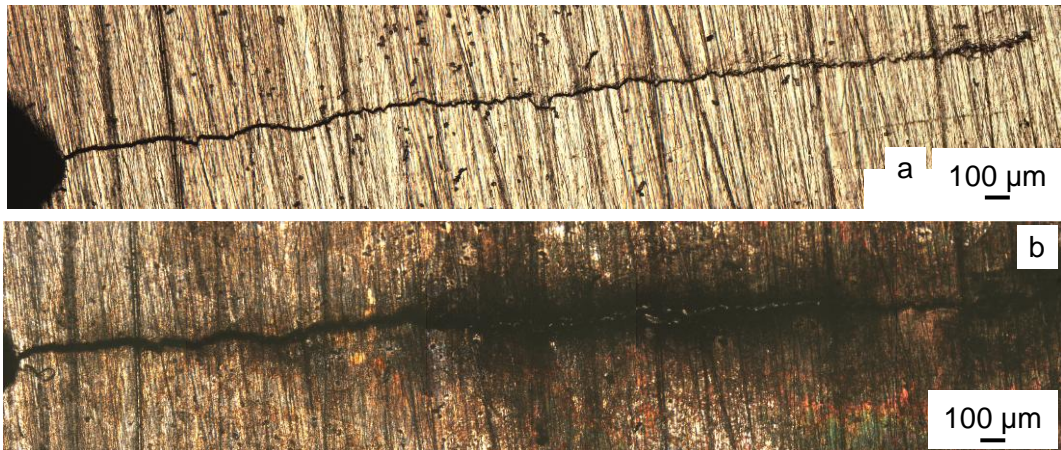
Figure 5.12: Optical micrographs showing the same specimen (a) with a fatigue pre-crack and (b) after exposure to condensing steam at 95°C for 5.8 kh.
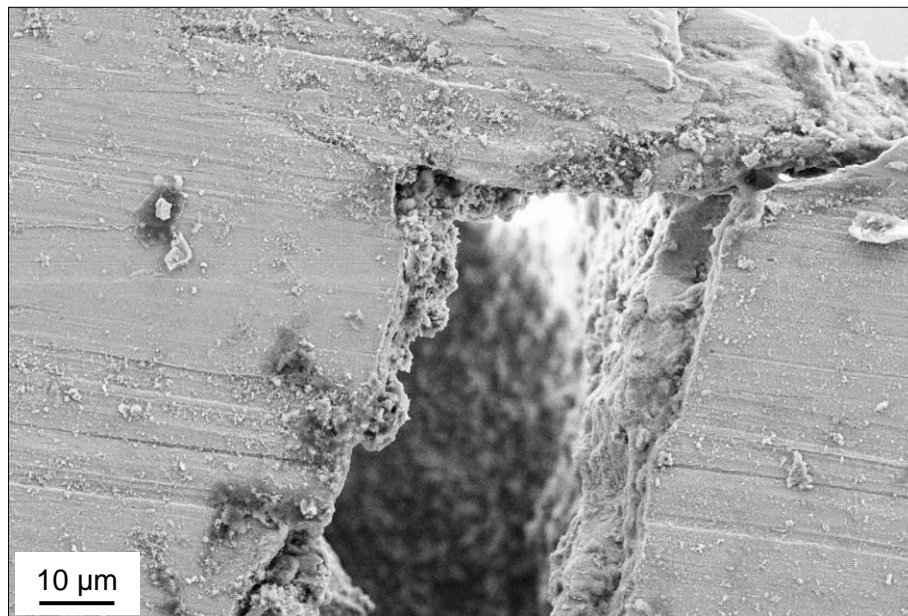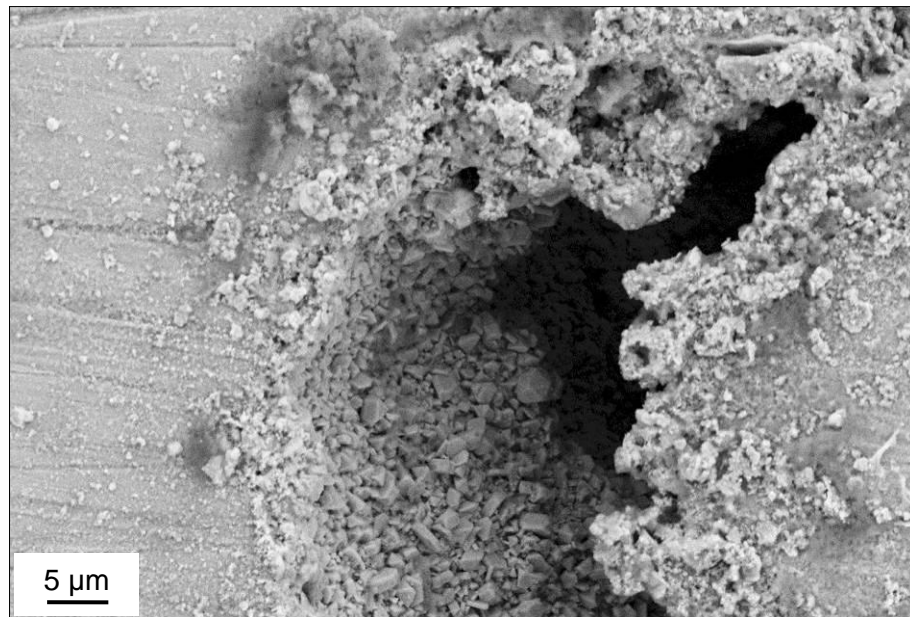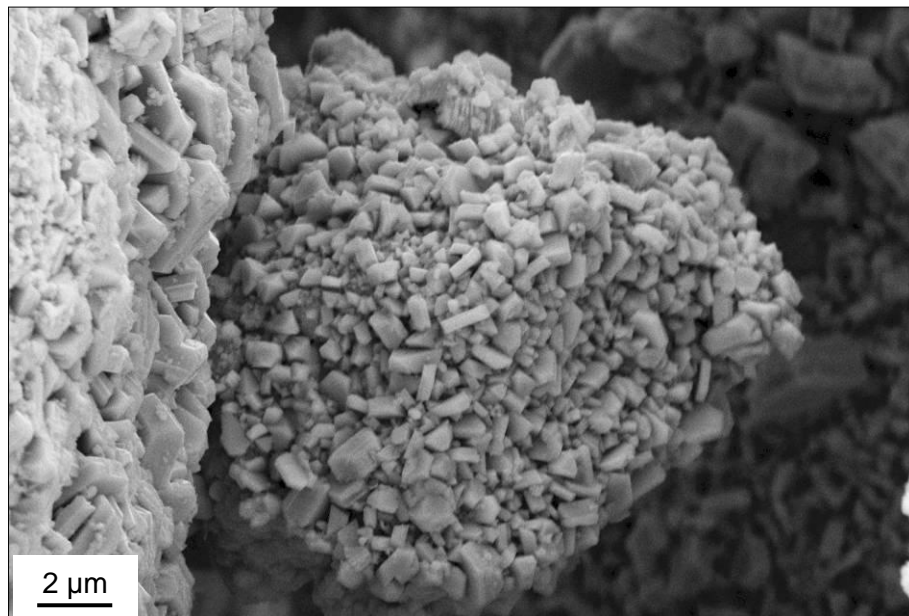

Figure 5.13: Secondary electron micrograph showing the crack initiation in a SENB specimen exposed to condensing steam at 95°C for 5.8 kh.

Figure 5.13 shows a secondary electron micrograph of the crack initiation in a SENB specimen exposed to condensing steam at 95°C for 5.8 kh. The micrograph shows that initiation occurred at the apex of the notch but propagation was off-centre. The crack is open so it is possible to see a layer of oxide coating the fatigue crack surfaces.

Figure 5.14 shows a secondary electron micrograph of the crack through a SENB specimen after exposure to condensing steam at 95°c for 5.8 kh. The crack is open and oxidation can be seen within the crack. It is particularly prominent on the left-hand crack surface, but this is due to the perspective of the image and the orientation in

which the crack propagated. The oxide within the crack has various morphologies including cubes, octahedrons and cuboctahedra, similar to the crack surfaces of the WOL specimens exposed to condensing steam at 95°C for 98.3 kh.

Figure 5.14: Secondary electron micrograph of the crack through a SENB specimen exposed to condensing steam at 95°C for 5.8 kh.

5.3.4. Exposure Time: 4.4 kh
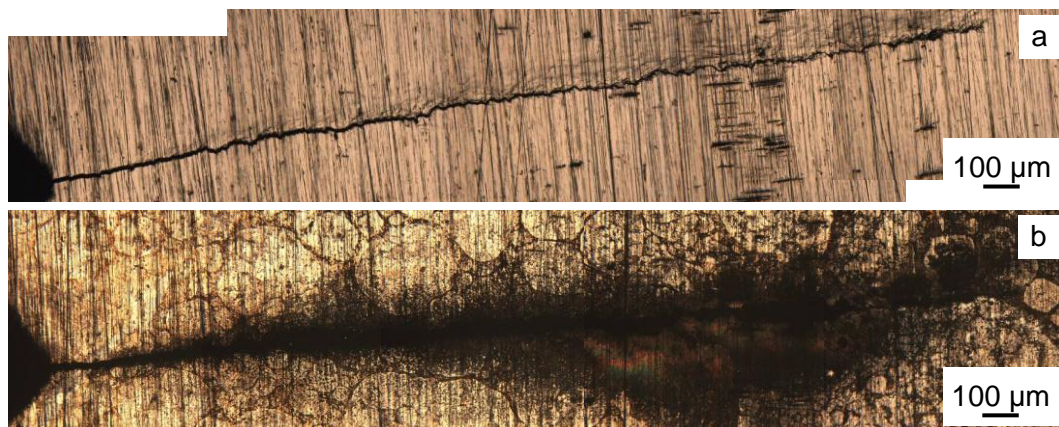
Figure 5.15: Optical micrographs showing the same specimen (a) with a fatigue pre-crack and (b) after exposure to condensing steam at 95°C for 4.4 kh.

Figure 5.15 (a) shows a SENB specimen with a fatigue crack. Figure 5.15 (b) shows the same specimen after exposure to condensing steam at 95°C for 4.4 kh. After exposure much of the crack is masked with oxidation and staining so it is not possible to identify any possible changes in the crack. There are numerous brown misshapen

147

circles on the external surface of the specimen which are likely to be a result of corrosion around the edges of water droplets that condensed on the specimen.
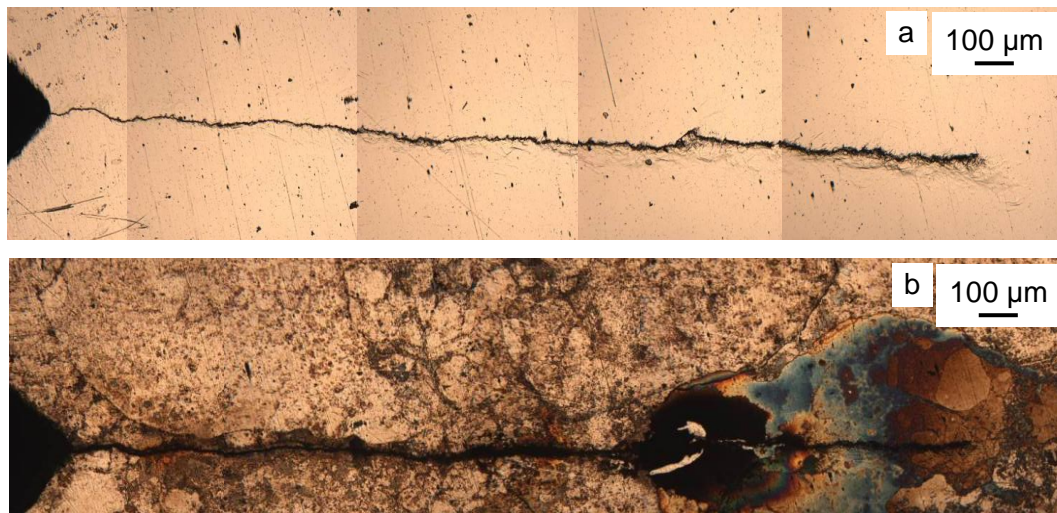

Figure 5.16: Secondary electron micrograph of a SENB specimen exposed to condensing steam at 95°C for 4.4 kh.

Figure 5.17: Secondary electron micrograph of an agglomeration of oxide particles within the crack of a SENB specimen exposed to condensing steam at 95°C for 4.4 kh.

Figure 5.16 shows the initiation region of the crack through a SENB specimen after exposure to condensing steam at 95°C. The crack is open and the crack surfaces are covered in corrosion with a platelet structure, similar to that seen on the crack surface of the WOL specimens exposed to condensing steam at 95°C for 98.3 kh.

Figure 5.17 shows one edge of the crack through the SENB specimen exposed to condensing steam for 4.4 kh. Figure 5.16 shows that the entire crack surfaces are coated in a layer of oxidation. In Figure 5.17 it is possible to see the oxide more closely and identify that it has a platelet structure. The focus of this micrograph is the agglomeration of flat platelet oxide particles which measures approximately 16 x 14 µm that has grown from the one crack surface of the specimen.

5.3.5. Exposure Time: 2.9 kh

Figure 5.18: Optical micrographs showing the same specimen (a) with a fatigue pre-crack and (b) after exposure to condensing steam at 95°C for 2.9 kh.
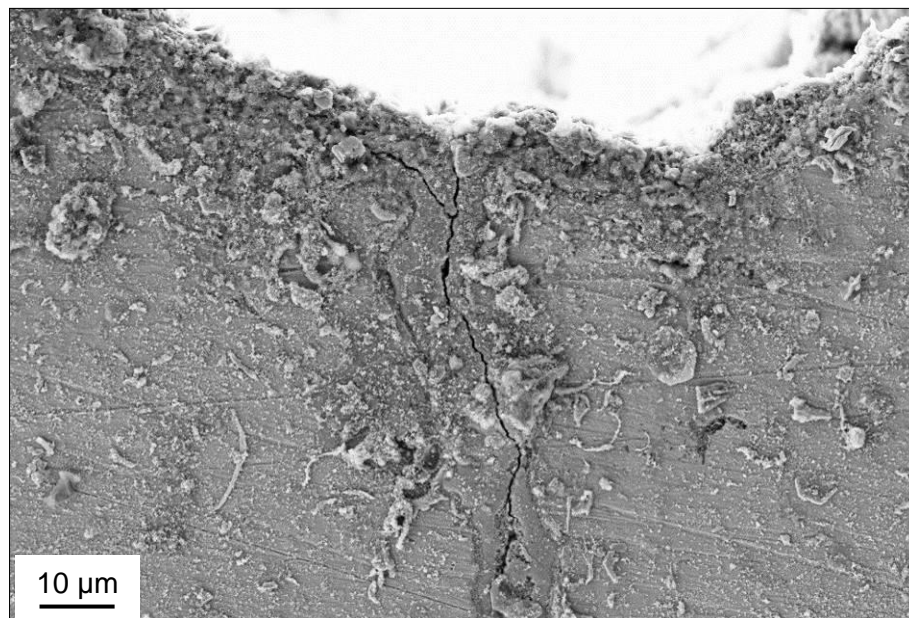
Figure 5.19: Secondary electron micrograph of a SENB specimen exposed to condensing steam at 95°C for 2.9 kh.

Figure 5.18 (a) shows an optical micrograph of a fatigue pre-crack in a SENB specimen. Figure 5.18 (b) shows an optical micrograph of the same specimen after exposure to condensing steam at 95°C for 2.9 kh. There is no obvious increase in

crack length but the crack is more open after exposure and the area surrounding the crack has oxidised.

Figure 5.19 shows the initiation region of the SENB specimen exposed to condensing steam at 95°C for 2.9 kh. The crack initiated away from the notch apex. In this specimen the crack is very narrow and closed, which is dissimilar to the other SENB specimens.
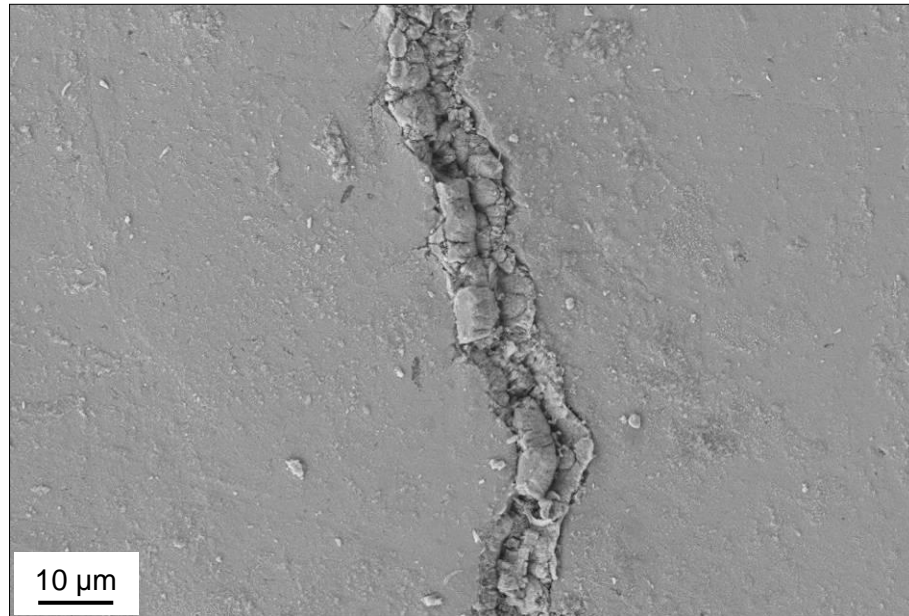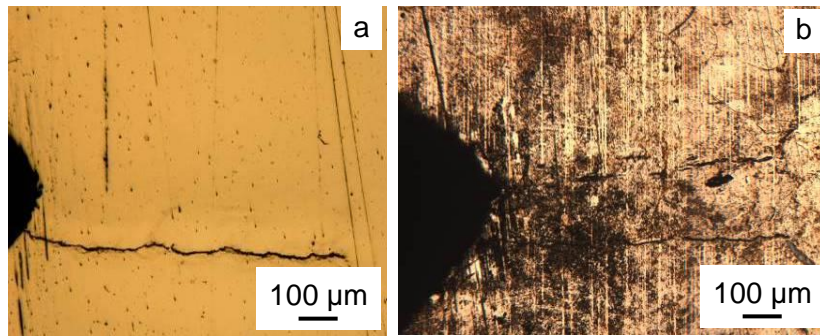
5.3.6. Exposure Time: 1.5 kh

Figure 5.20: Optical micrographs showing the same specimen (a) with a fatigue pre-crack and (b) after exposure to condensing steam at 95°C for 1.5 kh.
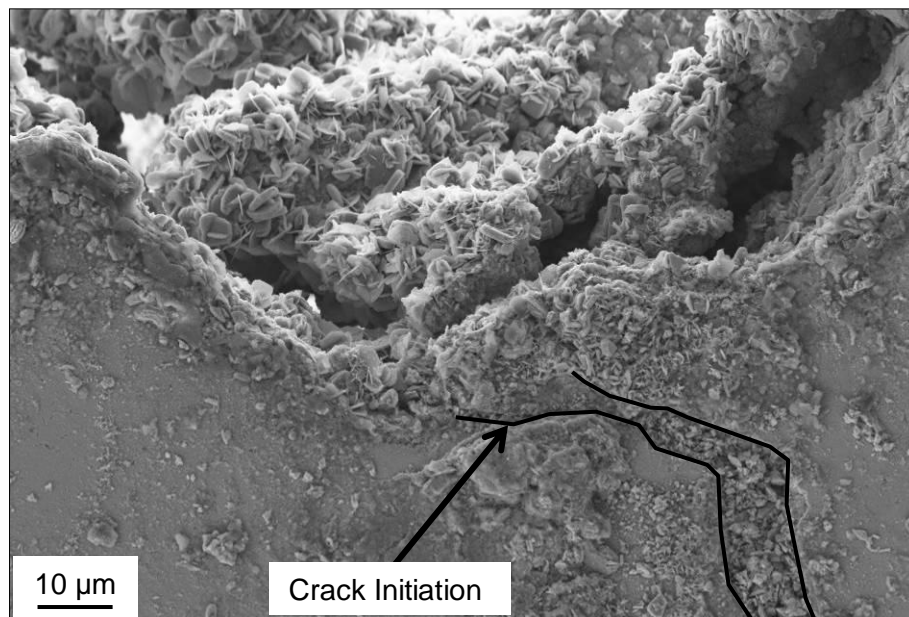
Figure 5.21: Secondary electron micrograph of the crack initiation region of a SENB specimen exposed to condensing steam at 95°C for 1.5 kh.

Figure 5.22: Secondary electron micrograph of a SENB specimen exposed to condensing steam at 95°C for 1.5 kh.

Figure 5.20 (a) shows an optical micrograph of a fatigue pre-crack in a SENB specimen. Figure 5.20 (b) shows an optical micrograph of the same specimen after exposure to condensing steam at 95°C for 1.5 kh. There is no obvious increase in crack length after exposure to condensing steam. The crack is more open after exposure, particularly from the initiation to approximately two thirds of the length. From visual inspection the final portion of the crack does not appear to have opened during exposure. The area surrounding the crack has oxidised, however this is clouded somewhat by the water stain on the final portion of the crack.

Figure 5.21 shows the crack initiation region of the SENB specimen exposed to condensing steam at 95°C for 1.5 kh. There is substantial oxide around the notch tip which has a platelet structure and the crack is filled with oxide. Figure 5.22 shows a section of the crack through the same specimen exposed to condensing steam for 1.5 kh. In this specimen the crack is approximately 10 µm wide and filled with various sized blocks of oxide throughout.
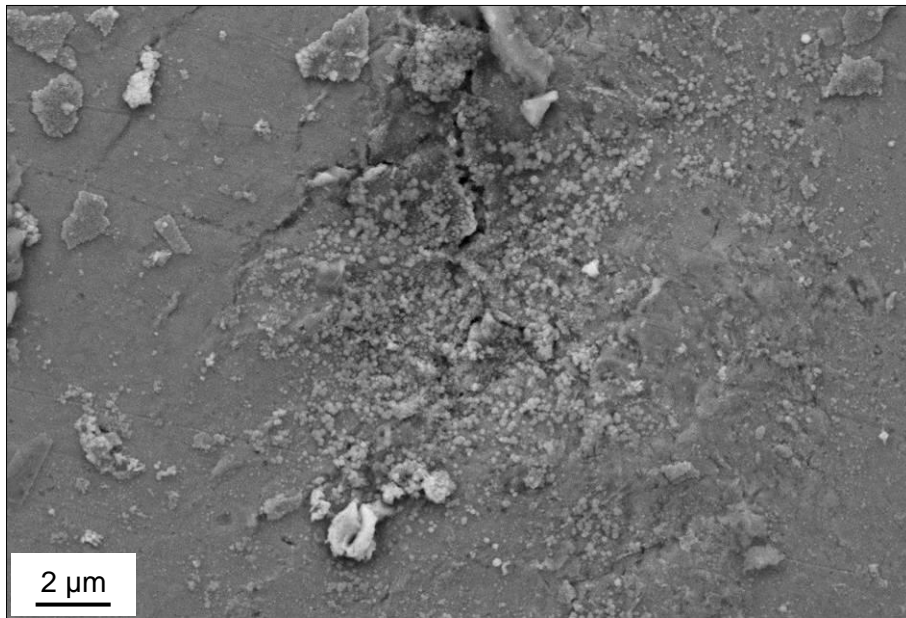
5.3.7. Exposure Time: 0.7 kh

Figure 5.23 shows optical micrographs of a SENB specimen (a) containing a fatigue crack and (b) after exposure to condensing steam at 95°C for 0.7 kh. There is no visible increase in crack length after exposure to condensing steam but there is some discolouration of the external surface of the specimen, particularly around the crack.

Figure 5.23: Optical micrographs showing the same specimen (a) with a fatigue pre-crack and (b) after exposure to condensing steam at 95°C for 0.7 kh.

Figure 5.24: Secondary electron micrograph of a SENB specimen exposed to condensing steam at 95°C for 0.7 kh.

Figure 5.24 shows the crack tip of the SENB specimen exposed for 0.7 kh. There is a cluster of small oxide particles surrounding the crack and some short crack branching around the crack tip. The branching in this specimen is shorter than that shown in Figure 5.10 and Figure 5.11.

5.3.8. Analysis of Crack Length

Optical micrographs have been shown of SENB specimens with fatigue pre-cracks and after exposure to condensing steam at 95°C for times of 8.8, 7.3, 5.8, 4.4, 2.9, 1.5 and 0.7 kh. For all exposure times, comparison of the "before" and "after" optical micrographs showed no evidence to suggest that any of the cracks had propagated further than the fatigue pre-crack length during exposure to condensing steam at 95°C. It is possible that there was no crack growth in any of the SENB specimens exposed to condensing steam or that the cracks did propagate during the exposure time, but the

distance was too small to be distinguishable at the magnification used for the optical micrographs. There was optical microscopy evidence that many of the cracks had opened during the exposure to condensing steam.

Examination using secondary electron microscopy showed evidence to suggest that stress corrosion cracks may have propagated in at least two of the SENB specimens exposed to condensing steam as crack branching was shown in Figure 5.10 and Figure 5.11 for the specimen exposed to condensing steam at 95°C for 7.3 kh and in Figure 5.24 for the specimen exposed for 0.7 kh. It is possible that this branching occurred during exposure to condensing steam, but it is also possible that the branching occurred during the fatigue pre-cracking process (Korda, Mutoh et al, 2006).

The crack branching was only found the SENB specimen exposed for the shortest time of 0.7kh and the SENB specimen exposed for the second longest time of 7.3 kh. All the specimens received the same number of cycles at the same minimum and maximum load. When comparing the optical micrographs of the specimens after pre-cracking but before exposure to condensing steam at 95°C, it is possible to see that all the cracks are relatively similar in length with one exception. The crack in the specimen that was later exposed to condensing steam for 0.7 kh has a noticeably shorter fatigue pre-crack than the other specimens. For consistency, the same load was applied to all the specimens. As the fatigue pre-crack was shorter in the specimen later exposed to condensing steam for 0.7 kh, the initial stress intensity at the crack tip would have been higher than all the other specimens with similar pre-crack lengths. This would mean that the likelihood of the crack propagating by SCC was higher for the specimen exposed to condensing steam for 95°C than the other specimens with similar pre-crack lengths. Many of the specimens exposed for greater than 0.7 kh had oxide covering the external surface of the specimen which may have masked any crack branching that would otherwise have been apparent.

All the SENB specimens were pre-cracked and stressed to a value that was hoped to be greater than the threshold stress intensity for SCC. (The stress was estimated using the pre-crack length and the Mode I displacement.) This does not mean that a crack would immediately start to grow as soon as the specimens were entered into the experimental conditions. In Section 2.11.6, it was stated that SCC has five stages: incubation, initiation, stable crack growth, accelerated crack growth by SCC, HCF or LCF and unstable crack growth or fracture (ASM International Handbook Committee, 1987). The incubation period is the time during which the specimen was stressed and

in condensing steam before a crack initiates. It is possible that the times for which the SENB specimens were exposed to the experimental conditions was less than the incubation period and therefore the cracks did not start to grow further than the fatigue pre-crack.

Previous experiments detailed in the ASM International Handbook Committee, 1987, found that crack growth has ceased in samples that are removed from solution, rinsed, dried and reinserted into solution. This suggested that the electrochemistry of a pre-existing pit is different from that of a pit generated in service. The SENB specimens were pre-cracked rather than pitted, however, the same thinking can be applied. The electrochemistry of a growing stress corrosion crack would be quite different from that of a fatigue crack at the instant it was subjected to condensing steam. It would take time for conditions to develop that would promote SCC propagation.

It has been shown that it is likely that the mouth of the crack would start to corrode before the tip of the crack as the condensing steam would have come into contact with the mouth of the crack first. It is possible that the pre-crack would have become closed, or at least reduced in width as a result of the developing oxide. This would have restricted the steam from reaching uncorroded metal and hence prevented SCC propagation. Karpenko and Vasilenko, 1979, explained the mechanical-electrochemical theory and the electrochemical theory. It is possible that, if the fatigue pre-cracks became filled with oxide, SCC would only propagate if the applied stress was sufficient to break the oxide within the crack to make a new path for the condensing steam to reach the uncorroded metal ahead.

5.3.9. Oxide Development

The secondary electron micrographs shown that oxide has developed within the fatigue pre-cracks generated in the SENB specimens prior to exposure to condensing steam at 95°C for various times. From comparison of the optical micrographs alone it is possible to identify that many of the cracks are more open after exposure to condensing steam than before. It is unclear as to whether the crack opening is primarily due to the mode I loading or to metal loss as a result of corrosion of the pre-crack surfaces.

Although there is oxide within the crack, Figure 5.5 shows that the crack surfaces match each other. This suggests that the crack has opened due to the mode I loading and there has been a small amount of corrosion within the crack as a result of

condensing steam entering the crack during the exposure time. The opposite is true in Figure 5.14. Whilst some parts of the crack are similar, there is evidence to suggest a portion of at least one pre-crack surface has corroded away.

There is no trend in oxide development within the SENB specimens examined. Some of the cracks are filled with solid oxide as shown in Figure 5.9 for the specimen exposed for 5.8 kh and to a lesser extent in Figure 5.6 which shows the specimen exposed for 8.8 kh and Figure 5.22 that shows the specimen exposed for 1.5 kh. Figure 5.14 shows that the oxide within the crack of the specimen exposed for 5.8 kh consists of multiple intertwined geometric-shaped oxide structures, similar to the agglomeration of oxide crystals shown in Figure 5.17 for the specimen exposed for 4.4 kh.

5.4. Crack Surface Morphology

After examining the cracks in cross-section they were fully separated into two pieces as described by Section 3.2. The crack surfaces were examined using SEM. In all micrographs displayed in this Section, the crack growth direction is left to right across the page.

5.4.1. Exposure Time: 8.8 kh

Figure 5.25, Figure 5.26 and Figure 5.27 show portions of the crack surface of the SENB specimen exposed to condensing steam at 95°C for 8.8 kh. Although only three locations are shown in the micrographs, they were selected because they are representative of the entire crack surface, which is covered with a la layer of oxide.
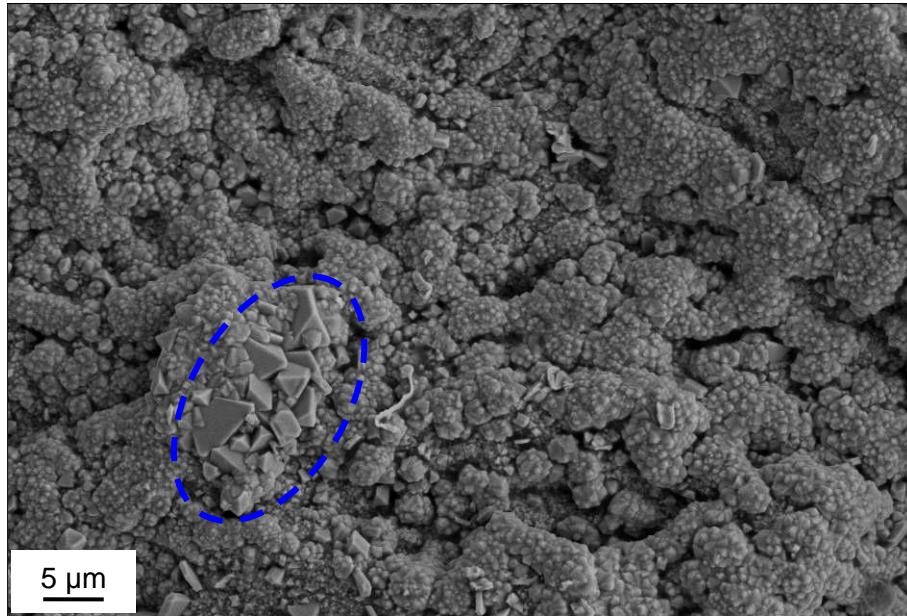
Figure 5.25: Secondary electron micrograph showing the oxide on the crack surface of the SENB exposed to condensing steam at 95°C for 8.8 kh.
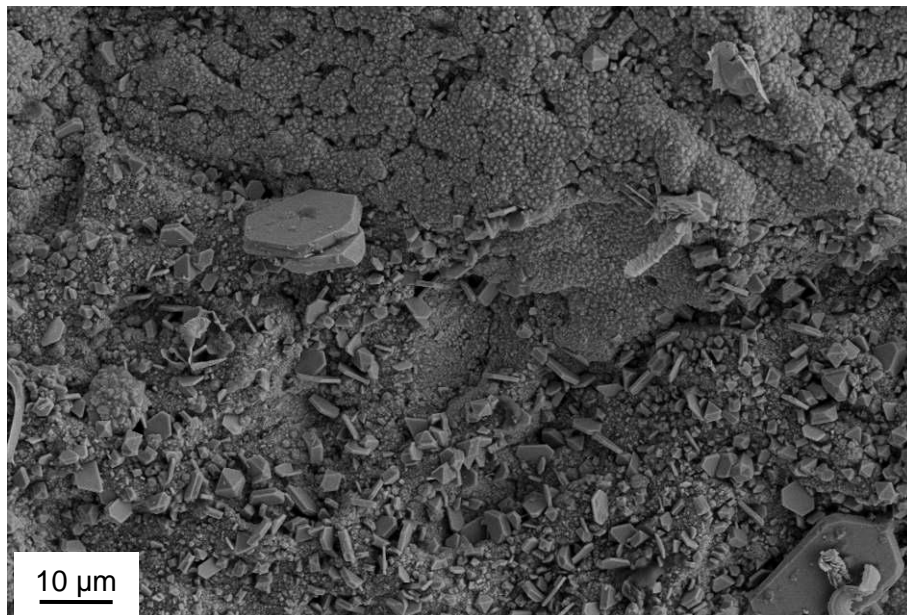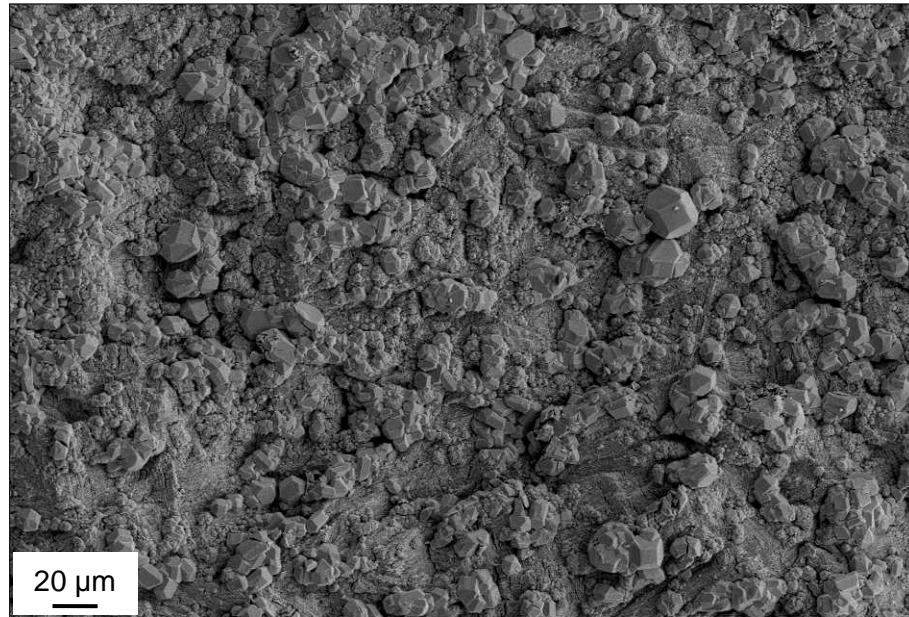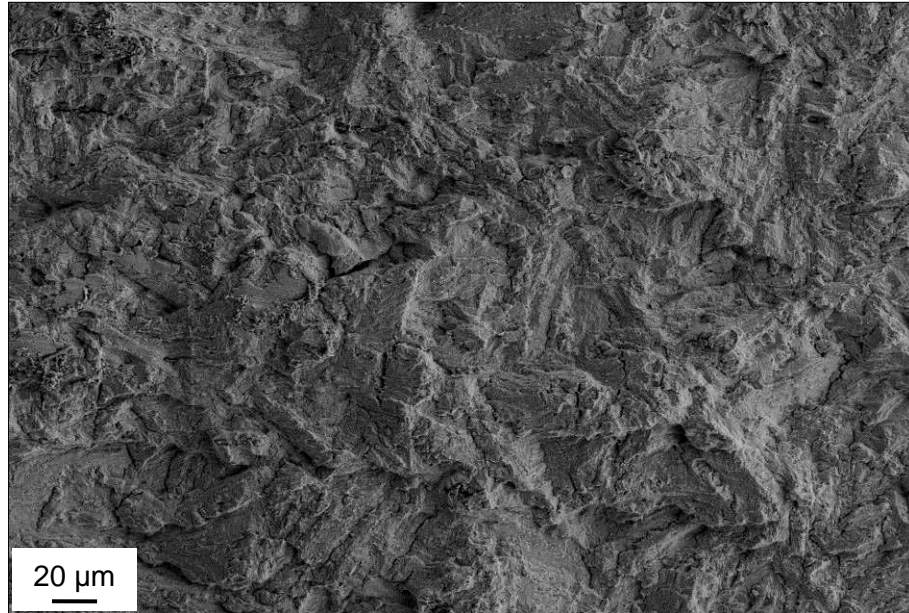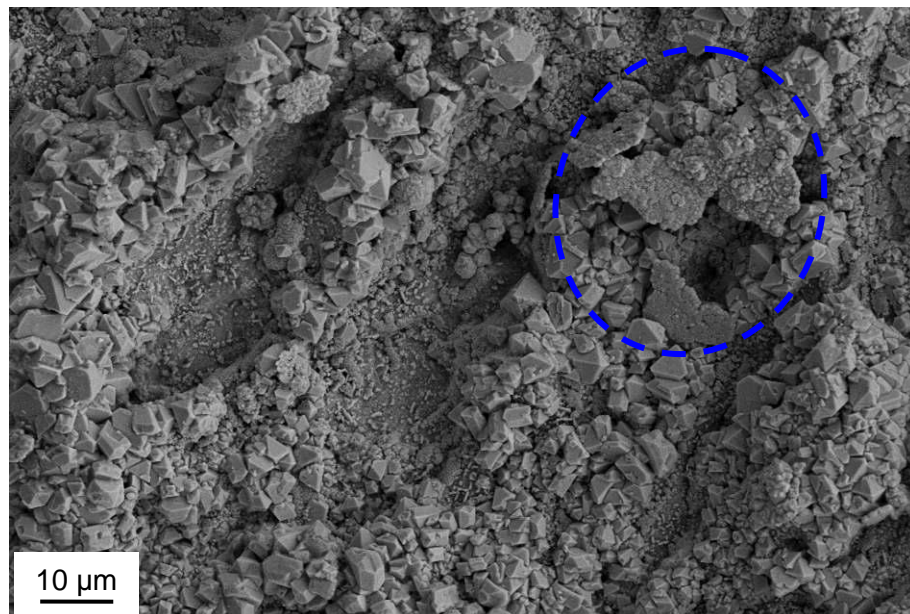

Figure 5.26: Secondary electron micrograph showing the large platelet oxide structures on the crack surface of the SENB exposed to condensing steam at 95°C for 8.8 kh.

Figure 5.25 shows an area of the crack where the surface is covered with agglomerations of oxide particles with some isolated octahedrons and cuboctahedra dotted around. Within the blue dashed ellipse there is a group of larger octahedron oxide particles, each measuring approximately 4 μm wide. The top section of Figure 5.26 shows a similar agglomeration of oxide particles as that covering the majority of the section shown in Figure 5.25. The bottom section of Figure 5.26 shows multiple hexagonal platelet oxide structures protruding from the underlying layer of oxide on the

crack surface. In two locations shown in Figure 5.26 the hexagonal platelets measure over 10 μm wide and are approximately 2 μm thick.

Figure 5.27: Secondary electron micrograph showing cuboctahderon and other geometric shaped oxide structures on the crack surface of the SENB exposed to condensing steam at 95°C for 8.8 kh.

Figure 5.27 shows a third location on crack surface of the specimen exposed for 8.8 kh. Here again there is an underlying layer of oxide as mentioned previously. The surface is littered with oxide particles which exhibit various morphologies including octahedrons, cuboctahedra and other multifaceted geometric shapes.

5.4.2. Exposure Time: 7.3 kh

Figure 5.28 is representative of the entire crack surface of the SENB specimen exposed to condensing steam at 95°C for 7.3 kh. Although there is a fine layer of oxide present throughout the crack surface, there is no visual evidence of oxide. There is an absence of features such as the octahedrons and cuboctahdrons shown in the specimen exposed for the longer time of 8.8 kh.

Figure 5.28: Secondary electron micrograph showing the crack surface of a SENB specimen exposed to condensing steam for 7.3 kh.
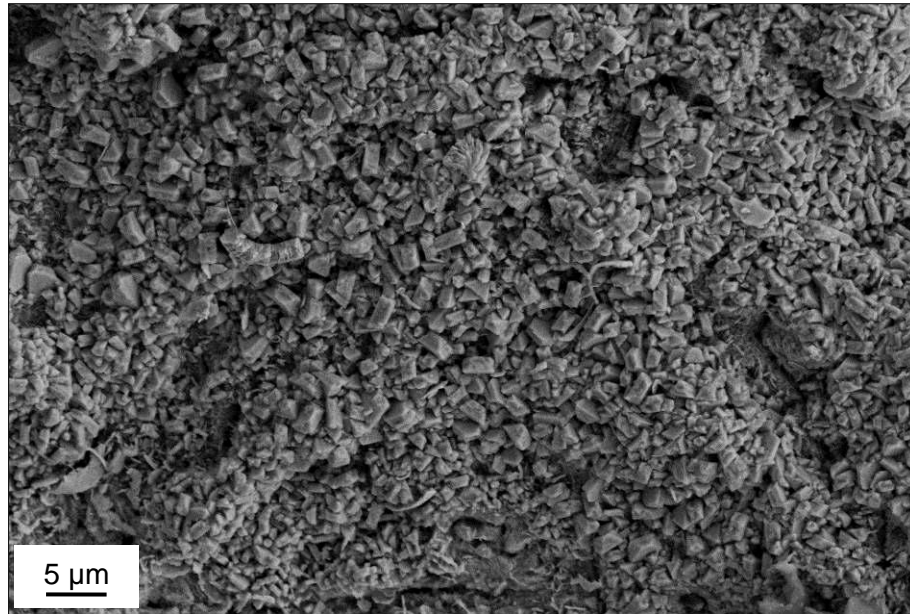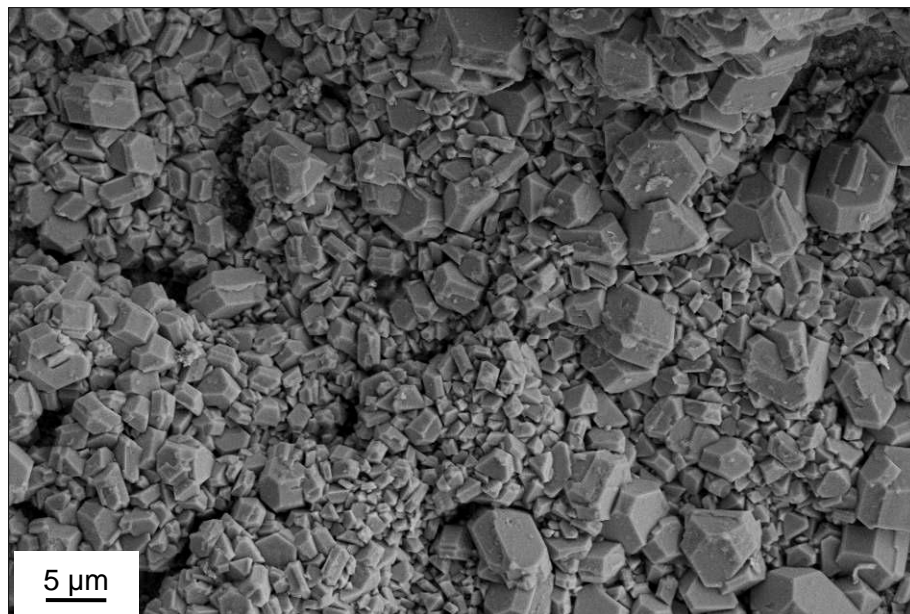
5.4.3. Exposure Time: 5.8 kh
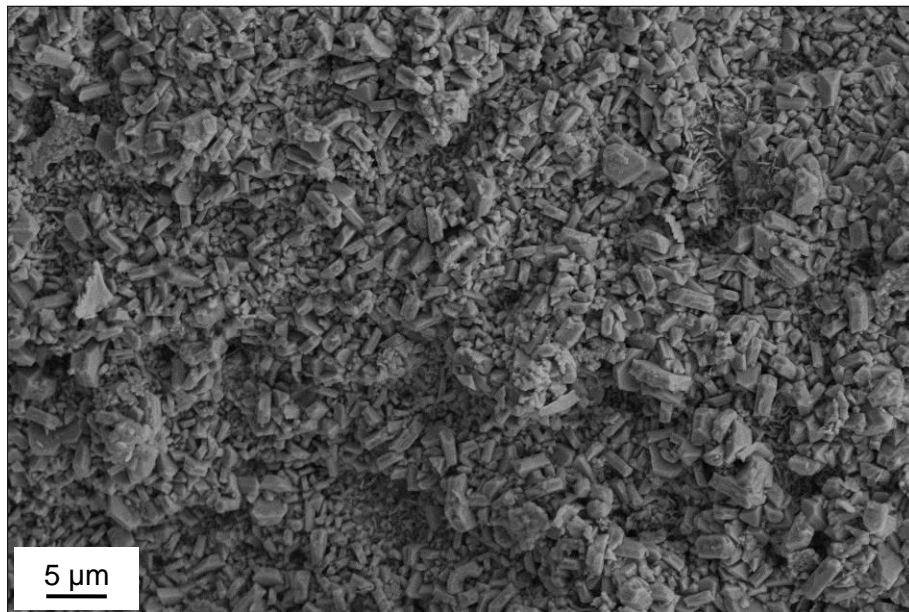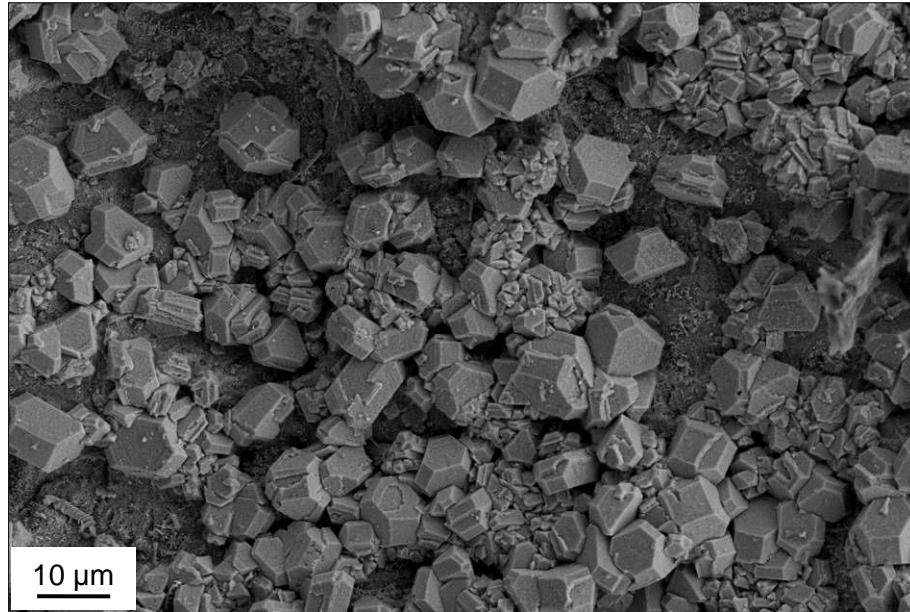

Figure 5.29: Secondary electron micrograph showing platelet oxide structure on the crack surface of a SENB specimen exposed to condensing steam for 5.8 kh.

Figure 5.29, Figure 5.30 and Figure 5.31 show three locations along the crack surface of the SENB specimen exposed to condensing steam at 95°C for 5.8 kh that exhibit different features. Figure 5.29 shows an area of the crack surface that is covered with intertwined platelet oxide. Figure 5.30 shows an area of the crack that is littered with cuboctahedra and other multifaceted geometric oxide morphologies. Figure 5.31

shows a similar area to that of Figure 5.30, but in Figure 5.31 there is a section of oxide highlighted within the blue dashed ring that looks like it may have spalled from another region of the crack and redeposited elsewhere. The oxide shown inside the ring has a similar appearance to that shown on the external surface of the specimen exposed to condensing steam at 95° for 8.8 kh (Figure 5.6).
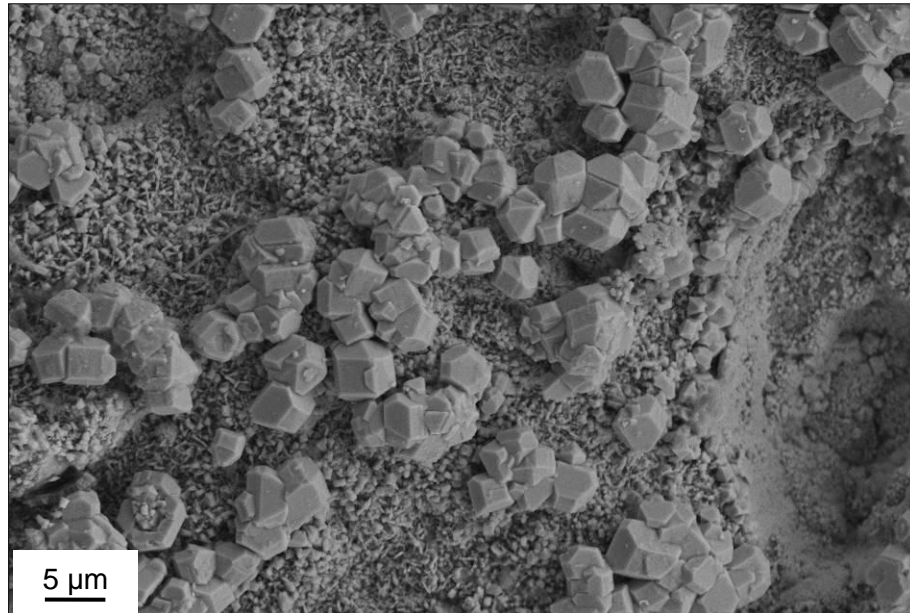
Figure 5.30: Secondary electron micrograph showing octahedron and cuboctahedron oxide on the crack surface of a SENB specimen exposed to condensing steam at 95°C for 5.8 kh.

Figure 5.31: Secondary electron micrograph showing octahedron oxide on the crack surface of a SENB specimen exposed to condensing steam at 95°C for 5.8 kh.

5.4.4. Exposure Time: 4.4 kh

Figure 5.32: Secondary electron micrograph showing oxide on the crack surface of a SENB specimen exposed to condensing steam at 95°C for 4.4 kh.

Figure 5.33: Secondary electron micrograph showing mixed geometric oxide morphologies on the crack surface of a SENB specimen exposed to condensing steam at 95°C for 4.4 kh.

Figure 5.32 shows a section along the crack surface of the SENB specimen exposed to condensing steam at 95°C for 4.4 kh which is covered with a layer of oxide that consists mainly of intertwined platelet structures. This is very similar to the area of the crack surface of the specimen exposed to condensing steam for 5.8 kh shown in Figure

5.29. Figure 5.33 and Figure 5.34 show areas of the crack surface of the specimen exposed to condensing steam for 4.4 kh where the oxide consists of cuboctahedra and other multifaceted geometric shapes, similar to those shown in Figure 5.30 and Figure 5.31.
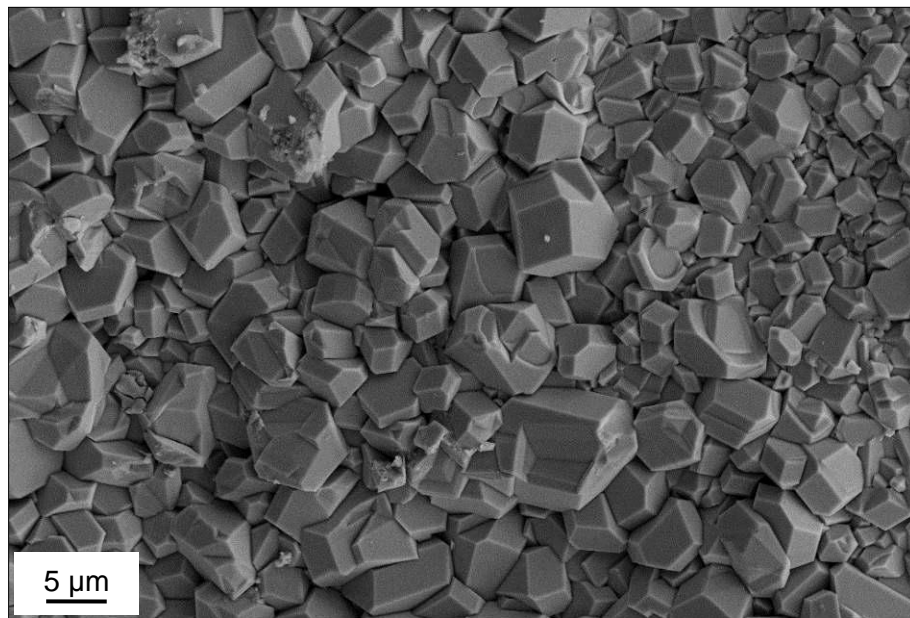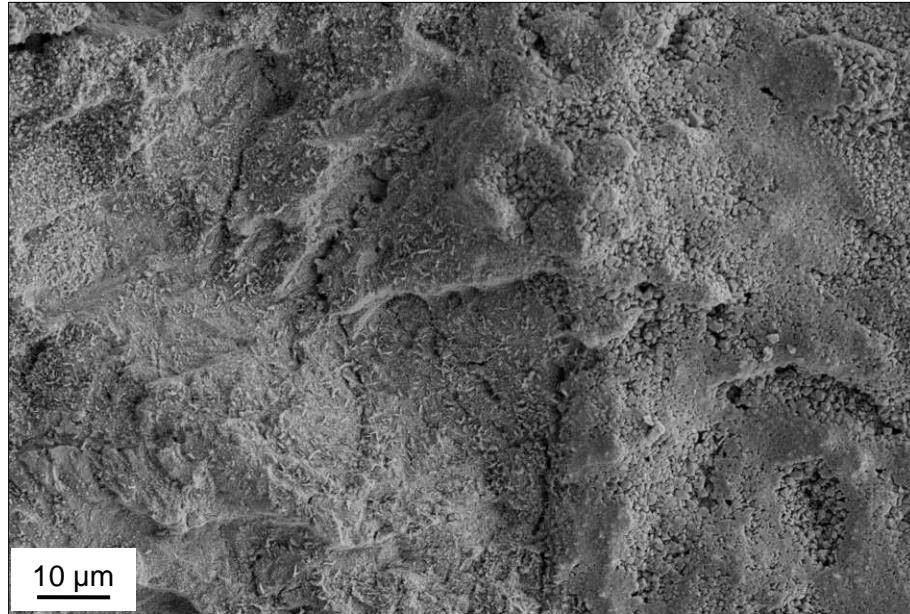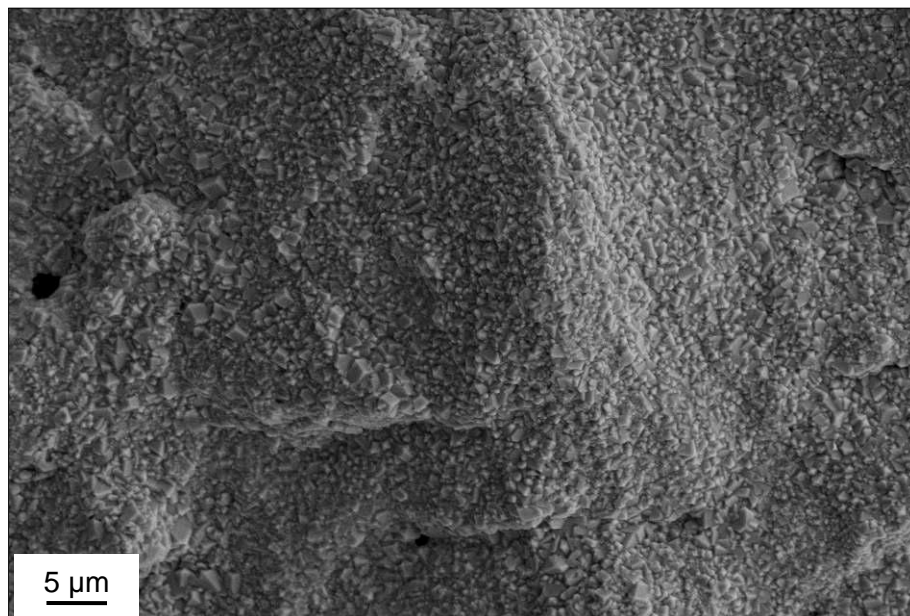

Figure 5.34: Secondary electron micrograph showing mixed geometric oxide morphologies on the crack surface of a SENB specimen exposed to condensing steam at 95°C for 4.4 kh.

5.4.5. Exposure Time: 2.9 kh
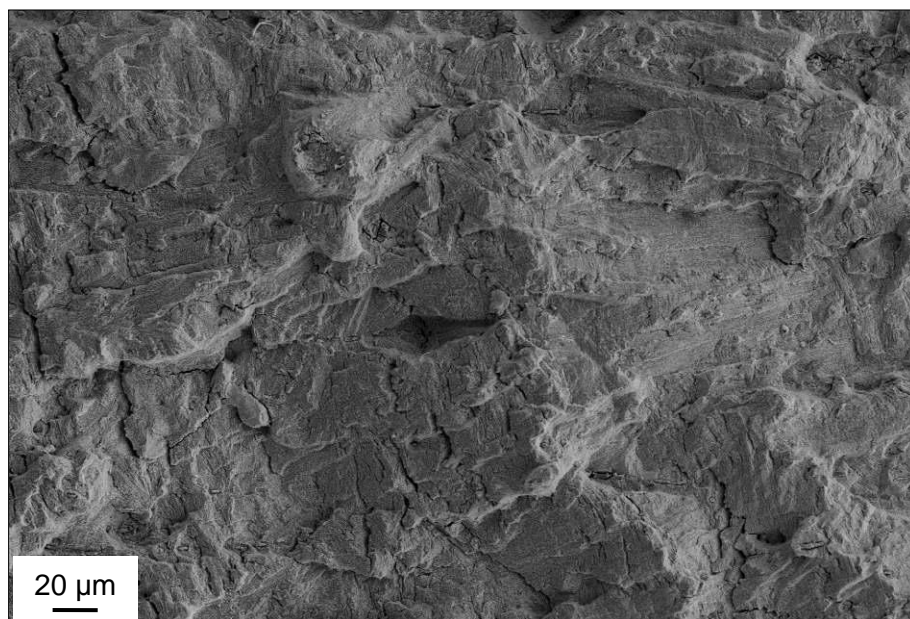
Figure 5.35: Secondary electron micrograph showing the crack surface of a SENB specimen exposed to condensing steam at 95°C for 2.9 kh.

The majority of the crack surface of the SENB specimen exposed to condensing steam at 95°C for 2.9 kh looks like that shown in Figure 5.35. There is a transgranular fracture surface as a result of the fatigue pre-crack induced in the specimen prior to exposure to the experimental conditions. There is no obvious oxide on the surface of the crack. Figure 5.36 shows a unique area of the crack surface of the specimen exposed for 2.9 kh where the oxide has a similar appearance to that shown in Figure 5.33. The oxide consists of various intertwined geometric shapes with clearly defined edges and smooth faces.

Figure 5.36: Secondary electron micrograph showing mixed geometric oxide morphologies on the crack surface of a SENB specimen exposed to condensing steam at 95°C for 2.9 kh.

5.4.6. Exposure Time: 1.5 kh

Figure 5.37 shows small particles of oxide on the crack surface of the SENB specimen exposed to condensing steam at 95°C for 1.5 kh. Figure 5.38 shows another area of the crack surface but in this micrograph the oxide particles are cube and octahedron shaped. The maximum dimension of the oxide particles in Figure 5.38 is approximately 3 µm.

Figure 5.37: Secondary electron micrograph showing the crack surface of a SENB specimen exposed to condensing steam at 95°C for 1.5 kh.

Figure 5.38: Secondary electron micrograph showing mixed geometric oxide morphologies on the crack surface of a SENB specimen exposed to condensing steam at 95°C for 1.5 kh.

5.4.7. Exposure Time: 0.7 kh

Figure 5.39: Secondary electron micrograph showing the crack surface of a SENB specimen exposed to condensing steam at 95°C for 0.7 kh.

Figure 5.39 shows a micrograph that is representative of the entire crack surface of the SENB specimen exposed to condensing steam at 95°C for 0.7 kh. The specimen exhibits a transgranular fracture surface as a result of the fatigue pre-crack induced before the specimen was exposed to condensing steam. There are only small areas with the first visible signs of oxide present.

5.4.8. Oxide Development

From examination of the crack surfaces of the SENB specimens exposed to condensing steam at 95°C for various times there is no obvious trend to be found with regards to oxide development over time. It would be expected that the specimens exposed to condensing steam for longer times would have greater oxide development within the crack, however, the results of the SENB specimens do not support this suggestion. The specimen exposed for 8.8 kh had substantial oxide present on the crack surface. The whole surface was covered with a layer of oxide and in several locations there were various geometric shaped oxide structures measuring ≥ 10 µm, as shown in Figure 5.26 and Figure 5.27.

Much of the surface of the specimen exposed to condensing steam for 4.4 kh had a similar appearance to that of the specimen exposed for 5.8 kh. The oxide morphologies shown in Figure 5.29 for the specimen exposed for 5.8 kh and Figure

5.32 for the specimen exposed for 4.4 kh are almost identical. The same is true for the cuboctahedron and other multifaceted shaped oxide structures shown in Figure 5.30 for the specimen exposed for 5.8 kh and Figure 5.34 for the specimen exposed for 4.4 kh.

From examining the surfaces it is unlikely that it would be possible to identify which of the specimens has been exposed for which time as the surfaces of the specimens exposed for 4.4 kh, 5.8 kh and 8.8 kh had very similar appearance.

There was no visible sign of oxide on the crack surface of the specimen exposed for 7.3 kh, which does not fit the idea that longer exposure time would lead to greater oxide development. The crack surface of the specimen exposed to condensing steam for 7.3 kh has a similar appearance to that of the specimen exposed for the shortest time of 0.7 kh, shown in Figure 5.39.

The majority of the surface of the specimen exposed for 2.9 kh had a similar appearance to the specimens exposed for 0.7 kh and 7.3 kh. However, Figure 5.36 shows one location where the oxide was highly developed and had a similar morphology to the oxide shown on the crack surface of the specimens exposed to condensing steam for 4.4, 5.8 and 8.8 kh. The majority of the surface of the specimen exposed for 1.5 kh showed signs of initial oxide growth, more than the specimen exposed for 2.9 kh, but there were no locations similar to that shown in Figure 5.36.

If it is true that during the experiment time the specimens remained within the incubation period of SCC, then this could explain why there was no trend in the oxide appearance. The range of exposure times was quite small, and therefore any variation in the appearance of the oxide development would be negligible.

5.5. Microstructural Characterisation of Specific Morphologies

Ion induced secondary electron imaging and TEM was used to examine some of the oxide morphologies that were observed on the surfaces of the stress corrosion cracks. Site specific samples were made using the dual beam FIB FEGSEM as described in Section 3.8. EDS spectra and selected area diffraction (SAD) patterns have been collected and analysed, the results of which are presented and discussed in this section.

5.5.1. Exposure Time: 7.3 kh
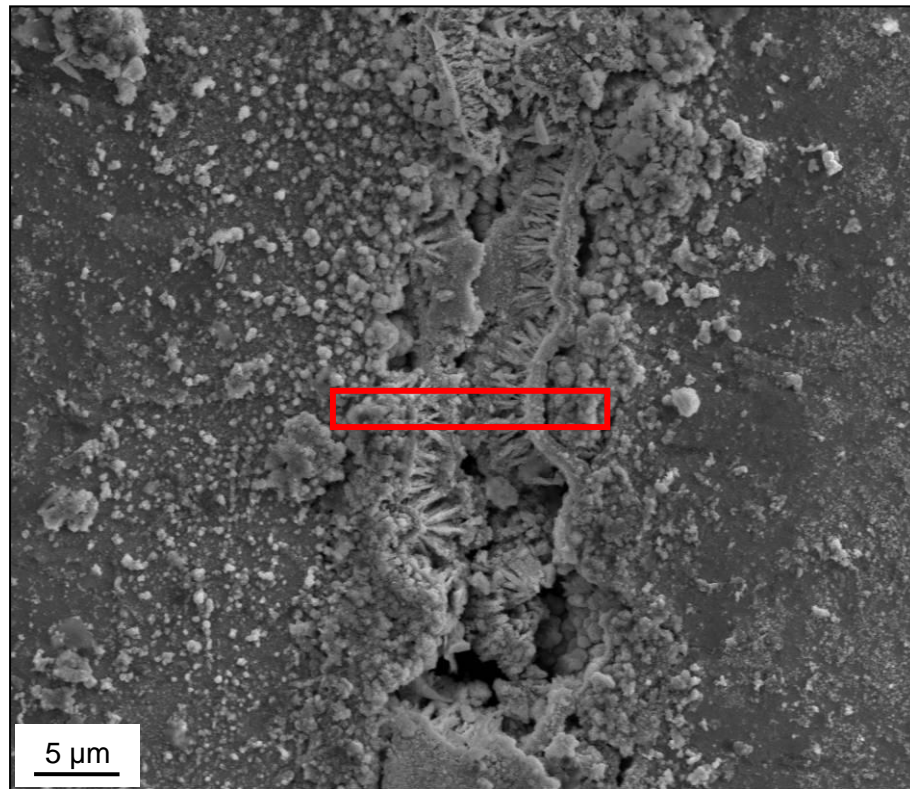
Figure 5.40: Secondary electron micrograph showing the crack through the SENB specimen exposed to condensing steam at 95°Cfor 7.3 kh.
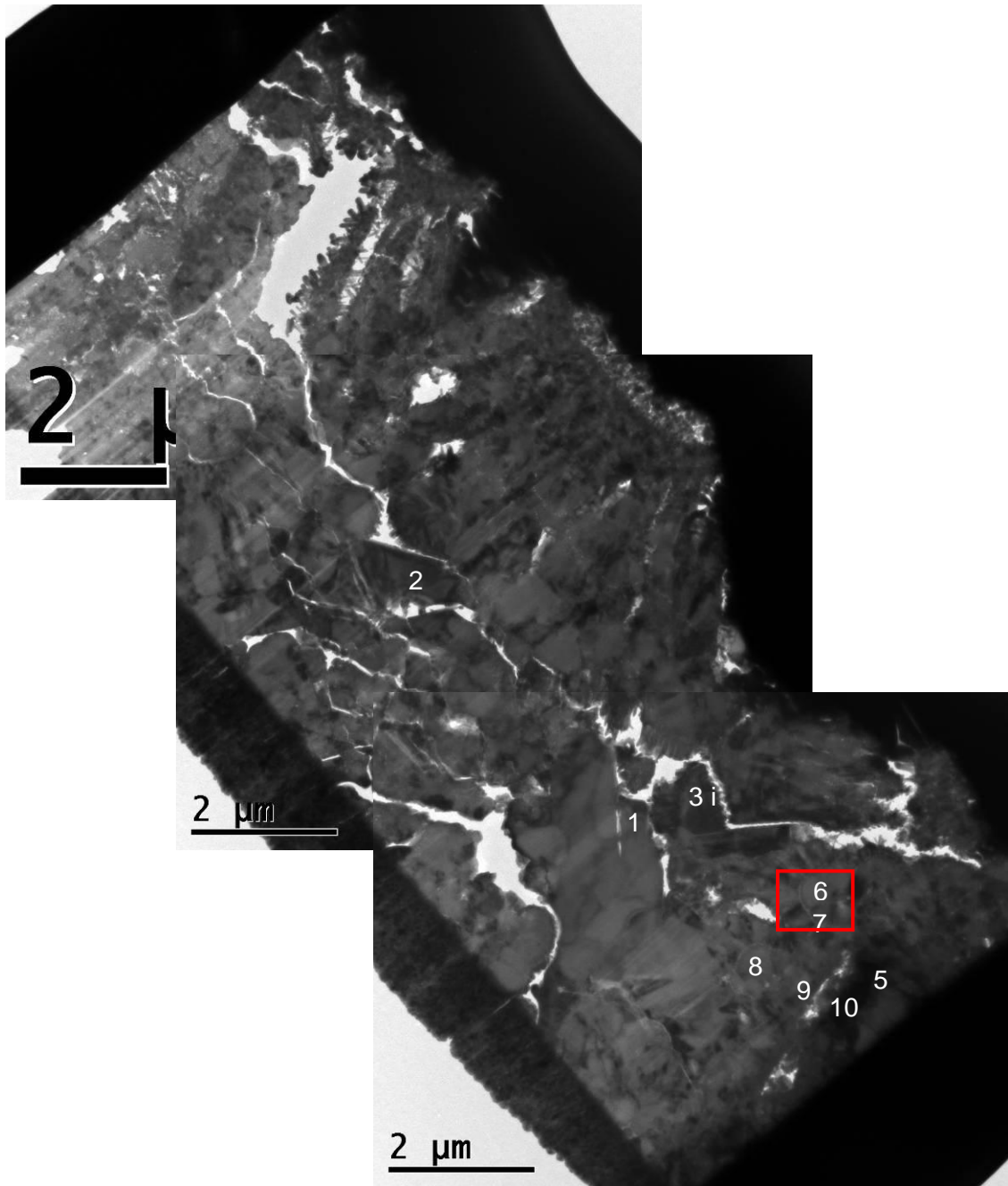
Figure 5.40 shows a secondary electron micrograph of the cross section through the crack in the SENB specimen exposed to condensing steam at 95°C for 7.3 kh. In this micrograph it is possible to identify both crack surfaces by the small void sections that are visible sporadically. There is a layer of oxide parallel to the crack surface with columnar oxide almost perpendicular to the crack surfaces. The appearance of the oxide suggests that the oxide has grown from the fatigue pre-crack surfaces until it met in the middle.

A site specific sample was removed from the SENB specimen using the dual beam FIB FEGSEM and examined using TEM. The location of the TEM specimen is shown by the red rectangle on the micrograph in Figure 5.40 and is perpendicular to the crack growth direction. A composite image of TEM micrographs is displayed in Figure 5.41. The sample is unavoidably orientated diagonally due to the constraints of the TEM sample holder. The black edges of the sample are parallel to the crack surfaces and the undulating edge shows the outer surface of the SENB specimen as seen in Figure 5.40. The outer edge of the sample contains very small grained oxide. The rest of the sample contains oxide grains of various size and orientation.

Figure 5.42 shows a TEM micrograph of the area in Figure 5.41 highlighted by the red rectangle. In this micrograph there is a thin almost semi-circular layer of small grained oxide, similar to that on the external surface of the sample shown in Figure 5.41, which encloses three larger grains of oxide. The semi-circle of oxide is orientated such that the flat edge is parallel with the fatigue pre-crack surface. On the outside of the semi-circle there are columnar grains of oxide which radiate outwards from the centre.

Analysis of the SAD pattern collected from point i of Figure 5.41 showed a solution for goethite only. One pattern is not a conclusive result, however, the EDS spectra for the same location showed only iron and oxygen present which is consistent with a solution of goethite. SAD patterns were also collected from the same points as the EDS spectra 1 and 2, but analysis of these did not match any of the reference oxides to which they were compared.

EDS spectra 1-10 are very similar; all but spectrum 5 contain only iron and oxygen, which is consistent with the crack being filled with iron oxide or iron hydroxide as hydrogen cannot be detected using EDS. Spectrum 5 contains iron, chromium and nickel in amounts consistent with the substrate metal. As there is no oxygen present in this spectrum and the location is consistent with the edge of the crack, it is likely that this spectrum was collected from a grain of substrate metal.

Figure 5.41: Composite image of transmission electron micrographs showing a site-specific cross-section through the crack of the SENB specimen exposed to condensing steam at 95°C for 7.3 kh at the location shown in Figure 5.40. The letter i corresponds to a selected area diffraction pattern shown in Figure 5.43 and the numbers 1 – 10 refer to EDS point spectra detailed in Table 5.1.
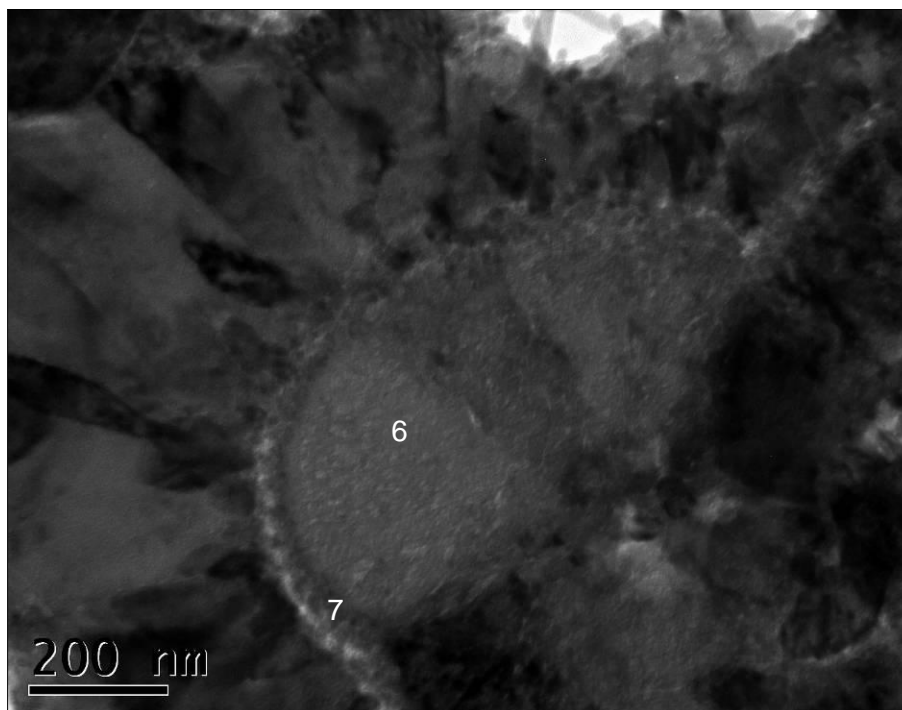
Figure 5.42: Transmission electron micrograph of the red boxed area highlighted in Figure 5.41

	h	k	l	d_1	h	k	l	d_2	u	v	w	Angle
Measured				2.514				2.207				29°
γ-Fe$_2$O$_3$												
Fe$_3$O$_4$												
Fe$_2$O$_3$												
FeO(OH)	0	2	$\bar{1}$	2.5833	1	$\bar{2}$	$\bar{1}$	2.2533	0	$\bar{1}$	2	29.3°
Cr$_2$O$_3$												
FeO												
NiCr$_2$O$_4$												
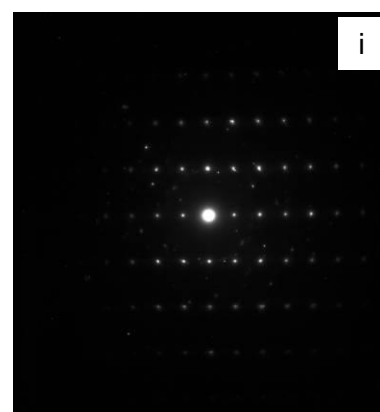
Figure 5.43: Selected area diffraction collected from point i in Figure 5.41.

169

Table 5.1: Quantitative EDS spectra collected from a site-specific sample extracted from the SENB specimen exposed to condensing steam at 95°C for 7.3 kh shown in Figure 5.41.

Spectrum Number		Element			
		O	Cr	Fe	Ni
1	Wt%	25.5		74.5	
	At%	54.4		45.6	
2	Wt%	23.9		76.1	
	At%	52.3		47.7	
3	Wt%	21.7		78.3	
	At%	49.2		50.8	
4	Wt%	30.3		69.7	
	At%	60.2		39.8	
5	Wt%		14.6	78.7	6.6
	At%		15.6	78.1	6.3
6	Wt%	26.6		73.4	
	At%	55.8		44.2	
7	Wt%	29.8		70.2	
	At%	59.7		40.3	
8	Wt%	27.0		73.0	
	At%	56.3		43.7	
9	Wt%	32.8		67.2	
	At%	63.1		36.9	
10	Wt%	33.2		66.8	
	At%	63.4		36.6	
11	Wt%	20.9		79.1	
	At%	47.9		52.1	

5.5.2. Exposure Time: 5.8 kh

Figure 5.44 shows a secondary electron micrograph of a portion of the crack through the SENB specimen exposed to condensing steam at 95°C for 5.8 kh. In this micrograph the crack direction is horizontal. The crack in this specimen is open and it is possible to see the oxide on the crack surfaces deep within the crack. In this specimen the oxide has not filled the crack in the way shown in the SENB specimen exposed for the longer time of 7.3 kh.
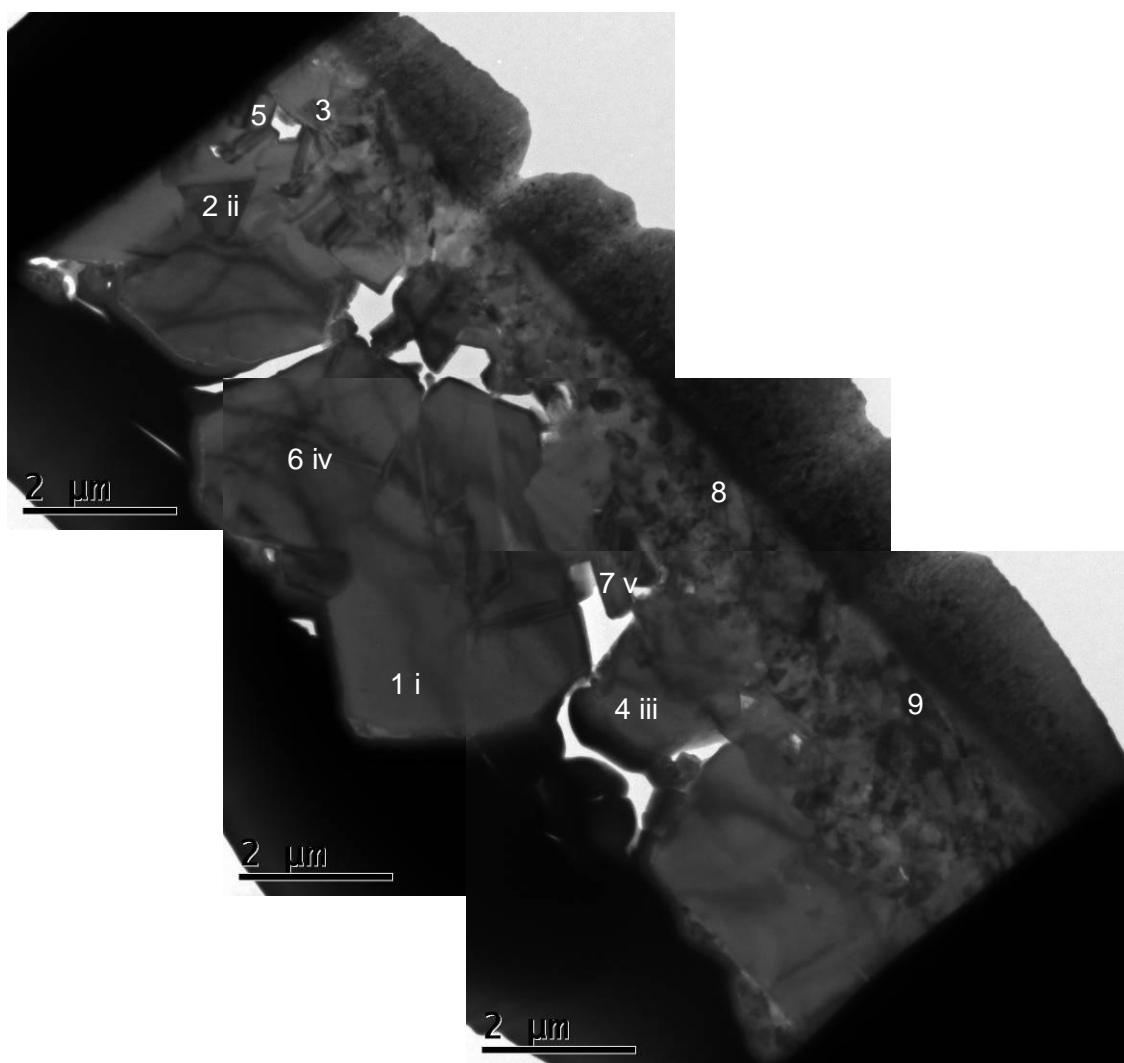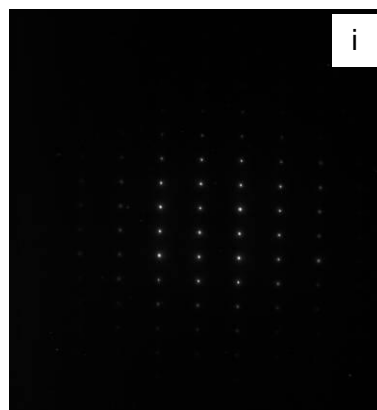
A site specific sample was removed from the SENB specimen using the dual beam FIB FEGSEM and examined using TEM. The location of the TEM specimen is shown by the red rectangle on the micrograph in Figure 5.44. It is parallel to the crack growth direction and cuts through several multifaceted oxide shapes on the edge of the crack surface. A composite image of TEM micrographs is displayed in Figure 5.45. The

sample is unavoidably orientated diagonally due to the constraints of the TEM sample holder. The sample is also orientated 180° relative to the sample shown in Figure 5.41. In Figure 5.45 the outer edge of the specimen is nearest to the micron markers. There are two distinct layers visible in the micrographs. The outer layer consists of crystals with dimensions measuring several microns whilst the inner layer consists of multiple sub micron-sized crystals. In the outer layer it is possible to see the geometric shape of the multifaceted oxide through which the TEM sample was collected. In between these layers there are locations which appear like a transition between the inner and outer layers as the oxide crystals have a geometric shape but the crystals are much smaller than those of the outer layer.
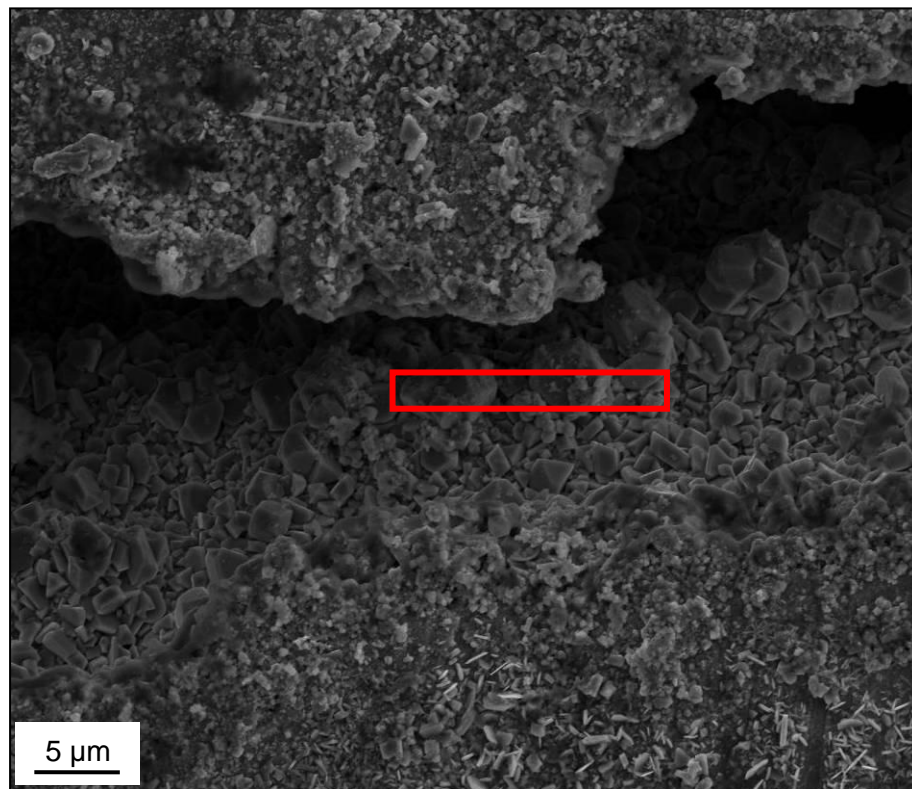
Figure 5.44: Secondary electron micrograph showing the crack through the SENB specimen exposed to condensing steam at 95°C for 5.8 kh.

Analysis of the SAD pattern collected from point i in Figure 5.45 gave solutions for maghemite (γ-Fe$_2$O$_3$), magnetite (Fe$_3$O$_4$), goethite (FeO(OH)) and nickel chromium oxide (NiCr$_2$O$_4$). Table 5.2 containts the EDS spectra data for the points 1-9 marked on Figure 5.45. EDS spectrum 1 was collected from the same crystal as the SAD pattern in Figure 5.46. It shows that only iron and oxygen were present, which eliminates nickel chromium oxide (NiCr$_2$O$_4$) as a possible solution for this crystal.

Figure 5.45: Composite image of transmission electron micrographs showing a site-specific sample removed from the crack through the SENB specimen exposed to condensing steam at 95°C for 5.8 kh. The letters i-iv correspond to the selected area diffraction patterns shown in Figure 5.46 - Figure 5.50 and the numbers 1-9 correspond to the EDS spectra displayed in Table 5.2.
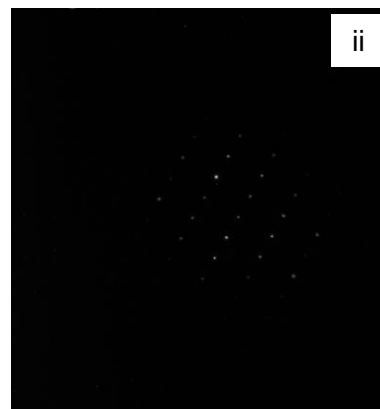
	h	k	l	d_1	h	k	l	d_2	u	v	w	Angle
Measured				2.966				2.514				31°
γ-Fe_2O_3	0	$\bar{2}$	$\bar{2}$	2.9483	1	$\bar{3}$	$\bar{1}$	2.5143	$\bar{2}$	$\bar{1}$	1	31.5°
Fe_3O_4	0	$\bar{2}$	$\bar{2}$	2.9684	1	$\bar{3}$	$\bar{1}$	2.5315	$\bar{2}$	$\bar{1}$	1	31.5°
Fe_2O_3												
FeO(OH)	0	0	$\bar{1}$	3.0220	0	$\bar{2}$	$\bar{1}$	2.5833	1	0	0	31.3°
FeO(OH)	0	$\bar{1}$	$\bar{1}$	2.8917	1	$\bar{1}$	$\bar{1}$	2.4494	0	$\bar{1}$	1	32.1°
Cr_2O_3												
FeO												
$NiCr_2O_4$	0	$\bar{2}$	$\bar{2}$	2.9402	1	$\bar{3}$	$\bar{1}$	2.5074	$\bar{2}$	$\bar{1}$	1	31.5°

Figure 5.46: Selected area diffraction pattern collected from point i in Figure 5.45.

172

	h	k	l	d_1	h	k	l	d_2	u	v	w	Angle
Measured				3.0146				2.575				32°
γ-Fe$_2$O$_3$	0	$\bar{2}$	$\bar{2}$	2.9483	1	$\bar{3}$	$\bar{1}$	2.5143	2	$\bar{1}$	1	31.5°
Fe$_3$O$_4$	0	$\bar{2}$	$\bar{2}$	2.9684	1	$\bar{3}$	$\bar{1}$	2.5315	2	$\bar{1}$	1	31.5°
Fe$_2$O$_3$												
FeO(OH)	0	0	$\bar{1}$	3.0220	0	$\bar{2}$	$\bar{1}$	2.5833	1	0	0	31.3°
FeO(OH)	0	$\bar{1}$	1	2.8917	1	$\bar{1}$	$\bar{1}$	2.4494	0	$\bar{1}$	1	32.1°
Cr$_2$O$_3$												
FeO												
NiCr$_2$O$_4$	0	$\bar{2}$	$\bar{2}$	2.9402	1	$\bar{3}$	$\bar{1}$	2.5074	2	$\bar{1}$	1	31.5°

Figure 5.47: Selected area diffraction pattern collected from point ii in Figure 5.45.

	h	k	l	d_1	h	k	l	d_2	u	v	w	Angle
Measured				4.8630				48630				71°
γ-Fe$_2$O$_3$												
Fe$_3$O$_4$	1	$\bar{1}$	$\bar{1}$	4.8474	1	$\bar{1}$	1	4.8474	1	$\bar{1}$	0	70.5°
Fe$_2$O$_3$												
FeO(OH)												
Cr$_2$O$_3$												
FeO												
NiCr$_2$O$_4$												

Figure 5.48: Selected area diffraction pattern collected from point iii in Figure 5.45

	h	k	l	d_1	h	k	l	d_2	u	v	w	Angle
Measured				2.966				2.472				64°
γ-Fe$_2$O$_3$												
Fe$_3$O$_4$	0	$\bar{2}$	$\bar{2}$	2.9684	1	$\bar{3}$	$\bar{1}$	2.5315	4	$\bar{1}$	1	64.5°
Fe$_2$O$_3$												
FeO(OH)												
Cr$_2$O$_3$												
FeO												
NiCr$_2$O$_4$												

Figure 5.49: Selected area diffraction pattern collected from point iv in Figure 5.45

173

	h	k	l	d_1	h	k	l	d_2	u	v	w	Angle
Measured				2.933				2.514				31°
γ-Fe_2O_3	0	$\bar{2}$	$\bar{2}$	2.9483	1	$\bar{3}$	$\bar{1}$	2.5143	2	$\bar{1}$	1	31.5°
Fe_3O_4	0	$\bar{2}$	$\bar{2}$	2.9684	1	$\bar{3}$	$\bar{1}$	2.5315	2	$\bar{1}$	1	31.5°
Fe_2O_3												
FeO(OH)	0	$\bar{1}$	$\bar{1}$	2.8917	1	$\bar{1}$	$\bar{1}$	2.4494	0	$\bar{1}$	1	32.1°
Cr_2O_3												
FeO												
$NiCr_2O_4$	0	$\bar{2}$	$\bar{2}$	2.9402	1	$\bar{3}$	$\bar{1}$	2.5074	2	$\bar{1}$	1	31.5°

Figure 5.50: Selected area diffraction pattern from point v in Figure 5.45

Table 5.2: Quantitative EDS spectra collected from a site-specific sample extracted from the SENB specimen exposed to condensing steam at 95°C for 5.8 kh shown in Figure 5.45

Spectrum Number		Element				
		O	Cr	Mn	Fe	Ni
1	Wt%	17.7			82.3	
	At%	42.9			57.1	
2	Wt%	21.0			79.0	
	At%	48.1			51.9	
3	Wt%	25.3			74.7	
	At%	54.4			45.9	
4	Wt%	23.9			76.1	
	At%	52.3			47.7	
5	Wt%				100	
	At%				100	
6	Wt%	21.1			78.9	
	At%	48.2			51.8	
7	Wt%	23.3			76.7	
	At%	51.4			48.6	
8	Wt%	16.5	5.6		75.7	2.2
	At%	40.8	4.3		53.5	1.5
9	Wt%		13.0		77.4	9.6
	At%		13.9		77.1	9.1

Figure 5.47 shows the SAD pattern collected from point ii on Figure 5.45. Analysis of this pattern shows the same solutions as the SAD pattern collected from point i in Figure 5.46. Table 5.2 shows that EDS spectrum 2 only contains iron and oxygen, which also rules out nickel chromium oxide ($NiCr_2O_4$) as a possible solution for this crystal.

Figure 5.48 shows the SAD pattern collected from point iii on Figure 5.45 and Figure 5.49 shows the SAD pattern collected from point iv on Figure 5.45. Analysis of both patterns show solutions for magnetite (Fe_3O_4) only. Table 5.2 shows that the corresponding EDS spectra 4 and 6 contain only iron and oxygen, which is consistent with a solution for magnetite (Fe_3O_4).

EDS spectra 8 and 9 show were collected from the inner layer of small particles on Figure 5.45. These spectra show iron, chromium and nickel is present but no oxygen. It is possible that the layer of smaller crystals is part of the substrate or that oxygen was undetectable at these points.

5.6. Summary

In this Chapter, the results from the SENB specimens have been presented and discussed. The SENB specimens have been examined using a combination of optical and electron microscopy and chemical analysis. The results from the examination of closed cracks and the crack surfaces are largely inconclusive. This is possibly because the range of exposure times was quite narrow and therefore the cracks may not have exceeded the incubation time required for SCC to propagate.

6. Results and Discussion: Free Surfaces

A set of specimens dubbed "free surfaces" were exposed to condensing steam at 95°C for times of 2.9, 4.4, 5.8, 7.3, 8.8 and 10.2 kh. These specimens were small cuboids 20 x 20 x 10 mm, cut from the same hot rolled slab of FV520B as the SENB specimens. One 20 x 20 mm surface of each specimen was prepared to either 1 µm or 220 grit finish and then one of each surface finish was exposed to condensing steam for the times stated above. The specimens are described as free surfaces because they were not stressed throughout the exposure time and the focus is the surface rather than a crack. The purpose of these specimens was to be able to compare the oxidation of a surface with that of a crack. After exposure they were examined using SEM, the results of which are presented and discussed in this Chapter.

6.1. Substrate Microstructure

The substrate microstructure was identical to that shown in Figure 5.2 as the Free Surface specimens were made from the same hot rolled slab of FV520B as the SENB specimens presented and discussed in Chapter 5.

6.2. Surface Analysis

The surface of the specimens prepared prior to exposure to condensing steam was examined using SEM.

6.2.1. Exposure Time: 10.2 kh

Figure 6.1 shows two secondary electron micrographs of the free surface specimen prepared to 1 µm and exposed to condensing steam at 95°C for 10.2 kh. After 14 months in the condensing steam environment there is fairly little damage to the surface. There are small amounts of oxide dotted around the surface and some evidence of pitting. In Figure 6.1 (a) there is a red rectangle highlighting one of the pits present on the specimen. This pit is shown in higher magnification in Figure 6.1 (b).

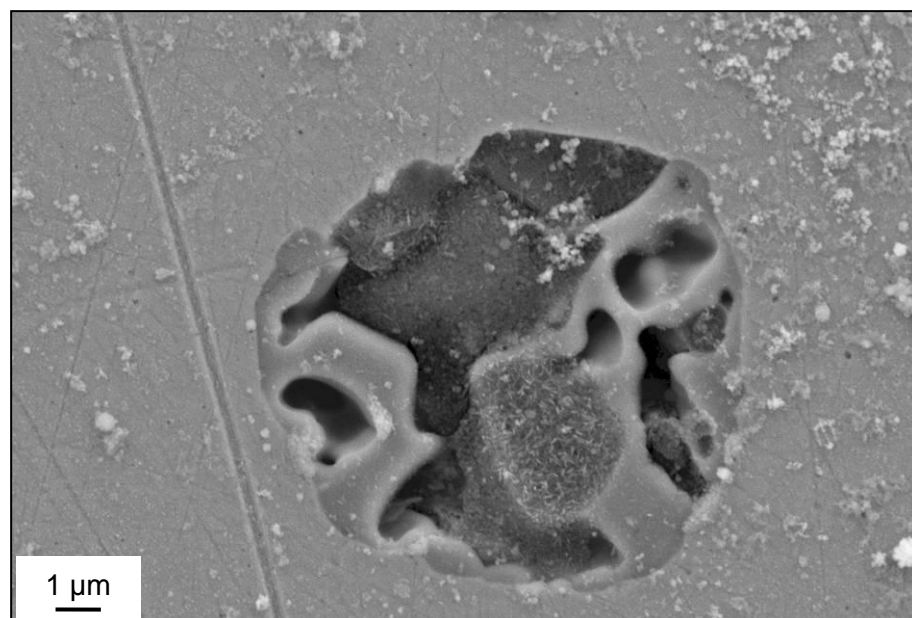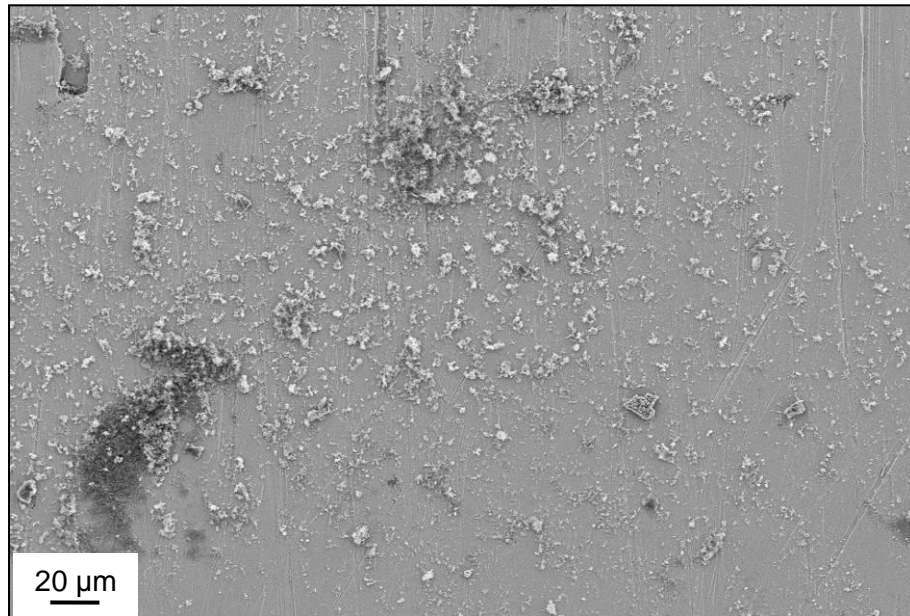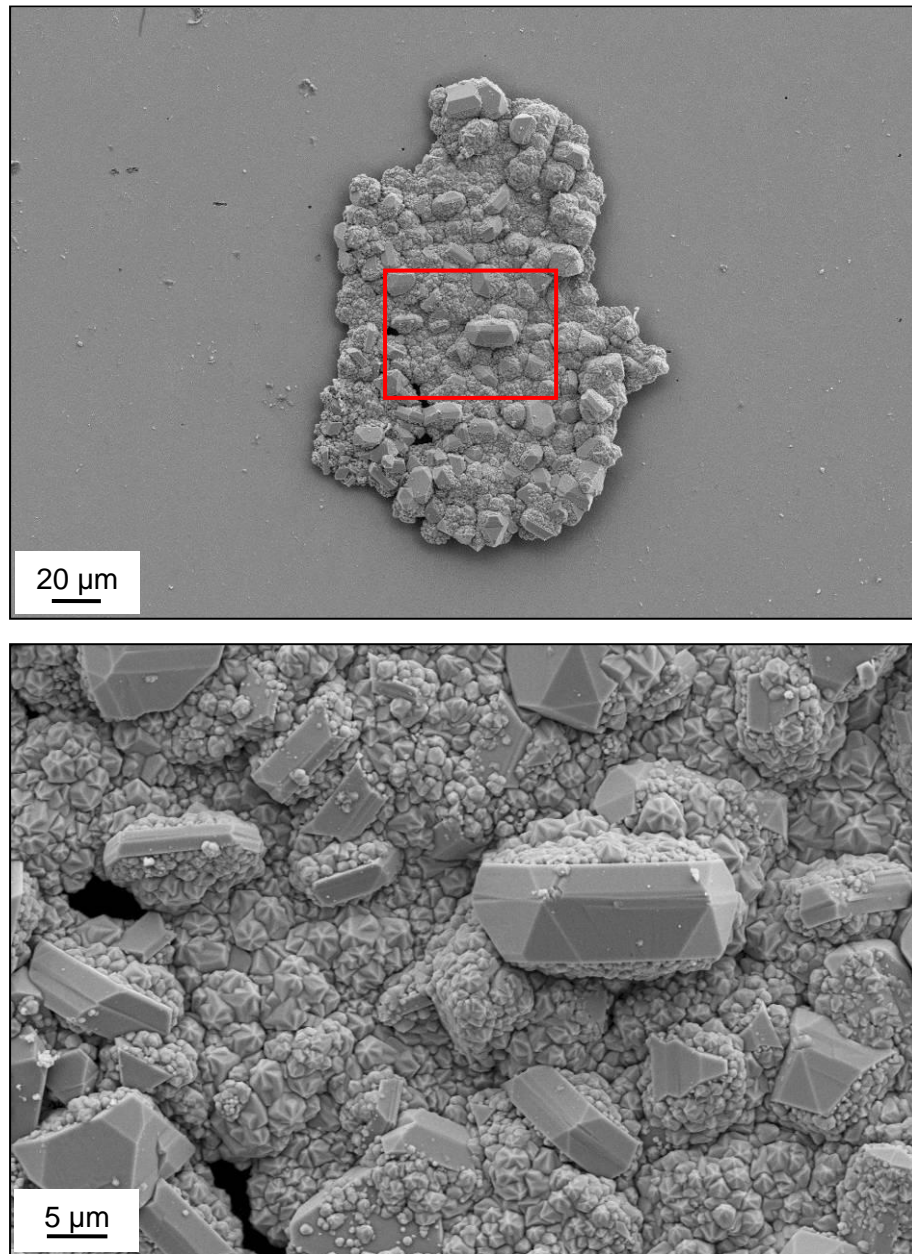Figure 6.2 shows a secondary electron micrograph of the free surface specimen prepared to 220 grit and exposed to condensing steam at 95°C for 10.2 kh. This micrograph is at the same magnification as Figure 6.1 so they are comparable with each other. The appearance of the oxide in Figure 6.2 is very similar to that in Figure 6.1, but the surface of the specimen prepared to 220 grit has corroded more than the specimen prepared to 1 µm grit for the same exposure time.
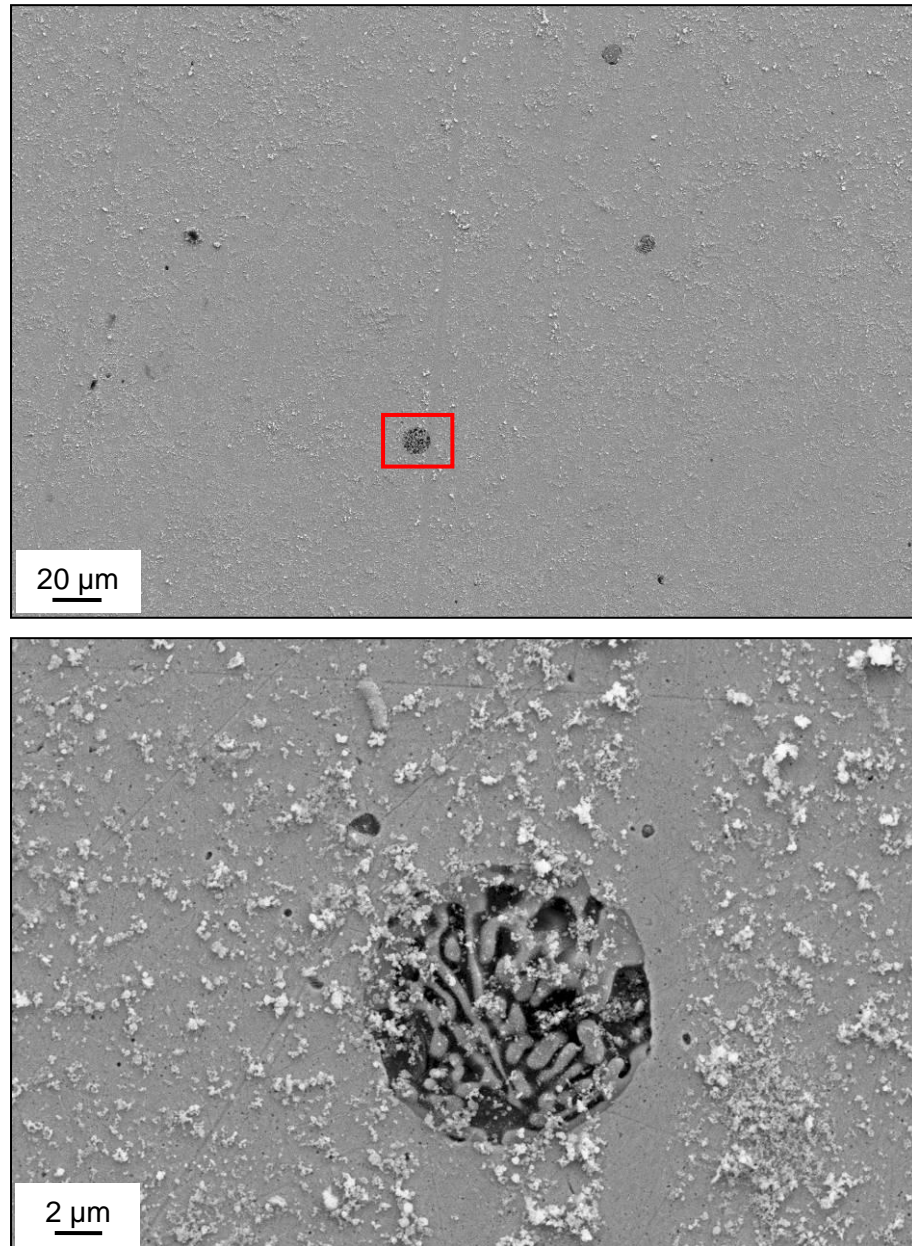
Figure 6.1: Secondary electron micrograph showing (a) the pitting and general oxidation on the free surface specimen prepared to 1 µm and exposed to condensing steam at 95°C for 10.2 kh and (b) a higher magnification micrograph of a pit highlighted by the red rectangle.

Figure 6.2: Secondary electron micrograph showing the free surface specimen prepared to 220 grit and exposed to condensing steam at 95°C for 10.2 kh.
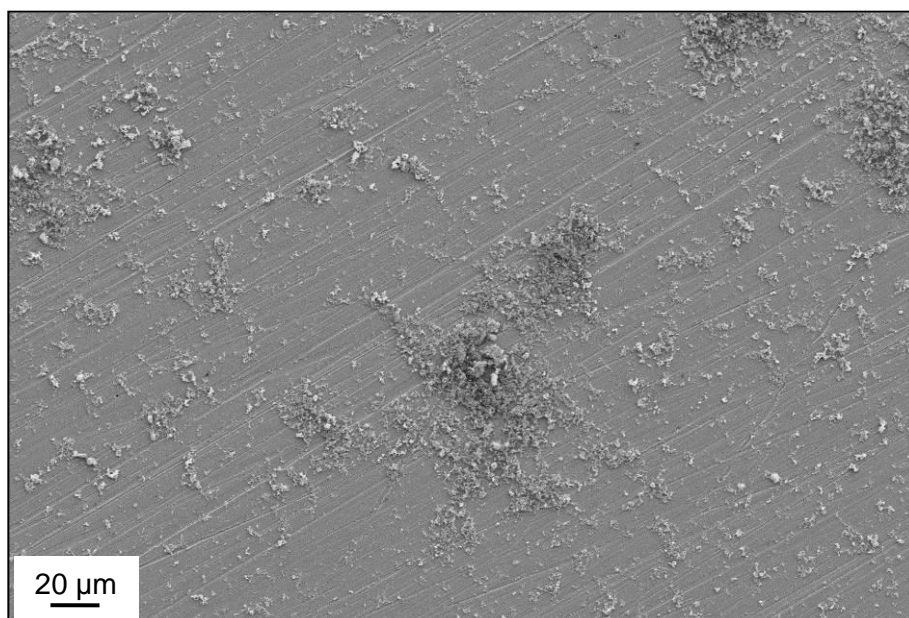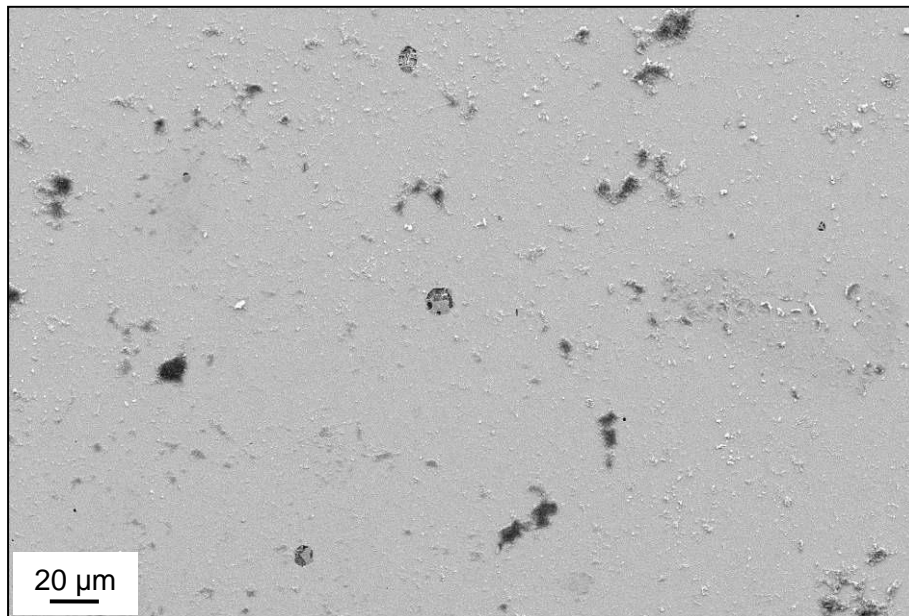
6.2.2. Exposure Time: 8.8 kh

Figure 6.3 and Figure 6.4 show secondary electron micrographs of the free surface specimen prepared to 1 µm surface finish and exposed to condensing steam at 95°C for 8.8 kh. The appearance of the specimen is very similar to that of the specimen prepared to 1 µm and exposed to condensing steam for the longer time of 10.2 kh. There is little oxide scattered about the surface but there are several pits ~5 µm in diameter, one of which is highlighted in Figure 6.4.

Figure 6.5 shows a secondary electron micrograph of the specimen prepared to 220 grit and exposed to condensing steam at 95°C for 8.8 kh. This specimen has more oxide on the surface than the specimen exposed for the same time but prepared to 1 µm and more than both the specimens exposed to condensing steam at 95°C for 10.2 kh.
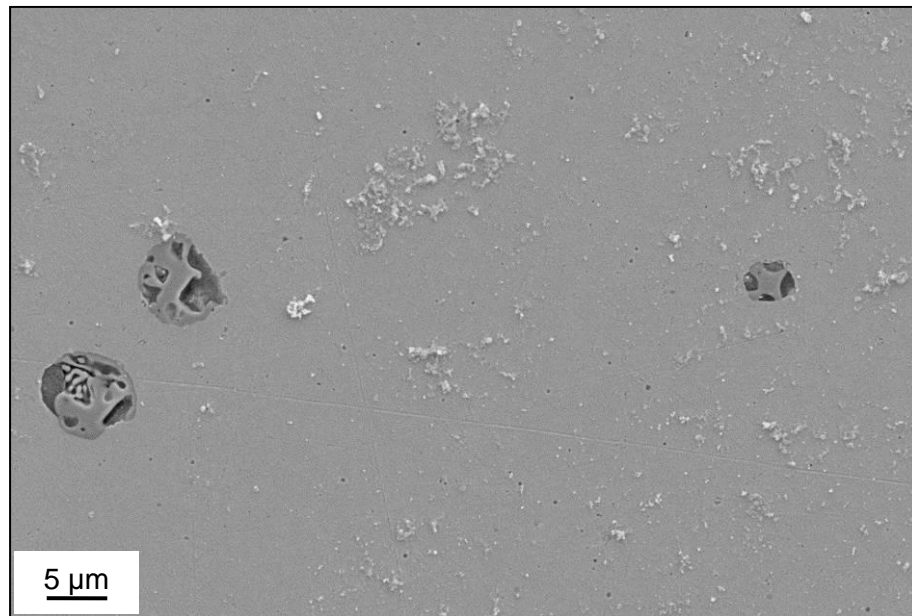
Figure 6.3: Secondary electron micrograph showing pitting and general corrosion on the free surface specimen prepared to 1 µm and exposed to condensing steam at 95°C for 8.8 kh.

Figure 6.4: Secondary electron micrograph showing a pit on the free surface specimen prepared to 1 µm and exposed to condensing steam at 95°C for 8.8 kh.
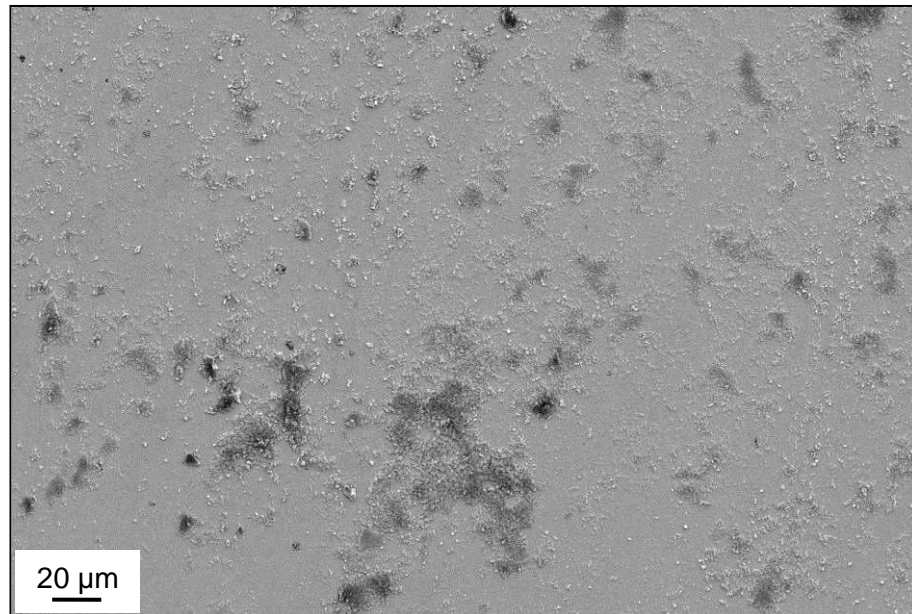
Figure 6.5: Secondary electron micrograph showing the free surface specimen prepared to 220 grit and exposed to condensing steam at 95°C for 8.8 kh.

6.2.3. Exposure Time: 7.3 kh

Figure 6.6 shows the free surface specimen prepared to 1 μm and exposed to condensing steam at 95°C for 7.3 kh. Figure 6.6 (a) shows an island of oxide on the surface of the specimen approximately 200 x 130 μm. This was the only island found on the specimen, however, there were some smaller oxide particles scattered over the surface, similar to the specimens exposed for longer times. Figure 6.6 (b) shows a higher magnification of the portion of the island of oxide highlighted by the red box in Figure 6.6 (a). The island consists of large geometric shaped oxide with smooth surfaces in a bed of smaller oxide.

Figure 6.7 shows a secondary electron micrograph of the free surface specimen prepared to 220 grit and exposed to condensing steam at 95°C for 7.3 kh. There are small amounts of oxide dotted about the surface, similar to the specimen prepared to 220 grit and exposed to condensing steam at 95°C for 8.8 kh.

Figure 6.6: Secondary electron micrograph showing (a) an agglomeration of oxide on the free surface prepared to 1 µm and exposed to condensing steam for 7.3 kh and (b) a higher magnification micrograph of a section of the oxide highlighted by the red rectangle.

Figure 6.7: Secondary electron micrograph showing the free surface specimen prepared to 220 grit and exposed to condensing steam at 95°C for 7.3 kh.
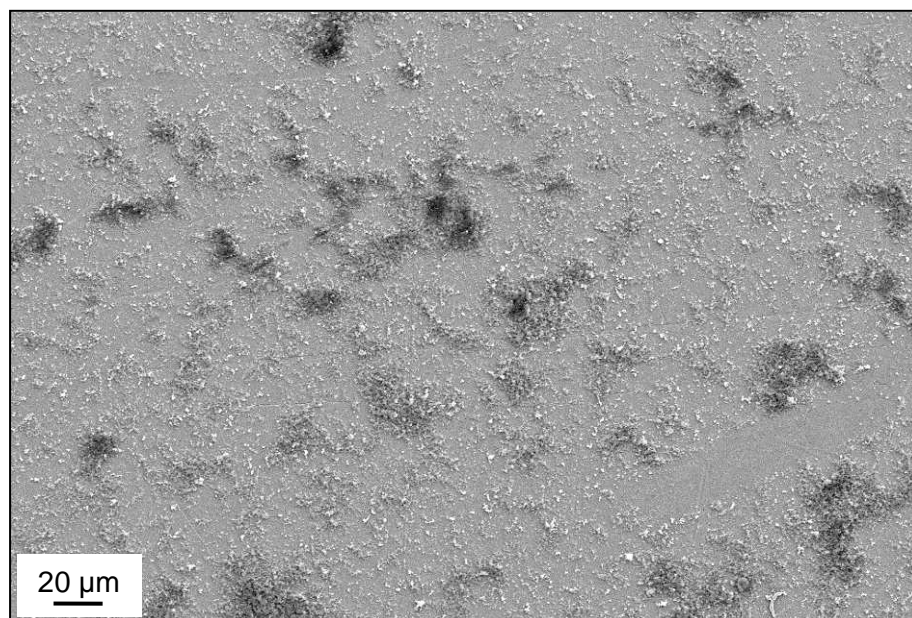
6.2.4. Exposure Time: 5.8 kh

Figure 6.8 shows a secondary electron micrograph of the specimen prepared to 1 μm and exposed to condensing steam for at 95°C for 5.8 kh. The appearance of the surface is similar to the specimens prepared to 1 μm and exposed to condensing steam for 10.2 kh (Figure 6.1) and 8.8 kh (Figure 6.3).

There are small amounts of oxide present on the surface and several pits. In general the oxide on the surface is present in larger agglomerations than the specimens exposed to the same conditions for longer times.

Figure 6.9 shows a secondary electron micrograph of the specimen prepared to 220grit and exposed to condensing steam at 95°C for 5.8 kh. Similarly to the other specimens, there is oxide scattered over the surface and the amount is greater than the specimen prepared to 1 μm prior to exposure to the experimental conditions.

Figure 6.8: Secondary electron micrograph showing oxidation and pitting on the free surface specimen prepared to 1 μm and exposed to condensing steam at 95°C for 5.8 kh.

Figure 6.9: Secondary electron micrograph showing the free surface specimen prepared to 220 grit and exposed to condensing steam at 95°C for 5.8 kh.

6.2.5. Exposure Time: 4.4 kh

Figure 6.10 shows a secondary electron micrograph of the specimen prepared to 1 μm finish and exposed to condensing steam at 95°C for 4.4 kh. Figure 6.11 shows a secondary electron micrograph of the specimen prepared to 220 grit and exposed to condensing steam at 95°C for 4.4 kh. Both specimens have very similar appearance. There are small particles of oxide littering the surfaces of both specimens with larger

areas of oxide which are a darker grey in the micrographs. The specimen prepared to 220 grit exhibits a slightly greater level of oxidation than the specimen prepared to 1 µm prior to exposure to condensing steam.

Figure 6.10: Secondary electron micrograph showing the free surface specimen prepared to 1 µm and exposed to condensing steam at 95°C for 4.4 kh.

Figure 6.11: Secondary electron micrograph showing the free surface specimen prepared to 220 grit and exposed to condensing steam at 95°C for 4.4 kh.

6.2.6. Exposure Time: 2.9 kh

Figure 6.12 shows a secondary electron micrograph of the free surface specimen prepared to 1 µm and exposed to condensing steam at 95°C for 2.9 kh. Figure 6.13

shows a secondary electron micrograph of the free surface specimen prepared to 220 grit and exposed to condensing steam at 95°C for 2.9 kh. The specimen prepared to 1 μm prior to exposure to experimental conditions has more oxide on the surface than the specimen prepared to 220 grit, which has very little oxidation present.
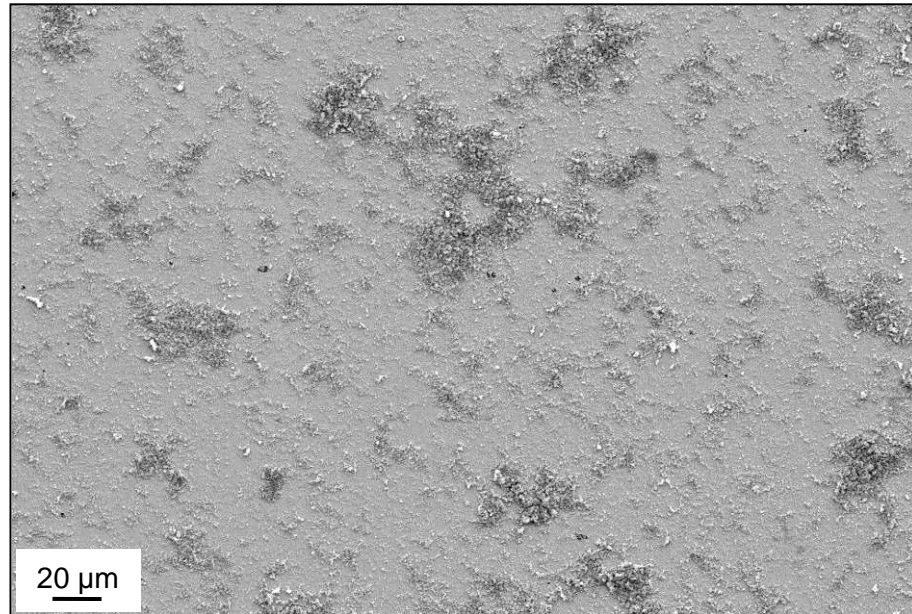
Figure 6.12: Secondary electron micrograph showing the free surface specimen prepared to 1 μm and exposed to condensing steam at 95°C for 2.9 kh.
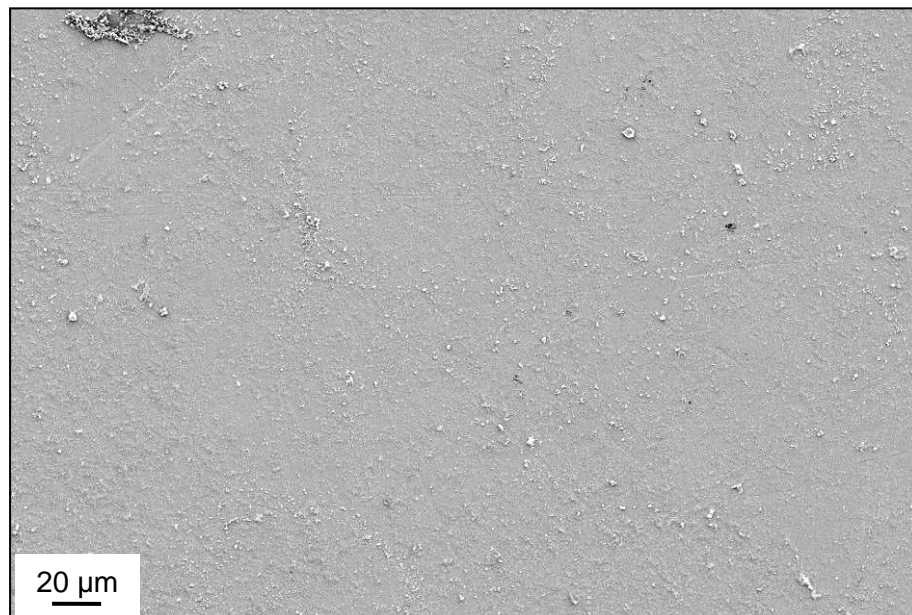
Figure 6.13: Secondary electron micrograph of the free surface specimen prepared to 220 grit and exposed to condensing steam at 95°C for 2.9 kh.

6.2.7. Oxide Development

The results of the examination of the prepared faces of the Free Surface specimens showed no trend with respect to oxide development at various exposure times. It was expected that the specimens exposed to condensing steam at 95°C for longer times would have corroded more than those exposed for shorter times. This was not found to be true as the majority of the specimens had an extremely similar amount of oxide present on the surface.

In general, for the same exposure time, the specimens prepared to 220 grit had slightly more oxidation that the specimens prepared to 1 µm. However, the specimen prepared to 1 µm and exposed to condensing steam for 2.9 kh showed more oxide than the specimen exposed for the same time but prepared to 220 grit prior to exposure to the experimental conditions. Pitting was only found in the specimens prepared to 1 µm and exposed for 10.2, 8.8 and 5.8 kh.

The most severe corrosion was the island of mixed morphology oxide shown in Figure 6.6; the specimen prepared to 1 µm and exposed to condensing steam at 95°C for 7.3 kh. None of the other specimens had anything similar on the surface.

The results of the examination of the Free Surface specimens show that environment created within a crack is very different from that experienced by the external surfaces of specimens exposed to the same experimental conditions. Very little corrosion damage was present on the Free Surface specimens. The evidence of pitting shows the potential for SCC to occur as pits can often be the precursors for crack initiation and propagation. Cracks could initiate if the appropriate conditions are created and the pit depth to diameter ratio becomes 10:1 (ASM International Handbook Committee, 1987).

6.3. Summary

The Free Surface specimens were prepared to a surface finish of either 220 grit or 1µm and exposed to condensing steam at 95°C for times between 2.9 and 10.2 kh. The results show that there is no trend in the amount of corrosion to the surface relative to the amount of time the specimens were exposed to the condensing steam. The results do show that the conditions experienced by the surface of a specimen is very different from that experienced within a crack.

7. Comparison of WOL and SENB Specimens

In Chapter 4 the results for a set of 16 WOL specimens exposed to condensing steam at 95°C for 7.5, 9.8, 13.0 and 98.3 kh were presented and discussed. In Chapter 5 the results for a set of SENB specimens exposed to condensing steam at 95°C for times between 0.7 and 8.8 kh were presented and discussed. In Chapter 6 the results from a set of Free Surface specimens exposed to condensing steam at 95°C for 2.9 – 10.2 kh were presented and discussed. In this Chapter the results from the WOL, SENB and Free Surface specimens are compared and contrasted.

The Free Surface specimens were exposed to condensing steam at 95°C for many of the same times as the SENB specimens. The aim of the Free Surface specimens was to be able to compare the oxidation present on an external, unstressed surface with that which forms on a newly created surface within a crack.

The results of the examination of the Free Surface specimens shown that in all but one specimen, there was very little oxidation present at any of the exposure times. There was no obvious trend in the amount of oxide present as again, all but one of the specimens had similar appearance. The oxide present on the Free Surface specimens resembled that which was on the outer surface surrounding the crack through many of the SENB specimens that were examined prior to breaking open the crack.

Excluding the specimen exposed for 7.3 kh, the appearance of the Free Surface specimens was very different from the appearance of the crack surfaces of the WOL and SENB specimens after exposure to condensing steam at 95°C for various times. The amount of oxidation within the cracks of the WOL and SENB specimens is far more severe than the Free Surface Specimens. The results support the idea that the localised conditions created within a crack are very different from those experienced by an open surface, even though they are exposed to the same surrounding environment.

The results of the Free Surface specimens show that corrosion pits form after prolonged exposure to condensing steam. Pits are often precursors to stress corrosion cracks (ASM International Handbook Committee, 1987), so if these specimens had been subject to loading during exposure to condensing steam at 95°C it is possible that SCC would have initiated.

Examination of the WOL and SENB specimens showed several similarities in the appearance of the oxide within the cracks. The WOL specimens exposed to condensing steam at 95°C for 98.3 kh had several different geometric shaped oxide particles present on the crack surfaces, including cubes, octahedrons and cuboctahedra etc. Figure 5.14 shows a cuboctahedron within the crack through the SENB specimen exposed to condensing steam at 95°C for 5.8 kh, similar to that shown in Figure 4.24. Figure 5.17 shows an agglomeration of hexagonal platelet oxide in a SENB specimen exposed to experimental conditions for 4.4 kh, which is similar to that shown in Figure 4.21 in the WOL specimen 799 (1061 MPa, 98.3 kh).

The WOL specimens exposed to condensing steam at 95°C for 7.5, 9.8 and 13.0kh were not pre-cracked prior to testing so it is unclear as to when the cracks initiated and when they propagated. The surfaces created when the cracks formed in the WOL specimens would only have been exposed to the steam for a portion of the total exposure time. As all the SENB specimens were pre-cracked prior to exposure to experimental conditions, the crack surfaces were exposed to steam for the entire testing time. Therefore, many of the SENB specimen cracks are likely to have been exposed to condensing steam for longer than the WOL specimens. This would explain why the oxide development within many of the SENB specimens, which were exposed for up to 8.8 kh, had an appearance that more closely resembled the WOL specimens exposed for 98.3 kh rather than the WOL specimens exposed for shorter times.

8. Conclusions

WOL, SENB and Free surface specimens have been exposed to condensing steam at 95°C for times between 0.7 and 98.3 kh. The conclusions from the examination of these specimens are detailed in this Chapter.

8.1. Substrate Microstructure

Optical microscopy was used to examine the substrate microstructure of the WOL specimens with different proof strengths of 1018, 1024, 1061 and 1072 MPa. The micrographs in Figure 4.2 showed that all the samples had a homogeneous martensitic microstructure, in all three planes, which was interspersed with precipitates within the grains and decorating the prior austenite grain boundaries. The prior austenite grain boundaries are identified by the uniform direction of the martensite laths within each visible grain. From these results it can be deduced that substrate microstructure played little part in the different crack lengths seen on the samples exposed to condensing steam for various times.

The SENB and Free Surface specimens were made from the same hot rolled slab of FV520B. The microstructure is shown in Figure 5.2. As all the specimens were made from the same slab of steel, the substrate microstructure is not a variable that contributed to any variation between the specimens after testing.

8.2. Proof Strength

The crack lengths of the WOL specimens were examined with respect to proof strength within the groups of identical exposure time. The show that the effect of proof strength SCC is inconclusive as for some specimens the cracks are longer in the specimens with higher proof strength but for others they are shorter. This is, however, not a direct comparison as proof strength was not the only variable that changed between the specimens exposed for the same time.

8.3. Initial Stress Intensity

The results show that initial stress intensity at the crack tip plays an important role in the initiation and possibly the propagation of stress corrosion cracks. From examination of the WOL specimens there was evidence to support that the threshold stress intensity value for SCC in FV520B was between 5 MPam$^{\frac{1}{2}}$ and 8 MPam$^{\frac{1}{2}}$. This is an approximation as the threshold stress intensity would be specific to the proof stress of the steel if the literature suggesting that higher proof strength steels are more susceptible to SCC is correct.

The initial stress intensity of specimen 800 (1061 MPa, 13.0 kh) was 8 MPam$^{\frac{1}{2}}$ and the crack length was shorter than specimen 802 (1061 MPa, 7.5 kh), which had the same proof strength but was exposed for a shorter time. This can be attributed to the fact that the initial stress intensity of specimen 802 (1061 MPa, 7.5 kh) was 62.5 MPam$^{\frac{1}{2}}$. The higher stress initial stress intensity meant that the crack could initiate earlier and therefore propagate further in a shorter overall exposure time. When the initial stress intensity was increased to around 16 MPam$^{\frac{1}{2}}$, as it was for specimens 804 (1024 MPa, 13.0 kh), 808 (1018 MPa, 13.0 kh) and 812 (1072 MPa, 13.0 kh), the cracks were longer than the specimens exposed to 7.5 kh in the respective proof strength groups. This suggests that the initial stress intensity is important to the incubation time before a crack initiates.

The SENB specimens show further evidence to support this idea. All the SENB had the same loading and number of cycles to form the fatigue pre-crack and had the same load applied during exposure to condensing steam at 95°C. The SENB specimens had pre-cracks of similar length apart from the specimen exposed for the shortest time of 0.7kh, which had a shorter pre-crack. This means that the initial stress intensity at the pre-crack tip would have been higher than all the other specimens for the same applied load. This specimen showed evidence that the crack may have grown during the very short exposure time. This supports the idea that the increased stress intensity at the crack tip promoted earlier crack initiation.

8.4. Oxide Characterisation

On the crack surfaces of the WOL and SENB specimens there were some large geometric oxide crystals including cubes, octahedrons and cuboctahedra. From examination of these crystals using a combination of FIB FEGSEM, TEM and EDS it

was possible to identify that these features had an iron oxide composition with some nickel substitution. Much of the smaller grained oxide on which the large features sat, contained chromium. The oxide within the cracks which branched into the substrate was also rich in chromium.

8.5. Crack Dating

Examination of the WOL specimens found evidence to suggest that the depth of cracks which branch from the main stress corrosion crack could be correlated with length of the main crack. The penetration depth of branching cracks into the substrate decreases with distance along the main crack for specimens 799 (1061 MPa, 98.3 kh), 803 (1024 MPa, 98.3 kh), 807 (1018 MPa, 98.3 kh) and 811 (1072 MPa, 98.3 kh).

Examination of the WOL specimens found evidence to suggest that the surface oxide appearance can be correlated with exposure time. With a few exceptions, the groups of specimens within each exposure time have crack surfaces with similar appearance to each other, but look different to specimens with other exposure times. The difference between the specimens exposed for 98.3 kh and the remaining specimens is the most dramatic, whereas distinguishing between the 13.0 kh, 9.8 kh and 7.5 kh specimens is more difficult.

Using the assumption that stress corrosion crack propagation is linear, it was possible to build up a map of oxide development with exposure time based on specimen 799 (1061 MPa, 98.3 kh). The crack initiation was assumed to have been exposed for the full 98.3 kh whereas the crack tip was exposed for 0 h. Portions of the crack have been shown to match the entire crack surfaces of specimens exposed to condensing steam for 13.0 kh and 7.5 kh.

The XRD data collected from the WOL specimens was consistent with the visual results collected from the crack surfaces of all the specimens. The strongest peaks were present in the XRD patterns for the specimens exposed for 98.3 kh. There were some small oxide peaks in the specimens exposed for 13.0 kh and it was difficult to determine any oxide peaks from the XRD patterns collected from the crack surfaces of the specimens exposed for 7.5 kh.

There were oxide peaks in the XRD patterns for the specimens exposed for 9.8 kh that were bigger than those seen for the specimens exposed for 13.0 kh but smaller than

those for the specimens exposed for 98.3 kh. This was consistent with the visual oxide evidence collected from the crack surfaces of the specimens exposed for 9.8 kh.

Using XRD it is possible to distinguish between the specimens exposed for 98.3 kh and the specimens exposed for 13.0, 9.8 and 7.5 kh. It is not possible to accurately differentiate the XRD patterns from the specimens exposed for 13.0 kh and 7.5 kh, but it is possible to distinguish them from the specimens exposed for 9.8 kh. With some further work it is possible that XRD could be used as a comparative tool to identify the exposure time of a stress corrosion crack.

There was no trend with exposure time for the SENB or Free Surface specimens examined in cross-section or surface. This is likely to be because the total exposure time was small and may have been within the incubation time for SCC.

9. Further Work

This thesis has been written based upon the results collected from WOL, SENB and Free Surface specimens that were exposed to condensing steam at 95°C for various times. The current study has shown SCC to be a complicated process with a number of factors that could influence crack initiation and propagation.   In this Chapter, suggestions for future experiments will be presented and discussed with reference to the variables to be tested.   These suggestions aim to improve the quality of the research into SCC to help to gain a better understanding of the phenomenon. Greater knowledge would benefit the future design and manufacture of low pressure turbine blades.

9.1. WOL Exposure Time

The WOL specimens were exposed to condensing steam at 95°C for 7.5, 9.8, 13.0 and 98.3 kh.   There is approximately one order of magnitude between the 7.5, 9.8 and 13.0 kh exposure times and the 98.3 kh exposure time.   Future experiments should include exposing some WOL specimens to the same steam environment for some times that are in between 13.0 kh and 98.3 kh. For example, WOL specimens could be exposed to condensing steam at 95°C at yearly intervals which would be 17.5, 26.3, 35.0, 43.8, 52.6, 61.3, 70.1, 78.8 and 87.6 kh. To achieve results most useful to power stations, it would be appropriate to expose specimens for times which are multiples of 10 kh as these are the times that safety cases are calculated on and predictions made for future component service life.

Specimens should be made from each of the four proof strengths, 1018, 1024, 1061 and 1072 MPa and exposed to condensing steam at 95°C for the additional times suggested, so that the variable of proof strength could be investigated in more detail. If the same batches of material are to be used for the experiments then tensile tests should be carried out to confirm that the provided proof stress values are correct or determine the actual proof strength values.

9.2. WOL Initial Stress Intensity

The WOL specimens all had different values of initial stress intensity at the crack tip or notch tip. This meant that no two specimens could realistically be directly compared with each other as there was always more than one variable that differed. Sets of specimens should be exposed for various times but all with initial values of stress intensity within the narrowest range experimentally possible. In this way it would be possible to investigate the effect of exposure time more accurately as stress intensity would be a constant rather than a variable.

To investigate the effect of initial stress intensity, a second set of specimens should be exposed to the same experimental conditions as mentioned previously, and all with initial stress intensity within a narrow range, but different to the previous specimens. In this way it would be possible to see the effect of both exposure time and stress intensity.

For example, the results from the WOL specimens showed that specimens exposed for 9.8 kh with a higher initial stress intensity could have longer cracks than specimens exposed for 13.0 kh with a lower initial stress intensity. The results also showed that there was a crossover point because when the initial stress intensity for a specimen exposed for 13.0 kh was lower than the stress intensity for a specimen exposed for 7.5 kh, the crack length was shorter. When the initial stress intensity for a specimen exposed for 13.0 kh was higher that the stress intensity for a specimen exposed for 7.5 kh, the crack length was longer.

Two sets of specimens exposed for the same times but with different stress intensities would help to build up a matrix of crack length/oxide development based on different conditions as there may be two sets of conditions that produce the same results.

9.3. WOL Repeatability

The results of this thesis have been based on one specimen of each experimental condition. Ideally there should be several specimens each exposed to identical conditions (proof strength, exposure time, initial stress intensity at the notch tip) so that they can be compared with each other and not just to the specimens exposed to different conditions. By exposing several specimens to the same conditions it should

be possible to identify any spurious results at the same time as testing the repeatability of the experiments.

The WOL specimens exposed to condensing steam at 98.3 kh were fatigue pre-cracked prior to exposure whereas the other WOL specimens were not fatigue pre-cracked. Either all or none of the specimens should have been pre-cracked so the specimens could have been directly compared with each other. At present, the specimens were difficult to compare with each other.

9.4. SENB Exposure Time

It would be useful to expose SENB specimens for longer to try to prove or disprove the theory that the specimens remained in the incubation period throughout the experimental time. It would be useful to identify the duration of the incubation period using the same conditions as the previous experiments. This information would be advantageous to understanding the conditions at which a LP turbine may initiate a stress corrosion crack.

9.5. SENB Repeatability

Several specimens should be exposed to the same conditions to see if the results can be repeated or if there are unavoidable variations that have not been considered already such as grain boundary energy.

9.6. SENB Characterisation

SENB specimens should be investigated further using some of the techniques used to examine the WOL specimens, for example XRD. It might be possible to see a trend in the oxide development given the regular intervals between the exposure times. It might also be useful to try a technique such as XPS to identify the composition of the layers of oxide relative to the depth.

10. References

ASM International Committee "*Metals Handbook Ninth Edition*" Volume 13 Corrosion, 1987

Bauer, J., *"Minerals, Rocks and Precious Stones"*, Treasure Press, London, 1987

Birks, N. and Meier, G.H., "*Introduction to High Temperature Oxidation of Metals*", Edward Arnold Publishers Ltd., London, 1983.

Bhadeshia, H. K. D. H. and Honeycombe, R. "*Steels Microstructure and Properties*" Third Edition, Elsevier, Oxford, 2006

Breeze, P., "*Power Generation Technologies*", Elsevier, Oxford, 2005

Brown, W.F., "Review of developments in plane strain fracture toughness testing", American Society for Testing and Materials, 1970

Callister, Jr. W. D., "*Materials Science and Engineering An Introduction*" Fifth Edition, John Wiley and sons, Inc., New York, 2000

Central Electricity Generating Board "*Ratcliffe-on-Soar Power Station*", CEGB, Solihol, 1983

Dieter, G., "*Mechanical Metallurgy*", Third Edition, McGraw-Hill Book Company, USA, 1986

E.ON UK, "*Ratcliffe –on-Soar Power Station*", E.ON UK, Coventry, 2004

Evans, H.E., Donaldson, A.T. and Gilmour, T.C., "*Mechanisms of Breakaway Oxidation and Application to a Chromia-Forming Steel*", Oxidation of Metals, Vol 52, No. 516,1998

Flis, J.G. and Hanson, A. "*An Introduction To Stainless Steel*" American Society For Metals, Ohio, 1965

Flis, J. and Scully, J., "*Transmission Electron Microscopical Study of Corrosion and Stress Corrosion of Mild Steel in Nitrate Solution*", Corrosion Science, Volume 8, Number 4, Page 235, 1968

Foster, D. and Parfitt, S., "*How electricity is made and transmitted*" Central Electricity Generated Board, Waterloo and Sons Ltd., London 1970

Giannuzzi, L.A. and Stevie, F.A., "*Introduction to Focused Ion Beams Instumentation, Theory, Techniques and Practise*", Springer Science and Business Media Inc., USA, 2005

Goodhew, P.J., "Electron Microscopy and Analysis", Taylor & Francis, London, 2001

Hammond, C., "*The Basics of Crystallography and Diffraction*", Oxford University Press Inc., New York, 2009

Haynes, R., "*Optical Microscopy of Materials*", Blackie & Son Ltd., Glasgow, 1984

Janssen, M., Zuidema, J., and Wanhill, R. "*Fracture Mechanics Second Edition*", Spon Press, Oxford, 2002

Karpenko, G.V., and Vasilenko, I.I., "*Stress Corrosion Cracking of Steels*", Freund Publishing House, Israel, 1979

Kearton, W.J., "*Steam Turbine Operation*", Seventh Edition, Sir Isaac Pitman and Sons Ltd., London, 1964

Kearton, W.J., "*Steam Turbine Theory and Practice*", Seventh Edition, Sir Isaac Pitman and Sons Ltd., London, 1958

Kiameh, P., "*Power Generation Handbook: Selection, Applications, Operation and Maintenance*", The McGraw-Hill Companies, Inc., New York, 2002

Korda, A., Mutoh, Y., Miyashita, Y., Sadasue, T., Mannan, SL., "*In situ observation of fatigue crack retardation in banded ferrite-pearlite microstructure due to crack branching*", Scripta Materialia, Volume 54, Pages 1835-1840, 2006

Kofstad, P., "*High Temperature Corrosion*", Elsevier Applied Science Publishers Ltd., Essex, 1988.

Kubaschewski, O., "*Iron Binary Phase Diagrams*", Springer-Verlag, Germany, 1982.

Lee, H., Kin, D, Jung, J, Pyoun, Y and Shin, K., "*Influence of peening on the corrosion properties of AISI 304 stainless steel*", Corrosion Science, Volume 51, Page 2826, 2009

Leu, K. and Helle, J., "*The Mechanism of Stress Corrosion of Austenitic Stainless Steels in Hot Aqueous Chloride Solutions*", Corrosion, Volume 14 Page 249, 1958.

Lula, R.A., "*Stainless Steel*", American Society For Metals, USA, 1985

Lyle, F.F. and Burghard, H.C., "*Steam Turbine Disc Cracking Experience*", EPRI, Palo Alto, 1982

Newville, M., "Fundamentals of XAFS", Consortium for Advanced Radiation Sources, 2004

Parr, J. And Hanson, A., "*An Introduction to Stainless Steel*", American Society for Metals, Ohio, 1965

Petty, E.R., "*Martensite*", Longman Group Limited, London, 1970

Randle, V., "*Theoretical Framework for Electron Backscatter Diffraction*" from Schwartz, A.J., Kumar. M. and Adams, B.L., "*Electron Backscatter Diffraction in Materials Science*", Kluwer Academic/Plenum Publishers, New York, 2000

Richman, R.H., McNaughton, W.P. and Paterson, S.R., "*The ASME Handbook on Water Technology for Thermal Systems*", New York, 1989

Roberge, P.R., "*Handbook of Corrosion Engineering*", McGraw Hill, New Jersey, 2000

Rooyen, D., "*Some Aspects of Stress Corrosion Cracking in Austenitic Stainless Steels*", Corrosion, Volume 16, Page 421, 1960

Talbot, D. and Talbot, J., "*Corrosion Science and Technology*", CRC Press LLC, USA, 1998

Thomas. G. And Goringe, M.J., "*Transmission Electron Microscopy of Materials*", John Wiley & Sons Inc., Canada, 1979

Turnbull, A. and Zhou, S., "*Overview of Steam Turbines Part 2 – Stress Corrosion Cracking of Turbine Disc Steels*", Corrosion Engineering, Science and Technology, Volume 38, Number 3, Page 177-191, 2003

Uhlig, H.H. and Sava, J., "*Effect of Heat Treatment of Stress Corrosion Cracking of Iron and Mild Steel*", Trans. ASM, Volume 56, No 3, Page 361, 1963

Viswanathan, R. and Bakker, W.T., "*Materials For Boilers In Ultra Supercritical Power Plants*", International Joint Power Generation Conference Proceedings, 2000

Was, G.S., Ampornrat, P., Gupta, G., Teysseyre, S., West, E.A., Allen, T.R., Sridharan, K., Tan, L., Chen, Y., Ren, X. and Pister, C., "*Corrosion and Stress Corrosion Cracking in Supercritical Water*", Journal of Nuclear Materials, Volume 371, Issue 1-3, Page 176-201, 2007

Wyatt, L.M., "*Materials of Construction for Steam Power Plant*", Applied Science Publishers Ltd., London, 1976

Zhou, S., "Environmental Assisted Cracking of Turbine Blade Steels", NPL Report, 2007

http://library.thinkquest.org/C006011/english/sites/dampfturbine.php3?v=2, date viewed 15 February 2007

http://ruby.colorado.edu/~smyth/min/corundum.html, date viewed 10 May 2007

http://ruby.colorado.edu/~smyth/min/spinel.html, date viewed 10 May 2007

11. Appendix 1

In Section 4.8 XANES data collected from the Diamond light source synchrotron was presented and discussed. One spectrum collected around the iron and chromium absorption edges were included as an example for each sample. The only exception to this was for the bulk crack surface of specimen 799 (1061 MPa, 98.3 kh) where analysis of the iron absorption edge produced no results. For completeness, all analysed spectra are presented in this section.

Figure 11.1 - Figure 11.7 shows XANES spectra collected around the chromium absorption edge for the crack surface of specimen 799 (1061 MPa, 98.3 kh).

Figure 11.8 - Figure 11.15 show the XANES spectra collected around the iron absorption edge from the site specific sample through three oxide cubes on the crack surface of specimen 799 (1061 MPa, 98.3 kh).
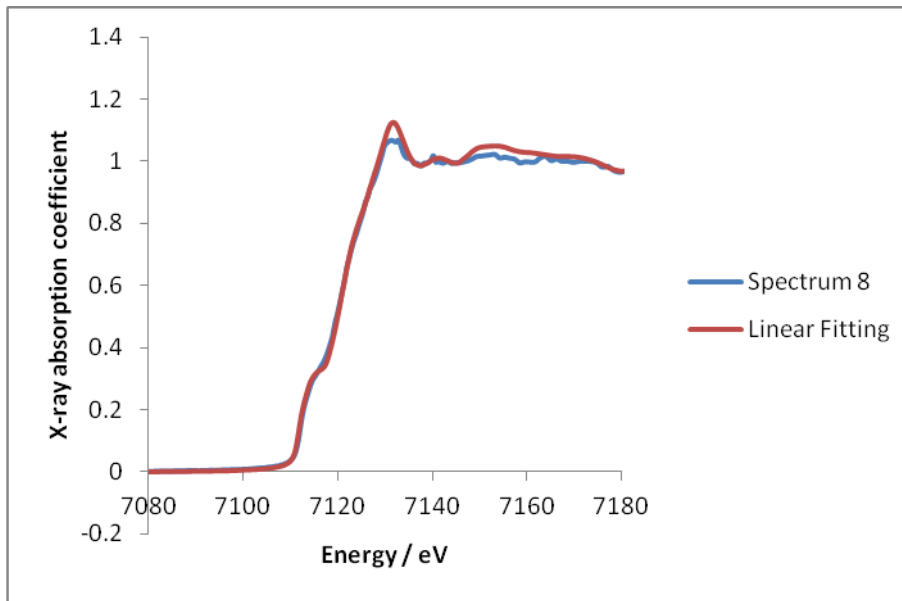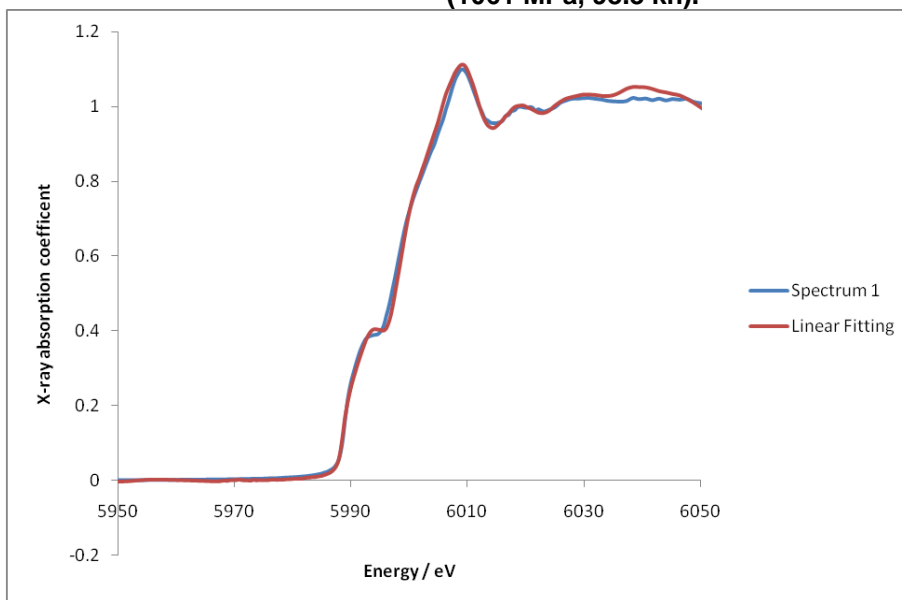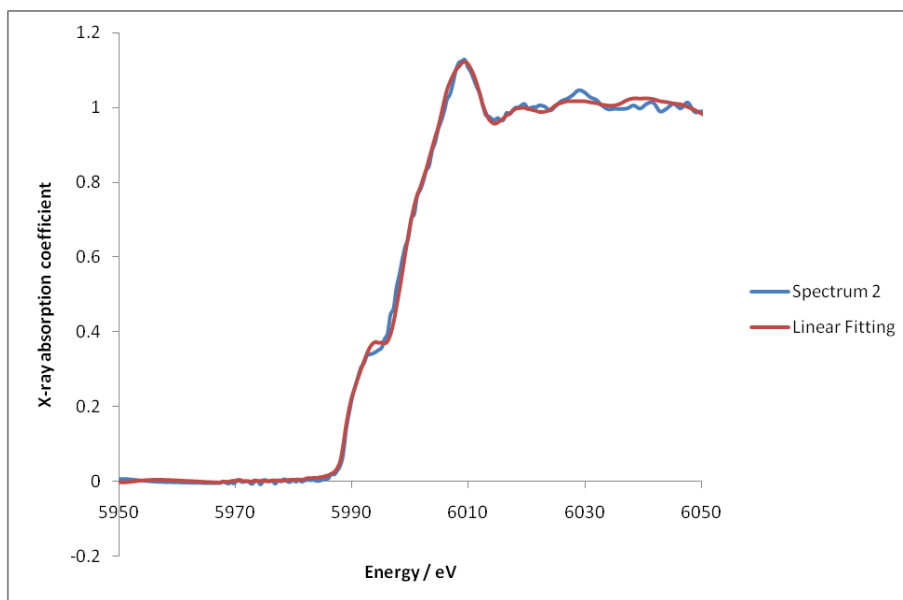
Figure 11.16 - Figure 11.34 show the XANES spectra collected around the chromium absorption edge from the site specific sample through three oxide cubes on the crack surface of specimen 799 (1061 MPa, 98.3 kh).

Figure 11.35 - Figure 11.38 show the XANES spectra collected around the iron absorption edge from the site specific sample through a line of oxide with mixed morphology on the crack surface of specimen 799 (1061 MPa, 98.3 kh).

Figure 11.39 - Figure 11.42 show the XANES spectra collected around the chromium absorption edge from the site specific sample through a line of oxide with mixed morphology on the crack surface of specimen 799 (1061 MPa, 98.3 kh).
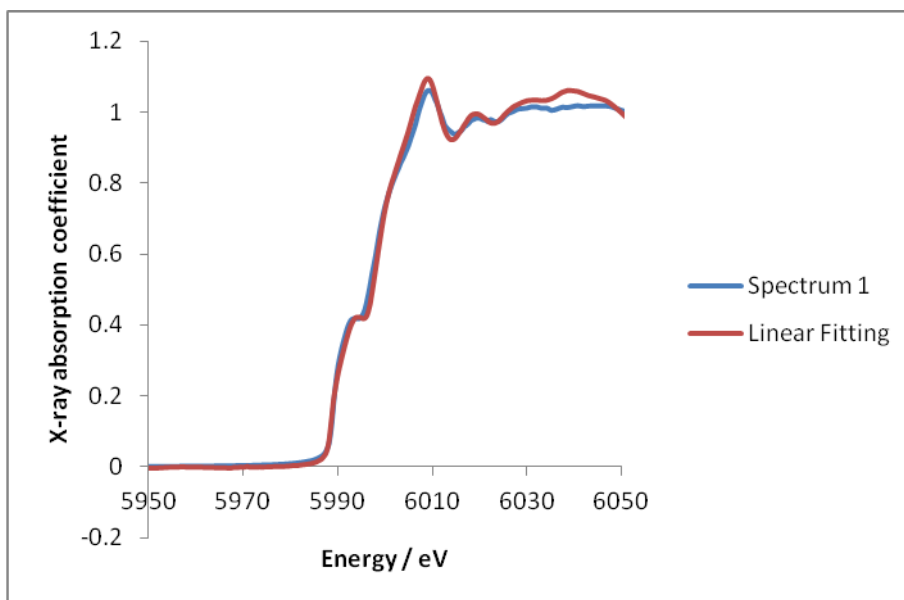
Figure 11.1: XANES spectrum 1 collected around the chromium absorption edge for the crack surface of specimen 799 (1061 MPa, 98.3 kh).
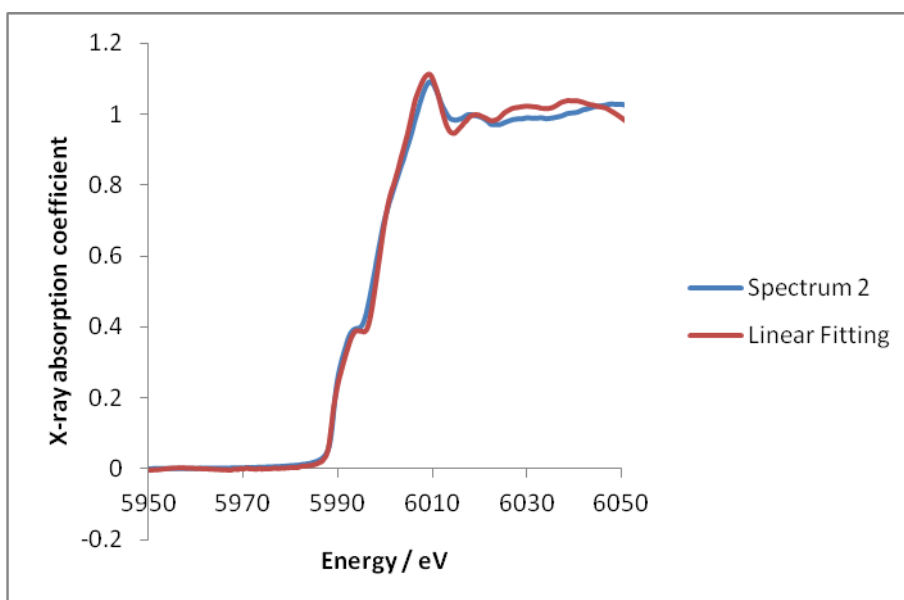
Figure 11.2: XANES spectrum 2 collected around the chromium absorption edge for the crack surface of specimen 799 (1061 MPa, 98.3 kh).
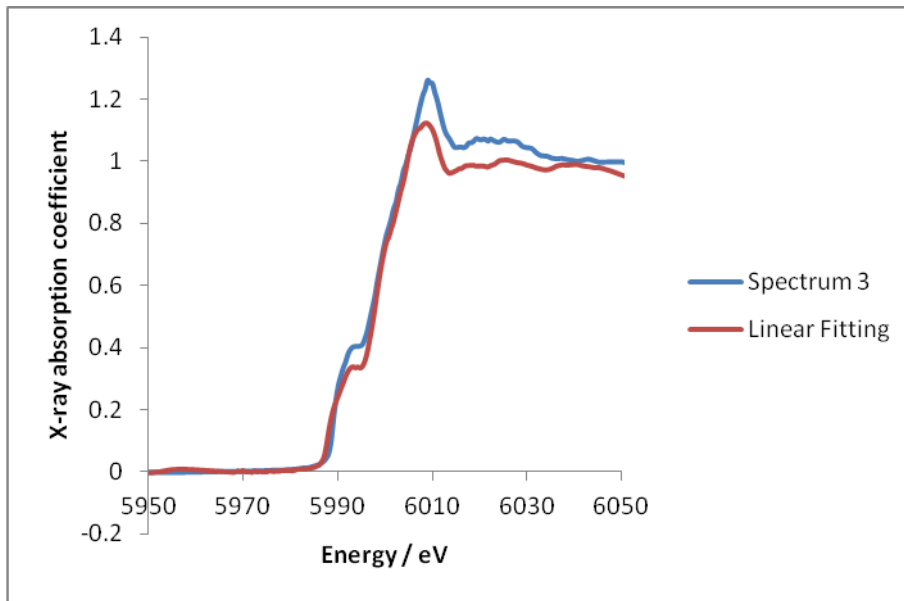
Figure 11.3: XANES spectrum 3 collected around the chromium absorption edge for the crack surface of specimen 799 (1061 MPa, 98.3 kh).
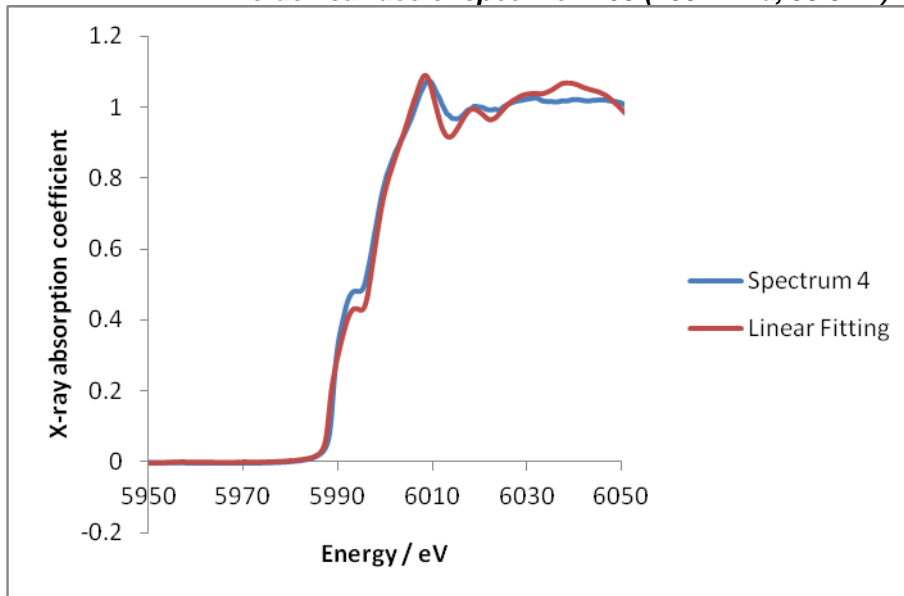
Figure 11.4: XANES spectrum 4 collected around the chromium absorption edge for the crack surface of specimen 799 (1061 MPa, 98.3 kh).
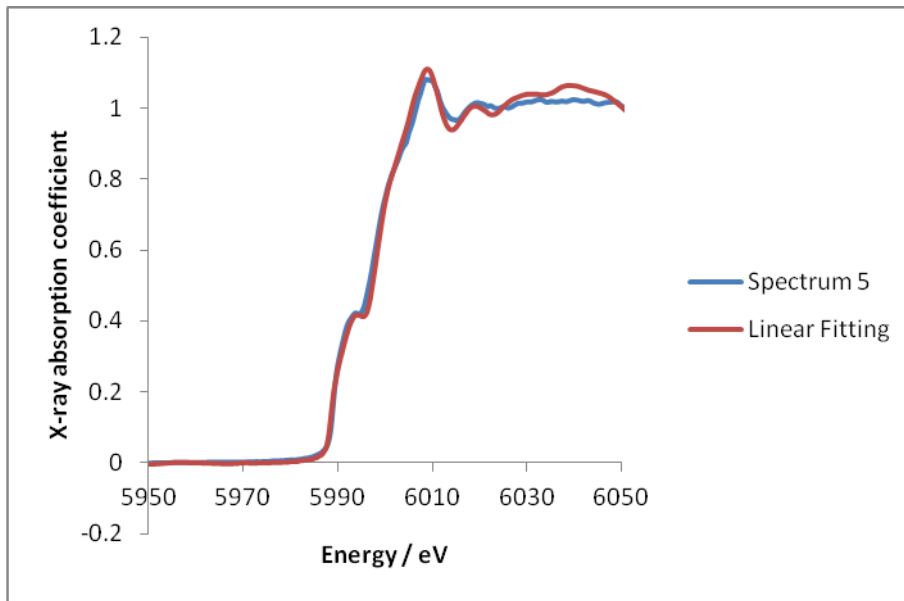
Figure 11.5: XANES spectrum 5 collected around the chromium absorption edge for the crack surface of specimen 799 (1061 MPa, 98.3 kh).
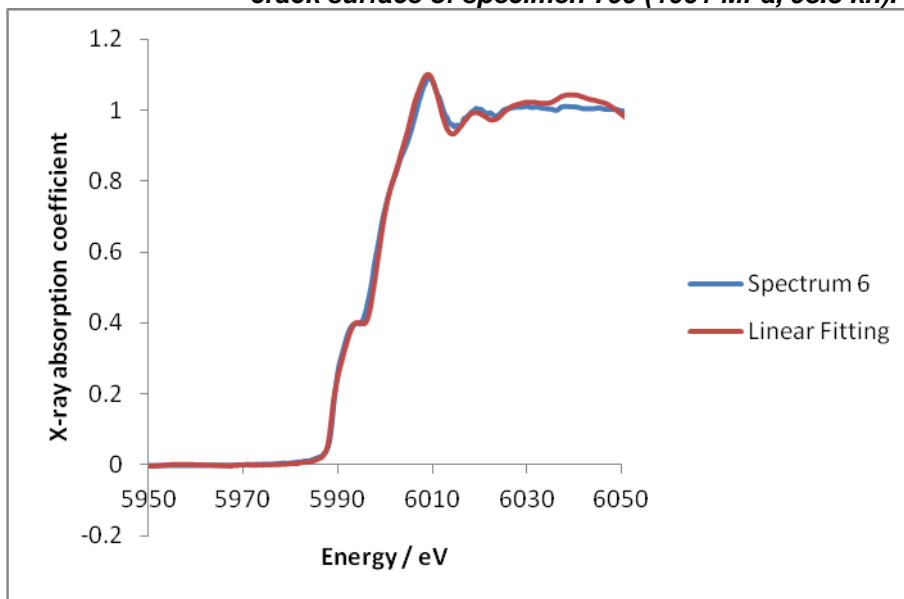
Figure 11.6: XANES spectrum 6 collected around the chromium absorption edge for the crack surface of specimen 799 (1061 MPa, 98.3 kh).
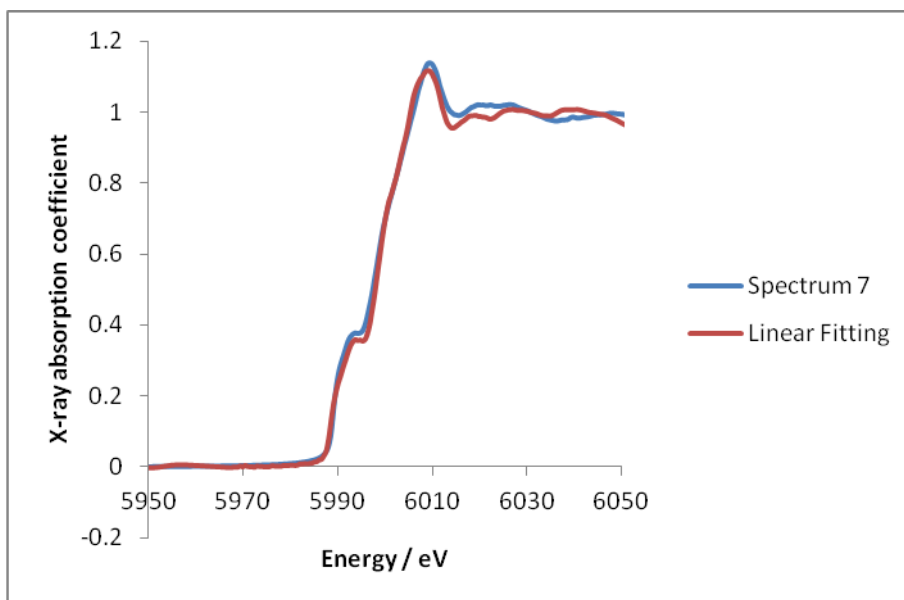
Figure 11.7: XANES spectrum 7 collected around the chromium absorption edge for the crack surface of specimen 799 (1061 MPa, 98.3 kh).
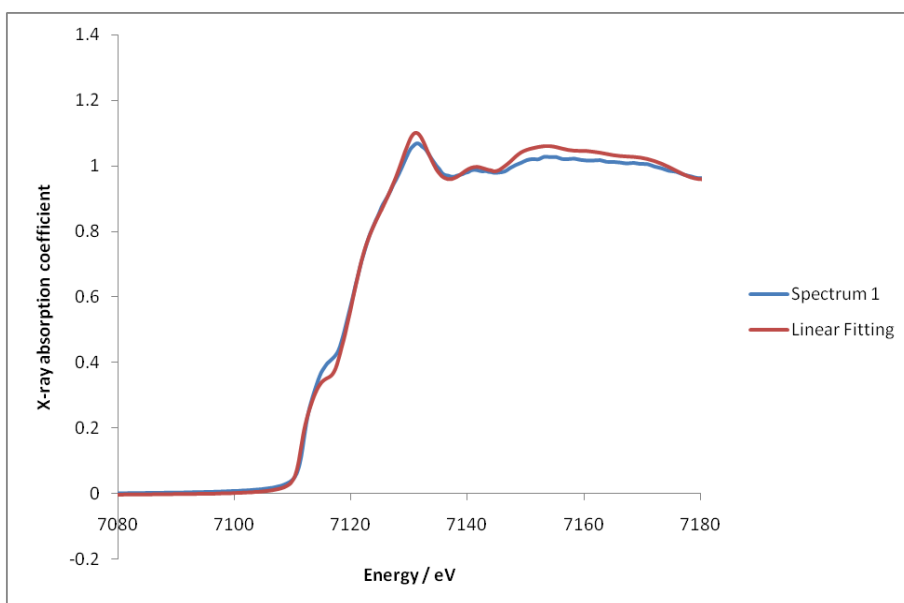
Figure 11.8: XANES spectrum 1 collected around the iron absorption edge from a site specific sample through three oxide cubes on the crack surface of specimen 799 (1061 MPa, 98.3 kh).
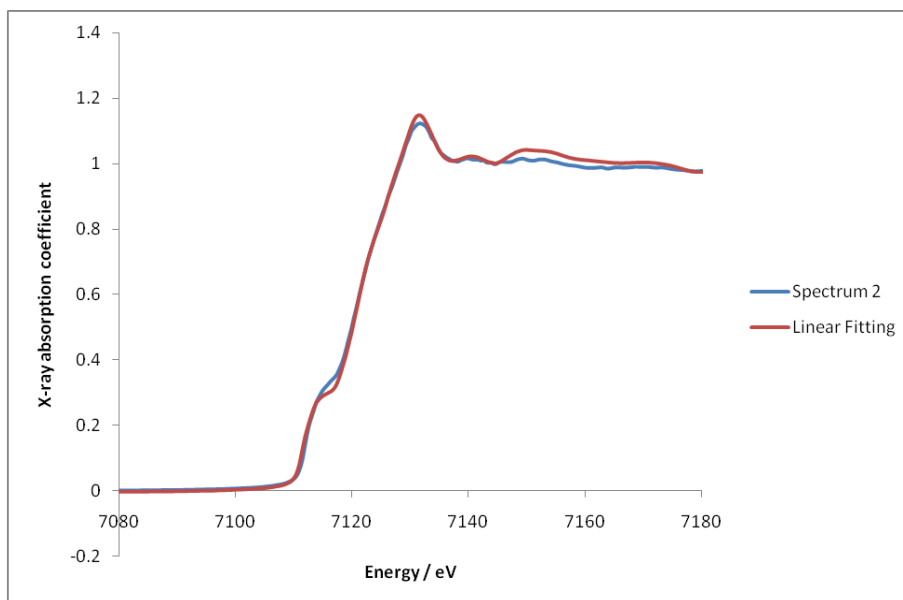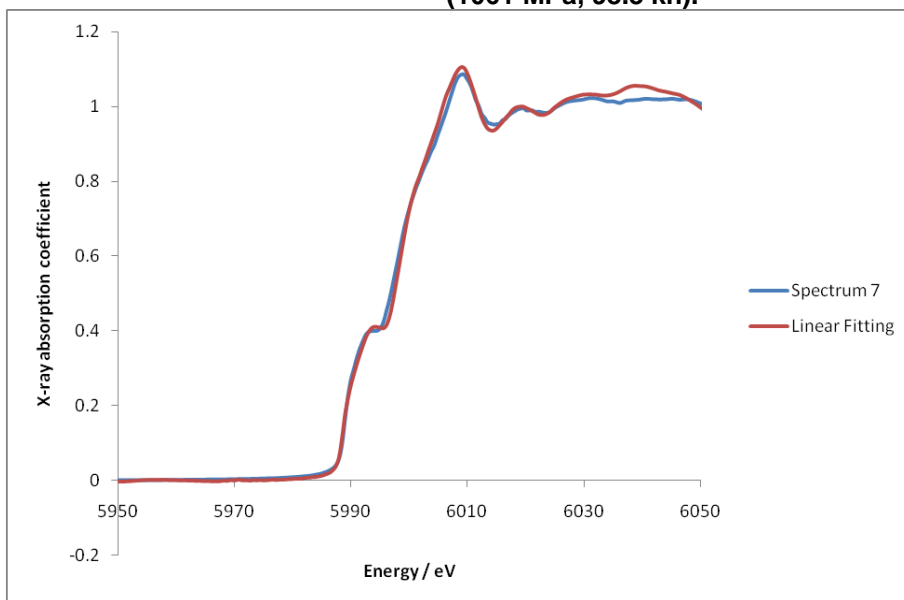
Figure 11.9: XANES spectrum 2 collected around the iron absorption edge from a site specific sample through three oxide cubes on the crack surface of specimen 799 (1061 MPa, 98.3 kh).
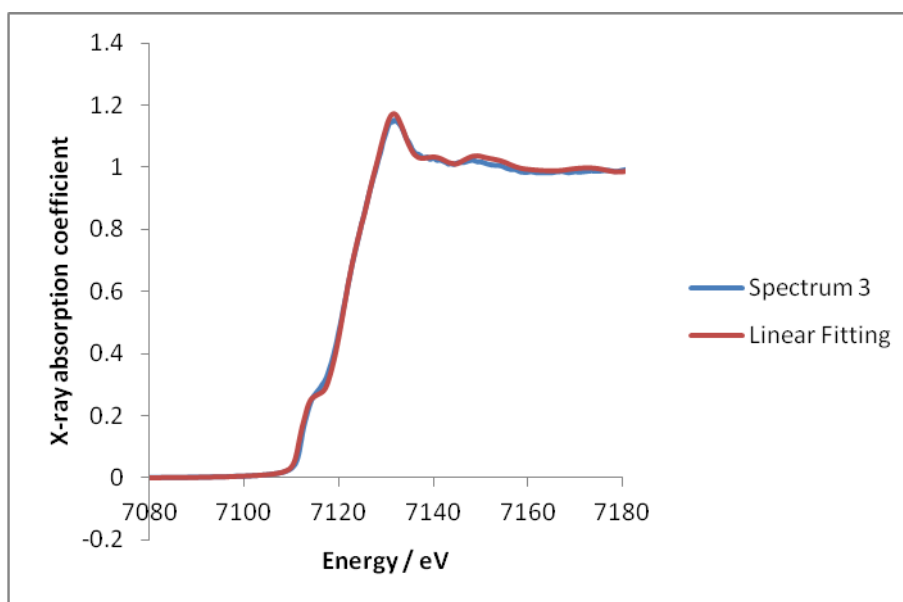
Figure 11.10: XANES spectrum 3 collected around the iron absorption edge from a site specific sample through three oxide cubes on the crack surface of specimen 799 (1061 MPa, 98.3 kh).
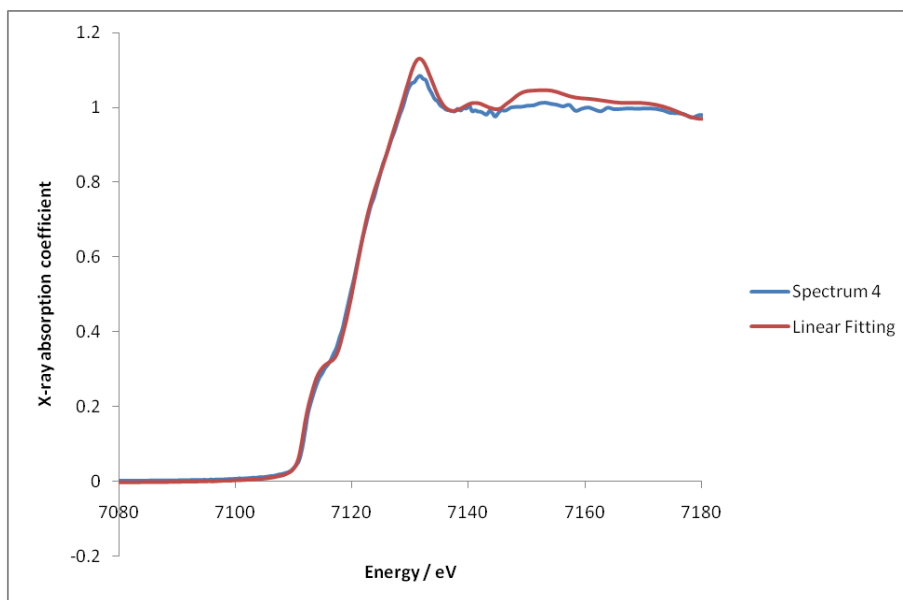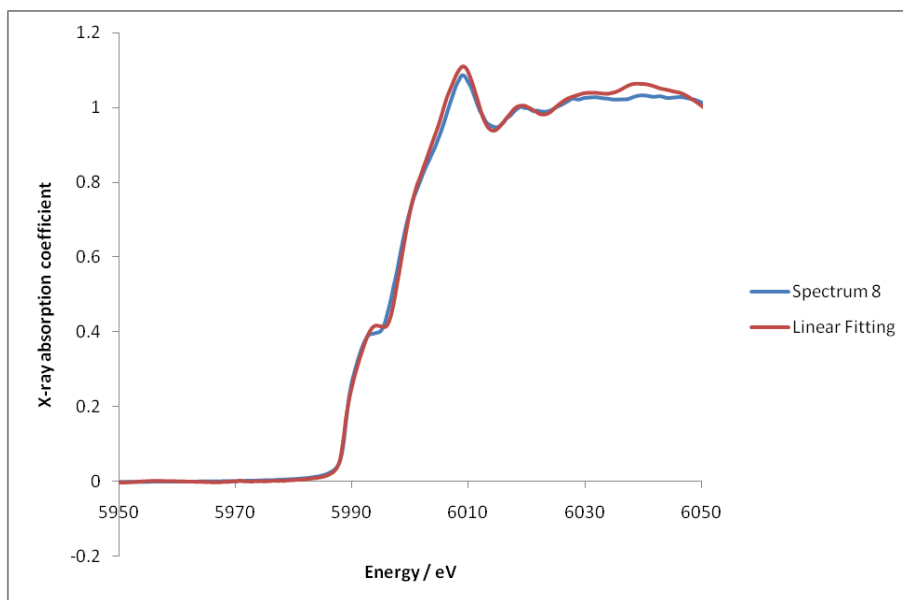
Figure 11.11: XANES spectrum 4 collected around the iron absorption edge from a site specific sample through three oxide cubes on the crack surface of specimen 799 (1061 MPa, 98.3 kh).
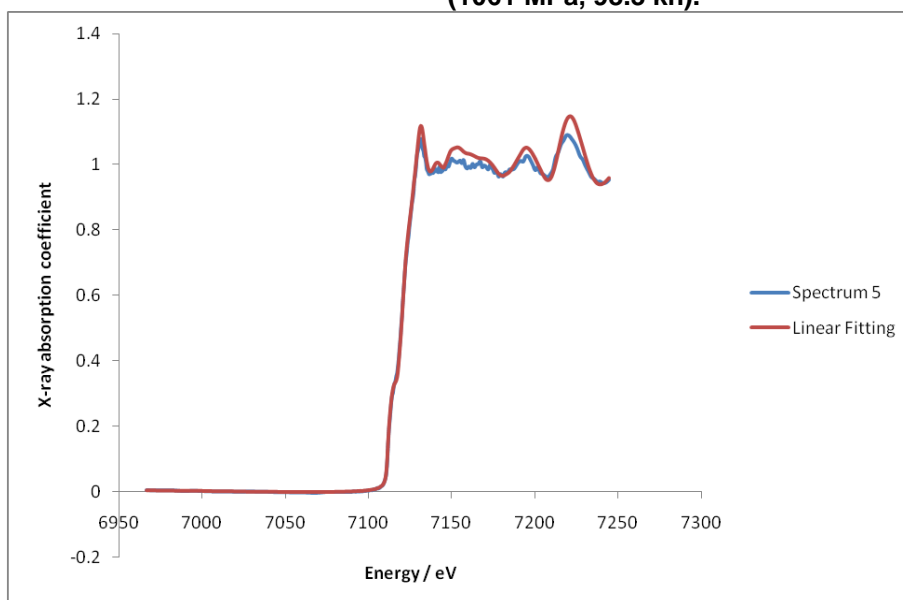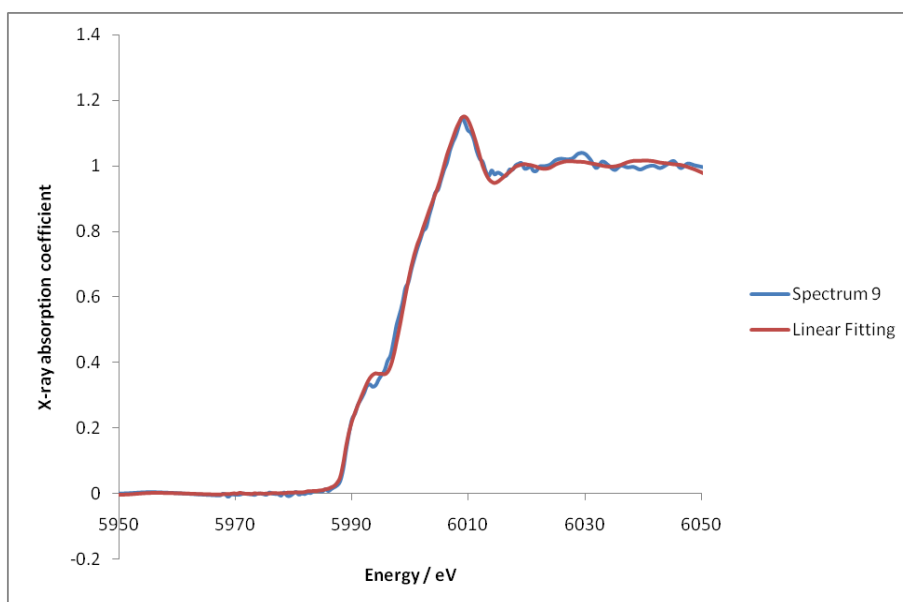

Figure 11.12: XANES spectrum 5 collected around the iron absorption edge from a site specific sample through three oxide cubes on the crack surface of specimen 799 (1061 MPa, 98.3 kh).
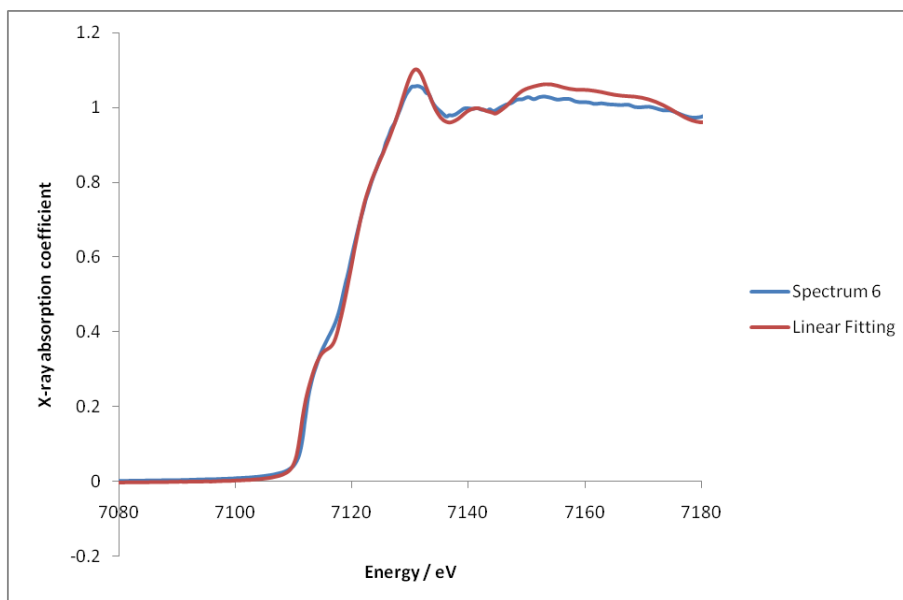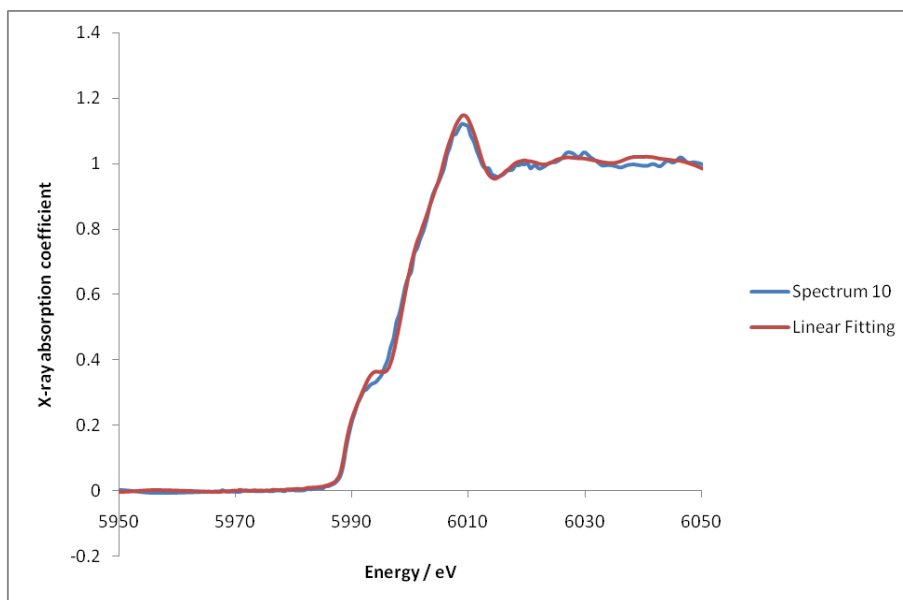
Figure 11.13: **XANES spectrum 6 collected around the iron absorption edge from a site specific sample through three oxide cubes on the crack surface of specimen 799 (1061 MPa, 98.3 kh).**
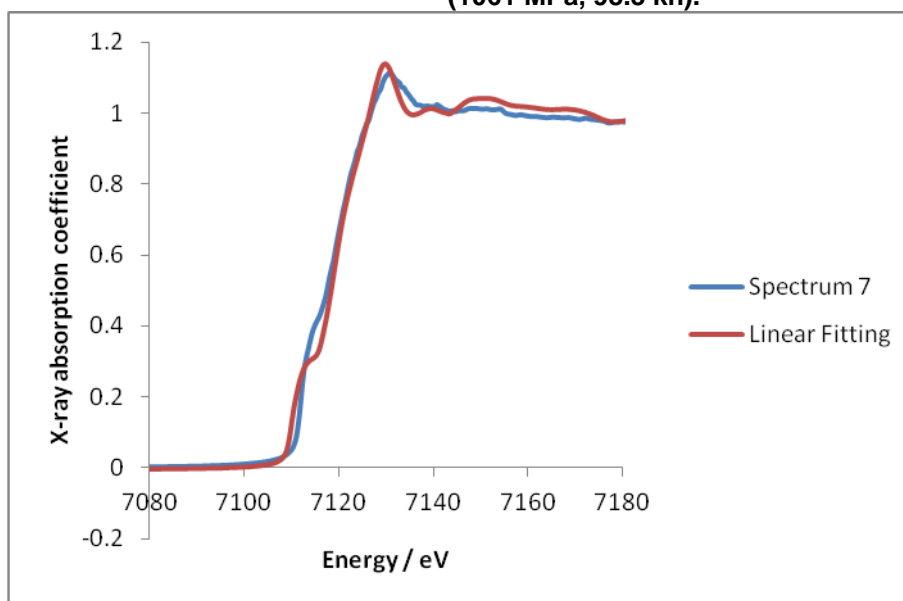
Figure 11.14: **XANES spectrum 7 collected around the iron absorption edge from a site specific sample through three oxide cubes on the crack surface of specimen 799 (1061 MPa, 98.3 kh).**

Figure 11.15: **XANES spectrum 8 collected around the iron absorption edge from a site specific sample through three oxide cubes on the crack surface of specimen 799 (1061 MPa, 98.3 kh).**

Figure 11.16: **XANES spectrum 1 collected around the chromium absorption edge from the site specific sample through three oxide cubes on the crack surface of specimen 799 (1061 MPa, 98.3 kh).**
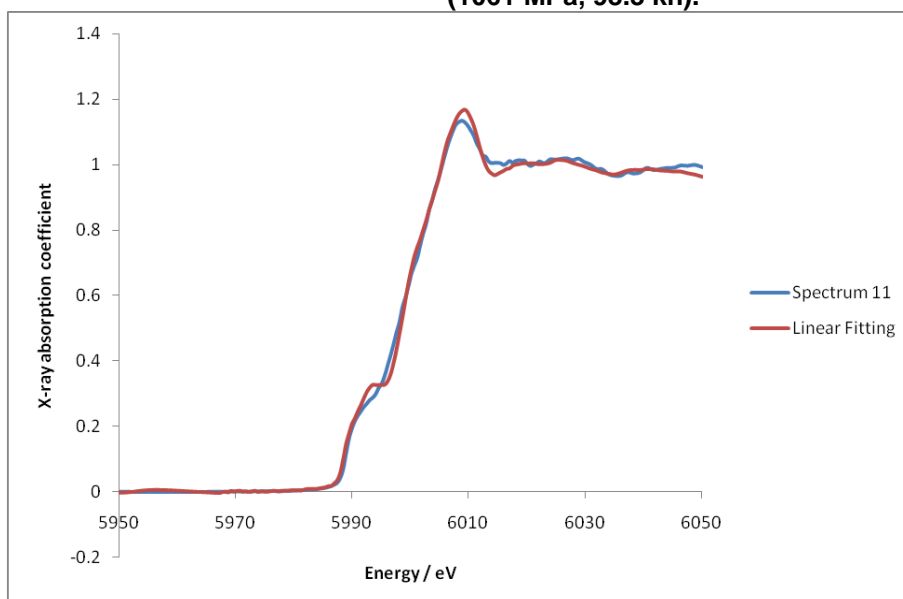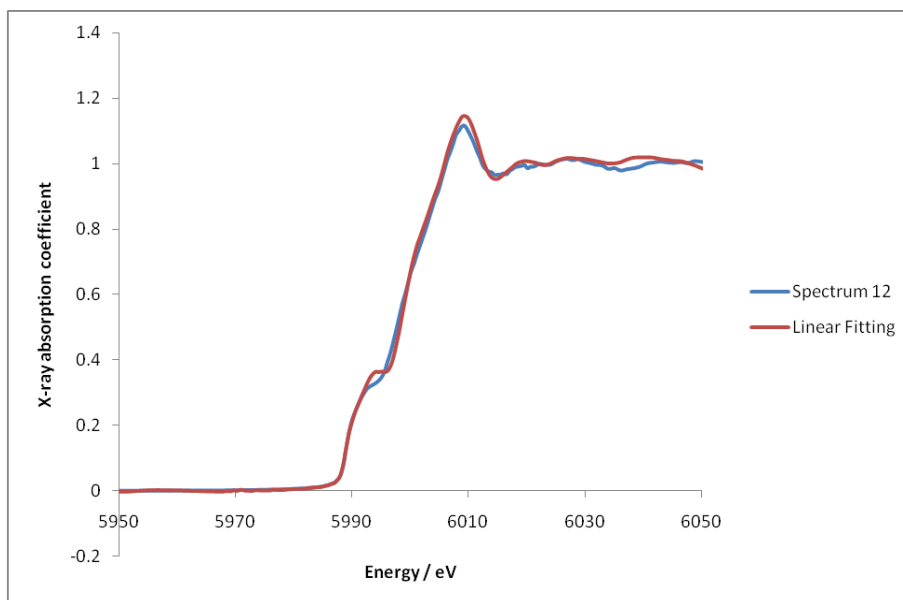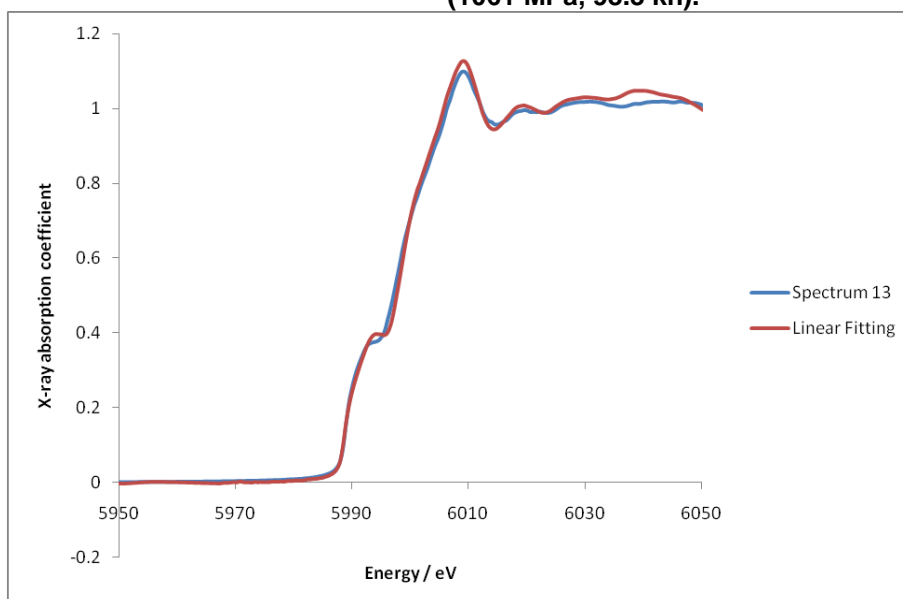
Figure 11.17: XANES spectrum 2 collected around the chromium absorption edge from the site specific sample through three oxide cubes on the crack surface of specimen 799 (1061 MPa, 98.3 kh).
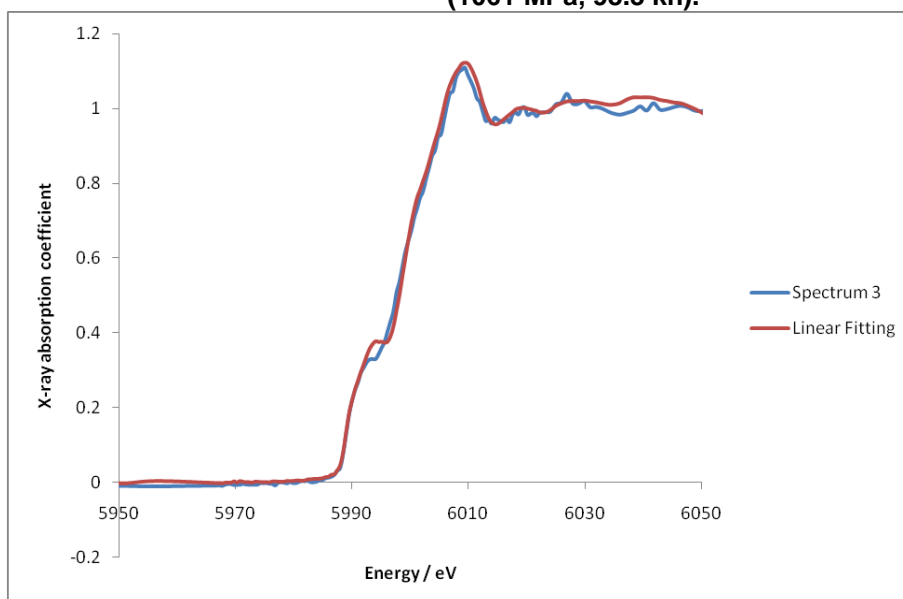
Figure 11.18: XANES spectrum 3 collected around the chromium absorption edge from the site specific sample through three oxide cubes on the crack surface of specimen 799 (1061 MPa, 98.3 kh).
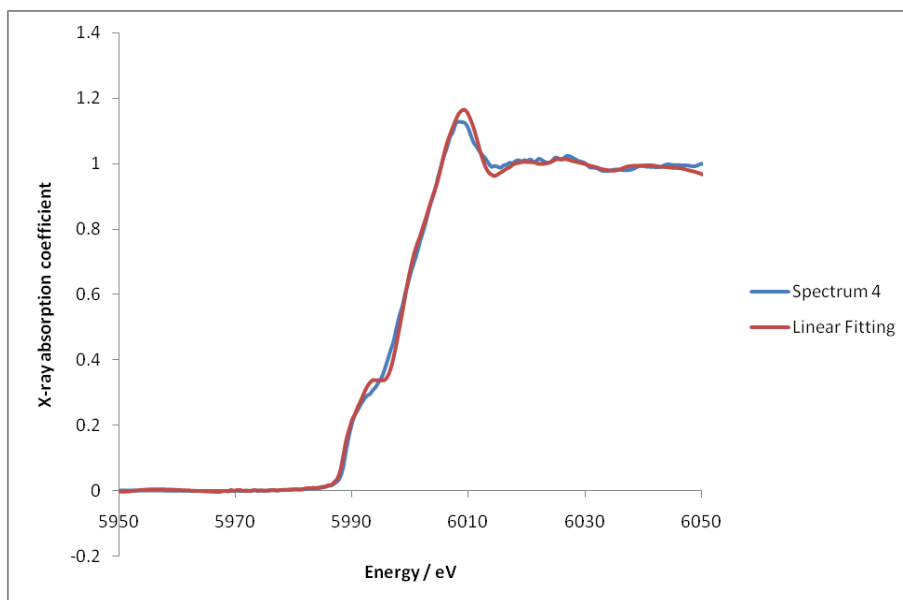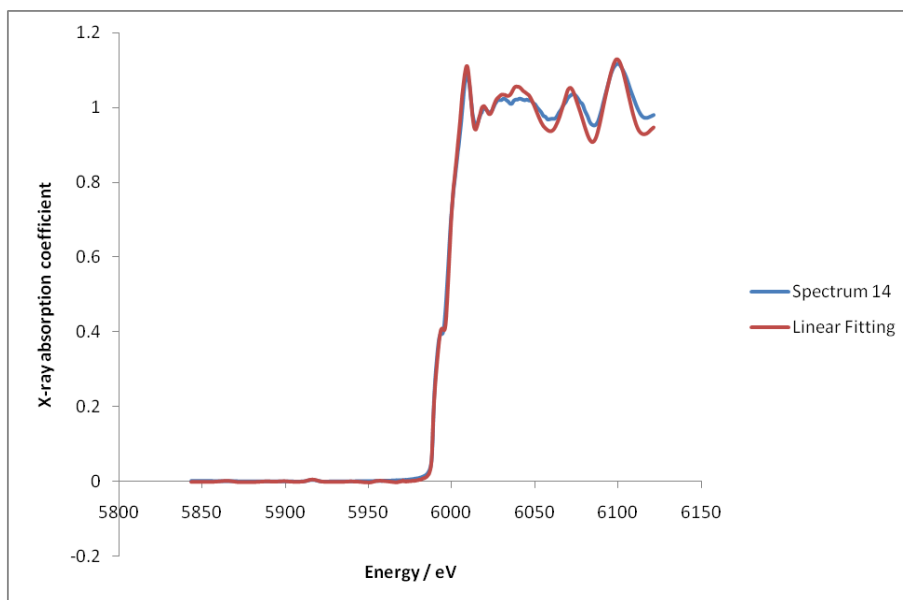
Figure 11.19: XANES spectrum 4 collected around the chromium absorption edge from the site specific sample through three oxide cubes on the crack surface of specimen 799 (1061 MPa, 98.3 kh).
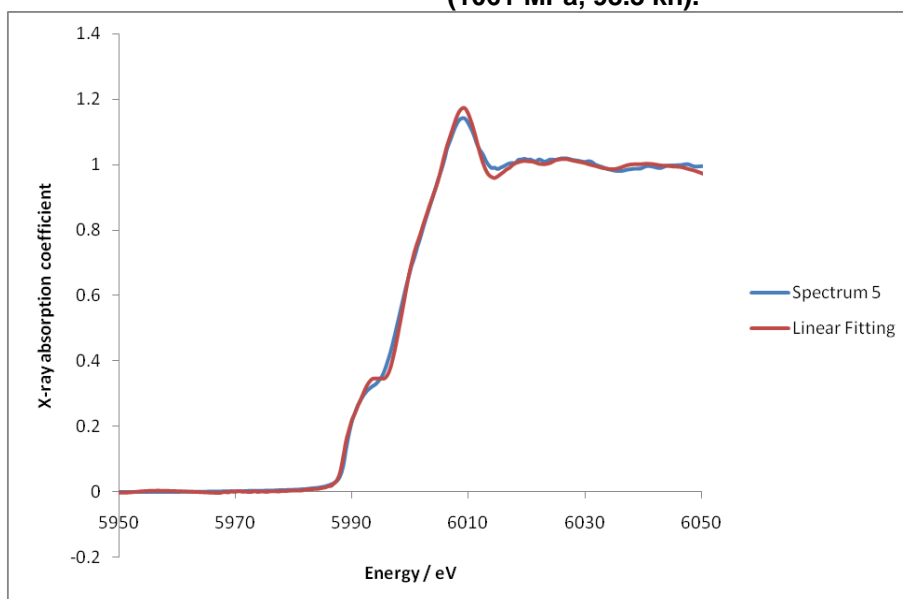
Figure 11.20: XANES spectrum 5 collected around the chromium absorption edge from the site specific sample through three oxide cubes on the crack surface of specimen 799 (1061 MPa, 98.3 kh).
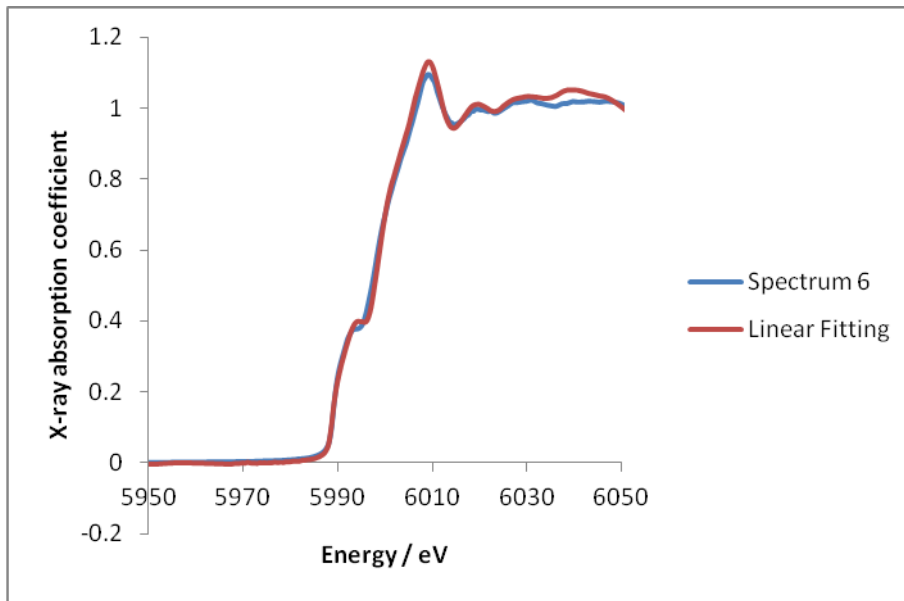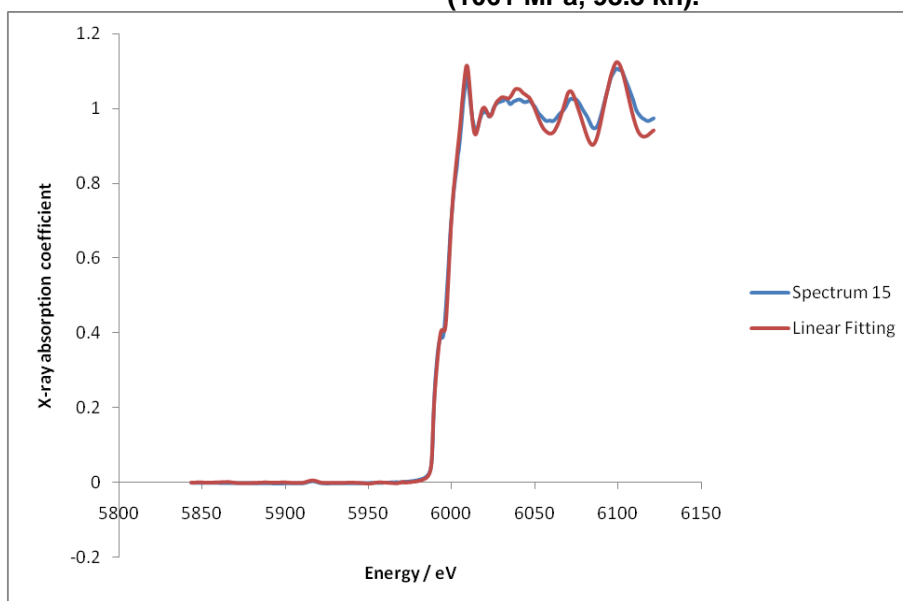
Figure 11.21: **XANES spectrum 6 collected around the chromium absorption edge from the site specific sample through three oxide cubes on the crack surface of specimen 799 (1061 MPa, 98.3 kh).**
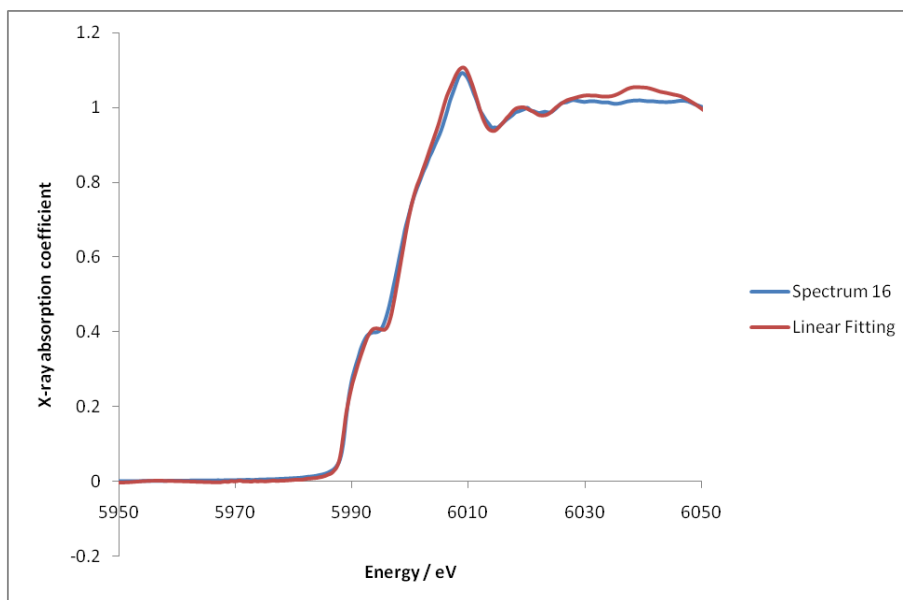

Figure 11.22: **XANES spectrum 7 collected around the chromium absorption edge from the site specific sample through three oxide cubes on the crack surface of specimen 799 (1061 MPa, 98.3 kh).**

Figure 11.23: XANES spectrum 8 collected around the chromium absorption edge from the site specific sample through three oxide cubes on the crack surface of specimen 799 (1061 MPa, 98.3 kh).
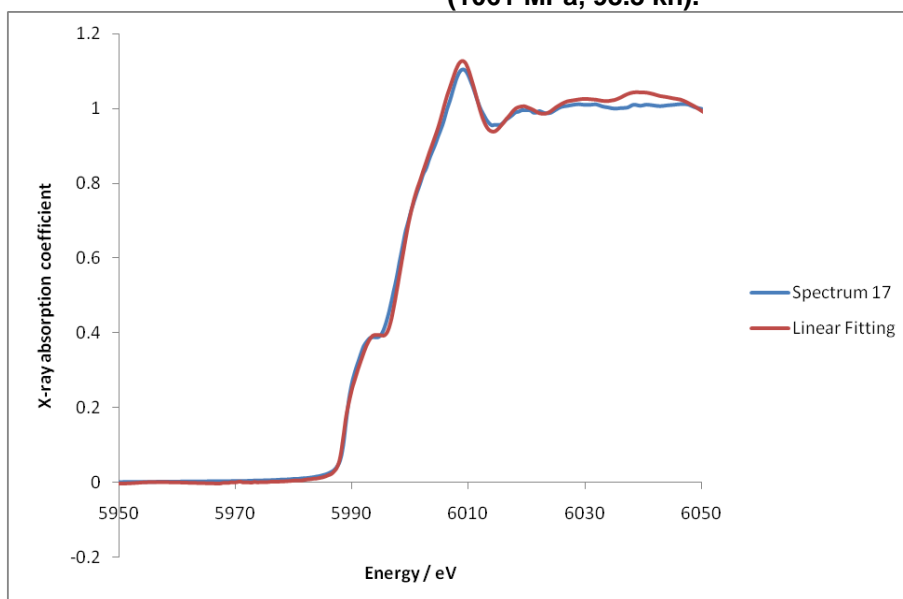

Figure 11.24: XANES spectrum 9 collected around the chromium absorption edge from the site specific sample through three oxide cubes on the crack surface of specimen 799 (1061 MPa, 98.3 kh).
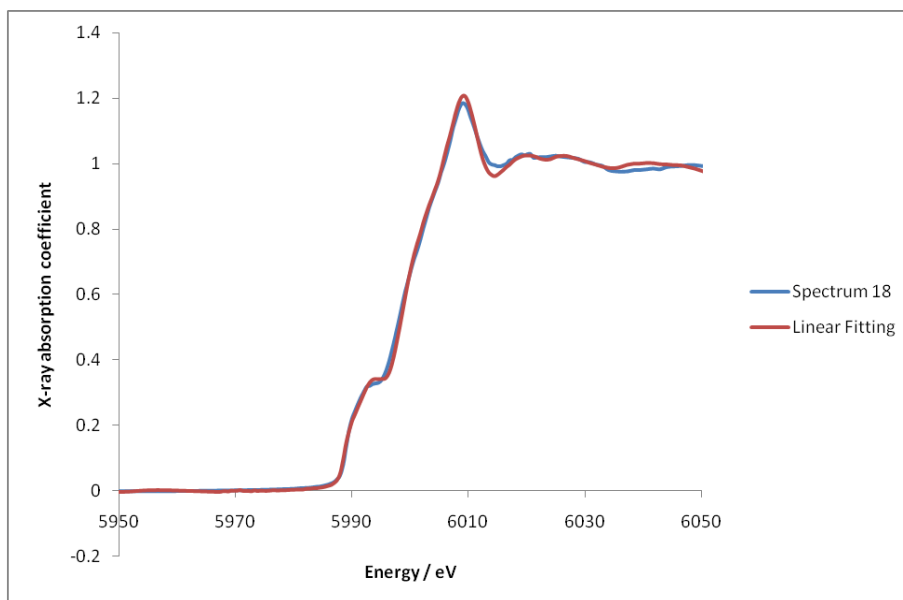
Figure 11.25: XANES spectrum 10 collected around the chromium absorption edge from the site specific sample through three oxide cubes on the crack surface of specimen 799 (1061 MPa, 98.3 kh).

Figure 11.26: XANES spectrum 11 collected around the chromium absorption edge from the site specific sample through three oxide cubes on the crack surface of specimen 799 (1061 MPa, 98.3 kh).
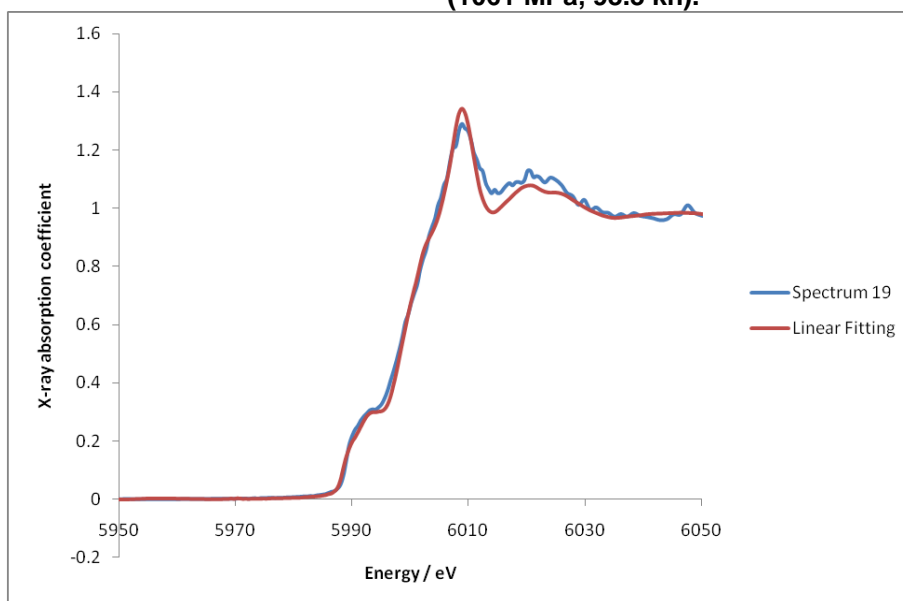
Figure 11.27: XANES spectrum 12 collected around the chromium absorption edge from the site specific sample through three oxide cubes on the crack surface of specimen 799 (1061 MPa, 98.3 kh).

Figure 11.28: XANES spectrum 13 collected around the chromium absorption edge from the site specific sample through three oxide cubes on the crack surface of specimen 799 (1061 MPa, 98.3 kh).
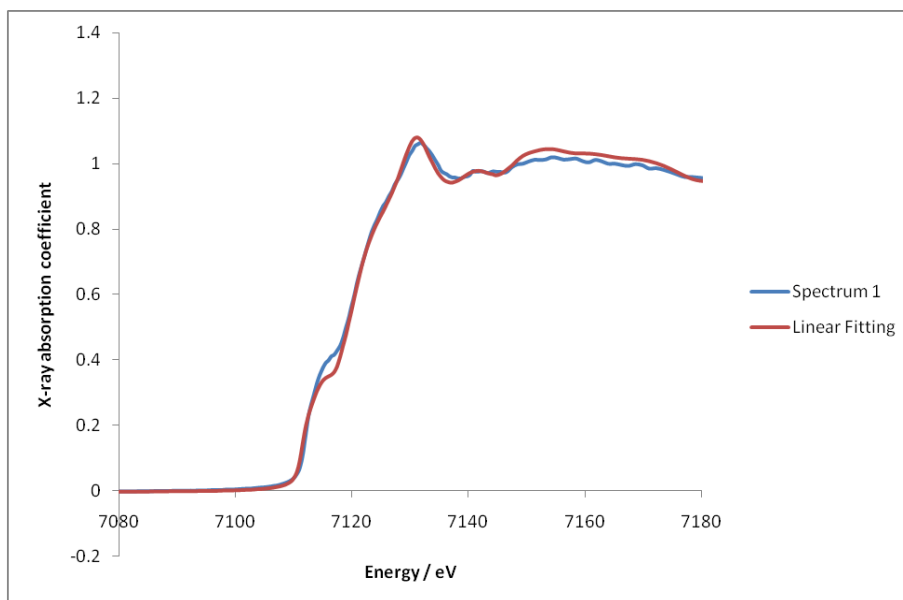
Figure 11.29: XANES spectrum 14 collected around the chromium absorption edge from the site specific sample through three oxide cubes on the crack surface of specimen 799 (1061 MPa, 98.3 kh).
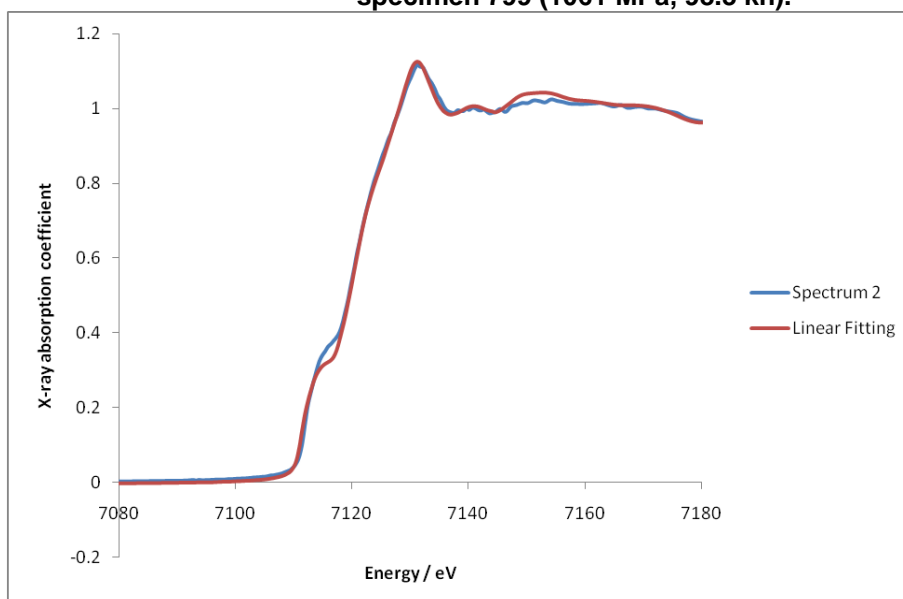

Figure 11.30: XANES spectrum 15 collected around the chromium absorption edge from the site specific sample through three oxide cubes on the crack surface of specimen 799 (1061 MPa, 98.3 kh).

Figure 11.31: **XANES spectrum 16 collected around the chromium absorption edge from the site specific sample through three oxide cubes on the crack surface of specimen 799 (1061 MPa, 98.3 kh).**
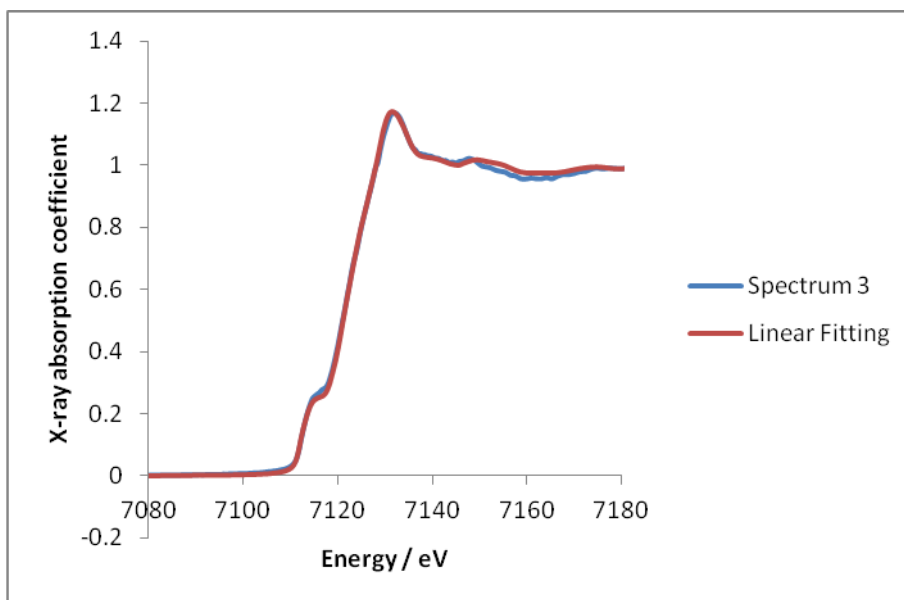

Figure 11.32: **XANES spectrum 17 collected around the chromium absorption edge from the site specific sample through three oxide cubes on the crack surface of specimen 799 (1061 MPa, 98.3 kh).**
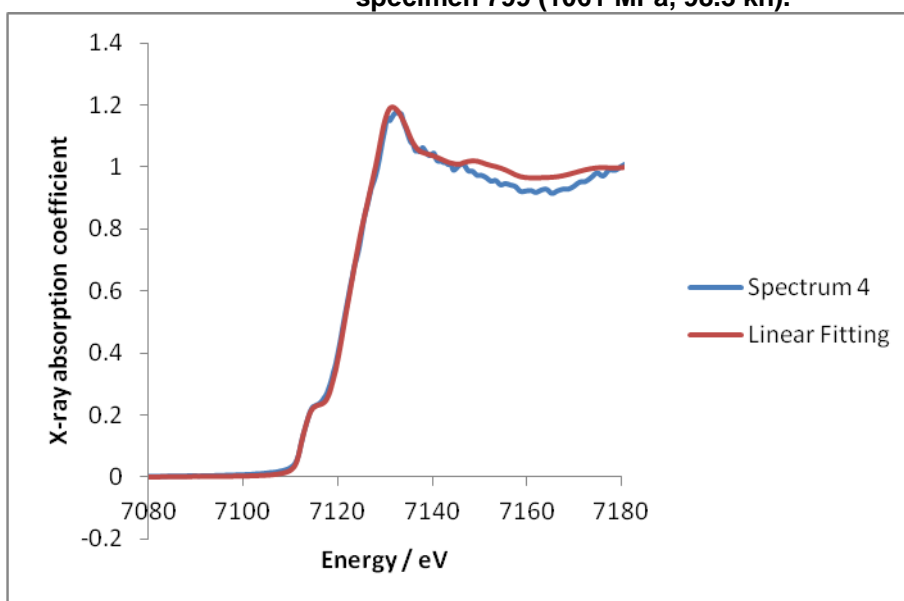
Figure 11.33: **XANES spectrum 1 collected around the chromium absorption edge from the site specific sample through three oxide cubes on the crack surface of specimen 799 (1061 MPa, 98.3 kh).**

Figure 11.34: **XANES spectrum 19 collected around the chromium absorption edge from the site specific sample through three oxide cubes on the crack surface of specimen 799 (1061 MPa, 98.3 kh).**

Figure 11.35: XANES spectrum 1 collected around the iron absorption edge from the site specific sample through a line of oxide with mixed morphology on the crack surface of specimen 799 (1061 MPa, 98.3 kh).
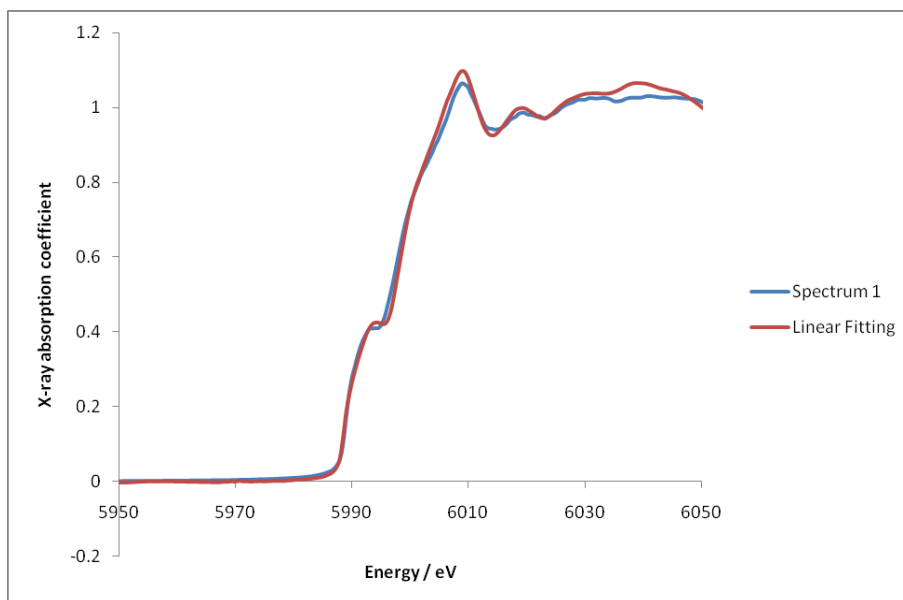

Figure 11.36: XANES spectrum 2 collected around the iron absorption edge from the site specific sample through a line of oxide with mixed morphology on the crack surface of specimen 799 (1061 MPa, 98.3 kh).

Figure 11.37: **XANES spectrum 3 collected around the iron absorption edge from the site specific sample through a line of oxide with mixed morphology on the crack surface of specimen 799 (1061 MPa, 98.3 kh).**
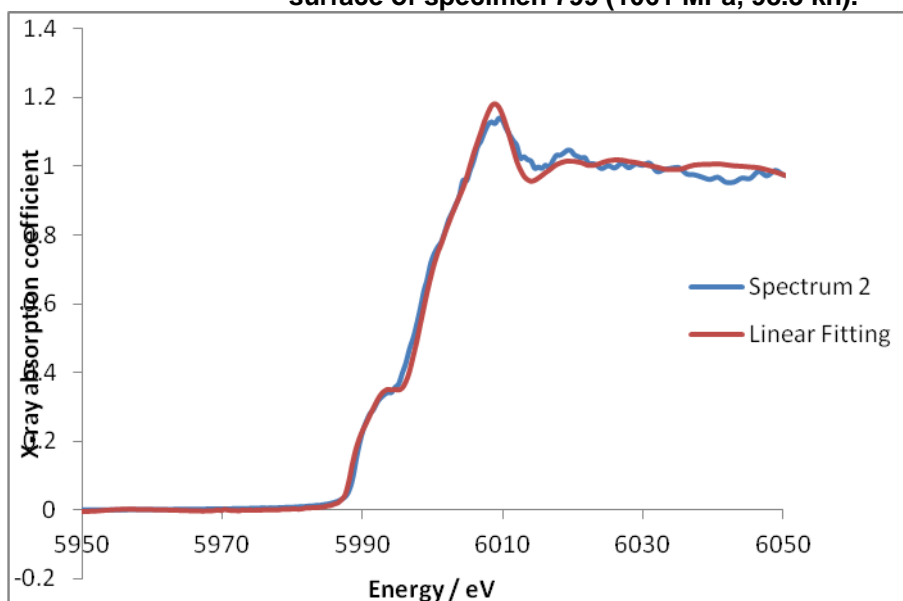

Figure 11.38: **XANES spectrum 4 collected around the iron absorption edge from the site specific sample through a line of oxide with mixed morphology on the crack surface of specimen 799 (1061 MPa, 98.3 kh).**
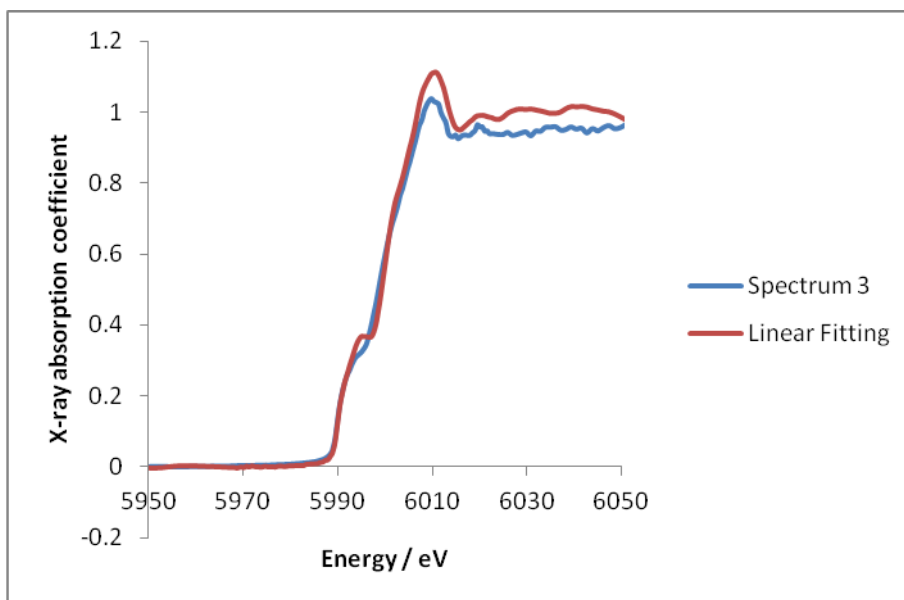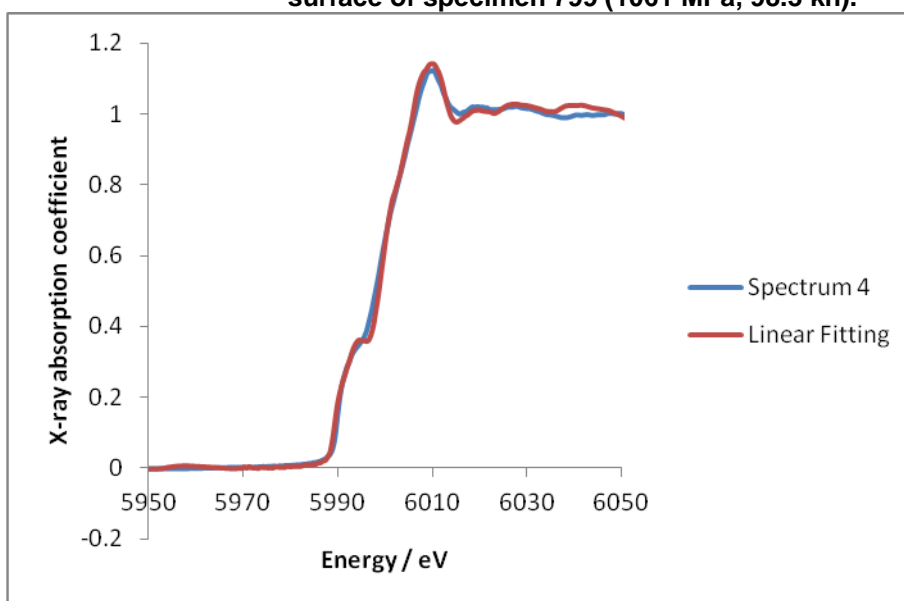
Figure 11.39: XANES spectrum 1 collected around the chromium absorption edge from the site specific sample through a line of oxide with mixed morphology on the crack surface of specimen 799 (1061 MPa, 98.3 kh).

Figure 11.40: XANES spectrum 2 collected around the chromium absorption edge from the site specific sample through a line of oxide with mixed morphology on the crack surface of specimen 799 (1061 MPa, 98.3 kh).

Figure 11.41: XANES spectrum 3 collected around the chromium absorption edge from the site specific sample through a line of oxide with mixed morphology on the crack surface of specimen 799 (1061 MPa, 98.3 kh).

Figure 11.42: XANES spectrum 4 collected around the chromium absorption edge from the site specific sample through a line of oxide with mixed morphology on the crack surface of specimen 799 (1061 MPa, 98.3 kh).